LHCb 上质子质子对撞中
粲偶素产生的实验研究

Experimental study of charmonium production in *pp* collisions at LHCb

(申请清华大学理学博士学位论文)

培 养 单 位： 工程物理系

学　　科： 物理学

研 究 生： 许　　立

指 导 教 师： 朱 相 雷　副教授

二〇二三年八月

Experimental study of charmonium production in pp collisions at LHCb

Dissertation submitted to

Tsinghua University

in partial fulfillment of the requirement

for the degree of

Doctor of Philosophy

in

Physics

by

Li Xu

Dissertation Supervisor: Professor Xianglei Zhu

August, 2023

公开评阅人和答辩委员会名单

公开评阅人名单

无（全隐名评阅）

答辩委员会名单

主席	王青	教授	清华大学
委员	CHEN SHAOMIN	教授	清华大学
	张黎明	副教授	清华大学
	杨振伟	教授	北京大学
	刘晓辉	教授	北京师范大学
	朱相雷	副教授	清华大学
秘书	屈三强	助理研究员	清华大学

关于学位论文使用授权的说明

本人完全了解清华大学有关保留、使用学位论文的规定，即：

清华大学拥有在著作权法规定范围内学位论文的使用权，其中包括：（1）已获学位的研究生必须按学校规定提交学位论文，学校可以采用影印、缩印或其他复制手段保存研究生上交的学位论文；（2）为教学和科研目的，学校可以将公开的学位论文作为资料在图书馆、资料室等场所供校内师生阅读，或在校园网上供校内师生浏览部分内容；（3）根据《中华人民共和国学位条例暂行实施办法》及上级教育主管部门具体要求，向国家图书馆报送相应的学位论文。

本人保证遵守上述规定。

作者签名：许立　　导师签名：[illegible]

日　　期：2023.5.26　　日　　期：2023.5.26

摘 要

量子色动力学（QCD）是描述强相互作用的基本理论。其在高能标下可以用微扰方法计算，但在低能标下的非微扰效应往往要用有效模型进行描述，且需要实验结果作为输入。在质子-质子（pp）对撞中，粲偶素的产生可以被因子化成微扰计算与非微扰参数化的两部分，是检验微扰 QCD 方法和研究非微扰效应的理想过程。本论文基于大型强子对撞机底夸克探测器（LHCb）采集的 pp 对撞数据，测量粲偶素及粲偶素对的产生并研究其产生机制，检验 QCD 理论。

利用 LHCb 采集的质心系能量 $\sqrt{s} = 5\,\text{TeV}$、积分亮度为 $9.13\,\text{pb}^{-1}$ 的 pp 对撞数据, 本论文测量了瞬发 J/ψ 介子和来自底强子衰变的 J/ψ 介子的产生截面随横动量 p_T 与快度 y 的变化关系。测量覆盖的运动学范围是 $p_\text{T} < 20\,\text{GeV}/c$ 和 $2.0 < y < 4.5$。本分析还计算了 $\sqrt{s} = 8$、$13\,\text{TeV}$ 的 J/ψ 介子截面与 $5\,\text{TeV}$ 截面的比值，精确检验了基于非相对论 QCD（NRQCD）因子化的理论预言和微扰 QCD 框架下固定项加次领头对数项（FONLL）的计算结果。对于瞬发 J/ψ 介子的比值，在高 p_T 区间，实验结果与次领头阶 NRQCD 的预言相符；在低 p_T 区间，实验结果与色玻璃凝聚有效理论与 NRQCD 相结合给出的预言不一致，说明理论上可能需要考虑额外的修正。对于来自底强子的 J/ψ 介子的比值，实验结果与 FONLL 的计算结果相符。

在 pp 对撞中，粲偶素对的产生来自两种过程：单部分子散射（SPS）和双部分子散射（DPS）。粲偶素对在 SPS 中的产生过程可以用来研究质子中胶子的横动量依赖（TMD）分布函数。这些非微扰的分布函数需要从实验中提取。对 DPS 的研究可以提供质子中部分子之间的关联信息。基于 LHCb 采集的 $\sqrt{s} = 13\,\text{TeV}$、积分亮度为 $4.18\,\text{fb}^{-1}$ 的 pp 对撞数据，本论文分别测量了 J/ψ 介子对和 J/ψ-$\psi(2S)$ 介子对的产生截面，及其随多个运动学变量的变化关系。测量覆盖的 J/ψ 和 $\psi(2S)$ 介子运动学范围是 $p_\text{T} < 14\,\text{GeV}/c$ 和 $2.0 < y < 4.5$。对于 J/ψ 介子对，本分析在统计上区分了 DPS 与 SPS 的贡献，并且从 DPS 贡献中提取出了有效截面 σ_eff。在 SPS 贡献中，利用 J/ψ 介子对的 p_T 谱和 J/ψ 介子的方位角分布研究了胶子的 TMD 分布函数。受限于数据样本的大小，没有观察到理论预言的 p_T 谱随质量增大而变宽的现象。测量出的方位角不对称性的显著度约为两倍标准差，暗示非极化质子中可能存在线性极化的胶子。测量精度同样主要受限于数据样本的统计涨落。随着 LHCb 实验升级后新数据采集的开展，有希望以更高的精度检验上述假设。

关键词：强相互作用；粲偶素；产生截面；质子-质子散射；LHCb 实验

ABSTRACT

Quantum chromodynamics (QCD) is the fundamental theory of the strong interaction between quarks and gluons. One of the most important properties of QCD is that the coupling constant increases with decreasing energy scale. The perturbative theory can be applied at large momentum transfer, while the non-perturbative effects at small momentum transfer challenge theoretical calculations and usually need to be described by effective theories or phenomenological models with inputs from experiments. Charmonium production in proton-proton (pp) collisions can be factorised into perturbative and non-perturbative parts separately, providing an ideal system not only to test the perturbative QCD framework but also to probe the non-perturbative effects. In this thesis, charmonium production and double charmonium production in pp collisions are measured using data collected by the LHCb experiment. These measurements are helpful to deeply understand the charmonium production mechanism and to test QCD predictions.

Production cross-sections of J/ψ mesons in pp collisions at a centre-of-mass energy of $\sqrt{s} = 5\,\text{TeV}$ are measured using a data sample corresponding to an integrated luminosity of $9.13\,\text{pb}^{-1}$ collected by the LHCb experiment. The cross-sections are measured differentially as a function of transverse momentum, p_T, and rapidity, y, and separately for J/ψ mesons produced promptly and from b-hadron decays (non-prompt) in the range $p_\text{T} < 20\,\text{GeV}/c$ and $2.0 < y < 4.5$. The J/ψ production cross-section ratios between 8 TeV and 5 TeV, and between 13 TeV and 5 TeV are also determined in order to provide precise tests of theoretical predictions, including the calculations based on the non-relativistic QCD (NRQCD) factorisation for prompt J/ψ mesons and the fixed order plus next-to-leading logarithms (FONLL) calculations in the framework of perturbative QCD for non-prompt J/ψ mesons. The measured prompt J/ψ cross-section ratios are in good agreement with next-to-leading order NRQCD calculations in the high-p_T region, but in the low-p_T region, a small tension is observed between the measured ratios of prompt J/ψ mesons and predictions from the framework combining colour glass condensate effective theory and NRQCD factorisation, which may indicate the need for further corrections in the theory model. The FONLL calculations describe the measured results for non-prompt J/ψ mesons well.

In pp collisions, double charmonium can be produced via the process of either single

parton scattering (SPS) or double parton scattering (DPS). The study of double charmonium production in SPS helps to further understand charmonium production mechanism. It is also an ideal process to probe the gluon transverse momentum dependent (TMD) parton distribution functions (PDFs). These non-perturbative gluon TMD PDFs remain very poorly known and need to be extracted from experiments. The study of DPS process provides valuable information on the correlations of the partons inside the proton. In this thesis, production cross-sections of di-J/ψ and J/ψ-$\psi(2S)$ in pp collisions at $\sqrt{s} = 13\,\text{TeV}$ are measured using a data sample corresponding to an integrated luminosity of $4.18\,\text{fb}^{-1}$ collected by the LHCb experiment. The measurement is performed with J/ψ and $\psi(2S)$ mesons in the range $p_\text{T} < 14\,\text{GeV}/c$ and $2.0 < y < 4.5$. The differential cross-sections of di-J/ψ and J/ψ-$\psi(2S)$ production as functions of several kinematic variables are also measured. For di-J/ψ production, DPS and SPS contributions are separated based on the study of the differential cross-section as a function of the absolute difference in the rapidities Δy between two J/ψ mesons. The extracted effective cross-section σ_eff from the DPS contribution is compatible with other extracted values from different measurements. For SPS process, the di-J/ψ transverse momentum $p_\text{T}^{\text{di-}J/\psi}$ spectra are measured in different intervals of di-J/ψ invariant mass $m_{\text{di-}J/\psi}$ in order to study the dependence of gluon TMD PDFs on scale. No obvious broadening of the $p_\text{T}^{\text{di-}J/\psi}$ spectrum with increasing $m_{\text{di-}J/\psi}$ is seen in the TMD region due to the large statistical uncertainties. As a probe of the presence of linearly polarised gluons inside unpolarised protons, the distribution of azimuthal angle ϕ_CS of one J/ψ meson in the Collins-Soper frame is studied in the TMD region. A hint with a significance of two standard deviations for azimuthal asymmetry is seen, but the precision is still limited by the large statistical fluctuation. With the following data taking after the LHCb upgrade, it is very promising to extract more precise information from the production cross-sections, and test the predictions of gluon TMD PDFs with higher precision.

Keywords: Strong Interaction; Charmonium; Production Cross-Section; Proton-Proton Scattering; LHCb Experiment

TABLE OF CONTENTS

LIST OF FIGURES

LIST OF TABLES

LIST OF SYMBOLS AND ACRONYMS

2D	Two Dimensional
ALICE	An experiment at the Large Hadron Collider
ATLAS	An experiment at the Large Hadron Collider
BNL	Brookhaven National Laboratory
CB	Crystal Ball function
CDF	An experiment at the Tevatron
CERN	European Organisation for Nuclear Research
CGC	Color Glass Condensate
CMS	An experiment at the Large Hadron Collider
CS	An acronym of Collins-Soper equation or Collins-Soper frame
D0	An experiment at the Tevatron
DGLAP	An acronym of Dokshitzer-Gribov-Lipatov-Altarelli-Parisi equation
DIS	Deep Inelastic Scattering
DPS	Double Parton Scattering
DSCB	Double-Sided Crystal Ball function
ECAL	Electromagnetic CALorimeter
FONLL	Fixed Order plus Next-to-Leading Logarithms
GEC	Global Event Cut
GIM	Glashow–Iliopoulos–Maiani mechanism
HCAL	Hadronic CALorimeter
HERA	Hadron-Electron Ring Accelerator
HLT	High-Level Trigger implemented in software
IP	Impact Parameter
IT	Inner Tracker
KDE	Kernel Density Estimation
L0	Level-0 trigger implemented in hardware
LDME	Long-Distance Matrix Element
LEP	Large Electron-Positron collider
LHC	Large Hadron Collider
LHCb	An experiment at the Large Hadron Collider
LO	Leading Order
MagDown	Magnet field direction pointing Downward

MagUp	Magnet field direction pointing Upward
MC	Monte Carlo
$\overline{\text{MS}}$	Modified Minimal Subtraction
NA3	An experiment at the Super Proton Synchrotron
NLL	Next-to-Leading Logarithms
NLO	Next-to-Leading Order
NLO* CS	Incomplete Next-to-Leading Order Color-Singlet prediction
NNLO	Next-to-Next-to-Leading Order
NRQCD	Non-Relativistic Quantum ChromoDynamics
nSPDHits	Number of hits in the Scintillating-Pad Detector
OT	Outer Tracker
OZI	Okubo-Zweig-Iizuka rule
PDF	Parton Distribution Function
pA	Proton-Nucleus
PID	Particle IDentification
pp	Proton-Proton
$p\overline{p}$	Proton-Antiproton
pQCD	Perturbative Quantum ChromoDynamics
PS	PreShower detector
PV	Primary Vertex
QCD	Quantum ChromoDynamics
QED	Quantum ElectroDynamics
RG	Renormalisation Group
RICH	Ring-Imaging CHerenkov detector
Run 1	First period of operation of the Large Hadron Collider
Run 2	Second period of operation of the Large Hadron Collider
Run 3	Third period of operation of the Large Hadron Collider
SDC	Short-Distance Coefficient
SLAC	Stanford Linear Accelerator Center
SPD	Scintillating-Pad Detector
SPS	Single Parton Scattering
T-stations	Tracking stations downstream of the magnet
Tevatron	A proton-antiproton collider
TIS	Trigger Independent of Signal
TMD	Transverse Momentum Dependent

TOS	Trigger On Signal
TT	Tracker Turicensis
VELO	VErtex LOcator

CHAPTER 1 INTRODUCTION

In November 1974, a new heavy particle with mass $m = 3100\,\mathrm{MeV}$[①] was discovered by S. Ting's research group in proton-induced reactions on beryllium target at the Brookhaven National Laboratory (BNL)[1]. The observation was made by measuring invariant mass spectrum of e^+e^-, as shown in Figure 1.1(a). Almost at the same time, another research group led by B. Richter discovered the same particle in e^+e^- annihilation at the Stanford Linear Accelerator Center (SLAC)[2]. A very sharp peak is observed in the cross-section for $e^+e^- \to$ hadrons, $\mu^+\mu^-$, e^+e^-, *etc.*, as shown in Figure 1.1(b). This particle was named as J particle by Ting's group and ψ particle by Richter's group, and finally is referred to as J/ψ particle. Only a few days after the discovery of J/ψ particle, another resonant state with a slightly higher mass $m = 3695\,\mathrm{MeV}$, which was called ψ'

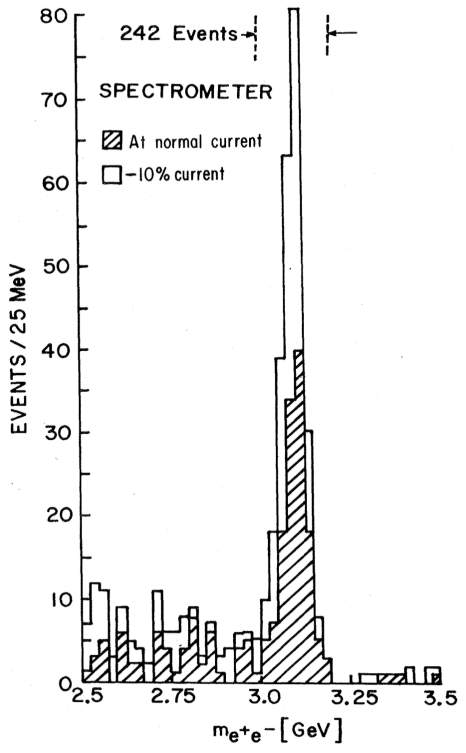

(a) Invariant mass spectrum of e^+e^- in proton-induced reactions on beryllium target showing the existence of J particle. The figure is taken from Ref. [1].

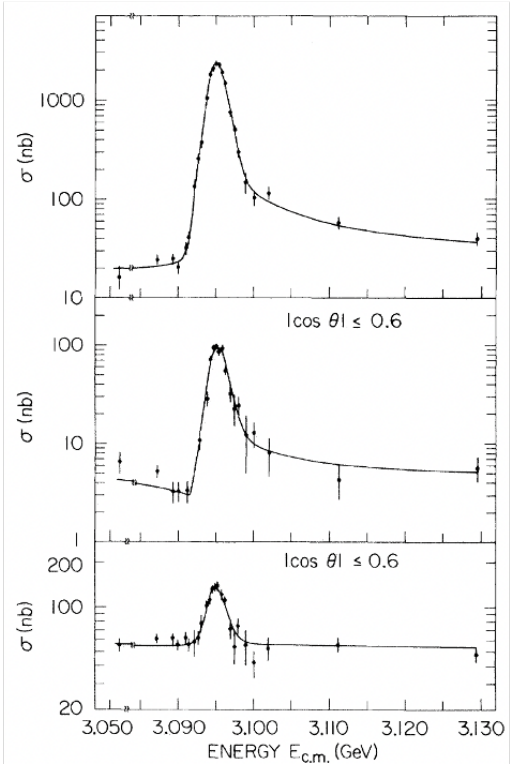

(b) Cross-sections as a function of energy in e^+e^- collisions for (top) multihadron, (middle) $\mu^+\mu^-$, $\pi^+\pi^-$, K^+K^-, and (bottom) e^+e^- final states. The figure is taken from Ref. [2].

Figure 1.1 First observations of J/ψ particle by (a) Ting's group and (b) by Richter's group.

① The natural units are used in this thesis. The speed of light $c = 1$ and the reduced Planck constant $\hbar = 1$.

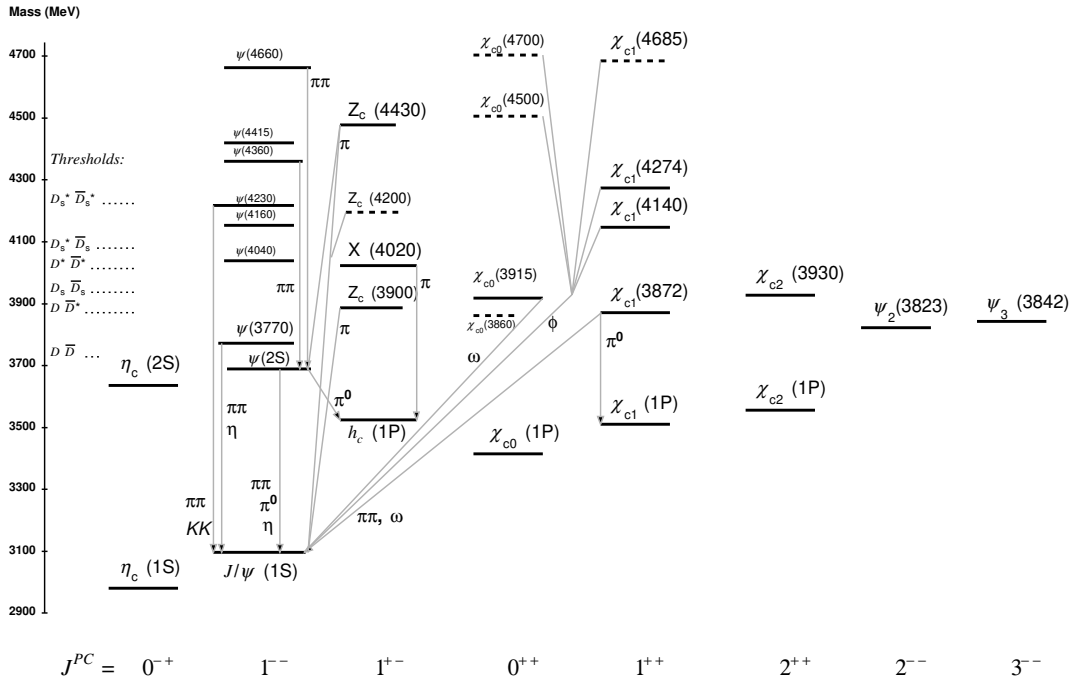

Figure 1.2 Charmonium system. The level scheme of meson states containing a minimal quark content of $c\bar{c}$. The figure is taken from Ref. [9].

particle, was observed by Richter's group[3].

The discovery of J/ψ particle was a big shock to the physics community. If J/ψ particle was interpreted as a hadron composed of known quarks at that time, up quark, down quark or strange quark, its measured decay width was about one thousand times smaller than expected. The extremely narrow width of J/ψ particle immediately provoked plenty of researches to probe its nature. The charmonium model[4-6] has emerged as the most successful theory. The charmonium is a meson consisting of a fourth quark, charm quark c, and its antiquark $\bar{c}$. The charm quark was first proposed by J. Bjorken and S. Glashow as far back as 1964[7], and then became essential in the Glashow–Iliopoulos–Maiani (GIM) mechanism proposed in 1970[8]. This discovery of J/ψ particle and its subsequent studies provided support for the theory that predicted the existence of a fourth quark, shed a new light on the quark model, and changed our understanding of particle physics profoundly. Ting and Richter were thus awarded the 1976 Nobel Prize in Physics.

In the following years, many other charmonium states were discovered. The currently known charmonium and charmonium-like states are summarised in Figure 1.2. These states are characterised by their quantum numbers in spectroscopic notation $(n_r + 1)^{2S+1}L_J$, where n_r denotes the excitation of the radial motion of the $c\bar{c}$ pair, S is the total spin, L is the orbital angular momentum and J is the total angular momentum. The parity

P and charge conjugation C can be determined by the quantum numbers L and S in the $c\bar{c}$ pair model: $P = (-1)^{L+1}$ and $C = (-1)^{L+S}$. The J/ψ meson is labelled as 1^3S_1, and the ψ' meson is its first radial excited level, labelled as 2^3S_1. Therefore, the ψ' meson is also called $\psi(2S)$ meson. The J/ψ and $\psi(2S)$ mesons have the same quantum numbers $J^{PC} = 1^{--}$. The world average values of mass and width for J/ψ and $\psi(2S)$ mesons[9] are

$$M(J/\psi) = 3096.900 \pm 0.006\,\text{MeV}, \quad \Gamma(J/\psi) = 92.6 \pm 1.7\,\text{keV},$$
$$M(\psi(2S)) = 3686.10 \pm 0.06\,\text{MeV}, \quad \Gamma(\psi(2S)) = 294 \pm 8\,\text{keV}.$$

The charmonium state is referred to as having hidden charm, while the mesons with a single charm or anticharm quark is called D mesons and referred to as having open charm. The mass values of J/ψ and $\psi(2S)$ mesons are both below the open charm threshold, and thus their decays to two D mesons are forbidden by energy conservation. Moreover, other hadronic decay modes are strongly suppressed due to the Okubo-Zweig-Iizuka (OZI) rule[10-12]. This explains why their widths are extremely narrow. The widths of charmonium states above the threshold producing a pair of D mesons, such as $\psi(3770)$, are measured in MeV level as expected.

The study of charmonium production can help us understand the strong interaction, one of the four fundamental interactions in the nature. Quantum chromodynamics (QCD) is the theory that describes the strong interaction between quarks and gluons. One of the most important features of QCD is that the coupling constant, which measures the strength of the interactions, becomes larger when the distance between the interacting quarks and gluons is larger, and the non-perturbative effects become more important. The charmonium state, which can be considered as a two-body system of $c\bar{c}$ pair, is one of the most simplest objects to probe QCD. The study of charmonium production in proton-proton (pp) collisions can provide important information to improve QCD predictions in the non-perturbative regime. The process of charmonium production involves two steps: the production of a $c\bar{c}$ pair system, followed by its hadronisation into the charmonium state. The step of $c\bar{c}$ pair production can be calculated perturbatively but the hadronisation step, being of non-perturbative nature, needs to be described by effective theories or phenomenological models with inputs from experiments. The production mechanism of charmonium is still an intriguing problem in QCD, which is not completely understood even after over forty years of study.

In experiments, the J/ψ and $\psi(2S)$ mesons have high yields in high-energy pp colli-

sions, and thus a large amount of data can be collected. In addition, their di-leptonic decay branching ratio are relatively high, which can be easily detected and provide clean signals in pp collisions. The LHCb detector at the Large Hadron Collider (LHC) is designed for the study of particles containing charm or bottom quarks, and it covers the forward rapidity region, providing access to a unique kinematic regime. Besides, the high integrated luminosity and excellent performance of the detector make it an ideal laboratory for production measurements. By virtue of these advantages, this thesis focuses on the experimental study of J/ψ and $\psi(2S)$ production in pp collisions at the LHCb experiment, using the di-muon decay channels, $J/\psi \to \mu^+\mu^-$ and $\psi(2S) \to \mu^+\mu^-$.

This thesis includes two measurements: the measurement of J/ψ production cross-sections in pp collisions at a centre-of-mass energy $\sqrt{s} = 5\,\text{TeV}$ [13], and the measurement of production cross-sections of double charmonium, including di-J/ψ and J/ψ -$\psi(2S)$, in pp collisions at $\sqrt{s} = 13\,\text{TeV}$. Chapter 2 sketches charmonium production mechanism in pp collisions, including the introduction to the QCD framework and several theoretical models, and then presents the motivations of two measurements. In Chapter 3, an brief introduction to the LHCb experiment is presented. In Chapter 4 and Chapter 5, two measurements are described separately in detail.

CHAPTER 2 CHARMONIUM PRODUCTION MECHANISM

The theoretical description of charmonium production in pp collisions can be separated into the hard and soft parts of the process, corresponding to large or small momentum transfers respectively, based on the factorisation theorem in the QCD framework. The hard part can be calculated by perturbative QCD, while the soft part is in the non-perturbative region and challenging theoretical calculations. Different treatments of the non-perturbative effects have brought about various theoretical models for charmonium production, including the colour-singlet model and the non-relativistic QCD (NRQCD). Theses theoretical treatments, and their successes and problems are discussed in this chapter, after a brief introduction to QCD and charmonium properties.

2.1 Quantum chromodynamics

The quantum field theory of the strong interaction, QCD, is a non-Abelian gauge theory with the SU(3) group. It emerged in 1973 based on the Yang–Mills theory[14] and many experimental and theoretical developments at that time. The quark model, which was proposed by M. Gell-Mann[15] and G. Zweig[11,16] in 1964, provided a successful classification of hadrons, but did not involve the quark dynamics inside hadrons. In 1967, a series of experiments on electron-proton deep inelastic scattering (DIS) was conducted at the SLAC to probe the inner structure of the nucleon. The Bjorken scaling[17], which means the structure functions are independent of the momentum transfer, was discovered in these experiments[18-19]. It can be explained by the parton model, which was proposed by R. Feynman[20] in 1969. In this model, the basic interaction in electron–proton DIS is the elastic scattering between the incident electron and point-like constituents, termed partons, inside the proton. Partons were indeed identified with quarks in this process. The discovery of Bjorken scaling provided a direct evidence for quarks and indicated that their interactions are weak at large momentum transfers, which is known as asymptotic freedom. Therefore, asymptotic freedom is an essential feature of the theory describing the quark interactions. In 1973, the asymptotic freedom of the non-Abelian gauge theory was discovered theoretically by D. Gross and F. Wilczek[21] and D. Politzer[22], which led to the construction of QCD. Besides, the colour of quarks as a new degree of freedom, characterised by the SU(3) group, was proposed to solve the spin-statistics paradox in the quark

model[23-24]. This was verified by experimental results such as the ratio of the hadronic cross section to the muon cross section in e^+e^- collisions[25], $R = \frac{\sigma(e^+e^-\to\text{hadrons})}{\sigma(e^+e^-\to\mu^+\mu^-)}$, and the number of colour N_c was determined to be three. The colour charge is the source of the strong interaction, just as the electric charge is the source of the electromagnetic interaction. Analogous to photons in quantum electrodynamics (QED), gluons are the force carriers in QCD, binding quarks together and forming hadrons such as protons and charmonia. Each quark carries a colour charge and couples to gluons. Although there are many experimental evidences for quarks and colour charges, no free quarks have been observed. This can be explained by the hypothesis of colour confinement, which states that free particles must be colour singlet states. The colour confinement is another important feature of QCD.

2.1.1 QCD Lagrangian

QCD is the gauge field theory of the strong interaction between quarks and gluons. Quarks are fermions with spin $\frac{1}{2}$. In QCD, the quark field is denoted by a Dirac spinor q_f^a, where f and a stand for the flavour and the colour charge. There are six flavours of quarks: up (u), down (d), charm (c), strange (s), top (t) and bottom (b), and three types of colour charge: Red (R), Blue (B) or Green (G). For each flavour there is a corresponding type of antiquark, which has the same mass and spin as the quark but carries the electric charge and other charges with the opposite sign. The antiquark field is denoted by a Dirac adjoint spinor $\overline{q}_f^a$. Gluons are massless vector gauge bosons and carry the colour charge themselves. The gluon field is a four-vector field characterising the propagation of the gluon. Eight different types of gluon fields, denoted by A_μ^C with C running from 1 to 8 and μ standing for components in spacetime, are introduced in QCD as the requirement of the SU(3) gauge symmetry.

The QCD Lagrangian is given by[9]

$$\mathcal{L} = \sum_f \overline{q}_f^a (i\gamma^\mu \partial_\mu \delta_{ab} - g_s \gamma^\mu t_{ab}^C \mathcal{A}_\mu^C - m_f \delta_{ab}) q_f^b - \frac{1}{4} F_{\mu\nu}^A F^{A\mu\nu}, \tag{2.1}$$

where the flavour index f and other repeated indices are summed over. The q_f^b and $\overline{q}_f^a$ are quark and antiquark fields respectively, where b and a are the indices for colour and anticolour and run from 1 to 3. The γ^μ are the four Dirac γ-matrices. The quantity g_s (or $\alpha_s = \frac{g_s^2}{4\pi}$) is the coupling constant of the strong interaction. The 3×3 matrices t_{ab}^C correspond to eight generators of the SU(3) colour group, and satisfy the commutation

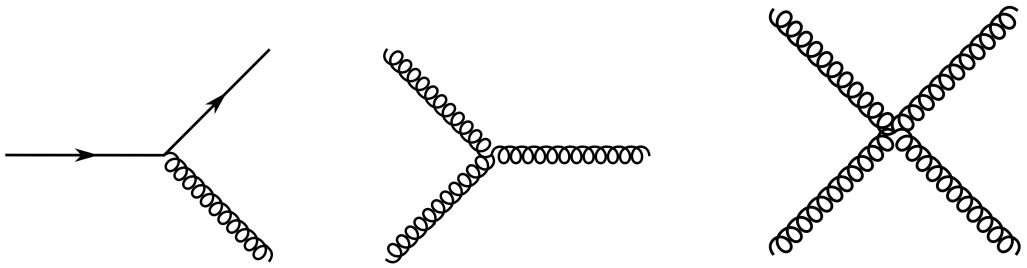

(a) The quark-gluon vertex. (b) The three-gluon vertex. (c) The four-gluon vertex.

Figure 2.1 Three types of QCD interaction vertices. The quark is represented by a straight line with an arrow and the gluon is represented by a "corkscrew" line. A point where lines connect with each other is a vertex.

relations

$$[t^A, t^B] = i f_{ABC} t^C, \tag{2.2}$$

where f_{ABC} are the structure constants of the SU(3) group and indices A, B and C run over eight values. The four-vector fields $\mathcal{A}_\mu^C$ correspond to eight kinds of gluon fields. The m_f is the quark mass for flavour f. The field tensor $F_{\mu\nu}^A$ is defined as

$$F_{\mu\nu}^A = \partial_\mu \mathcal{A}_\nu^A - \partial_\nu \mathcal{A}_\mu^A - g_s f_{ABC} \mathcal{A}_\mu^B \mathcal{A}_\nu^C. \tag{2.3}$$

The quark mass m_f and the QCD coupling constant α_s are fundamental parameters of QCD.

From first principles, QCD predictions can be obtained in the framework of perturbative QCD (pQCD) if the coupling constant is small enough. The Feynman rules derived from QCD Lagrangian involve three vertices: a quark-gluon vertex, a three-gluon vertex and a four-gluon vertex, as shown in Figure 2.1. The quark-gluon vertex is analogous to the electron-photon vertex in QED, while the rest two vertices, indicating gluon self-interactions, have no equivalent in QED. Gluon self-interactions originate from the presence of the last term in Eq. 2.3, and make QCD have two essential features that do not appear in QED: asymptotic freedom and colour confinement. These two features are both related to the running of QCD coupling constant.

2.1.2 The running of coupling constant

QCD is a renormalisable quantum field theory. The ultraviolet divergences in the calculations of physical observables can be controlled by regularisation and renormalisation. The regularisation is the method to separate divergent quantities from finite observables

by introducing a regulator, and the renormalisation is the method to eliminate divergent quantities by shifting the fields and the parameters in the Lagrangian. In this case, the renormalised QCD coupling constant α_s acquires the dependence on the renormalisation scale μ_R, which is known as the running of coupling constant.

In the framework of pQCD, predictions for physical observables are expanded in powers of the renormalised coupling constant $\alpha_s(\mu_R^2)$. The energy scale μ_R is usually set as the momentum transfer Q in a given process so that the coupling constant $\alpha_s(Q^2)$ stands for the effective strength of the strong interaction in that process. The running behaviour of the coupling constant α_s can be described by the renormalisation group (RG) equation,

$$\mu_R^2 \frac{\mathrm{d}\alpha_s}{\mathrm{d}\mu_R^2} = \beta(\alpha_s), \tag{2.4}$$

where the μ_R-dependence of α_s is encoded into the beta function $\beta(\alpha_s)$. In the region that α_s is much smaller than 1, the beta function can be computed in perturbation theory in terms of α_s. The one-loop beta function is

$$\begin{aligned} \mu_R^2 \frac{\mathrm{d}\alpha_s}{\mathrm{d}\mu_R^2} &= \beta(\alpha_s) = -b_0 \alpha_s^2, \\ b_0 &= \frac{33 - 2n_f}{12\pi}, \end{aligned} \tag{2.5}$$

where n_f is the number of quark flavours that contribute to the loops effectively. An analytic solution to the Eq. 2.5 is

$$\alpha_s(\mu_R^2) = \frac{\alpha_s(\mu_0^2)}{1 + b_0 \alpha_s(\mu_0^2) \ln(\mu_R^2/\mu_0^2)}. \tag{2.6}$$

As long as the coupling constant is given at a certain energy scale μ_0, its value at other energy scale μ_R is obtained by Eq. 2.6 at the lowest order. Since $n_f \leq 6$, the coefficient b_0 is positive, which results in asymptotic freedom, *i.e.* that coupling constant decreases when the energy scale increases. This feature guarantees the validity of pQCD at large momentum transfers. On the contrary, the coupling constant increases with decreasing energy scale, and thus the perturbative method would fail at small momentum transfers. According to Eq. 2.6, the α_s diverges at the energy scale Λ_{QCD}, given by

$$\Lambda_{\mathrm{QCD}}^2 = \mu_0^2 \exp\left[-\frac{1}{b_0 \alpha_s(\mu_0^2)}\right]. \tag{2.7}$$

With the definition of Λ_{QCD}, the running behaviour of α_s is expressed as

$$\alpha_s(\mu_R^2) = \frac{1}{b_0 \ln(\mu_R^2/\Lambda_{\mathrm{QCD}}^2)}. \tag{2.8}$$

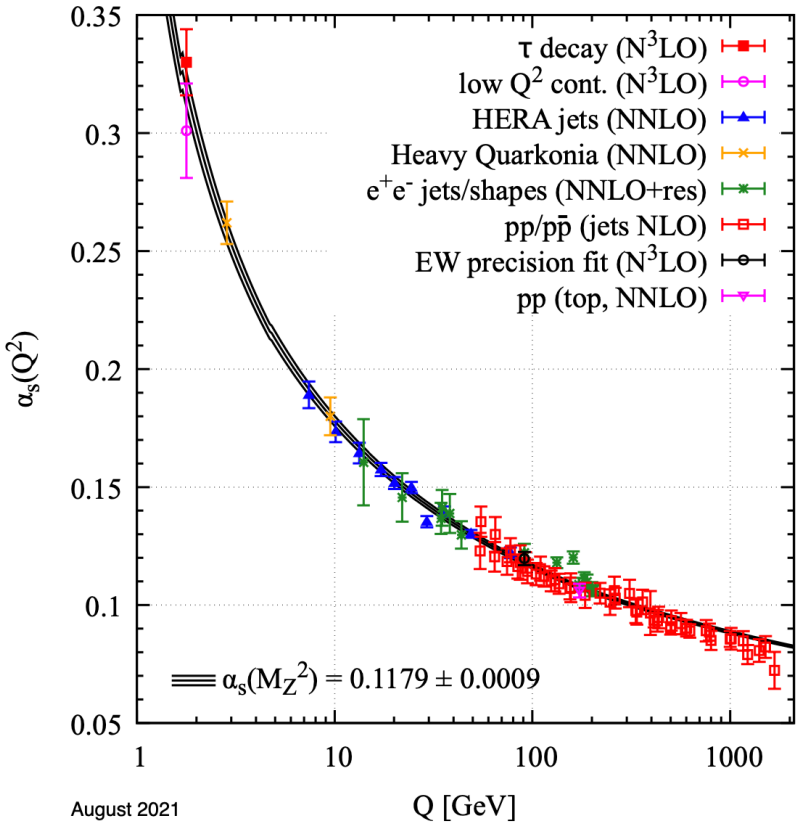

Figure 2.2 Extracted values of the coupling constant α_s at different energy scales, compared with the QCD predictions for the running of α_s based on the world average value of $\alpha_s(M_Z^2)$. The figure is taken from Ref. [9].

Although the Λ_{QCD} is defined in the framework of pQCD, its value indicates the energy range where non-perturbative dynamics dominates. In QCD, it is considered as the scale to separate the perturbative region, $Q \gg \Lambda_{\mathrm{QCD}}$, and the non-perturbative region, $Q \lesssim \Lambda_{\mathrm{QCD}}$.

The values of α_s, which depend on the renormalisation scheme and cannot be measured directly, have been inferred from measurements of various processes at different energy scales. As shown in Figure 2.2, these extracted values are consistent with the QCD predictions for the running of α_s based on the world average value of α_s at the scale of Z boson mass M_Z, $\alpha_s(M_Z^2) = 0.1179 \pm 0.0009$[9]. From Figure 2.2, for momentum transfers in the range from 100 GeV to 1 TeV, which are the typical scales for modern collider experiments, $\alpha_s \sim 0.1$ is small enough for perturbative calculations. However, it increases rapidly when the energy scale decreases from 10 GeV to 1 GeV and the non-perturbative contributions become more and more important. The value of Λ_{QCD} can be inferred from the extracted results of α_s and the QCD calculations with higher-order corrections. Based on the result of $\alpha_s(M_Z^2)$, the value is $\Lambda_{\mathrm{QCD}} \approx 340$ MeV for $n_f = 3$[26]. Therefore, for

$Q < 1$ GeV, below the energy range shown in the Figure 2.2, the non-perturbative effects are significant.

The colour confinement, the phenomenon that quarks and gluons cannot be isolated from hadrons, is an important feature of QCD in the non-perturbative region. Currently, there is not an analytic proof of this phenomenon, but it can be understood qualitatively by considering the picture of pulling apart a quark-antiquark pair. With the distance between two quarks increasing, the coupling constant α_s become larger and larger and two quarks are strongly interacted by exchanging gluons. There are attractive interactions between these exchanged gluons, which lead to that the colour field between the quarks are squeezed into a narrow flux tube. The energy stored in the colour field is proportional to the distance between quarks, giving a linear term in the potential, $V(r) \sim \kappa r$, where r denotes the distance, and $\kappa \sim 1$ GeV/ fm determined experimentally [27]. When the energy keeps increasing linearly with distance, it eventually becomes more favorable to produce a new quark-antiquark pair, rather than extending the colour field further. As a result, quarks are always produced in pairs and hadronised into colourless hadrons in collider experiments.

2.1.3 QCD factorisation

Experiments at hadron colliders, which usually cover multiple energy scales and thus involve both perturbative and non-perturbative effects, can provide good tests of QCD predictions. A natural idea is to factorise the scattering process into two parts: hard part, which is at short distance and can be calculated perturbatively, and soft part, which is at long distance and needs to be treated non-perturbatively. For the non-perturbative part, the parton model developed for DIS was applied to other processes, such as the Drell–Yan process, the production of a lepton pair l^+l^- through quark-antiquark $q\bar{q}$ annihilation, by S. Drell and T.-M. Yan [28]. In the parton model, the underlying structure of the hadron is reflected by the parton distribution function (PDF), defined as the probability density $f_{a/A}(x)$ for finding a quark or gluon a in the hadron A with a certain longitudinal momentum fraction, the Bjorken x. In this way, the cross-section for the Drell–Yan process is expressed as

$$\mathrm{d}\sigma(AB \to l^+l^-X) = \sum_{a,b} \int \mathrm{d}x_a \mathrm{d}x_b f_{a/A}(x_a) f_{b/B}(x_b) \mathrm{d}\hat{\sigma}(ab \to l^+l^-), \qquad (2.9)$$

where A and B are hadrons and X means anything, ab denotes $q\bar{q}$. The PDFs can be extracted from data, and the partonic cross-section $\mathrm{d}\hat{\sigma}(ab \to l^+l^-)$ should be calculable

perturbatively.

However, infrared divergences appear in the perturbative calculations of the partonic cross-sections, making QCD predictions challenging. The QCD factorisation theorem[29-30] was developed to deal with this problem. The infrared divergences are factorised out of the partonic cross-sections and absorbed into the PDFs, which need to be universal, *i.e.* independent of processes. In the framework of collinear factorisation, the momentum components of partons transverse to the hadron momentum are neglected. The infrared divergences that cannot be cancelled arise from collinear emissions for initial states. It is natural to consider these emissions as modifying the momentum fraction of the parton rather than the effect of interactions between the parton and others. The factorisation of infrared divergences results in that the PDFs depend on the factorisation scale μ_F, just like the μ_R-dependence of the coupling constant due to the renormalisation of ultraviolet divergences. Then, the cross-section for the Drell–Yan process is expressed as

$$\mathrm{d}\sigma(AB \to l^+l^-X) = \sum_{a,b} \int \mathrm{d}x_a \mathrm{d}x_b f_{a/A}(x_a, \mu_F^2) f_{b/B}(x_b, \mu_F^2) \mathrm{d}\hat{\sigma}(ab \to l^+l^-), \quad (2.10)$$

where $\mathrm{d}\hat{\sigma}(ab \to l^+l^-)$ is expanded in powers of $\alpha_s(\mu_R^2)$ in the framework of pQCD,

$$\mathrm{d}\hat{\sigma}(ab \to l^+l^-) = \sum_{n=0}^{\infty} \alpha_s^n(\mu_R^2) \mathrm{d}\hat{\sigma}_n(\mu_F^2, \mu_G^2). \quad (2.11)$$

The μ_F-dependence of PDFs is governed by the Dokshitzer-Gribov-Lipatov-Altarelli-Parisi (DGLAP) equations[31-34], and the x-dependence of PDFs is extracted from experimental results. If the cross-section is calculated to all orders, it will be independent of the choice of μ_R and μ_F, as the μ_R-dependence of α_s and μ_F-dependence of PDFs are exactly compensated by the corresponding scale dependence of $\hat{\sigma}_n$ series. In practice, the cross-section is usually calculated at the leading order (LO) with finite higher-order corrections, and thus it varies with the choice of μ_R and μ_F, which has to be considered within the theoretical uncertainties. For the production of charmonium in hadron-hadron collisions, the cross-section can also be factorised into a similar expression as Eq. 2.10. Nevertheless, it involves the hadronisation of $c\overline{c}$, which makes the theoretical calculations more complex. It is discussed in the following Sections 2.3 and 2.4 of this chapter.

The framework of collinear factorisation has been widely used in various QCD predictions and verified by many experiments. However, in the small Bjorken-x region, the intrinsic transverse momentum of the parton becomes non-negligible, and the collinear

factorisation is not applicable any more. The framework of transverse momentum dependent (TMD) factorisation[35] has been established. The PDF $f_{a/A}(x)$ is extended to include the transverse momentum of the parton $\boldsymbol{k}_{\mathrm{T}}$, denoted as the TMD PDF $f_{a/A}(x, \boldsymbol{k}_{\mathrm{T}})$. The TMD PDFs encode the confined motion of quarks and gluons inside the hadron, and need to be extracted from experimental data as well. The TMD PDFs acquire dependence on two energy scales, a factorisation scale μ and a rapidity scale ζ, corresponding to ultraviolet divergences and rapidity divergences respectively, as a consequence of the TMD factorisation. The μ-dependence of TMD PDFs is governed by RG equation, while the ζ-dependence is governed by Collins-Soper (CS) equation[36]. The TMD factorisation formula for the cross-section of Drell-Yan process is expressed as[36]

$$\mathrm{d}\sigma \sim \sum_{a,b} \mathcal{H}_{ab}(Q, \mu) \int \mathrm{d}^2\boldsymbol{b}_{\mathrm{T}} e^{i\boldsymbol{q}_{\mathrm{T}}\cdot\boldsymbol{b}_{\mathrm{T}}} \tilde{f}_{a/A}(x_A, \boldsymbol{b}_{\mathrm{T}}, \mu, \zeta_A) \tilde{f}_{b/B}(x_B, \boldsymbol{b}_{\mathrm{T}}, \mu, \zeta_B) + Y, \quad (2.12)$$

which is valid up to power-suppressed corrections $\mathcal{O}(\frac{q_{\mathrm{T}}^2}{Q^2})$. Here, the quantity Q is the invariant mass of the leptonic pair l^+l^-. The two-vector $\boldsymbol{q}_{\mathrm{T}}$ is the transverse momentum of l^+l^-, and $q_{\mathrm{T}} = |\boldsymbol{q}_{\mathrm{T}}|$. The hard scattering part $\mathcal{H}_{ab}(Q, \mu)$ is calculated by pQCD. The two functions $\tilde{f}_{a/A}(x_A, \boldsymbol{b}_{\mathrm{T}}, \mu, \zeta_A)$ and $\tilde{f}_{b/B}(x_B, \boldsymbol{b}_{\mathrm{T}}, \mu, \zeta_B)$ are the TMD PDFs Fourier transformed into the position space, where the two-vector $\boldsymbol{b}_{\mathrm{T}}$ is the transverse position, x_A and x_B are longitudinal momentum fractions. The fractions $x_{A,B} = Qe^{\pm y}/\sqrt{s}$, where y is the rapidity of l^+l^- and $\sqrt{s}$ is the centre-of-mass energy of hadron-hadron collisions. The two rapidity scales obey $\zeta_A\zeta_B = Q^4$. In the TMD region, $q_{\mathrm{T}} \ll Q$, the result of TMD factorisation, which is the first term of the cross-section in Eq. 2.12, provides a good description of the process. The second term Y, which is negligible in the TMD region, is introduced to match TMD factorisation with collinear factorisation at high q_{T}. The TMD factorisation formula in Eq. 2.12 makes the TMD PDFs contain all the non-perturbative contributions to the cross-section. Some of the quark TMD PDFs have been extracted and studied from low-q_{T} Drell-Yan and semi-inclusive DIS measurements, while the gluon TMD PDFs remain poorly known. The di-J/ψ production at the LHC is one of the promising processes to study gluon TMD PDFs, as detailed in Section 2.6.2.

2.2 Charmonium properties

Charmonium, discovered shortly after the emergence of QCD, provides an ideal laboratory to test pQCD and to study the underlying non-perturbative dynamics. The valence quarks inside the charmonium, charm and anticharm quarks, have very large masses even

close to half the mass of the lowest energy level of charmonium. The c-quark mass m_c is 1.27 ± 0.02 GeV in the modified minimal subtraction ($\overline{\text{MS}}$) scheme, and 1.67 ± 0.07 GeV in the on-shell scheme[9]. As a consequence, the typical velocity v of c-quark inside the charmonium is small compared to the speed of light, and the charmonium can be approximate to a non-relativistic two-body $c\bar{c}$ system.

2.2.1 Potential models

In the non-relativistic approximation, the charmonium states can be described by the Schrödinger equation in analogy with the hydrogen atom,

$$\left[-\frac{1}{2m'}\nabla^2 + V(r)\right]\Psi_n(\vec{x}) = E_n\Psi_n(\vec{x}), \tag{2.13}$$

where $m' = \frac{1}{2}m_c$ is the reduced mass, $V(r)$ is the potential depending on the distance $r = |\vec{x}|$ between charm and anticharm quarks inside the charmonium, E_n is the energy eigenvalue, and $\Psi_n(\vec{x})$ is the wave function of the $c\bar{c}$ bound state in the centre-of-mass frame.

Once the potential $V(r)$, which describes the interaction between charm and anticharm quarks, is determined, the mass spectrum of $c\bar{c}$ bound states can be given by

$$M_n(c\bar{c}) = 2m_c + E_n(m_c, V). \tag{2.14}$$

Many potential models have been proposed and used to study the charmonium system[37]. Some of them are completely phenomenological, such as power-law and logarithmic potentials, while the others use theoretical guidance from QCD. At small distances, the potential is dominated by the Coulomb-like term due to the gluon exchange,

$$V(r) \sim -\frac{4}{3}\frac{\alpha_s}{r}. \tag{2.15}$$

At large distances, the effects of colour confinement become important and the potential takes the linear form,

$$V(r) \sim kr, \tag{2.16}$$

as described in Section 2.1.2. A simplest interpolation from small to large distances is given by a superposition of both terms[6], and the potential is

$$V(r) = -\frac{a}{r} + kr. \tag{2.17}$$

Furthermore, a potential incorporating both linear confinement and asymptotic freedom was proposed[38], and used to describe the charmonium system successfully. According to potential model calculations, the square of typical velocity, v^2, is around 0.3 for

Table 2.1 Values of the momentum scales for charmonium[40].

Momentum scales	Values
m_c	1.5 GeV
$m_c v$	0.9 GeV
$m_c v^2$	0.5 GeV

charmonium[38-39].

2.2.2 Energy scales in charmonium

Several different energy scales (or momentum scales) play important roles in the dynamics of a charmonium. The most important momentum scales are the c-quark mass m_c, the typical momentum of c-quark $m_c v$ in the rest frame of the charmonium, and the typical kinetic energy of c-quark $m_c v^2$. The c-quark mass m_c sets the scale of kinematic threshold for charmonium production and the overall energy scale for annihilation processes. The inverse of the typical momentum indicates the size of the bound $c\bar{c}$ state, $m_c v \sim \frac{1}{r}$. The typical kinetic energy $m_c v^2$ is the scale of binding energy and corresponds to the energy splittings between radial excited levels and between orbital excited levels in the charmonium spectrum. Estimates of these momentum scales[40] are given in Table 2.1. Because the energy splitting between J/ψ and $\psi(2S)$ states is around 0.6 GeV and that between J/ψ and χ_c states is around 0.4 GeV, the average of two values, 0.5 GeV, is considered as an estimate of $m_c v^2$. The c-quark mass m_c is estimated as half the mass of the lowest energy level of charmonium, 1.5 GeV. For the typical momentum $m_c v$, it is estimated as the geometric mean of the estimates of m_c and $m_c v^2$, 0.9 GeV. From these estimations, v^2 is $\frac{1}{3}$, consistent with the value obtained from potential models.

Apart from the three intrinsic momentum scales for charmonium, another important scale is $\Lambda_{\rm QCD}$, the scale related to non-perturbative effects involving light quarks and gluons. As mentioned in Section 2.1.2, $\Lambda_{\rm QCD} \approx 340$ MeV for $n_f = 3$. The c-quark mass m_c is much larger than $\Lambda_{\rm QCD}$ and $\alpha_s(m_c) \sim 0.2$ as inferred from Figure 2.2, so the effects at the scale m_c can be calculated perturbatively. However, the non-perturbative effects are significant at the scales $m_c v$ and $m_c v^2$.

For the charmonium production, the hard-scattering scale $Q_{\rm hard}$, which is of the order of the charmonium transverse momentum $p_{\rm T}$ in the case of hadroproduction, is involved into the description relevant to the production process of a $c\bar{c}$ pair. This process of a $c\bar{c}$ pair production usually can be calculated in the framework of pQCD as $Q_{\rm hard} \gg \Lambda_{\rm QCD}$,

but the following process, the hadronisation of $c\bar{c}$ pair into charmonium is at a momentum scale much less than the c-quark mass m_c, which is non-perturbative in principle. Many theoretical models are proposed to deal with the non-perturbative transition from $c\bar{c}$ pair to charmonium, such as the colour-singlet model and the NRQCD.

2.3 Colour-singlet model

The colour-singlet model[41-48] was proposed soon after the discovery of charmonium states, based on the following assumptions or approximations:

- It is assumed that the charmonium production can be factorised into two steps. The first step is the production of a pair of on-shell $c\bar{c}$ quarks, which can be calculated perturbatively. The second step is the $c\bar{c}$ pair binding to form the meson, and is described by a universal wave function.
- The charmonium is only considered as two-body system made up of the $c\bar{c}$ pair, and the two constituent quarks are supposed to be at rest approximately in the charmonium rest frame. This is called the static approximation.
- The intermediate $c\bar{c}$ pair is assumed to be colourless, *i.e.* in a colour-singlet state, and have the same angular-momentum quantum numbers, S, L and J, as the charmonium. This assumption gives the name of the colour-singlet model.

This model is a very natural application of QCD to charmonium production. As inspired by the factorisation theorem of QCD, The non-perturbative part, hadronisation of $c\bar{c}$, is factorised in a universal wave function. The charmonium production cross-section is related to the wave function (or its derivatives) of the colour-singlet $c\bar{c}$ pair around the origin. These quantities are the only inputs in the colour-singlet model, and can be extracted from experimental data on charmonium decay or calculated with potential models.

In the colour-singlet model, the production cross-section of the charmonium state ${}^{2S+1}L_J$ is factorised as[49]

$$\mathrm{d}\sigma({}^{2S+1}L_J) = \left|\frac{\mathrm{d}^l}{\mathrm{d}r^l}R_{nl}(0)\right|^2 \mathrm{d}\sigma(c\bar{c}[{}^{2S+1}L_J]), \tag{2.18}$$

where R_{nl} is the radial wave function with the radical and orbital quantum numbers n and l, and $\mathrm{d}\sigma(c\bar{c}[{}^{2S+1}L_J])$ is the production cross-section of a $c\bar{c}$ pair in the ${}^{2S+1}L_J$ state. The cross-section $\mathrm{d}\sigma(c\bar{c}[{}^{2S+1}L_J])$ in hadron-hadron collisions can be descried as a similar

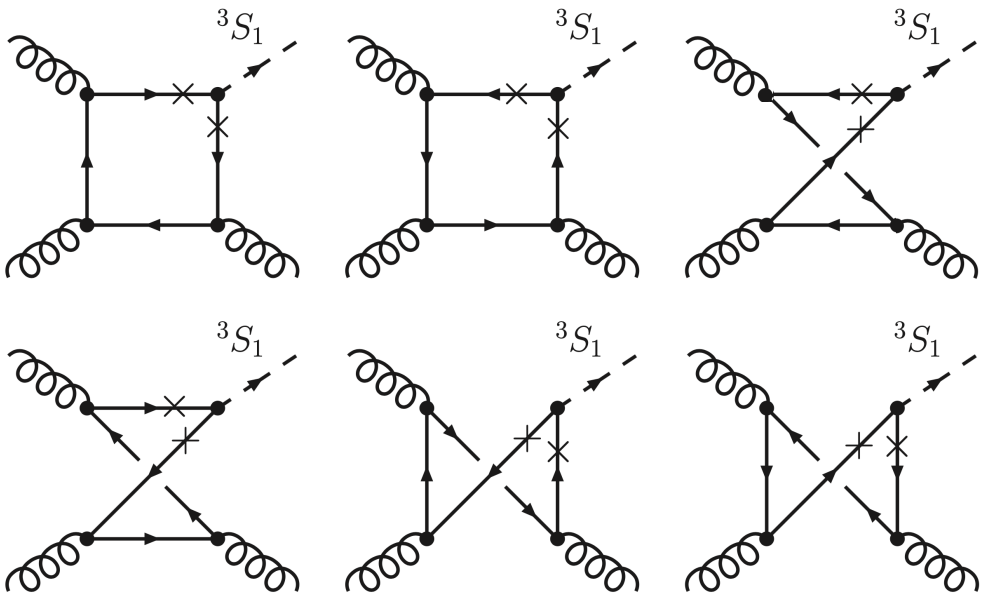

Figure 2.3 The diagrams for $gg \to {}^3S_1 g$ in the colour-singlet model at LO. The figure is taken from Ref. [50].

expression to Eq. 2.10,①

$$\mathrm{d}\sigma(c\bar{c}[^{2S+1}L_J]) = \sum_{a,b} \int \mathrm{d}x_a \mathrm{d}x_b f_{a/A}(x_a) f_{b/B}(x_b) \mathrm{d}\hat{\sigma}(ab \to c\bar{c}[^{2S+1}L_J]X), \qquad (2.19)$$

where A and B are hadrons, a and b are partons, $f_{a/A}(x_a)$ and $f_{b/B}(x_b)$ are PDFs, and X means anything. The $\mathrm{d}\hat{\sigma}(ab \to c\bar{c}[^{2S+1}L_J]X)$ is calculated in the framework of pQCD. The leading contribution of charmonium production in high-energy hadron-hadron collisions comes from the gluon fusion process, where the partons a and b are both gluons g. For the production of $^3S_1$ states, such as J/ψ and $\psi(2S)$ states, the Feynman diagrams at the LO are shown in Figure 2.3. Due to the conservation laws, the $^3S_1$ states have to be produced associated with a gluon in this LO process ($gg \to {}^3S_1 g$), which is at the order of α_s^3.

The LO colour-singlet model succeeded in predicting the charmonium hadroproduction cross-sections at relatively low energies (from a few GeV to a few hundreds GeV)[49]. However, for the direct J/ψ and $\psi(2S)$ production (*i.e.* not from the feed-down of excited charmonium states or decays of b-hadrons) at the CDF experiment in proton-antiproton ($p\bar{p}$) collisions at $\sqrt{s}$ =1.8 TeV[51], it was found that the predictions of the LO colour-singlet model underestimated the experimental data by more than one order of magnitude, as shown in Figure 2.4. With the increase of the transverse momentum p_{T} of J/ψ or $\psi(2S)$

① The dependence on μ_R or μ_F of quantities in this expression is the same as that in Eq. 2.10, and omitted for simplicity.

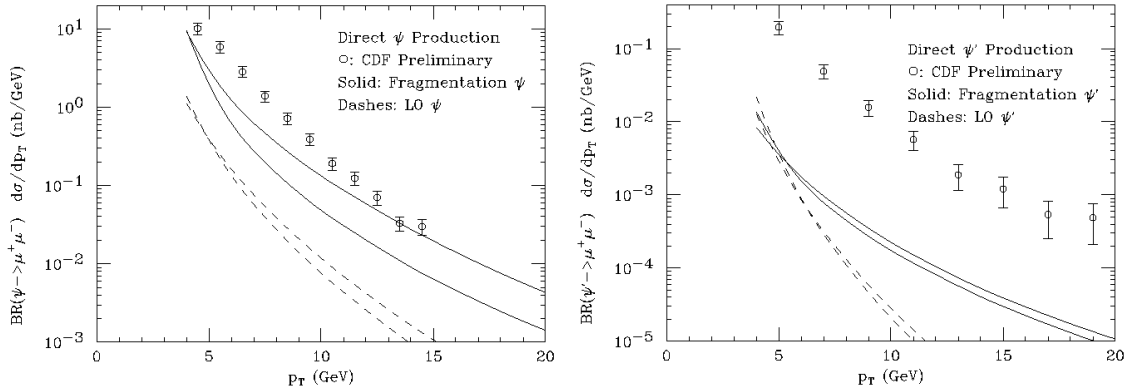

(a) Direct J/ψ production cross-section. (b) Direct $\psi(2S)$ production cross-section.

Figure 2.4 Comparisons of (a) J/ψ and (b) $\psi(2S)$ production cross-sections between CDF data[51] and the colour-singlet model calculations[52] for LO (dashed curves) and fragmentation (solid curves). The figures are taken from Ref. [52].

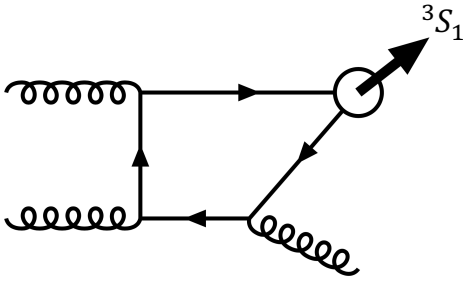

$$\frac{\mathrm{d}\sigma}{\mathrm{d}p_\mathrm{T}^2} \sim \alpha_s^3 \frac{(2m_c)^4}{p_\mathrm{T}^8}, \text{ for } p_\mathrm{T} \gg m_c$$

(a) Gluon fusion process at the LO in the colour-singlet model.

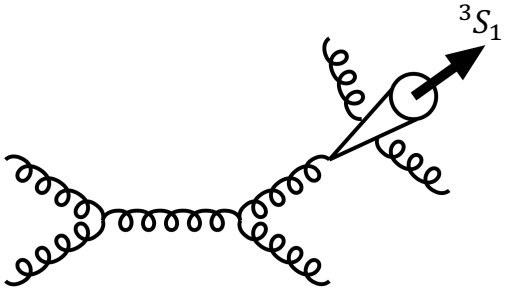

$$\frac{\mathrm{d}\sigma}{\mathrm{d}p_\mathrm{T}^2} \sim \alpha_s^5 \frac{1}{p_\mathrm{T}^4}, \text{ for } p_\mathrm{T} \gg m_c$$

(b) Gluon fragmentation process in the colour-singlet model.

Figure 2.5 Representative diagrams for the J/ψ or $\psi(2S)$ hadroproduction in the colour-singlet model, along with the p_T scaling behaviour of the cross-sections. The figures are taken from Ref. [53].

meson, the huge gaps between data and theory even become much larger, especially for the $\psi(2S)$ meson. This problem was then referred to as the $\psi(2S)$ surplus puzzle. To explain the gaps, the fragmentation process, that a high-energy parton produced in the hard scattering splits into a charmonium and other partons, was considered into the calculations at that time[52]. A representative diagram for the fragmentation process along with the p_T

scaling behaviour of its cross-section is shown in Figure 2.5, compared with that for the gluon fusion process at the LO. Although the fragmentation process is of higher order in α_s, it prevails over the gluon fusion process at the LO in the large-p_{T} region due to its harder p_{T} spectrum. With the fragmentation process included, the previous disagreement was reduced a lot for J/ψ production, while the theoretical calculations were still dramatically below the CDF results for $\psi(2S)$ production, as shown in Figure 2.4. In addition to the $\psi(2S)$ surplus puzzle, the colour-singlet model is known to be inconsistent in the production and decay of P-wave states because there are infrared divergences that cannot be cancelled in the calculations[54-55]. Subsequently, a self-consistent theory model called NRQCD emerged, incorporated and surpassed the colour-singlet model.

2.4 Non-relativistic quantum chromodynamics

The NRQCD[56-58] is an effective field theory of QCD to describe the physics of heavy quarkonium, namely charmonium and bottomonium.① For charmonium, as mentioned in Section 2.2.2, the effects at the scale m_c are perturbative while those at the scales $m_c v$ and $m_c v^2$ are nonperturbative. The factorisation approach in the framework of NRQCD aims to separate the short-distance effects involving the scale m_c or larger ones from the long-distance effects involving the smaller scales $m_c v$, $m_c v^2$ and Λ_{QCD}. Based on the full QCD, an ultraviolet cutoff Λ of the order m_c is introduced in this framework, and the effects at larger energy scales are integrated out. These relativistic dynamics are compensated by adding new local interactions to the Lagrangian and matching coefficients of the Lagrangian.

2.4.1 NRQCD Lagrangian and velocity-scaling rules

The most general NRQCD Lagrangian takes the form[56]

$$\mathcal{L}_{\mathrm{NRQCD}} = \mathcal{L}_{\mathrm{light}} + \mathcal{L}_{\mathrm{heavy}} + \delta\mathcal{L}, \tag{2.20}$$

where the $\mathcal{L}_{\mathrm{light}}$ is the QCD Lagrangian for gluons and three light quarks as expressed in Eq. 2.1 with the flavour index f only denoting u, d and s, and the $\mathcal{L}_{\mathrm{heavy}}$ is given by

$$\mathcal{L}_{\mathrm{heavy}} = \psi^{\dagger}\left(iD_0 + \frac{\vec{D}^2}{2m_c}\right)\psi + \chi^{\dagger}\left(iD_0 - \frac{\vec{D}^2}{2m_c}\right)\chi. \tag{2.21}$$

Since the relativistic charm and anticharm quarks are excluded by the cutoff Λ, it is convenient to use two-component Pauli spinor fields ψ and χ to describe the charm and an-

① The discussions in this section still focus on the charmonium, but they are applicable to the bottomonium as well.

Table 2.2 Estimates of the magnitudes of NRQCD operators in terms of m_c and v[59].

Operator	Estimate	Description
ψ	$(m_c v)^{3/2}$	charm quark field
χ	$(m_c v)^{3/2}$	anticharm quark field
D_0	$m_c v^2$	covariant time derivative (acting on ψ or χ)
$\vec{D}$	$m_c v$	covariant spatial derivative (acting on ψ or χ)
$g_s\vec{E}$	$m_c^2 v^3$	chromoelectric field
$g_s\vec{B}$	$m_c^2 v^4$	chromomagnetic field
$g_s A_0$	$m_c v^2$	scalar potential (in Coulomb gauge)
$g_s\vec{A}$	$m_c v^3$	vector potential (in Coulomb gauge)

ticharm quarks respectively. The covariant derivative $(D_0, \vec{D})$ is $D_\mu = \partial_\mu + ig_s A_\mu$, where $A_\mu = (A_0, \vec{A})$ is the SU(3) gauge field, and g_s is the QCD coupling constant. In Eq. 2.20, the last term $\delta\mathcal{L}$ includes all the correction terms in order to reproduce the full QCD dynamics at scales of order $m_c v$ and smaller. In principle, the number of the required correction terms are infinite, but in practice, only a finite number of them should be considered for the precision up to any given order in the typical velocity v. The relative importance of these correction terms can be assessed using the velocity-scaling rules[59], derived from basic qualitative properties of charmonium or by analysing the equations of motion for the NRQCD operators. The velocity-scaling rules are summarised in Table 2.2, where the estimates of the magnitudes of NRQCD operators are expressed in terms of m_c and v. In Table 2.2, the order in m_c can be obtained from dimensional analysis simply, so only the scaling with v is nontrivial.

According to the velocity-scaling rules, the $\mathcal{L}_{\text{heavy}}$ ($\sim m_c^4 v^5$) multiplied by the charmonium size ($\sim m_c^{-3} v^{-3}$) is of the order $m_c v^2$, which is the typical kinetic energy of c-quark. The leading correction terms in the $\delta\mathcal{L}$, suppressed by $\mathcal{O}(v^2)$ relative to the $\mathcal{L}_{\text{heavy}}$, are bilinear in the charm or anticharm quark field (ψ or χ),

$$\begin{aligned}\delta\mathcal{L}_{\text{bilinear}} = &\frac{c_1}{8m_c^3}\psi^\dagger\vec{D}^4\psi + \frac{c_2}{8m_c^2}\psi^\dagger(\vec{D}\cdot g_s\vec{E} - g_s\vec{E}\cdot\vec{D})\psi \\ &+ \frac{c_3}{8m_c^2}\psi^\dagger(i\vec{D}\times g_s\vec{E} - g_s\vec{E}\times i\vec{D})\cdot\vec{\sigma}\psi + \frac{c_4}{2m_c}\psi^\dagger g_s\vec{B}\cdot\vec{\sigma}\psi \\ &+ \text{charge conjugate terms.}\end{aligned} \tag{2.22}$$

The three-vectors $E^i = F^{0i}$ and $B^i = \frac{1}{2}\epsilon^{ijk}F_{jk}$ are the chromoelectric and chromomagnetic components of the gluon field tensor $F^{\mu\nu}$ respectively, and the tensor $F^{\mu\nu}$ is defined

in Eq. 2.3. The dimensionless coefficients c_1, c_2, c_3 and c_4 in the $\delta\mathcal{L}_{\text{bilinear}}$ can be determined by matching calculations in NRQCD with those in full QCD.

2.4.2 NRQCD factorisation and long-distance matrix elements

In the framework of NRQCD, the production cross-section of a charmonium $\mathcal{Q}$ is given by the factorisation formula[56]

$$\mathrm{d}\sigma_{\mathcal{Q}} = \sum_n \mathrm{d}\sigma[n](\Lambda)\langle\mathcal{O}^{\mathcal{Q}}[n](\Lambda)\rangle, \tag{2.23}$$

with short-distance and long-distance effects separated. The index n denotes the $c\bar{c}$ state ${}^{S+1}L_J^{[C]}$ with the colour quantum number C and angular-momentum quantum numbers S, L and J collectively. The scale Λ is the ultraviolet cutoff of the effective theory. The $\mathrm{d}\sigma_n$ is the short-distance coefficient (SDC) describing the production of a $c\bar{c}$ pair in the state n, which is at the scale m_c or larger. The SDC is proportional to the partonic cross-sections $\mathrm{d}\hat{\sigma}(ab \to c\bar{c}[n]X)$, convolved with PDFs in the case of hadroproduction. The SDCs are expanded in powers of α_s and determined by matching calculations in NRQCD with those in full QCD perturbatively[60]. The $\langle\mathcal{O}^{\mathcal{Q}}[n]\rangle$ is the long-distance matrix element (LDME) describing the transition probability from the $c\bar{c}$ pair in the state n to the charmonium $\mathcal{Q}$. The LDMEs are defined as the vacuum expectation values of local four-fermion operators in NRQCD, $\langle 0|\mathcal{O}^{\mathcal{Q}}[n]|0\rangle$. The form of a local four-fermion operator for charmonium production is①

$$\begin{aligned}\mathcal{O}^{\mathcal{Q}}[n] &= \chi^\dagger \mathrm{K}_n \psi \left(\sum_{X,m_J} |\mathcal{Q}+X\rangle\langle\mathcal{Q}+X| \right) \psi^\dagger \mathrm{K}'_n \chi \\ &= \chi^\dagger \mathrm{K}_n \psi (a_{\mathcal{Q}}^\dagger a_{\mathcal{Q}}) \psi^\dagger \mathrm{K}'_n \chi,\end{aligned} \tag{2.24}$$

where the $2J+1$ spin states of the charmonium $\mathcal{Q}$ and any other particles X in the final state are summed over. The factors K_n and K'_n may contain the Pauli matrices σ^i, colour matrices t^C, and covariant derivatives $\vec{D}$. For example, the local four-fermion operators whose dimension of mass is six are

$$\mathcal{O}^{\mathcal{Q}}[{}^1S_0^{[1]}] = \chi^\dagger \psi (a_{\mathcal{Q}}^\dagger a_{\mathcal{Q}}) \psi^\dagger \chi, \tag{2.25}$$

$$\mathcal{O}^{\mathcal{Q}}[{}^3S_1^{[1]}] = \chi^\dagger \sigma^i \psi (a_{\mathcal{Q}}^\dagger a_{\mathcal{Q}}) \psi^\dagger \sigma^i \chi, \tag{2.26}$$

$$\mathcal{O}^{\mathcal{Q}}[{}^1S_0^{[8]}] = \chi^\dagger t^C \psi (a_{\mathcal{Q}}^\dagger a_{\mathcal{Q}}) \psi^\dagger t^C \chi, \tag{2.27}$$

$$\mathcal{O}^{\mathcal{Q}}[{}^3S_1^{[8]}] = \chi^\dagger \sigma^i t^C \psi (a_{\mathcal{Q}}^\dagger a_{\mathcal{Q}}) \psi^\dagger \sigma^i t^C \chi. \tag{2.28}$$

① This is only for summing over quarkonium polarisation. The form for the polarised case is in Ref.[60].

The operator creates a $c\bar{c}$ pair in a state specified by K'_n, projects it onto an intermediate state containing a charmonium $\mathcal{Q}$ plus anything, and annihilates a $c\bar{c}$ pair specified by K_n from that state. All the effects at the scale $m_c v$ or smaller are involved in the LDMEs, which have to be calculated by non-perturbative approaches or determined from experimental data. The LDMEs are supposed to be universal, *i.e.* independent of the process, and their relative magnitude is ordered in powers of v derived from the velocity-scaling rules[53]. Therefore, the charmonium production cross-section takes the form of a double expansion in α_s and v. For a certain accuracy, the summation can be truncated and only a few LDMEs need to be taken into account in practice. The convergence of the expansion, as well as the universality of LDMEs, is a guarantee of the predictive power of the NRQCD factorisation approach.

As indicated in Eq. 2.23, both the colour-singlet and colour-octet channels contribute to the charmonium production in the NRQCD factorisation approach. If the colour-octet contributions are set to zero, the NRQCD approach will turn into in the colour-singlet model. Thanks to the colour-octet mechanism, the NRQCD approach succeeded in solving the problem of infrared divergences and the $\psi(2S)$ surplus puzzle in the colour-singlet model, as discussed in the following.

2.4.3 Successes of colour-octet mechanism

In the colour-singlet model, the short-distance cross-sections for P-wave state production and decay exhibit logarithmic infrared divergences originated from the soft gluon emission. The infrared divergences cannot be factorised into the non-perturbative wave function, indicating the incompleteness of the colour-singlet model. The colour-octet mechanism in NRQCD approach provides a natural solution to this problem, through absorbing the infrared divergences into colour-octet LDMEs[61]. As an example, the χ_c production cross-section can be expressed as

$$\mathrm{d}\sigma_{\chi_c} = \mathrm{d}\sigma[^3P_J^{[1]}]\langle\mathcal{O}^{\chi_c}[^3P_J^{[1]}]\rangle + \mathrm{d}\sigma[^3S_1^{[8]}]\langle\mathcal{O}^{\chi_c}[^3S_1^{[8]}]\rangle + \mathcal{O}(v^2). \tag{2.29}$$

The colour-singlet LDME $\langle\mathcal{O}^{\chi_c}[^3P_J^{[1]}]\rangle$ and the colour-octet LDME $\langle\mathcal{O}^{\chi_c}[^3S_1^{[8]}]\rangle$ both scale with v^5, and other terms in Eq. 2.29 are suppressed by v^2 or more, according to the velocity-scaling rules. The infrared singularity encountered in the calculations of $\mathrm{d}\sigma[^3P_J^{[1]}]$ can be cancelled by a corresponding infrared singularity from the radiative corrections to the colour-octet LDME $\langle\mathcal{O}^{\chi_c}[^3S_1^{[8]}]\rangle$.

The inclusion of colour-octet contributions is crucial not only to cancel the infrared

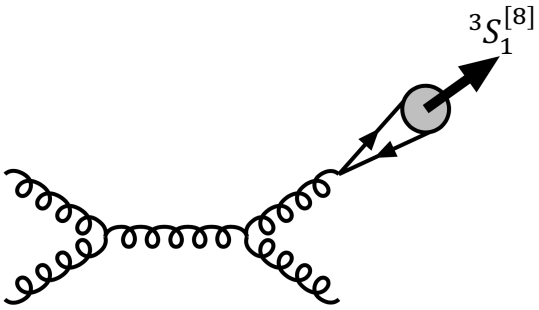

$$\frac{\mathrm{d}\sigma}{\mathrm{d}p_\mathrm{T}^2} \sim \alpha_s^3 \frac{1}{p_\mathrm{T}^4} v^4, \text{ for } p_\mathrm{T} \gg m_c$$

(a) Production at the LO in α_s with the colour-octet intermediate state $c\bar{c}[^3S_1^{[8]}]$.

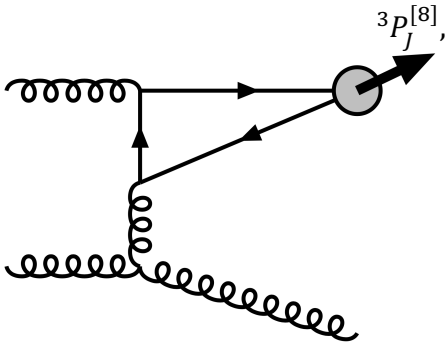

$$\frac{\mathrm{d}\sigma}{\mathrm{d}p_\mathrm{T}^2} \sim \alpha_s^3 \frac{(2m_c)^2}{p_\mathrm{T}^6} v^4, \text{ for } p_\mathrm{T} \gg m_c$$

(b) Production at the LO in α_s with the colour-octet intermediate state $c\bar{c}[^3P_J^{[8]}]$ or $c\bar{c}[^1S_0^{[8]}]$.

Figure 2.6 Representative diagrams for the J/ψ or $\psi(2S)$ hadroproduction through colour-octet channels, along with the scaling behaviour of the cross-sections at large p_T. The figures are taken from Ref. [53].

divergences, but also to explain the $\psi(2S)$ surplus puzzle. For J/ψ or $\psi(2S)$ production, the intermediate $c\bar{c}$ pair produced in the hard scattering do not have to be in the $^3S_1^{[1]}$ state, and the intermediate $c\bar{c}$ states that predominantly contribute to the production are determined according to the velocity-scaling rules. The leading LDME is a colour-singlet one $\langle \mathcal{O}^{J/\psi}[^3S_1^{[1]}]\rangle$ scaling as v^3. Three colour-octet LDMEs $\langle \mathcal{O}^{J/\psi}[^3S_1^{[8]}]\rangle$, $\langle \mathcal{O}^{J/\psi}[^3P_J^{[8]}]\rangle$ and $\langle \mathcal{O}^{J/\psi}[^1S_0^{[8]}]\rangle$ scale as v^7, and all the other LDMEs $\langle \mathcal{O}^{J/\psi}[n]\rangle$ scale as v^{11} or smaller. Although the colour-octet LDMEs are suppressed by at least v^4 relative to the colour-singlet one, their contributions can be enhanced by the corresponding SDCs at large p_T. At the LO in α_s, the partonic differential cross-section of the colour-octet $c\bar{c}$ state $^3S_1^{[8]}$ ($^3P_J^{[8]}$ or $^1S_0^{[8]}$) is scaled as p_T^{-4} (p_T^{-6}), which prevails over the colour-singlet contribution that scaled as p_T^{-8}. The representative diagrams for the J/ψ or $\psi(2S)$ hadroproduction through these colour-octet channels at the LO in α_s are shown in Figure 2.6, along with the scaling behaviour of the cross-sections at large p_T. With the leading colour-octet contributions $^3S_1^{[8]}$, $^3P_J^{[8]}$ and $^1S_0^{[8]}$ included and their LDMEs obtained from fits to the CDF data[62],

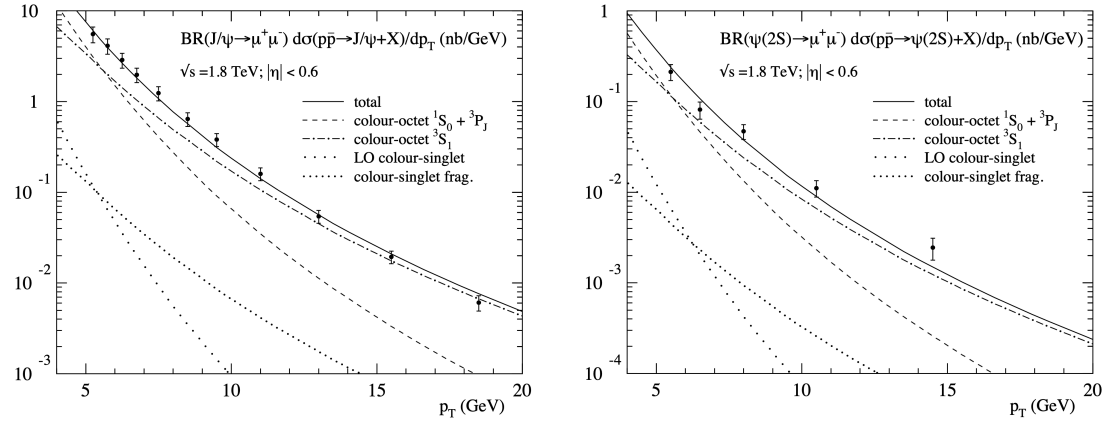

(a) Direct J/ψ production cross-section. (b) Direct $\psi(2S)$ production cross-section.

Figure 2.7 Comparisons of (a) J/ψ and (b) $\psi(2S)$ production cross-sections between CDF data[62] and NRQCD calculations[53]. The figures are taken from Ref. [53].

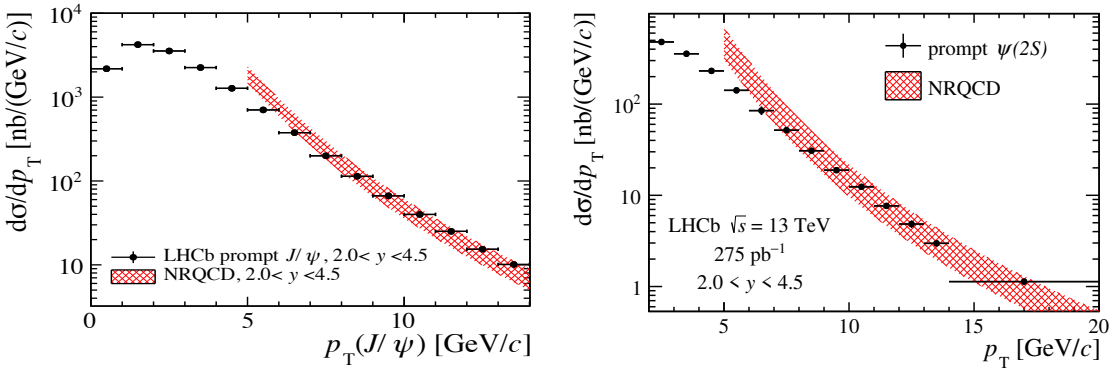

(a) Prompt J/ψ production cross-section. The figure is taken from Ref. [63].

(b) Prompt $\psi(2S)$ production cross-section. The figure is taken from Ref. [64].

Figure 2.8 Comparisons of (a) J/ψ and (b) $\psi(2S)$ production cross-sections between LHCb data[63-64] and NLO NRQCD calculations[65].

the theoretical calculations agreed with the J/ψ and $\psi(2S)$ production at the CDF experiment perfectly, as shown in Figure 2.7. However, it did not provide a convincing test of the NRQCD factorisation approach because there are free parameters in the calculations which are adjusted to fit the data. The LDMEs obtained from fits to the CDF data in $p\bar{p}$ collisions at the Tevatron should be universal and can be used in the predictions for other experiments.

After the LHC started operating, plenty of data in pp collisions at high energies were collected and provided good tests of NRQCD factorisation. NRQCD calculations, especially those up to the next-to-leading order (NLO) in α_s[65-66], with LDMEs fixed using the Tevatron data described the high-p_{T} charmonium production at the experiments in pp collisions at the LHC very well. For instance, for J/ψ and $\psi(2S)$ production in pp col-

lisions at $\sqrt{s} = 13\,\text{TeV}$, the comparisons between LHCb data[63-64] and NLO NRQCD calculations[65] are shown in Figure 2.8. Good agreement between data and theory was observed in the high-p_T region both for J/ψ and $\psi(2S)$ production. Based on these tests, the $\psi(2S)$ surplus puzzle seems to be solved by the NRQCD factorisation approach successfully via the inclusion of the colour-octet mechanism. Nevertheless, some problems still remain unsolved and new ones have shown up, which motivates the further study of charmonium production.

2.4.4 Problems of NRQCD factorisation

In the NRQCD factorisation approach, the SDCs for hadroproduction are usually calculated as the partonic cross-sections convolved with PDFs in the framework of collinear factorisation. The NRQCD factorisation is only applicable in the high-p_T region, $p_\text{T} \gtrsim 2m_c$, where the collinear factorisation is known to hold and soft gluon emissions from the produced $c\bar{c}$ pairs cannot alter the large p_T of charmonium. And thus in the low-p_T region, NRQCD calculations fail to describe the charmonium production at high-energy hadron colliders. The TMD factorisation is an alternative to the collinear factorisation, but the combination of NRQCD and TMD factorisation is very difficult because many effects in the charmonium production may break the TMD factorisation[67]. Such a factorisation has been established only for η_c production so far[68]. In order to describe the charmonium production at low p_T, another approach is to combine the color glass condensate (CGC) effective theory with the NRQCD framework[69], which is introduced in the Section 2.5.1.

In addition, the validity of the NRQCD factorisation is heavily relies on the universality of LDMEs, but currently various determinations of LDMEs cast doubt on it. The colour-octet LDMEs extracted from fits to data using different methods by different groups are not consistent with each other[70]. Especially, the discrepancy of colour-octet LDMEs between hadroproduction and photoproduction is significant. For the linearly combined colour-octet LDME of J/ψ production

$$M_{0,r_0}^{J/\psi} = \langle \mathcal{O}^{J/\psi}[^1S_0^{[8]}] \rangle + \frac{r_0}{m_c^2} \langle \mathcal{O}^{J/\psi}[^3P_0^{[8]}] \rangle, \tag{2.30}$$

the values extracted from the Tevatron data (hadroproduction)[66] and from the B-factories data (photoproduction)[71] are

$$M_{0,3.9}^{J/\psi} = (7.4 \pm 1.9) \times 10^{-2}\,\text{GeV}^3, \text{ in } p\bar{p} \text{ collisions},$$

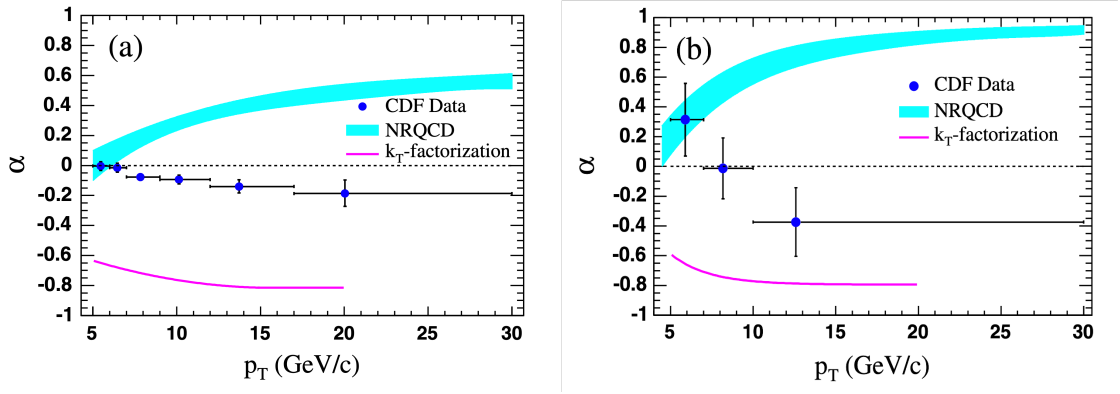

(a) J/ψ polarisation. (b) $\psi(2S)$ polarisation.

Figure 2.9 Comparisons of (a) J/ψ and (b) $\psi(2S)$ polarisation between CDF data[72] and NRQCD calculations[73-74]. The figures are taken from Ref. [72].

$$M_{0,4.0}^{J/\psi} < (2.0 \pm 0.6) \times 10^{-2}\,\mathrm{GeV}^3, \text{ in } e^+e^- \text{ collisions.}$$

The extracted colour-octet LDMEs for photoproduction are much smaller than those for hadroproduction, bring the universality of LDMEs and the importance of colour-octect contributions into question.

Another crucial problem of NRQCD factorisation is the polarisation puzzle. At the LO in α_s, the dominate contribution to the J/ψ and $\psi(2S)$ production at large p_T is from the gluon fragmentation process via the ${}^3S_1^{[8]}$ channel due to its scaling behaviour of p_T^{-4}, as shown in Figure 2.6(a). As a result, the LO NRQCD predicts that J/ψ and $\psi(2S)$ produced with large-p_T in hadron-hadron collisions are transversely polarised. On the contrary, only small longitudinal polarisation was found in the measurement at the CDF experiment[72], as shown in Figure 2.9. The polarisation parameter α in Figure 2.9 is defined in the angular distribution of the di-muon decay,

$$\frac{\mathrm{d}\sigma}{\mathrm{d}\cos\theta} \propto 1 + \alpha\cos^2\theta, \tag{2.31}$$

where θ is the angle between direction of μ^+ in the charmonium rest frame and the chosen axis, the charmonium direction in the laboratory frame in this case. For the fully transverse (longitudinal) polarisation, the parameter $\alpha = +1(-1)$, while the measured results shown in Figure 2.9 are consistent with zero. The results of the almost zero polarisation, known as the polarisation puzzle, have been confirmed by measurements at the LHC later[75-77]. When NRQCD calculations are extended to the NLO in α_s[66], the prediction of J/ψ polarisation may become different from that at the LO. At the NLO, both the processes via ${}^3S_1^{[8]}$ and ${}^3P_J^{[8]}$ channels scale as p_T^{-4}, and their transversely polarised contributions cancel each other. Using the colour-octet LDMEs fixed from Tevatron data with $p_\mathrm{T} > 7\,\mathrm{GeV}$,

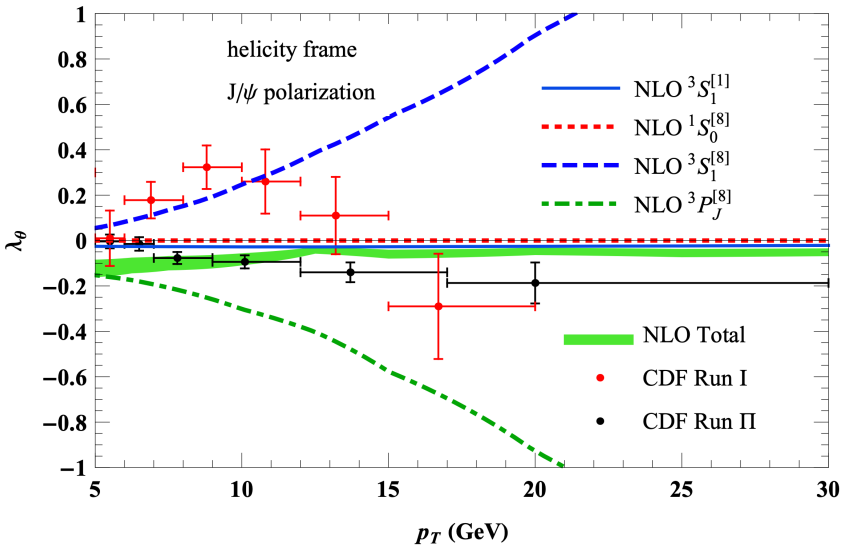

Figure 2.10 Comparison of J/ψ polarisation between CDF data[72,81] and NLO NRQCD calculations[78]. The figure is taken from Ref. [78].

the NLO NRQCD predicts that J/ψ mesons are approximately unpolarised[78], as show in Figure 2.10, but the predictions may be different with other LDME sets[79-80]. The polarisation parameter λ_θ in the helicity frame in Figure 2.10 is actually the parameter α in Eq. 2.31. For the $\psi(2S)$ polarisation, such cancellation between $^3S_1^{[8]}$ and $^3P_J^{[8]}$ channels is weak[65], and it is still difficult to explain its polarisation. If the LDMEs are fixed using Tevatron data with a higher-p_T cut, $p_T > 11$ GeV, a compatible description of $\psi(2S)$ polarisation can be obtained[65], which implies that the NRQCD factorisation perhaps is only valid at large enough p_T range, $p_T \gg 2m_c$. In any case, no satisfactory solution has been achieved to interpret differential cross-section and polarisation simultaneously in the whole kinematic region thus far.

In the meantime, there is still a debate on how significant the colour-octet contributions are in the charmonium production. In the colour-singlet model, it was found that large corrections appear at the NLO and next-to-next-to-leading order (NNLO) in α_s at high energies.[82-83]. With all these corrections included, the inconsistency between predictions of LO colour-singlet model and data are reduced a lot, and the colour-octet mechanism become less important than before. Besides, as mentioned above, the photoproduction data indicated that the colour-octet contributions might be overestimated for the hadroproduction. Since the higher-order corrections in the colour-singlet model have large uncertainties and various colour-octet LDME sets are not consistent with each other, it is still controversial if the color-octet processes substantially contribute to the charmonium production.

In summary, the NRQCD factorisation approach faces many problems at present. The issue that NRQCD calculations fail to describe the charmonium production in the low-p_{T} region may be solved by combining CGC effective theory and NRQCD factorisation, but this CGC+NRQCD framework still needs to be checked by experiments additionally. The most crucial problems are the inconsistency of different LDME sets and the polarisation puzzle. Moreover, the importance of the colour-octet mechanism has been questioned. In this case, more precise measurements of charmonium production and polarisation are needed to clarify these intractable problems. Since these problems are related to higher-order corrections more or less, the study of double charmonium production, in which the leading contribution is at the higher order in α_s, can be helpful to understand such issues and provide new tests of the NRQCD factorisation.

2.5 Charmonium production in pp collisions

In pp collisions, charmonium can be produced through three processes:

- The first kind of charmonium directly comes from hard scattering of partons, which is called direct charmonium. It originates from the primary vertex (PV) of pp collision.
- The second is produced via the feed-down of excited charmonium states. It comes from the primary vertex similar to direct charmonium. Thus both of these two types are called prompt charmonium.
- Charmonium can also be produced through week decays of b-hadrons. As b-hadrons has a relatively long lifetime, the decay vertices of b-hadrons are typically separated from the PV. The charmonium originating from b-hadron decay vertex is called charmonium from b, or non-prompt charmonium.

A certain fraction of prompt J/ψ mesons come from the feed-down of χ_c and $\psi(2S)$ mesons, while for $\psi(2S)$ production, there is no significant feed-down contribution. Prompt charmonium production at high-p_{T} can be described by the NLO NRQCD calculations, as introduced in the previous section. For prompt charmonium production at low p_{T}, a new framework combining CGC effective theory and NRQCD factorisation has been developed[69]. The study of non-prompt charmonium production can help us understand the b-quark production mechanism. The inclusive b-hadron production cross-section can be calculated in the fixed order plus next-to-leading logarithms (FONLL) framework[84]. With the known branching fractions of b-decay, such as $\mathcal{B}(b \to J/\psi\, X) =$

$(1.16 \pm 0.10)\%$ [9], the measured cross-sections of non-prompt charmonium can provide good tests of FONLL calculations.

2.5.1 CGC+NRQCD calculations for prompt charmonium at low-p_{T}

As mentioned in Section 2.4.4, the NRQCD factorisation is invalid for the low-p_{T} prompt charmonium production, and an alternative method is to combine the CGC effective theory and NRQCD factorisation [69]. In the combination, the short-distance $c\bar{c}$ pair production cross-section is calculated in the CGC framework, and the transition possibility that the $c\bar{c}$ pair evolves into a charmonium is described by the LDME in the NRQCD framework as usual.

For charmonium produced in high-energy pp collisions, its low-p_{T} range corresponds to the small Bjorken-x region where the phenomenon of gluon saturation becomes important. The CGC effective theory can be used to describe the high gluon density effects [85]. Regarding its name, "colour" denotes the colour charge of gluons, "glass" means that gluons are disordered and their positions do not change rapidly, and "condensate" refers to high density of gluons. In the CGC framework, hadron-hadron collisions between a dilute projectile and a dense target, typically proton-nucleus (pA) collisions, can be studied semi-analytically. For the dilute projectile, the density-enhanced effects are only kept to the lowest order, while for the dense target, such corrections are resummed to all orders. In addition to pA collisions, pp collisions can also be treated as the dilute-dense system for measurements at forward rapidity where the wave-function of one projectile is probed at large Bjorken-x and that of the other at small Bjorken-x.

The expressions of SDCs, the $c\bar{c}$ pair production cross-sections in pp collisions, are given in Ref. [69] within this dilute-dense CGC framework. Then, the SDCs calculated with parameters fixed from DIS data at the Hadron-Electron Ring Accelerator (HERA) are combined with the NRQCD LDMEs fixed from Tevatron data, thus predictions of charmonium production at low-p_{T} can be obtained [69] and compared with various measurements, as shown in Figure 2.11. The CGC+NRQCD calculations provide a good description of the low-p_{T} data, but due to the large uncertainties, more precise tests of this framework is necessary.

2.5.2 FONLL calculations for non-prompt charmonium

A precise knowledge of b-quark production is very important in order to evaluate the accuracy of QCD calculations and test theoretical predictions that are used to estimate

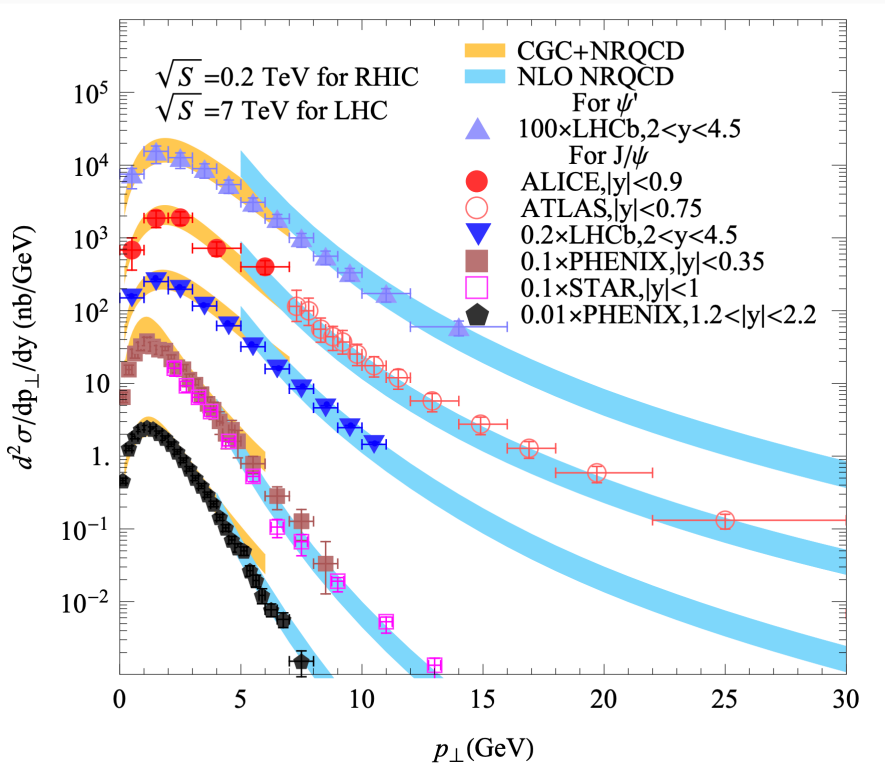

Figure 2.11 Comparisons of $\psi(2S)$ (top curve) and J/ψ (other four curves) differential cross-sections between CGC+NRQCD predictions[69] and various measurements[86-91]. NLO NRQCD predictions[92] for high-p_T are also shown. The figure is taken from Ref. [69].

backgrounds in searches for new physics. In the NLO QCD calculations for b-quark production, large logarithms of the ratio between p_T and mass m of the b-quark appear at all orders in the perturbative expansion, and ruin its convergence. Thus the resummation of the large logarithms to all perturbative orders is necessary. In the FONLL framework[84], fixed NLO QCD calculations[93-94] are matched with all-order resummation to next-to-leading logarithms (NLL) accuracy in the limit where the p_T of b-quark is much larger than its mass m_b[95].

The FONLL framework can give a good description of non-prompt charmonium production cross-sections with the branching fractions of b-decay as inputs. The comparisons between FONLL predictions[96-97] and measured results for non-prompt J/ψ production at the LHCb experiment[63] are shown in Figure 2.12. Good agreement is seen between FONLL calculations and LHCb data, but for the cross-section ratio between 13 TeV and 8 TeV in the high p_T region, it becomes a bit poorer although they are also consistent within uncertainties. More precise measurements of non-prompt charmonium production will be helpful to further test the FONLL framework.

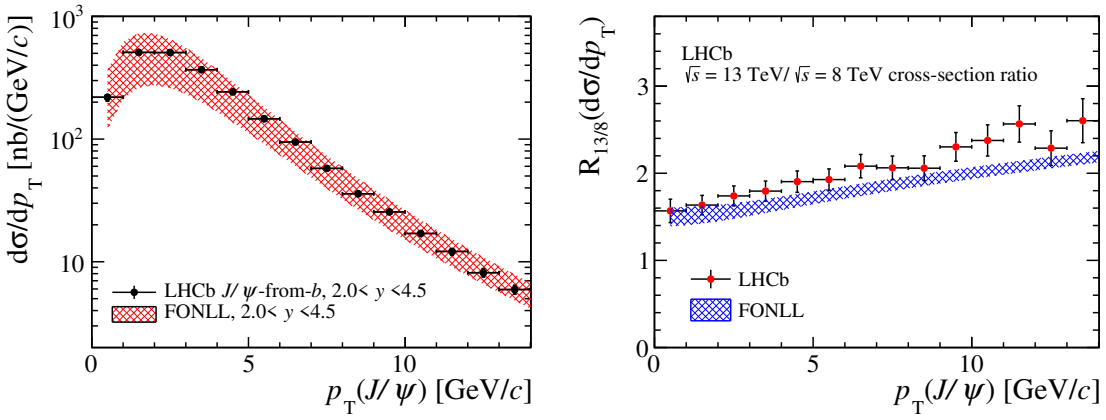

(a) Differential cross-section of non-prompt J/ψ production as a function of p_T.

(b) Non-prompt J/ψ cross-section ratio between 13 TeV and 8 TeV.

Figure 2.12 Comparisons of cross-section results of non-prompt J/ψ mesons between LHCb data[63] and FONLL calculations[96-97]. The figures are taken from Ref. [63].

2.5.3 Measurements of J/ψ and $\psi(2S)$ production at the LHC

Despite of decades of theoretical and experimental studies after the discovery of J/ψ, the charmonium production mechanism has not been well understood yet. The operation of the LHC took the studies of charmonium into a new era, due to the huge amounts of statistics that enables more precise measurements and makes new observables available. At the LHC, all of the four large experiments, LHCb, ATLAS, CMS and ALICE, have contributed to the studies significantly. With different characteristics of detectors, these four experiments cover complementary kinematic ranges and can provide a more comprehensive knowledge of the charmonium production. The measurements of J/ψ and $\psi(2S)$ production at the LHC are summarised in the following.

The differential cross-sections for prompt and non-prompt J/ψ mesons in pp collisions were measured at forward rapidity $2.0 < y < 4.5$ by the LHCb collaboration at centre-of-mass energies of $\sqrt{s} = 2.76\,\text{TeV}$[98], $5\,\text{TeV}$[13], $7\,\text{TeV}$[88], $8\,\text{TeV}$[99] and $13\,\text{TeV}$[63]. They were measured by the ATLAS collaboration in the mid-y region $|y| < 2$ at $\sqrt{s} = 5\,\text{TeV}$[100], $7\,\text{TeV}$[89,101], $8\,\text{TeV}$[101] and 13 TeV (for very high p_T)[102], by the CMS collaboration at $\sqrt{s} = 5\,\text{TeV}$[103] and $7\,\text{TeV}$[104-105] at central rapidity $|y| < 2.4$, and by the ALICE collaboration at $\sqrt{s} = 5\,\text{TeV}$[106] and $13\,\text{TeV}$[106] at mid-rapidity $|y| < 0.9$ as well. Prompt J/ψ production cross-sections were also measured by the CMS collaboration at $\sqrt{s} = 13\,\text{TeV}$[107] in the region $|y| < 1.2$ and by the ALICE collaboration at $\sqrt{s} = 7\,\text{TeV}$[108] in the region $|y| < 0.9$. The measurements for inclusive J/ψ mesons, which include both prompt and non-prompt contributions, were performed by the ALICE

collaboration at $\sqrt{s} = 2.76\,\text{TeV}$[109], $5\,\text{TeV}$[110-112], $7\,\text{TeV}$[87,113] and $13\,\text{TeV}$[114-115] in the rapidity ranges $|y| < 0.9$ and $2.5 < y < 4.0$, and at $\sqrt{s} = 8\,\text{TeV}$[116] at forward rapidity $2.5 < y < 4.0$.

For $\psi(2S)$ production, prompt and non-prompt cross-sections were measured at forward rapidity $2.0 < y < 4.5$ by the LHCb collaboration at $\sqrt{s} = 7\,\text{TeV}$[64] and $13\,\text{TeV}$[64]. They were measured by the ATLAS collaboration in the mid-y region $|y| < 2$ at $\sqrt{s} = 5\,\text{TeV}$[100], $7\,\text{TeV}$[101,117], $8\,\text{TeV}$[101] and $13\,\text{TeV}$ (for very high p_{T})[102], and by the CMS collaboration at $\sqrt{s} = 7\,\text{TeV}$[105] at central rapidity $|y| < 2.4$ as well. Prompt $\psi(2S)$ production cross-sections were also measured by the CMS collaboration at $\sqrt{s} = 5\,\text{TeV}$[118] for $|y| < 2.4$ and at $13\,\text{TeV}$[107] for $|y| < 1.2$. The measurements for inclusive $\psi(2S)$ mesons were performed by the ALICE collaboration at $\sqrt{s} = 5\,\text{TeV}$[112], $7\,\text{TeV}$[113], $8\,\text{TeV}$[116] and $13\,\text{TeV}$[114] at forward rapidity $2.5 < y < 4.0$.

In this thesis, the measurement of J/ψ production cross-sections, separately for prompt and non-prompt contributions, in pp collisions at $\sqrt{s} = 5\,\text{TeV}$[13] is presented in Chapter 4, using a data sample corresponding to an integrated luminosity of $9.13 \pm 0.18\,\text{pb}^{-1}$ collected by the LHCb experiment. The measured results are compared with the NLO NRQCD, CGC+NRQCD and FONLL predictions respectively.

2.6 Double charmonium production in pp collisions

In pp collisions, double charmonium can be produced via two processes: single parton scattering (SPS) and double parton scattering (DPS). The schematic diagrams of SPS and DPS in a pp collision is shown in Figure 2.13. For SPS, the two charmonia in the final-state originate from the same scattering process, while for DPS, they come from two distinct scattering processes of two pairs of partons respectively. The study of double charmonium production in SPS can provide a new test of the NRQCD approach, helping to further understand the charmonium production mechanism. It is also a very promising process to study the gluon TMD PDFs, which remain very poorly known. The DPS process is of great concern since it provides valuable information on the profile and correlations of partons inside the proton. Besides, the DPS process is an important background in searches for new physics through the channels $Z + b\bar{b}$, $W^{\pm} + W^{\pm}$, *etc.*, thus a thorough understanding of the DPS process is essential to these studies.

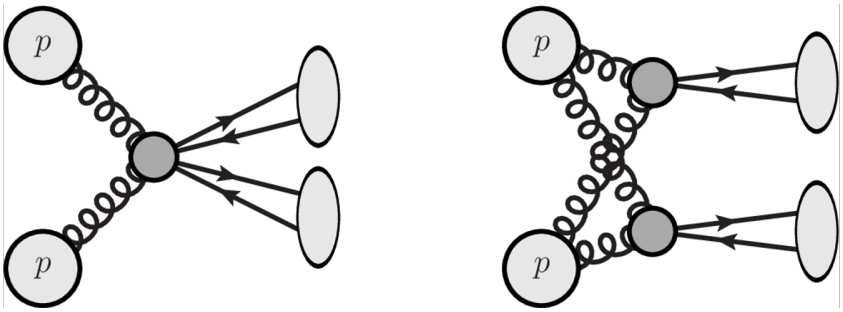

(a) SPS. (b) DPS.

Figure 2.13 The schematic diagrams of (a) SPS and (b) DPS in a pp collision. The figures are taken from Ref. [119].

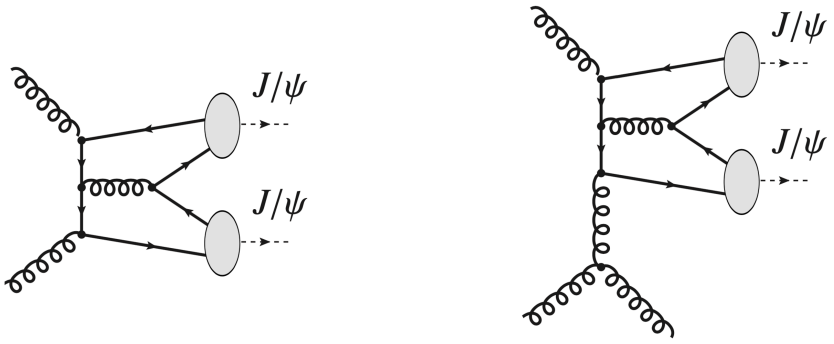

(a) LO (α_s^4). (b) NLO (α_s^5).

Figure 2.14 Representative diagrams of di-J/ψ production in SPS at the (a) LO and (b) NLO in the colour-singlet model. The figures are taken from Ref. [120].

2.6.1 Double charmonium production in SPS

In the framework of NRQCD, the production cross-section of double charmonium $\mathcal{Q}_1\mathcal{Q}_2$ in SPS can be given by

$$\mathrm{d}\sigma_{\mathcal{Q}_1\mathcal{Q}_2} = \sum_{n_1,n_2} \mathrm{d}\sigma(pp \to c\bar{c}[n_1]c\bar{c}[n_2]X)\langle\mathcal{O}^{\mathcal{Q}_1}[n_1]\rangle\langle\mathcal{O}^{\mathcal{Q}_2}[n_2]\rangle, \tag{2.32}$$

where the SDC $\mathrm{d}\sigma(pp \to c\bar{c}[n_1]c\bar{c}[n_2]X)$ describes the production of two pairs of $c\bar{c}$ in the states n_1 and n_2, and $\langle\mathcal{O}^{\mathcal{Q}_2}[n_1]\rangle$ and $\langle\mathcal{O}^{\mathcal{Q}_2}[n_2]\rangle$ are the corresponding LDMEs respectively.

Take di-J/ψ production in high-energy pp collisions as an example. In the NRQCD approach at the LO in v^2 or equally the colour-singlet model, $n_{1,2} = {}^3S_1^{[1]}$, and the colour-singlet LDME can be obtained from the potential model calculations. The leading contribution is from the gluon fusion process $gg \to J/\psi\, J/\psi$, at the LO in α_s in the colour-singlet model, as shown in Figure 2.14(a). At the NLO in α_s, a representative diagram for the real emission corrections $gg \to J/\psi\, J/\psi\, g$ is shown in Figure 2.14(b). For the colour-octet contributions, whose LDMEs are suppressed by powers of v, explicit calculations[121] in-

dicate these corrections are much smaller than colour-singlet contributions except in some peripheries of the phase space.

For an accurate description, the effects of intrinsic initial-k_{T} smearing, where k_{T} is the transverse momentum of the gluons, should be taken into account[122]. In fact, di-J/ψ production can be considered as a probe of the transverse dynamics of the gluons in the framework of TMD factorisation, as discussed in Section 2.6.2. For predictions in the framework of collinear factorisation, the k_{T} smearing is applied as a makeshift.

For feed-down contributions to di-J/ψ production in SPS, the fraction from the feed-down of J/ψ-$\psi(2S)$ or di-$\psi(2S)$ production is expected to be large (around 46%)[123]. The processes $gg \to J/\psi\,\chi_c$ and $gg \to \psi(2S)\chi_c$ are suppressed at the LO by the conservation of C-parity, and the feed-down from $gg \to \chi_c\chi_c$ is suppressed by the square of $\chi_c \to J/\psi$ branching fraction.

2.6.2 Study of gluon TMD PDFs via SPS process

In the framework of TMD factorisation, which is briefly introduced in Section 2.1.3, the gluon TMD PDFs play an important role in describing the three-dimensional picture of hadrons, yet the current understanding is very limited due to the lack of data for extraction. The di-J/ψ production via SPS process in pp collisions has great potential to probe the gluon TMD PDFs inside protons, since its leading contribution is from gluon fusion processes and the colour-octet corrections that may break the TMD factorisation are suppressed.

More specifically, gluons inside unpolarised protons can be described by two independent TMD PDFs, $f_1^g(x, \boldsymbol{k}_{\mathrm{T}}^2)$ and $h_1^{\perp g}(x, \boldsymbol{k}_{\mathrm{T}}^2)$, at the leading twist[124]. The first one $f_1^g(x, \boldsymbol{k}_{\mathrm{T}}^2)$ is the distribution of unpolarised gluons, and the second one $h_1^{\perp g}(x, \boldsymbol{k}_{\mathrm{T}}^2)$ is the distribution of linearly polarised gluons. The presence of linearly polarised gluons can alter the transverse-momentum spectrum and leads to the azimuthal asymmetries for di-J/ψ production[125].

The general expression of the TMD-based differential cross-section for di-J/ψ production from gluon fusion is given by[126]

$$\begin{aligned}\frac{\mathrm{d}\sigma}{\mathrm{d}M_{QQ}\mathrm{d}Y_{QQ}\mathrm{d}^2\boldsymbol{P}_{\mathrm{T}QQ}\mathrm{d}\Omega} = \frac{\sqrt{M_{QQ}^2 - 4M_Q^2}}{(2\pi)^2 8 s M_{QQ}^2}\Big\{ & F_1 C[f_1^g f_1^g] + F_2 C[w_2 h_1^{\perp g} h_1^{\perp g}] \\ & + \Big(F_3 C[w_3 f_1^g h_1^{\perp g}] + F_3' C[w_3' h_1^{\perp g} f_1^g]\Big)\cos 2\phi_{\mathrm{CS}} + \Big(F_4 C[w_4 h_1^{\perp g} h_1^{\perp g}]\Big)\cos 4\phi_{\mathrm{CS}}\Big\}.\end{aligned} \tag{2.33}$$

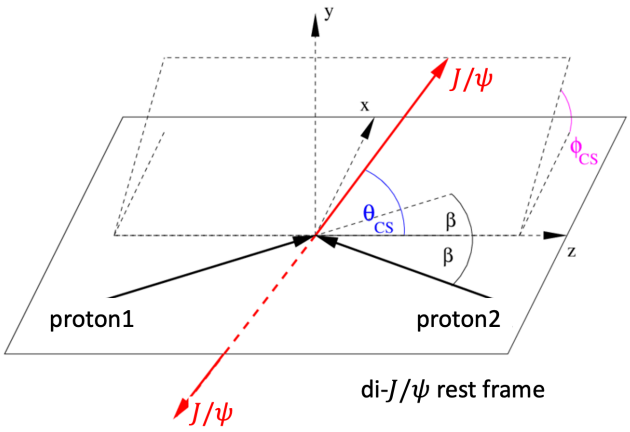

Figure 2.15 Schematic diagram of the CS frame.

where QQ denotes the J/ψ pair, M_{QQ}, Y_{QQ} and $\boldsymbol{P}_{\mathrm{T}QQ}$ are the invariant mass, rapidity and transverse momentum of the pair respectively, and $\mathrm{d}\Omega = \mathrm{d}\cos\theta_{\mathrm{CS}}\mathrm{d}\phi_{\mathrm{CS}}$. The angles θ_{CS} and ϕ_{CS} are defined in the CS frame[127], which is shown in Figure 2.15 schematically. The CS frame is the di-J/ψ rest frame. The z-axis is defined as the bisector of angle between $\vec{p}_1$ and $-\vec{p}_2$, where $\vec{p}_1$ and $\vec{p}_2$ are the three-momenta of the colliding protons in the di-J/ψ rest frame, the y-axis is defined as along the vector product $\vec{p}_1 \times \vec{p}_2$, and the x-axis is defined to complete a right-handed coordinate system. The polar angle θ_{CS} and the azimuthal angle ϕ_{CS} denote the direction of one J/ψ meson in the CS frame. The transverse momentum $P_{\mathrm{T}QQ} = |\boldsymbol{P}_{\mathrm{T}QQ}|$ and rapidity Y_{QQ} are defined in the laboratory frame. The M_Q is the mass of the J/ψ meson and the s is the square of the centre-of-mass energy of the collision. The hard-scattering coefficients F_i only depend on M_{QQ} and θ_{CS}, and their expressions can be found in Ref. [126]. The convolutions of TMD PDFs in Eq. 2.33 are given by

$$\begin{aligned} C[wfg] = &\int \mathrm{d}^2\boldsymbol{k}_{\mathrm{T}1} \int \mathrm{d}^2\boldsymbol{k}_{\mathrm{T}2}\delta^2(\boldsymbol{k}_{\mathrm{T}1} + \boldsymbol{k}_{\mathrm{T}2} - \boldsymbol{P}_{\mathrm{T}QQ}) \\ &\times w(\boldsymbol{k}_{\mathrm{T}1}, \boldsymbol{k}_{\mathrm{T}2}) f(x_1, \boldsymbol{k}_{\mathrm{T}1}^2) g(x_2, \boldsymbol{k}_{\mathrm{T}2}^2), \end{aligned} \tag{2.34}$$

where the TMD weights $w(\boldsymbol{k}_{\mathrm{T}1}, \boldsymbol{k}_{\mathrm{T}2})$ can be found in Ref. [128], and $x_{1,2} = M_{QQ}e^{\pm Y_{QQ}}/\sqrt{s}$. The Eq. 2.33 is only applicable in the TMD region, $P_{\mathrm{T}QQ} \ll M_{QQ}$. In practice, the TMD region is usually set as $P_{\mathrm{T}QQ} < \langle M_{QQ}\rangle/2$, where $\langle M_{QQ}\rangle$ is the expected value of a mass interval.

For the study of $P_{\mathrm{T}QQ}$ spectrum, the dependence of ϕ_{CS} in Eq. 2.33 can be integrated out as

$$\frac{1}{2\pi}\int \mathrm{d}\phi_{\mathrm{CS}} \frac{\mathrm{d}\sigma}{\mathrm{d}M_{QQ}\mathrm{d}Y_{QQ}\mathrm{d}^2\boldsymbol{P}_{\mathrm{T}QQ}\mathrm{d}\Omega} = F_1 C[f_1^g f_1^g] + F_2 C[w_2 h_1^{\perp g} h_1^{\perp g}], \tag{2.35}$$

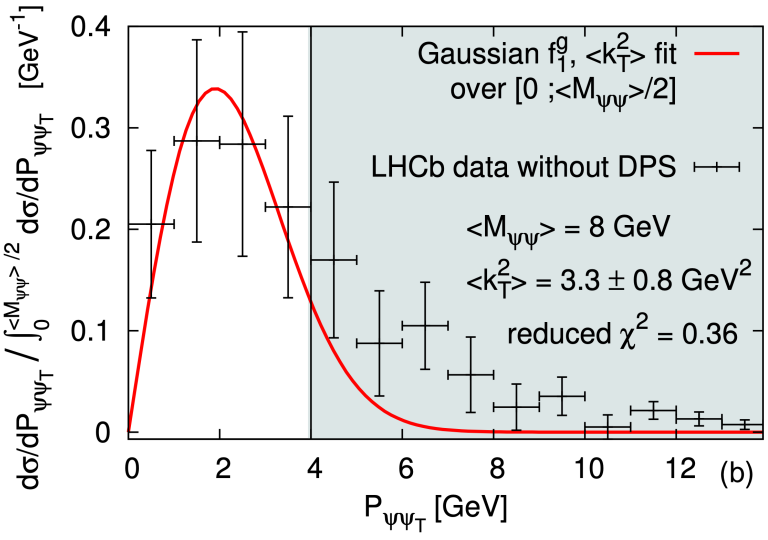

Figure 2.16 The normalised P_{TQQ} dependence of di-J/ψ cross-section obtained from the fit to LHCb data[130] using a Gaussian f_1^g with $\langle k_T^2 \rangle$. The data in the gray zone, where the TMD framework is not applicable, were not used for the fit. The figure is taken from Ref. [126].

and the dependence of the transverse momentum is encoded into the TMD convolutions $\mathcal{C}[f_1^g f_1^g]$ and $\mathcal{C}[w_2 h_1^{\perp g} h_1^{\perp g}]$ entirely. Since F_2 is much smaller than F_1 [126], only the convolution $\mathcal{C}[f_1^g f_1^g]$ is significant in the P_{TQQ} spectrum. Due to the limited knowledge of gluon TMD PDFs, a simple Gaussian model is used to describe the f_1^g, as[129]

$$f_1^g(x, \boldsymbol{k}_T^2, \mu) = \frac{g(x,\mu)}{\pi \langle k_T^2 \rangle} e^{-\boldsymbol{k}_T^2/\langle k_T^2 \rangle}, \tag{2.36}$$

where $g(x,\mu)$ is the collinear PDF and $\langle k_T^2 \rangle$ depends on the factorisation scale μ implicitly. Using the Gaussian model with $\langle k_T^2 \rangle$, a fit to LHCb data for di-J/ψ production at $\sqrt{s}$ = 13 TeV[130] was performed[126], as shown in Figure 2.16. For the fit result, $\langle k_T^2 \rangle = 3.3 \pm 0.8\,\text{GeV}^2$, which was the first time for the extraction of information on gluon TMD PDFs from the measurement of a gluon fusion process.

For the study of azimuthal asymmetries (ϕ_{CS} distribution), the expected value of $\cos n\phi_{CS}$ can be defined as

$$\langle \cos n\phi_{CS} \rangle = \frac{\int \mathrm{d}\phi_{CS} \cos n\phi_{CS} \frac{\mathrm{d}\sigma}{\mathrm{d}M_{QQ}\mathrm{d}Y_{QQ}\mathrm{d}^2\boldsymbol{P}_{TQQ}\mathrm{d}\Omega}}{\int \mathrm{d}\phi_{CS} \frac{\mathrm{d}\sigma}{\mathrm{d}M_{QQ}\mathrm{d}Y_{QQ}\mathrm{d}^2\boldsymbol{P}_{TQQ}\mathrm{d}\Omega}}. \tag{2.37}$$

In this case, the $\langle \cos 2\phi_{CS} \rangle$ and $\langle \cos 4\phi_{CS} \rangle$ can be respectively expressed as

$$\langle \cos 2\phi_{CS} \rangle = \frac{1}{2} \frac{F_3 \mathcal{C}[w_3 f_1^g h_1^{\perp g}] + F_3' \mathcal{C}[w_3' h_1^{\perp g} f_1^g]}{F_1 \mathcal{C}[f_1^g f_1^g] + F_2 \mathcal{C}[w_2 h_1^{\perp g} h_1^{\perp g}]}, \tag{2.38}$$

$$\langle \cos 4\phi_{\rm CS} \rangle = \frac{1}{2} \frac{F_4 \mathcal{C}[w_4 h_1^{\perp g} h_1^{\perp g}]}{F_1 \mathcal{C}[f_1^g f_1^g] + F_2 \mathcal{C}[w_2 h_1^{\perp g} h_1^{\perp g}]}. \tag{2.39}$$

The presence of the linearly polarised gluon denoted by TMD PDF $h_1^{\perp g}$ results in non-zero $\langle \cos 2\phi_{\rm CS} \rangle$ and $\langle \cos 4\phi_{\rm CS} \rangle$. Although the theoretical predictions of these two expected value are only in the percent level[125], which is very difficult to measure them currently, it is helpful to investigate the azimuthal asymmetries experimentally.

2.6.3 DPS process and effective cross-section

The mechanism of the DPS process has not been fully understood yet. Its description is usually based on factorisation assumptions and approximations. The production cross-section of double charmonium $\mathcal{Q}_1\mathcal{Q}_2$ in DPS can be calculated as[131]

$$\begin{aligned} \sigma^{\rm DPS}_{\mathcal{Q}_1\mathcal{Q}_2} &= \frac{1}{1+\delta_{\mathcal{Q}_1\mathcal{Q}_2}} \sum_{i,j,k,l} \int {\rm d}x_1 {\rm d}x_2 {\rm d}x_1' {\rm d}x_2' {\rm d}^2\boldsymbol{b}_1 {\rm d}^2\boldsymbol{b}_2 {\rm d}^2\boldsymbol{b} \\ &\times \Gamma_{ij}(x_1, x_2, \boldsymbol{b}_1, \boldsymbol{b}_2) \hat{\sigma}_{ik}^{\mathcal{Q}_1}(x_1, x_1') \hat{\sigma}_{jl}^{\mathcal{Q}_2}(x_2, x_2') \Gamma_{kl}(x_1', x_2', \boldsymbol{b}_1 - \boldsymbol{b}, \boldsymbol{b}_2 - \boldsymbol{b}), \end{aligned} \tag{2.40}$$

where the $\frac{1}{1+\delta_{\mathcal{Q}_1\mathcal{Q}_2}}$ is the factor to account for the symmetry of the final state and $\delta_{\mathcal{Q}_1\mathcal{Q}_2}$ is the Kronecker symbol. The index i and j denotes two partons from one proton with the longitudinal fractions x_1 and x_2 and the transverse impact parameters $\boldsymbol{b}_1$ and $\boldsymbol{b}_2$, while the index k and l denotes those from the other proton with the fractions x_1' and x_2' and parameters $\boldsymbol{b}_1 - \boldsymbol{b}$ and $\boldsymbol{b}_2 - \boldsymbol{b}$. The parameter $\boldsymbol{b}$ is the transverse displacement of the two protons. The $\hat{\sigma}_{ik}^{\mathcal{Q}_1}(x_1, x_1')$ and $\hat{\sigma}_{jl}^{\mathcal{Q}_2}(x_2, x_2')$ are the partonic cross-sections for the production of the single charmonium $\mathcal{Q}_1$ and $\mathcal{Q}_2$ respectively. The generalised double parton distributions $\Gamma_{ij}(x_1, x_2, \boldsymbol{b}_1, \boldsymbol{b}_2)$ is assumed to be factorised into longitudinal and transverse parts as

$$\Gamma_{ij}(x_1, x_2, \boldsymbol{b}_1, \boldsymbol{b}_2) = D_{ij}(x_1, x_2) T_{ij}(\boldsymbol{b}_1, \boldsymbol{b}_2). \tag{2.41}$$

Furthermore, the two partons are assumed to be uncorrelated, leading to the factorisation of

$$D_{ij}(x_1, x_2) = f_i(x_1) f_j(x_2), \tag{2.42}$$

$$T_{ij}(\boldsymbol{b}_1, \boldsymbol{b}_2) = T_i(\boldsymbol{b}_1) T_j(\boldsymbol{b}_2), \tag{2.43}$$

respectively. Then if ignoring the parton-flavour dependence in $T_i(\boldsymbol{b}_m)$, a transverse overlapping function $F(\boldsymbol{b}_m)$ can be defined as

$$F(\boldsymbol{b}_m) = \int {\rm d}^2\boldsymbol{b}_m T(\boldsymbol{b}_m) T(\boldsymbol{b}_m - \boldsymbol{b}), \tag{2.44}$$

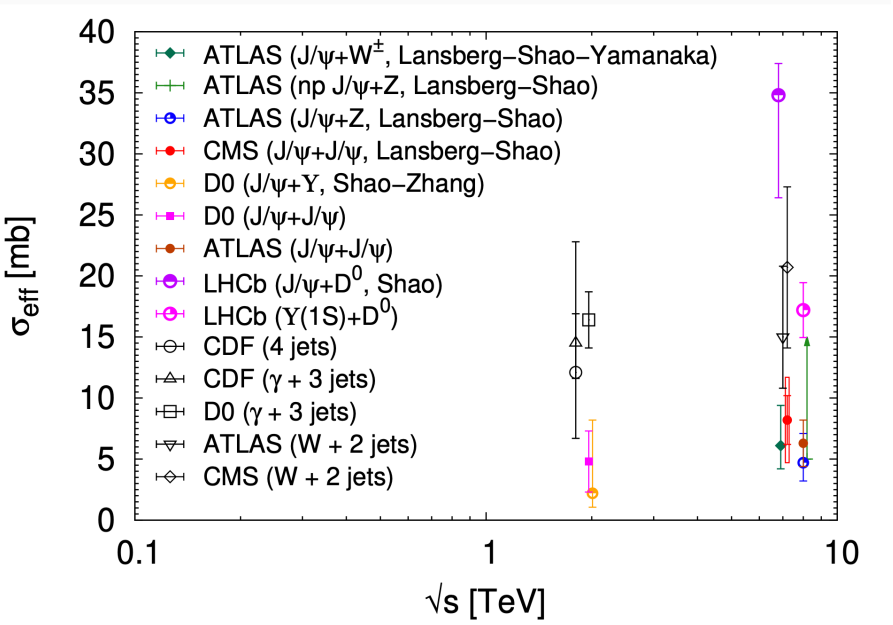

Figure 2.17 The extracted values of σ_{eff} from different measurements in pp or $p\bar{p}$ collisions[123,134-147]. The figure is taken from Ref. [148].

and the effective cross-section is defined as

$$\sigma_{\text{eff}} = \left[\int \mathrm{d}^2\boldsymbol{b} F^2(\boldsymbol{b})\right]^{-1}. \tag{2.45}$$

With the effective cross-section σ_{eff}, Eq. 2.40 can be simplified as the "pocket formula"

$$\sigma^{\text{DPS}}_{\mathcal{Q}_1\mathcal{Q}_2} = \frac{1}{1+\delta_{\mathcal{Q}_1\mathcal{Q}_2}} \frac{\sigma_{\mathcal{Q}_1}\sigma_{\mathcal{Q}_2}}{\sigma_{\text{eff}}}, \tag{2.46}$$

where $\sigma_{\mathcal{Q}_1}$ and $\sigma_{\mathcal{Q}_2}$ are the hadroproduction cross-sections of single charmonium $\mathcal{Q}_1$ and $\mathcal{Q}_2$ respectively. The DPS cross-sections can be derived according to the pocket formula as long as $\sigma_{\mathcal{Q}_1}$, $\sigma_{\mathcal{Q}_2}$ and σ_{eff} are known.

The effective cross-section σ_{eff} characterises the effective spatial area of the parton-parton interactions. Under the assumptions discussed above, the σ_{eff} should be independent of the process, as well as the centre-of-mass energies. However, it is indicated that some effects may break the factorisation assumptions[132-133], and thus the universality of σ_{eff} must be test by experiments to investigate the parton correlations that are not taken into account in the pocket formula. The values of σ_{eff} can be extracted from measurements of DPS cross-sections in various processes, not only for the double charmonium production. The extracted values at the LHC and Tevatron are summarised in Figure 2.17, which are around 2–35 mb with large uncertainties. A definite conclusion still cannot be drawn from the comparison of the extracted values, and more precise measurements for the DPS process are required.

2.6.4 Measurements of double charmonium hadroproduction

The evidence for di-J/ψ production was found by the NA3 collaboration for the first time in pion-platinum interactions in 1982[149], and then in proton-platinum interactions in 1987[150]. At the energies of the NA3 experiment (around a few hundreds of GeV), the di-J/ψ production is mainly through the process of the quark-antiquark annihilation, while at the energies of Tevatron and LHC, the leading contribution arises from the gluon fusion process. Until recent years, the di-J/ψ production cross-section was measured by the LHCb collaboration in pp collisions at $\sqrt{s} = 7\,\text{TeV}$[151], as a start of the experimental studies of di-J/ψ production at high-energy (more than 1 TeV) hadron colliders. It was pointed out that significant DPS contributions present in this measurement, and that the rapidity difference between two J/ψ mesons Δy can be considered as a useful variable for the separation of DPS and SPS contributions[152]. Then, the D0 collaboration reported the first extraction of DPS cross-sections of di-J/ψ production in $p\overline{p}$ collisions at $\sqrt{s} = 1.96\,\text{TeV}$[139], using the yield dependence on the $\Delta\eta$, the pseudo-rapidity difference between two J/ψ mesons. Besides, the di-J/ψ production cross-sections were also measured by the CMS collaboration in pp collisions at $\sqrt{s} = 7\,\text{TeV}$[153], by the ATLAS collaboration at $\sqrt{s} = 8\,\text{TeV}$[140], and by the LHCb collaboration at $\sqrt{s} = 13\,\text{TeV}$[130]. For the LHCb measurement at $\sqrt{s} = 13\,\text{TeV}$[130], due to the limitation of statistics and relatively narrow range of Δy, the separation of DPS and SPS contributions depended on different SPS models. Moreover, the production of double charmonium involving other states, such as J/ψ-$\psi(2S)$ and J/ψ-χ_c has not been measured before.

In this thesis, the measurement of di-J/ψ and J/ψ-$\psi(2S)$ production cross-sections in pp collisions at $\sqrt{s} = 13\,\text{TeV}$ is presented in Chapter 5, using a data sample corresponding to an integrated luminosity of $4.18 \pm 0.08\,\text{fb}^{-1}$ collected by the LHCb experiment. For di-J/ψ production, the statistics of this measurement is about 15 times that of the previous one[130], and the contributions from SPS and DPS are separated based on the differential cross-section as a function of Δy. The p_{T} spectrum of di-J/ψ production and the distribution of the azimuthal angle ϕ_{CS} in the CS frame are also measured for the study of gluon TMD PDFs. For J/ψ-$\psi(2S)$ production, this is the first measurement at hadron colliders.

CHAPTER 3 LHCB EXPERIMENT

The LHCb experiment is one of four main particle physics experiments located at the LHC. In this chapter, a brief introduction to the LHC is firstly presented, followed by an overview of the LHCb detector. Then, the tracking, particle identification (PID) and trigger systems of the LHCb experiment are introduced respectively.

3.1 Large Hadron Collider

The LHC is the largest particle accelerator operated at the highest energy in the world to date. It lies in an underground circular tunnel with a 27 km circumference straddling the French-Swiss border near Geneva. It was built by the European Organisation for Nuclear

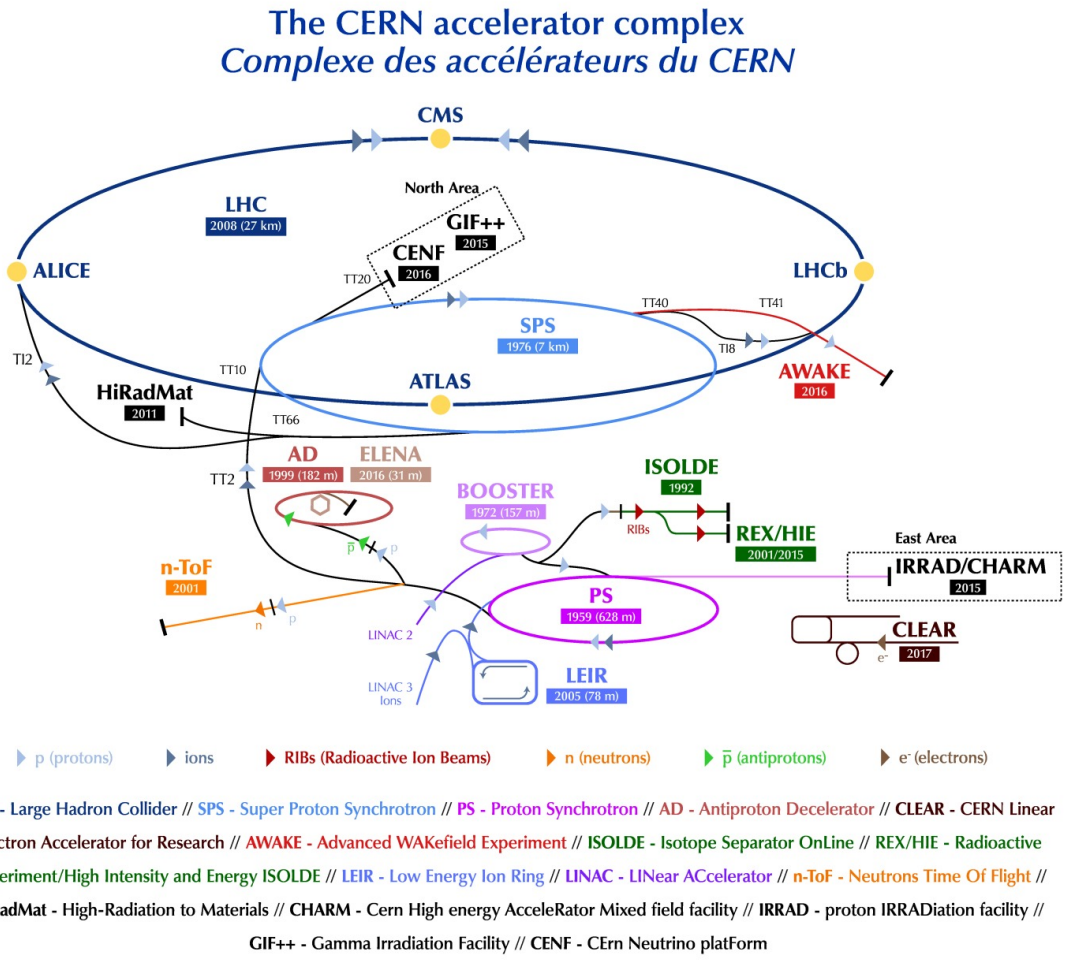

Figure 3.1 Schematic diagram of the CERN accelerator complex, including the LHC and its injectors. The figure is taken from Ref. [154].

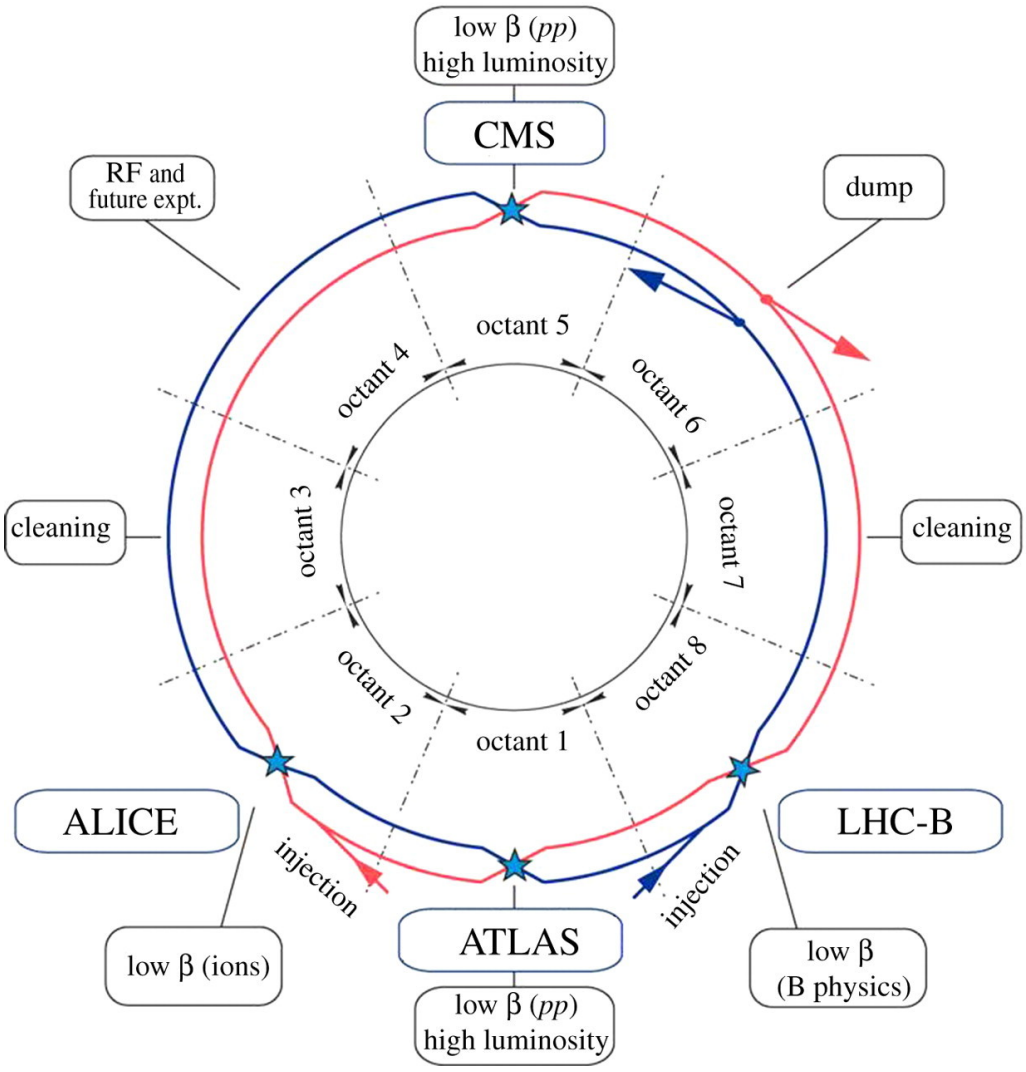

Figure 3.2 Schematic layout of the LHC. The figure is taken from Ref. [155].

Research (CERN), and the high energy beams at the LHC are obtained from a multi-stage process with the help of the CERN accelerator complex, as shown in Figure 3.1. The acceleration of protons starts with a linear accelerator, where the protons are accelerated up to 50 MeV after leaving their source. The proton beams from the LINAC are boosted in energy to 1.4 GeV in the Proton Synchrotron Booster, and then further accelerated by the Proton Synchrotron to 26 GeV. At the end of the injection chain, the Super Proton Synchrotron receives the beams from the Proton Synchrotron, accelerates them to 450 GeV and transports them to the LHC. The proton beams at the LHC are finally accelerated to an energy of up to 7 TeV using a specially designed superconducting radio-frequency system. In addition to protons, heavy ions can also be accelerated sequentially by a linear accelerator for ions and the Low Energy Ion Ring, and then by the Proton Synchrotron and the Super Proton Synchrotron, and finally by the LHC.

A schematic layout of the LHC is shown in Figure 3.2. Two beams are injected into two independent vacuum pipes at the LHC, circulating in opposite directions. There are four beam intersection points, and four main experiments, ATLAS, CMS, ALICE and LHCb, are located at each of these points. Two of them, ATLAS and CMS, are two general-purpose experiments at the LHC. The ALICE experiment mainly focuses on the heavy ion physics, and the LHCb experiment is specialised for heavy flavour physics. In spite of their different primary design purposes, all of these four experiments can make great contributions to the study of charmonium production.

Particles in the beam are bundled together into discrete bunches rather than being continuous. Detectors installed at the four intersection points record the products from particle collisions during the bunch crossing. In order to obtain more events of interest, it is important for the LHC to have a high instantaneous luminosity $\mathcal{L}_{\text{inst}}$, which is defined by the relation between the event rate R and the process' cross-section σ,

$$R = \sigma \mathcal{L}_{\text{inst}}. \tag{3.1}$$

The instantaneous luminosity of central pp collisions can be expressed as[156]

$$\mathcal{L}_{\text{inst}} = \frac{k f_{\text{rev}} N^2}{4\pi \sigma_x \sigma_y}, \tag{3.2}$$

where k is the number of bunches in the beam, f_{rev} is the revolution frequency, N is the number of protons per bunch, and σ_x and σ_z denote the horizontal and vertical beam sizes respectively at the collision point with the assumption of Gaussian distribution. In this case, a high luminosity requires a large number of bunches, a high bunch population and small beam transverse section. At the LHC, up to 2808 bunches can be filled with around 10^{11} protons per bunch, and they are separated by at least 7.5 m or 25 ns, corresponding to a bunch crossing rate of 40 MHz. The bunch at the collision point has a transverse section of around $20\,\mu\text{m} \times 20\,\mu\text{m}$, and a typical length of around 8 cm[156]. The designed instantaneous luminosity of the LHC is $10^{34}\,\text{cm}^{-2}\,\text{s}^{-1}$, which was first achieved in 2016. At the LHCb experiment, the designed luminosity is reduced to $2\text{–}4 \times 10^{32}\,\text{cm}^{-2}\,\text{s}^{-1}$, which corresponds to 1–2 pp collisions per bunch crossing, for the sake of precise heavy-flavour measurements.

For pp collisions, a tremendous amount of data have been collected at the LHC at different centre-of-mass energies. From 2010 to 2013, the first period of operation (Run 1), most of the pp collision data were taken at $\sqrt{s} = 7\,\text{TeV}$ and 8 TeV. After the LHC was shut down and upgraded between 2013 and 2015, the centre-of-mass energy of pp colli-

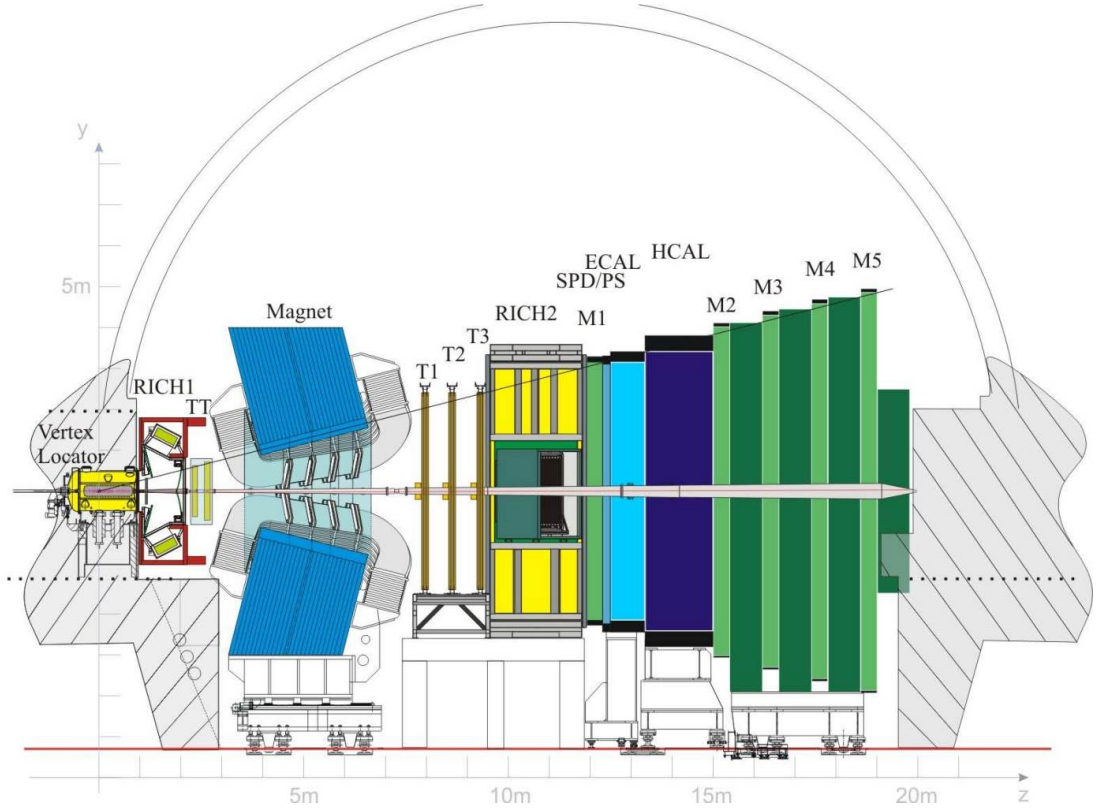

Figure 3.3 Schematic layout of the LHCb detector for Run 1 and Run 2. The figure is taken from Ref. [160].

sions reached 13 TeV during the second period of operation (Run 2). At the end of 2018, the LHC was shut down again for further upgrades, and it started its third period of operation (Run 3) in 2022. The pp collision data were also collected in a short period at $\sqrt{s} = 2.76$ TeV during Run 1, and at $\sqrt{s} = 5$ TeV during Run 2. The main goal of these short runs was to provide a reference for the study of heavy ion collisions at the same centre-of-mass energy per nucleon pair, but they can also complement the measurements on the charmonium production in pp collisions at these specific energies.

3.2 LHCb detector

The LHCb detector[157-158] is a single-arm forward spectrometer, which is designed for the study of particles containing bottom or charm quarks. It covers the pseudo-rapidity range $2 < \eta < 5$, and thus can probe PDFs in the small Bjorken-x region, providing unique information on QCD[159].

A schematic layout of the LHCb detector is shown in Figure 3.3, as well as a right-handed coordinate system, defined with z-axis along the beam towards the detector, y-axis vertical and x-axis horizontal. The pp interaction region is encompassed by the Vertex Lo-

cator (VELO), a silicon-strip vertex detector that can separate primary pp collision vertex and secondary vertex from b-hadron decays. Apart from the VELO, the tracking system, which is described in Section 3.3, consist of the Tracker Turicensis (TT) and three tracking stations (T-stations) as well. A spectrometer magnet is placed between the TT and T-stations, used for the momentum measurement of charged particles. It is a warm dipole magnet, and provides an integrated magnetic field of about 4 Tm. The direction of the magnetic field is vertical, and the collision data can be taken by the LHCb detector with the magnet field direction pointing upward (MagUp) or downward (MagDown). Charged particles from collisions are deflected in the horizontal plane. Different types of particles are distinguished using information from Cherenkov detectors, calorimeters and muon stations, as described in Section 3.4. The five muon stations, M1–M5, provide not only good muon identification, but also fast information for the trigger at the hardware stage. The trigger system is described in Section 3.5, including the hardware stage based on information from calorimeters and muon stations, and the software stage using information from full reconstruction.

The architecture of the front-end electronics is to a great extent determined by the requirement of making a hardware trigger with very short latency, as detailed in Ref. [161-162]. The detector signals are captured at the 40 MHz bunch crossing rate, and stored in 4 µs deep pipeline buffers until the hardware trigger decision accepts or rejects this event. Accepted data are transferred to derandomising buffers, and then collected, zero-suppressed and finally formatted by the following front-end electronics to be sent to the data acquisition system.

3.3 Tracking system

The tracking system is composed of the vertex detector VELO surrounding the pp collision region, the sub-detector TT placed upstream of the magnet, and three T-stations T1–T3 located downstream of the magnet. Silicon micro-strip detectors are used in VELO and TT. The T-stations contain silicon micro-strip detectors in the inner region close to the beam pipe, called the Inner Tracker (IT), and straw tubes employed in the outer region, called the Outer Tracker (OT). The hits in the VELO, TT and T-stations are used to reconstruct trajectories of the charged particles. In this thesis, charmonium candidates are combined with the long tracks, which traverse the full tracking system. A schematic diagram of the long track and other track types is illustrated in Figure 3.4. The momentum

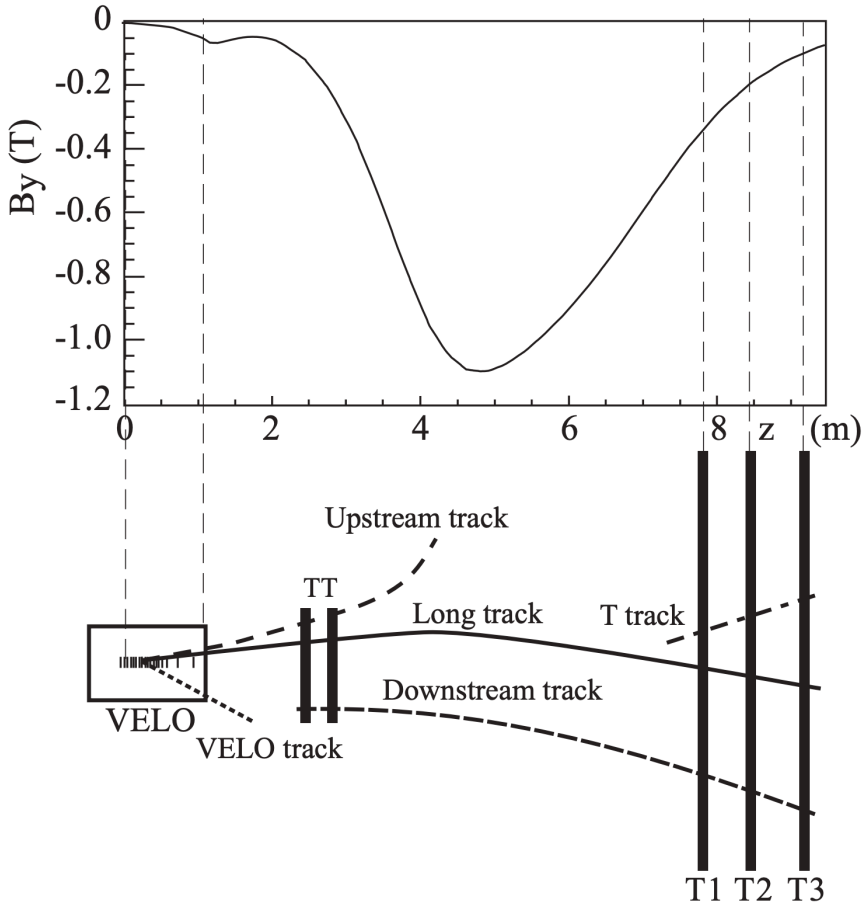

Figure 3.4 Schematic diagram of the long track and other track types, together with the main magnetic field component B_y as a function of the z coordinate as a reference. The figure is taken from Ref. [158].

resolution of the long tracks achieved by the high-precision tracking system varies from 0.5% at low momentum to 1.0% at 200 GeV [158].

3.3.1 Vertex Locator

The VELO comprises 21 stations arranged along the beam z-axis, and each station is assembled in two halves, two semicircular silicon modules. The cross section of the 42 VELO modules in the (x, z) plane at $y = 0$ is shown in Figure 3.5, as well as the interaction region encompassed by these modules. Two halves of each station are fully closed only in the case of stable beams for detector safety. The front face of two modules is also shown in Figure 3.5 in the fully closed and open positions. Each module is made up of two senors, R-sensor and Φ-sensor, measuring r and ϕ coordinates respectively in the cylindrical coordinate system (r, ϕ, z). The pitch within a module increases linearly from 38 µm at the inner radius of 8.2 mm to 102 µm at the outer radius of 42 mm. The VELO

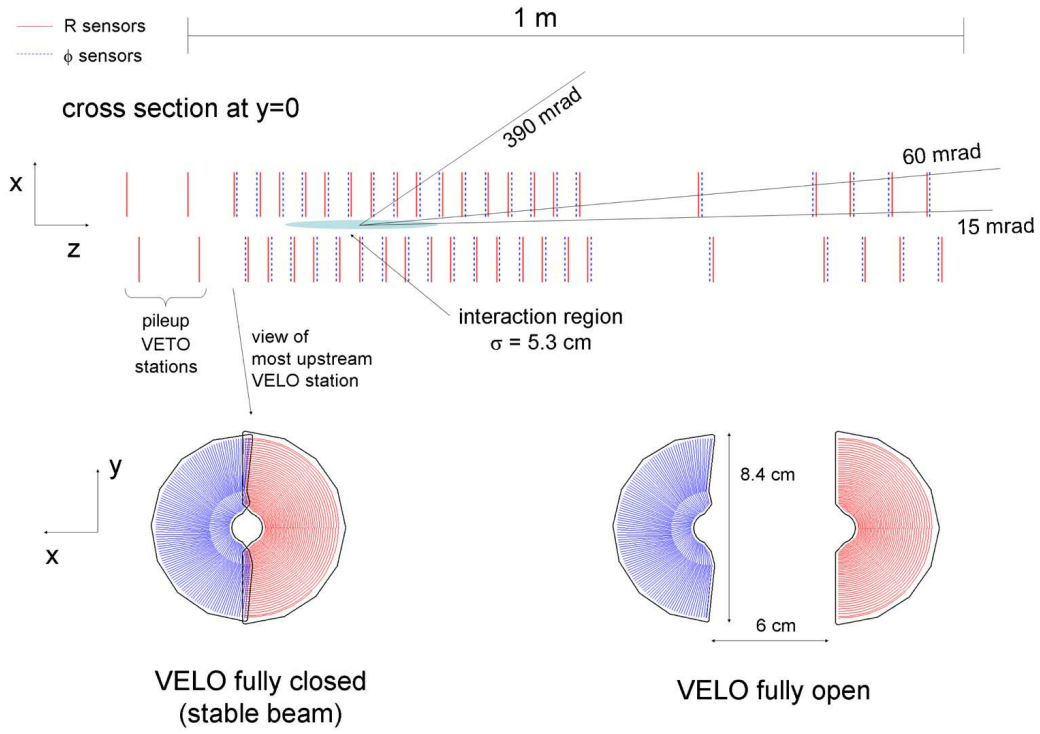

Figure 3.5 Cross section of the VELO stations in the (x, z) plane at $y = 0$. The front face of one VELO station is also shown in the fully closed and open positions. The figure is taken from Ref. [157].

geometry is designed to cover the angular acceptance of the downstream sub-detectors so that all the tracks emerging from the interaction region with a polar angle between 15 mrad and 300 mrad with respect to the beam axis cross at least three VELO stations.

A detailed review of the VELO performance can be found in Ref. [163]. The tracking efficiency of the VELO is above 98% typically. A spatial resolution of 13 µm in the (x, y) plane and of 71 µm along the beam z-axis is achieved for PVs reconstructed by 25 tracks. The minimum distance of a track to a PV, which is referred to the impact parameter (IP), is measured by the VELO with an uncertainty of $(15 + 29/p_{\mathrm{T}})$ µm, where p_{T} is its momentum component transverse to the beam in unit of GeV. The distance between the decay vertex of a hadron and the PV can be used to calculate the proper time. The VELO gives a typical proper time resolution of 50 fs that much smaller than the lifetime of b-hadrons in the ground state, which is vital to the separation of prompt and non-prompt charmonium in the production measurements.

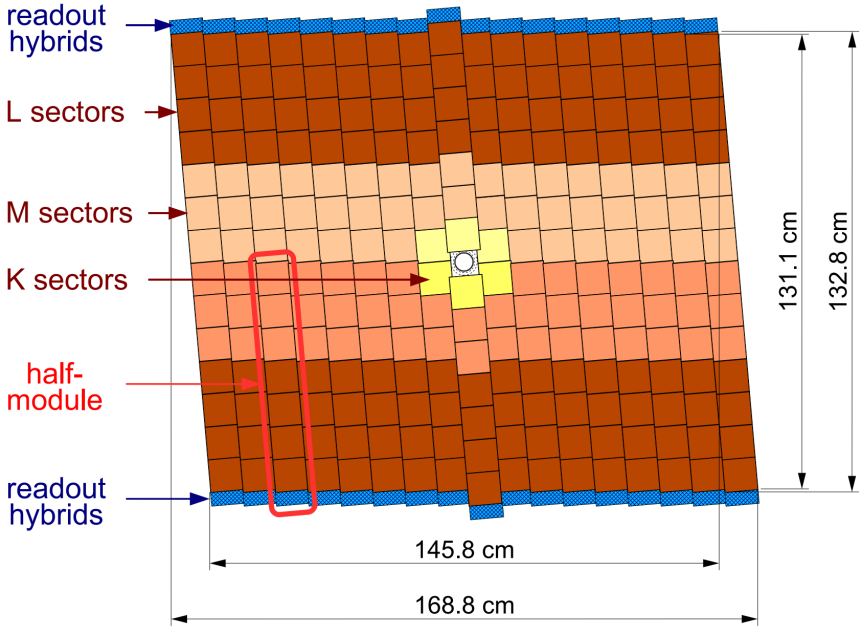

Figure 3.6 Schematic layout of the third detection layer in TT. The figure is taken from Ref. [157].

3.3.2 Tracker Turicensis

The TT is a tracking station with a width of about 150 cm and a height of about 130 cm located upstream of the dipole magnet. Silicon micro-strip sensors are used in the TT and the strip pitch is 183 µm. There are four detection layers in the tracking station placed in an arrangement of $x-u-v-x$ layers. Strips in the first and the last layer (two x-layers) are vertical, while those in the middle two layers (u-layer and v-layer) are rotated by an angle of $\pm 5^{\circ}$ with respect to the y-axis in order to provide measurements of three-dimensional hit positions. A schematic layout of the v-layer is shown in Figure 3.6. The overall hit efficiency for TT is larger than 99.7%, and the single-hit resolution is around 53 µm[158].

3.3.3 T-stations

For the three T-stations T1–T3 located downstream of the dipole magnet, each station has four detection layers in the $x-u-v-x$ arrangement similar to the TT. The IT detector in the centre of the T-stations is composed of silicon micro-strip sensors with a strip pitch of 198 µm. A schematic layout of the first x-layer in IT is shown in Figure 3.7. The overall hit efficiency for IT is larger than 99.8%, and the single-hit resolution is around 53 µm[158].

The large area of the T-stations in the outer region are covered by the OT detector. It is a gaseous straw-tube detector, where the straw tube is 2.4 m in length with an inner diameter of 4.9 mm and the filled gas is a mixture of Ar (70.0%), CO_2 (28.5%) and O_2

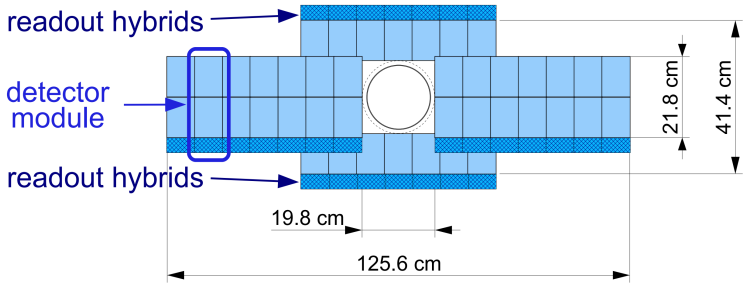

Figure 3.7 Schematic layout of the first detection layer in IT. The figure is taken from Ref. [157].

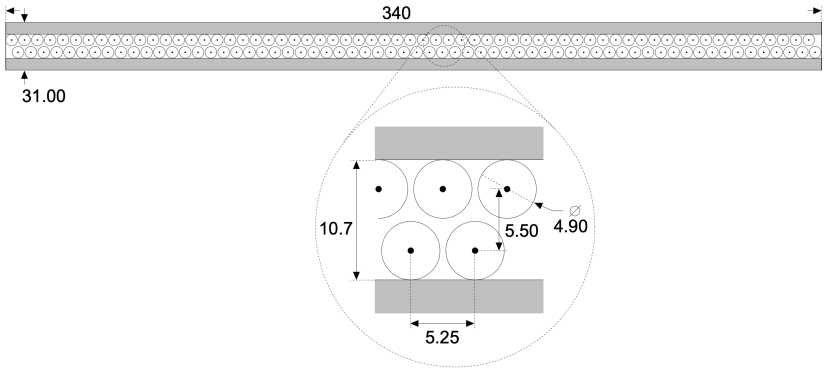

Figure 3.8 Cross section of one straw-tube module in OT. The figure is taken from Ref. [164].

(1.5%), which enables a fast drift-time of less than 50 ns. A module in one detection layer is made up of two staggered layers of drift tubes, and the cross section of one module is shown in Figure 3.8. The arrangement of OT modules in layers and stations is shown in Figure 3.9. The hit efficiency is about 99.2% for tracks across the central half of the straw, and the single-hit resolution is approximately 200 µm for OT.

3.4 Particle identification

At the LHCb experiment, charged hadrons (π, K and p) are identified by two ring-imaging Cherenkov detectors (RICH1 and RICH2), and electrons, photons and hadrons are identified by the calorimeters including a scintillating-pad detector (SPD), a preshower detector (PS), an electromagnetic calorimeter (ECAL) and a hadronic calorimeter (HCAL). Muon identification is provided by the dedicated muon detection system, composed of five muon stations M1–M5. Cherenkov detectors, calorimeters and muon stations are introduced in the following respectively.

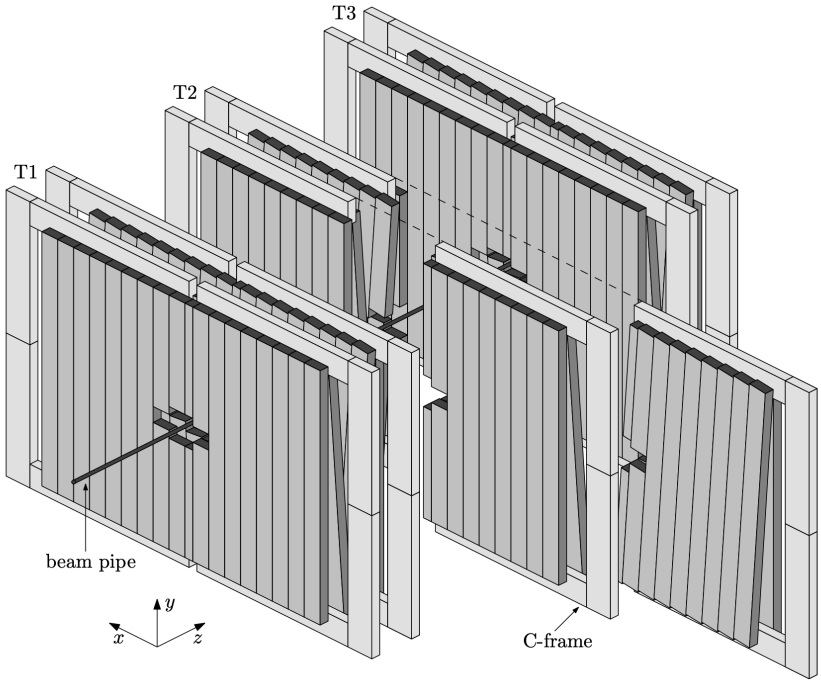

Figure 3.9 Arrangement of OT modules in layers and stations. The figure is taken from Ref. [164].

3.4.1 Cherenkov detectors

RICH1 and RICH2 distinguish different charged particles by measuring the angle θ_c of the Cherenkov radiation emitted when traversing a transparent refractive medium with a velocity greater than the light speed through this material. The Cherenkov angle θ_c is related to the velocity v of the charged particle as

$$\cos\theta_c = \frac{c}{nv}, \tag{3.3}$$

where c is the speed of light in vacuum and n is the refractive index of the medium. With the help of the momentum of the charged particle provided by the tracking system, its mass can be determined and used to identify its type.

RICH1 is placed upstream of the magnet, between the VELO and the TT. It uses Aerogel and C_4F_{10} gas as radiators, and covers the low momentum range 1–60 GeV. A side-view schematic layout of RICH1 is shown in Figure 3.10(a). RICH2 is located downstream of the magnet, between the last T-station and the first muon station. It uses CF_4 as a radiator, and covers the high momentum range 15–100 GeV. A top-view schematic layout of RICH2 is shown in Figure 3.10(b).

Figure 3.11 shows the reconstructed Cherenkov angle as a function of track momentum in the C_4F_{10} gas radiator. The distinct bands of events for pions, kaons and protons

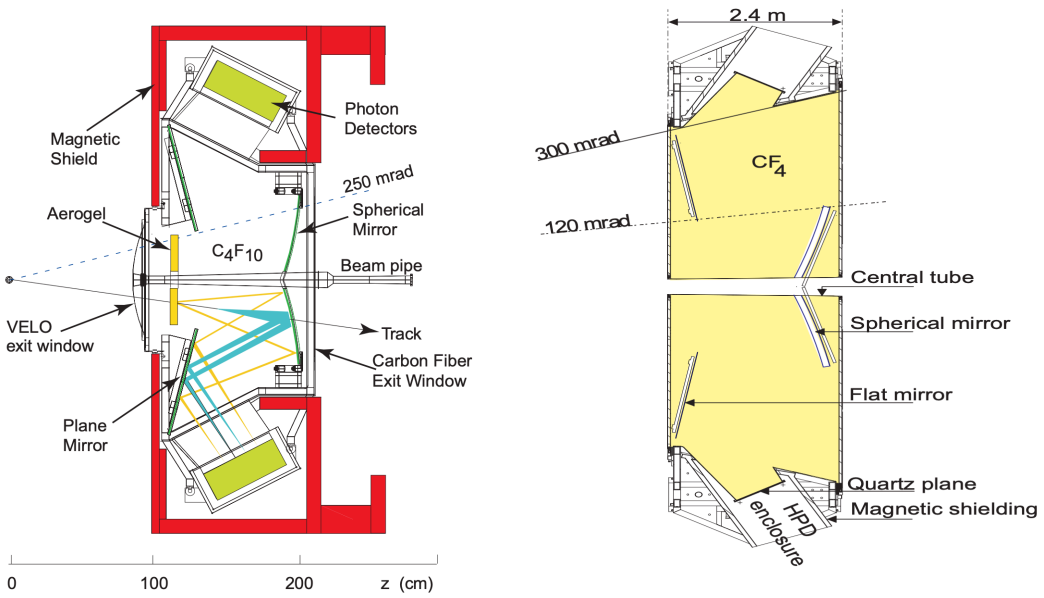

(a) Side view of RICH1. (b) Top view of RICH2.

Figure 3.10 Schematic layouts of (a) RICH1 and (b) RICH2. The figures are taken from Ref. [157].

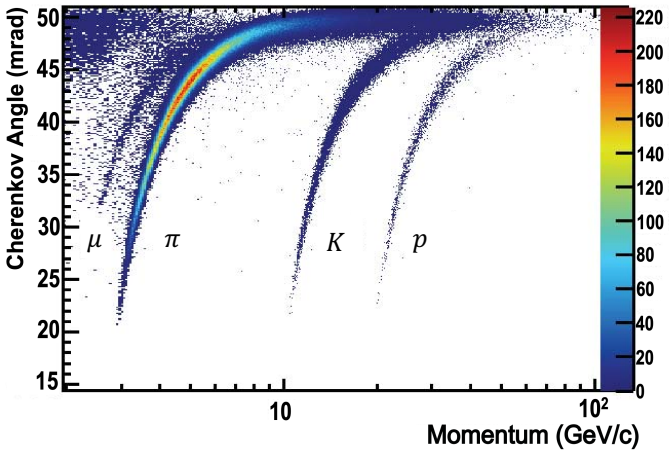

Figure 3.11 Reconstructed Cherenkov angle as a function of track momentum in the C_4F_{10} gas radiator. The figure is taken from Ref. [165].

are seen clearly as expected.

3.4.2 Calorimeters

The calorimeter system consists of the SPD, PS, ECAL and HCAL, which are arranged along the beam z-axis downstream of the tracking stations and Cherenkov detectors. A schematic layout of the calorimeter system is shown in Figure 3.12. The SPD and PS are two planes of scintillating pads separated by a lead absorber with a thickness of 2.5 radiation lengths (X_0). The ECAL is a shashlik-type calorimeter made of a sampling

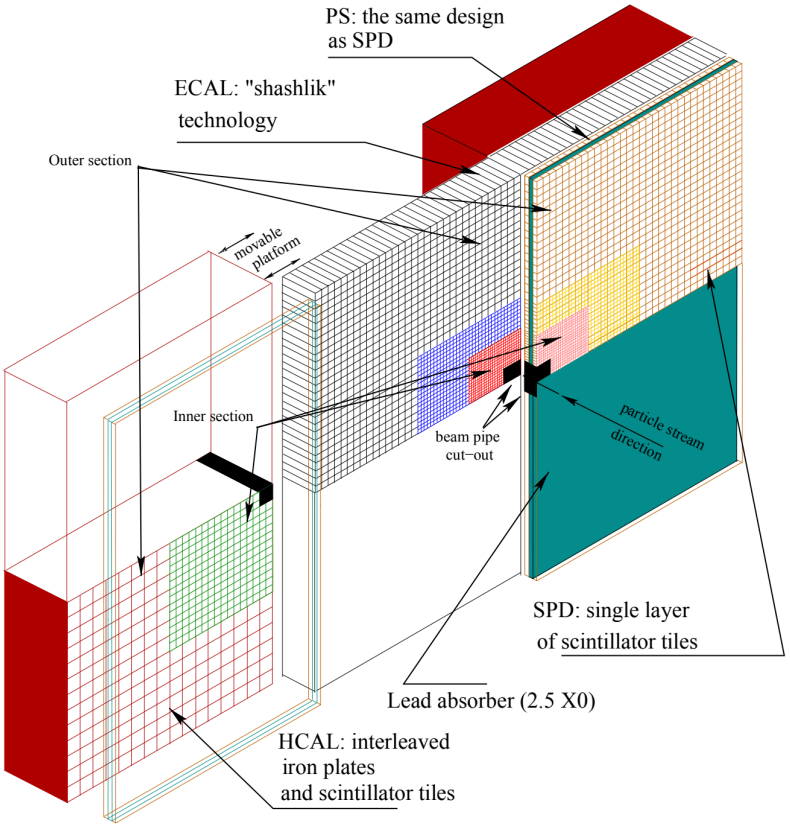

Figure 3.12 Schematic layout of the calorimeter system. The figure is taken from Ref. [166].

structure with scintillator and lead layers. The HCAL is a sampling detector with iron plates as absorber and scintillating tiles as active material. The ECAL has a thickness of 25 X_0, which ensures the full containment of the electromagnetic showers, while the thickness of HCAL is 5.6 nuclear interaction lengths (λ_i), which is limited by the space.

A signal recorded by the SPD indicates the presence of a charged particle, which helps to separate electrons from photons. An electromagnetic shower is started with the energy deposition in the PS, and is mostly detected in the ECAL. The HCAL records hadronic showers and distinguishes hadrons from others. Apart from identifying electrons, photons and hadrons, the calorimeters provide fast information for the hardware trigger, which is described in Section 3.5.1.

3.4.3 Muon stations

The muon system comprises five muon stations M1–M5. The stations M2-M5 are the most downstream sub-detectors of the LHCb detector, while the M1 station is placed upstream of the calorimeter system in order to improve the p_{T} measurement of the muon candidate for the hardware trigger. The five muons stations are mostly instrumented with

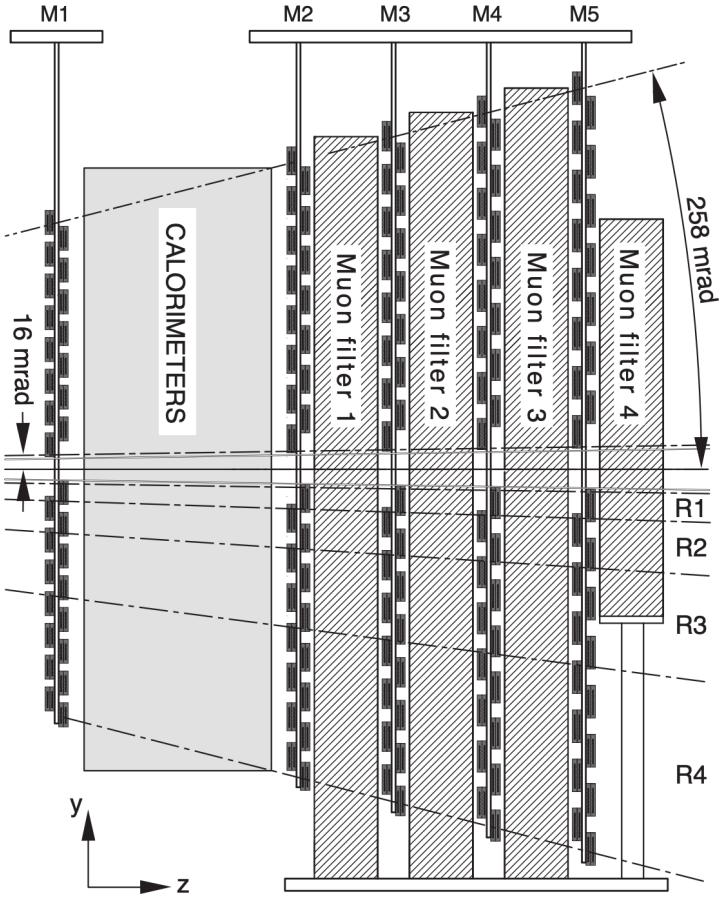

Figure 3.13 Schematic layout of the muon system. The figure is taken from Ref. [157].

multi wire proportional chambers, except in the inner region of the M1 station, where the gas electron multipliers are used. A schematic layout of the muon system is shown in Figure 3.13. The stations M2-M5 are interleaved with iron absorbers with a thickness of 80 cm. The minimum momentum of a muon track that penetrates the five stations is 6 GeV approximately, as the total thickness of absorbers including the calorimeters is around 20 λ_i.

For muon identification, a loose binary selection of muon candidates, called IsMuon, is applied according to the matching of hits in the muon stations to the track extrapolation[167]. The efficiency of the IsMuon selection as a function of p in p_{T} intervals is shown in Figure 3.14, together with the mis-identification probabilities of protons, pions and kaons as muon candidates. In addition, another two discriminating variables with PID information from other sub-detectors combined are usually used in analyses. The first one is the logarithm of the likelihood ratio between the muon and pion hypotheses, denoted as DLLμ. The second variable ProbNNμ is determined using multivariate techniques[168],

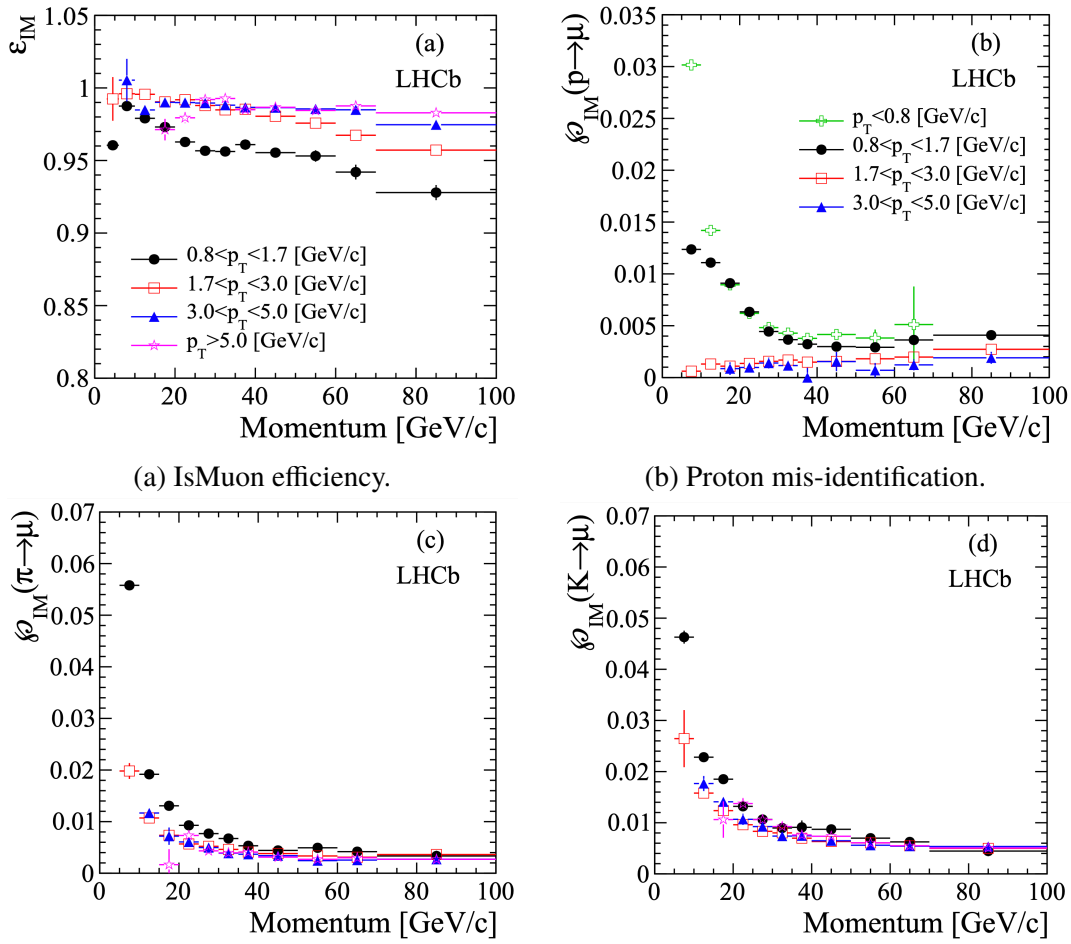

(a) IsMuon efficiency.

(b) Proton mis-identification.

(c) Pion mis-identification.

(d) Kaon mis-identification.

Figure 3.14 IsMuon efficiency and the mis-identification probabilities as a function of p in p_T intervals. The figures are taken from Ref. [167].

with correlation between the sub-detector systems taken into account and additional information included. A selection applied to the variable DLLμ or ProbNNμ can reject non-muon tracks further, and the selection criteria is usually determined based on the compromise between efficiency and purity in a specific study.

3.5 Trigger system

The LHCb trigger system is of great importance to select events of interest from pp collisions at the 40 MHz brunch crossing rate online. It consists of a hardware level-0 (L0) trigger, and a high-level trigger (HLT) implemented in software. A schematic diagram of the LHCb trigger system and the data flow in Run 2 is shown in Figure 3.15. The event rate is reduced by the L0 trigger to 1 MHz, at which all the sub-detectors can be read out. It is further reduced by the HLT to around 12.5 kHz, and then the remaining events are

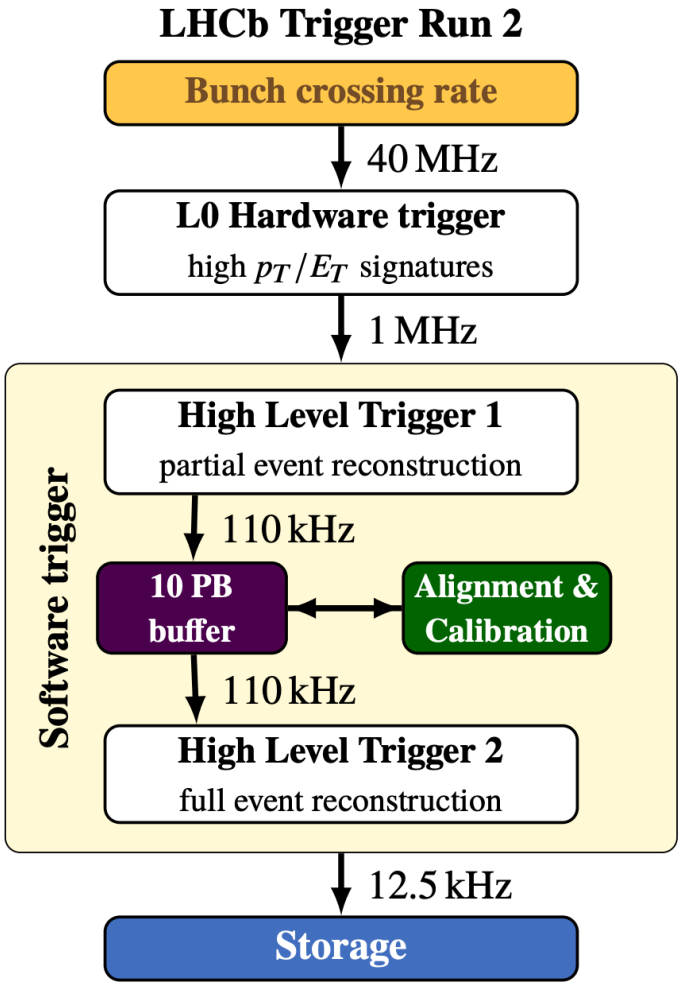

Figure 3.15 Schematic diagram of the LHCb trigger system and the data flow. The figure is taken from Ref. [169].

permanently stored for offline analysis.

Both L0 and HLT triggers contain a series of selections covering various physics processes, and each selection called a trigger line returns a decision on an event. Since an event consists of many tracks and some of them are combined into a signal, the events are classified as two types:

- Trigger on signal (TOS). The signal candidate is sufficient to trigger this event regardless of the rest tracks.
- Trigger independent of signal (TIS). The trigger is caused by the rest of the event rather than the signal candidate.

The TOS and TIS decisions are usually used in offline data analyses, as well as in this thesis.

3.5.1 Hardware trigger

The L0 trigger utilises the fast information provided by the calorimeter system and the muon stations to make decisions with a latency of 4 μs. The L0 calorimeter trigger selects clusters with high transverse-energy E_{T}, measured by the ECAL and HCAL, and the clusters are identified as hadron, electron and photon candidates by the calorimeter system. The total number of hits in the SPD (nSPDHits) is determined as a measure of the charged track multiplicity, and can be used to veto events with very high multiplicity in order to enable a faster reconstruction in HLT. The L0 muon trigger searches for muon tracks with high p_{T}. A stand-alone algorithm of muon track reconstruction is used in the L0 trigger, requiring aligned hits in all the five muon stations. Assuming that the muon track originates from the interaction point, its p_{T} is determined by the hit positions in the first two stations M1 and M2 with a relative resolution of roughly 20%. Two muon tracks with the highest p_{T} in each quadrant are selected, and up to eight candidates are considered in the L0 muon trigger. The trigger line L0Muon sets a threshold on the highest p_{T} of the eight candidates, while the line L0DiMuon requires the product of the largest two p_{T} values larger than a set threshold.

3.5.2 Software trigger

The HLT, the second and the last trigger stage, is divided into two levels, the first level HLT1 and the second level HLT2. Based on a partial event reconstruction, the HLT1 trigger is used to confirm the L0 candidates by adding information from the tracking system. Selections are usually applied on the p_{T}, which is measured more precisely, and the IP with respect to the PV, which is determined from track segments in the VELO, in the HLT1 trigger to further reduce the event rate. Di-muon candidates are selected with a large invariant mass in some HLT1 lines, such as the Hlt1DiMuonHighMass line used in the analyses in this thesis.

In the HLT2 trigger, a full reconstruction is performed on the events selected by the HLT1 trigger. In Run 2, its algorithm is identical to that of the offline reconstruction, which enables the Turbo stream[170], bypassing the offline reconstruction and discarding raw events. In this thesis, the first analysis is based on the data in the Turbo stream, while the second one still utilises the full-stream data, which keeps full raw information.

CHAPTER 4 J/ψ PRODUCTION MEASUREMENT

In this chapter, the measurement of J/ψ production in pp collisions at $\sqrt{s} = 5\,\text{TeV}$ at the LHCb experiment[13] is reported. The differential cross-sections are measured as functions of p_T and y in the kinematic range $0 < p_\text{T} < 20\,\text{GeV}$ and $2.0 < y < 4.5$, separately for prompt and no-prompt J/ψ mesons. The cross-section ratios between 8 TeV and 5 TeV, and between 13 TeV and 5 TeV are also measured. The results of prompt J/ψ mesons are compared with the NLO NRQCD, CGC+NRQCD predictions, and the results of non-prompt J/ψ mesons are compared with the FONLL predictions.

4.1 Analysis strategy

The double differential cross-section of J/ψ production in a given (p_T,y) bin is calculated as

$$\frac{\mathrm{d}^2\sigma}{\mathrm{d}p_\text{T}\mathrm{d}y} = \frac{N(J/\psi \to \mu^+\mu^-)}{\mathcal{L} \times \varepsilon_\text{tot} \times \mathcal{B}(J/\psi \to \mu^+\mu^-) \times \Delta p_\text{T} \times \Delta y}, \tag{4.1}$$

where

- N($J/\psi \to \mu^+\mu^-$) is the yield of J/ψ signals in this (p_T,y) interval, reconstructed through the $J/\psi \to \mu^+\mu^-$ decay channel, and the signal extraction is described in Section 4.4;
- ε_tot is the total efficiency in this (p_T,y) interval, described in Section 4.5 in detail;
- $\mathcal{L} = 9.13 \pm 0.18\,\text{pb}^{-1}$ [171] is the integrated luminosity;
- $\mathcal{B}(J/\psi \to \mu^+\mu^-) = 5.961 \pm 0.033\%$ [9] is the branching fraction of the $J/\psi \to \mu^+\mu^-$ decay channel;
- Δp_T is the interval width of the J/ψ transverse momentum p_T;
- Δy is the interval width of the J/ψ rapidity y.

The following boundaries are used for the (p_T,y) binning scheme of the J/ψ mesons:

- p_T boundaries: 0, 1, 2, 3, 4, 5, 6, 7, 8, 10, 14 GeV;
- y boundaries: 2.0, 2.5, 3.0, 3.5, 4.0, 4.5.

The cross-section of another interval of $14 < p_\text{T} < 20\,\text{GeV}$ and $2.0 < y < 4.5$ is measured as well. Thus for the differential cross-section $\mathrm{d}\sigma/\mathrm{d}p_\text{T}$, the p_T range is extended to 20 GeV with $2.0 < y < 4.5$, while for the $\mathrm{d}\sigma/\mathrm{d}y$, the y range is from 2.0 to 4.5 with integrating the p_T intervals that only less than 14 GeV.

To determine the double differential cross-section of prompt and non-prompt J/ψ mesons separately, the yields of prompt and non-prompt J/ψ signals in (p_{T},y) intervals are extracted from a two-dimensional (2D) fit to the distributions of the di-muon invariant mass $m_{\mu^+\mu^-}$ and the pseudo-proper time t_z in each kinematic interval, as described in Section 4.4.2 in detail. The pseudo-proper time t_z of the J/ψ meson is defined as

$$t_z = \frac{z_{J/\psi} - z_{\mathrm{PV}}}{p_z/m_{J/\psi}}, \tag{4.2}$$

where $z_{J/\psi}$ and z_{PV} are positions of the J/ψ decay vertex and the PV along the beam axis z, p_z is the projection of the measured momentum of the J/ψ meson along the z axis, and $m_{J/\psi}$ is the known J/ψ mass[9]. This variable was found to give a good approximation of the b-hadron proper lifetime, in which the J/ψ momentum is used instead of the exact b-hadron momentum given that b-hadrons are not fully reconstructed. The prompt J/ψ signals have almost zero lifetime, while the t_z distribution for J/ψ from b is approximately exponential as seen from simulation[172]. The pseudo-proper time t_z allows the separation of prompt and non-prompt contributions to the J/ψ production statistically.

4.2 Data and simulated samples

The data sample used in this analysis was collected by the LHCb detector in pp collisions at $\sqrt{s} = 5\,\mathrm{TeV}$ in 2015. This data sample was taken with the magnet field direction set as MagDown, corresponding to an integrated luminosity of $9.13 \pm 0.18\,\mathrm{pb}^{-1}$[171].

Simulated samples, or called Monte Carlo (MC) samples, are required to study the behaviour of signals and to determine corrections for the acceptance and efficiencies. The pp collisions are modelled using Pythia[173-174] with a specific LHCb configuration[175]. In the Pythia model, J/ψ mesons are generated with zero polarisation, and both colour-singlet and colour-octet contributions[174,176] are considered in prompt J/ψ production. Decays of unstable particles are described by EvtGen[177] with QED final-state radiation handled by Photos[178]. The interactions of the generated particles with the detector are modelled using the Geant4 toolkit[179-180] as described in Ref. [181]. A generator-level sample with 10 million events is used for the determination of the acceptance, and a full-simulation sample with 6 million events is used mainly in order to determine the efficiency in this analysis. These simulated events include both prompt and non-prompt J/ψ mesons, and they can be separated by the truth information in simulation.

Table 4.1 Selection criteria in the HLT1DiMuonHighMass line.

Variable	Value
track p_{T}	$> 0.5\,\mathrm{GeV}$
track p	$> 3\,\mathrm{GeV}$
track χ^2/ndf	< 3
track PID	IsMuon
$m_{\mu^+\mu^-}$	$> 2.7\,\mathrm{GeV}$

Table 4.2 Selection criteria in the HLT2DiMuonJpsiTurbo line.

Variable	Value
track χ^2/ndf	< 4
di-muon vertex χ^2/ndf	< 25
$\lvert m_{\mu^+\mu^-} - m_{J/\psi}\rvert$	$< 150\,\mathrm{MeV}$

4.3 Online and offline selection

The J/ψ candidates are reconstructed through the $J/\psi \to \mu^+\mu^-$ decay channel and are selected through two trigger stages. The hardware L0 trigger line called L0Muon selects events with at least one muon candidate with $p_{\mathrm{T}} > 0.9\,\mathrm{GeV}$. The HLT1 and HLT2 trigger lines used in this analysis are HLT1DiMuonHighMass and HLT2DiMuonJpsiTurbo. The selection criteria of these two trigger lines are summarised in Table 4.1 and Table 4.2 respectively. Altogether, the software trigger requires two loosely identified muons, whose $p_{\mathrm{T}} > 0.5\,\mathrm{GeV}$ and $p > 3\,\mathrm{GeV}$, to form a good-quality vertex, and selects a rough mass window of the invariant mass of each J/ψ candidate, $m_{\mu^+\mu^-}$.

In the offline selection the muon identification requirement is tightened and both tracks are required to have $p_{\mathrm{T}} > 0.65\,\mathrm{GeV}$ and $2.0 < \eta < 4.9$. The background from fake tracks is reduced by a neural-network based algorithm using a variable called ghost probability[182]. The invariant mass $m_{\mu^+\mu^-}$ is required to be within a range of $\pm 120\,\mathrm{MeV}$ around the known J/ψ mass[9]. All events are required to have at least one reconstructed PV. For candidates with multiple PVs in the event, the one with the smallest χ^2_{IP} is taken as the associated PV, where χ^2_{IP} is defined as the difference in the vertex-fit χ^2 of a given PV reconstructed with and without the J/ψ candidate under consideration. A final selection is applied to J/ψ candidates using the pseudo-proper time t_z and its uncertainty σ_{t_z}, which is calculated by combining the estimated uncertainties on the z position of the J/ψ decay

Table 4.3 Offline selection criteria of J/ψ candidates.

Variable	Value
number of PVs	≥ 1
track p_{T}	$> 0.65\,\mathrm{GeV}$
track η	$2 < \eta < 4.9$
track DLL_{μ}	> 0
track ghost probability	< 0.3
di-muon vertex χ^2/ndf	< 8
$\lvert m_{\mu^+\mu^-} - m_{J/\psi} \rvert$	$< 120\,\mathrm{MeV}$
pseudo-proper time t_z	$\lvert t_z \rvert < 10\,\mathrm{ps}$
t_z uncertainty σ_{t_z}	$< 0.3\,\mathrm{ps}$

vertex and that of the associated PV. Candidates with $|t_z| < 10\,\mathrm{ps}$ and $\sigma_{t_z} < 0.3\,\mathrm{ps}$ are selected for further analysis. The offline selection criteria are summarised in Table 4.3.

4.4 Signal extraction

4.4.1 Extraction of the inclusive J/ψ signal yields

The number of inclusive J/ψ signals, which is the sum of prompt and non-prompt yields, is extracted from an extended unbinned maximum likelihood fit to the invariant mass distribution of the selected J/ψ candidates in each (p_{T},y) interval. The mass distribution of J/ψ signals is described by the sum of two Crystal Ball (CB) functions with a common mean value (μ) and independent widths (σ_1 and σ_2), while only one CB function is used in intervals with low statistics. The CB function is defined as[183]

$$F_{\mathrm{CB}}(m;\mu,\sigma,\alpha,n) = \begin{cases} (\frac{n}{\alpha})^n e^{-\frac{1}{2}\alpha^2} (\frac{n}{\alpha} - \alpha - \frac{m-\mu}{\sigma})^{-n}, & \frac{m-\mu}{\sigma} < -\alpha; \\ e^{-\frac{1}{2}(\frac{m-\mu}{\sigma})^2}, & \frac{m-\mu}{\sigma} > -\alpha. \end{cases} \tag{4.3}$$

The tails in CB functions are used to model the final-state radiation effects, which leads to some J/ψ candidates with lower invariant masses and makes the mass distribution asymmetric. The parameter n is fixed to one according to the QED calculations of the photon emission, which is the main cause of the final-state radiation. The α is parameterised from simulation as a function of the σ,

$$\alpha = -7.84 \times 10^{-5}\sigma^2 + 6.09 \times 10^{-3}\sigma + 2.08, \tag{4.4}$$

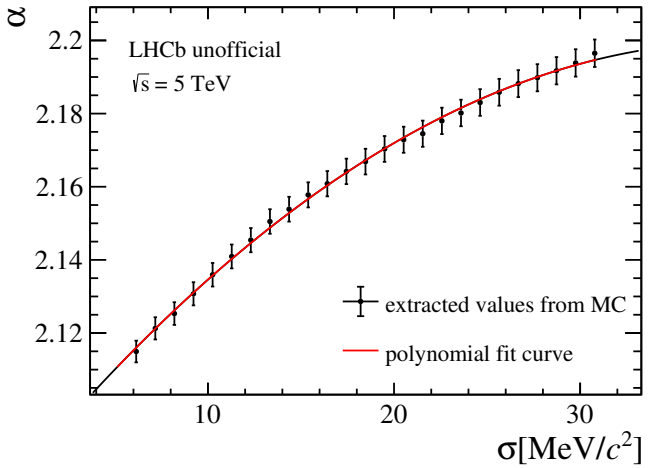

Figure 4.1 The relation between the parameters α and σ of the CB function from the study of simulation.

for σ in unit of MeV. This function is obtained from the study of simulated event at the generator level, in which the invariant mass of di-muon differs from the true J/ψ mass due to the final-state radiation effects. The invariant mass of di-muon is smeared by a Gaussian distribution with zero mean value and a standard deviation σ_{res}, emulating the Gaussian detector resolution. Then, a fit to the smeared invariant mass distribution is performed using a CB function with n fixed to one and other parameters free. By repeating this procedure with different σ_{res}, the relation between the α and σ can be determined by a polynomial fit, as shown in Figure 4.1. With the tail parameters fixed, only the mean and widths of the CB functions and the ratio between the two functions are left as free shape parameters in the fit. The distribution of the combinatorial background is modelled with an exponential function.

The invariant mass fit is performed in each (p_{T},y) interval, and the mass distribution together with the fit result of an example interval of $2 < p_{\text{T}} < 3$ GeV and $3.0 < y < 3.5$ is shown in Figure 4.2. Through performing the fits, the yields of inclusive J/ψ signals in (p_{T},y) intervals are obtained, as well as parameters of the mass shape, which are useful to determine the initial values in the 2D fit. The yields of inclusive J/ψ signals as a function of p_{T} in intervals of y are shown in Figure 4.3.

4.4.2 Extraction of the prompt and non-prompt signal yields

The yields of prompt and non-prompt J/ψ mesons are simultaneously extracted from an unbinned extended maximum-likelihood fit to the 2D distribution of $m_{\mu^+\mu^-}$ and t_z independently in each (p_{T},y) interval. There are four components: prompt J/ψ signal, non-

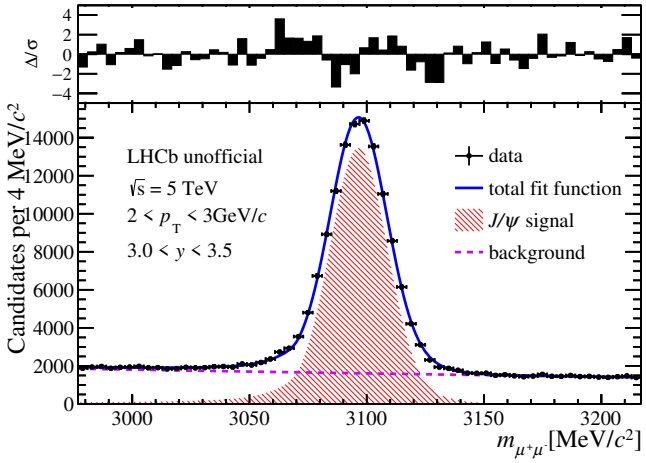

Figure 4.2 The mass distribution together with the fit result of an example interval of $2 < p_T < 3$ GeV and $3.0 < y < 3.5$.

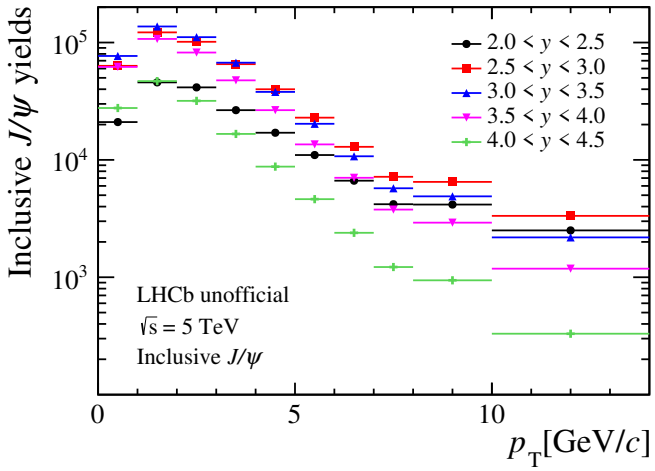

Figure 4.3 The yields of inclusive J/ψ signals as a function of p_T in intervals of y.

prompt J/ψ signal, J/ψ signal with incorrect PV association, and non-J/ψ background from random tracks. The first three J/ψ signals have the same mass shape, as described in Section 4.4.1, but their t_z distributions are different.

The true t_z values for prompt J/ψ mesons are assumed to be zero while those for non-prompt J/ψ mesons are assumed to follow an exponential function. These distributions are convolved with a resolution function F_{res} to model the detector resolution. The function F_{res} is described by the sum of two Gaussian functions,

$$F_{\text{res}}(t_z|\sigma_{t_z}; b, S_1, S_2, \beta) = \frac{\beta}{\sqrt{2\pi}S_1\sigma_{t_z}} e^{-\frac{(t_z-b)^2}{S_1^2\sigma_{t_z}^2}} + \frac{1-\beta}{\sqrt{2\pi}S_2\sigma_{t_z}} e^{-\frac{(t_z-b)^2}{S_2^2\sigma_{t_z}^2}}, \tag{4.5}$$

where the parameter β is the fraction of one Gaussian function, the b is the bias of the measured t_z that shared by two Gaussian functions, the two widths are proportional to the

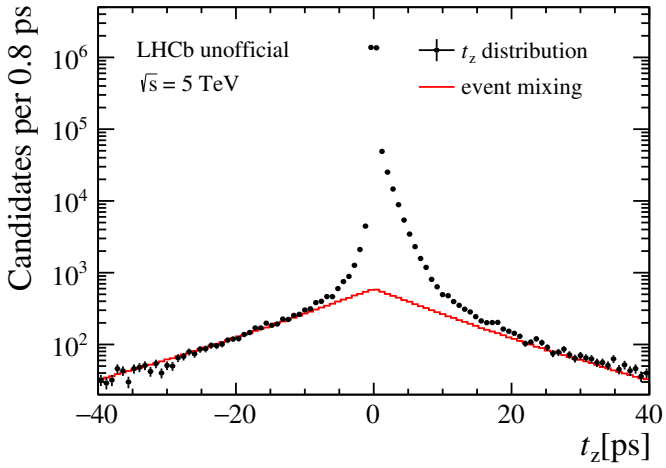

Figure 4.4 Comparison of the t_z distribution of reconstructed events and that obtained from event mixing. The areas in the region $-40 < t_z < -10$ ps are scaled to be the same.

t_z uncertainty σ_{t_z} and the scale factors are S_1 and S_2 respectively.

For the J/ψ signal with wrong PV association, there are two cases:

- The true PV is reconstructed, but the J/ψ candidate is associated to a wrong PV accidentally;
- The true PV is not reconstructed, and the J/ψ candidate is associated to the nearest reconstructed PV in this event.

The first case only happens when the true PV and the wrong PV are close enough so that its t_z distribution is almost the same as those signals associated with true PV. The fraction of this case was even found to be less than 1% in the measurement at $\sqrt{s} = 13\,\text{TeV}$[63], so its effect on the t_z distribution is negligible. However, the second case is different from the first one, and contributes to the long tail present in the t_z distribution. This component can be modelled from data by event mixing, *i.e.*, calculating t_z with the J/ψ candidate associated to the closest PV in the next event of the sample, as

$$t_z^{\text{next}} = \frac{z_{J/\psi} - z_{\text{PV}}^{\text{next}}}{p_z/m_{J/\psi}}. \tag{4.6}$$

The reconstructed t_z distribution is compared with that obtained from event mixing with the areas in the region $-40 < t_z < -10$ ps are scaled to be the same, as shown in Fig 4.4. It is clearly seen that the t_z^{next} is a reasonable quantity to model the long tail. The t_z distribution of this component is not convolved with the resolution function, and is described by a histogram $H_{\text{tail}}(t_z)$.

The t_z distribution of the non-J/ψ background is described by an empirical function composed of a delta function and five exponential functions that are convolved with the

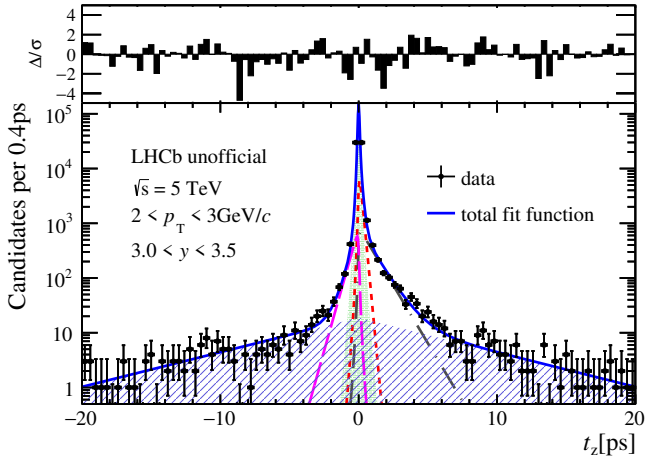

Figure 4.5 The t_z distribution for the mass sidebands together with the fit result of an example interval of $2 < p_{\mathrm{T}} < 3$ GeV and $3.0 < y < 3.5$.

sum of two Gaussian resolution functions,

$$F_{\mathrm{bkg}}(t_z|\sigma_{t_z}) = \left[(1-f_1-f_2-f_3-f_4)\delta(t_z) + \theta(t_z)\left(\frac{f_1}{\tau_1}e^{-t_z/\tau_1} + \frac{f_2}{\tau_2}e^{-t_z/\tau 2}\right)\right.$$
$$\left. + \theta(-t_z)\frac{f_3}{\tau_3}e^{t_z/\tau_3} + \frac{f_4}{2\tau_4}e^{-|t_z|/\tau_4}\right] \otimes \left(\frac{\beta'}{\sqrt{2\pi}S_1'\sigma_{t_z}}e^{-\frac{(t_z-b')^2}{S_1'^2\sigma_{t_z}^2}} + \frac{1-\beta'}{\sqrt{2\pi}S_2'\sigma_{t_z}}e^{-\frac{(t_z-b')^2}{S_2'^2\sigma_{t_z}^2}}\right), \tag{4.7}$$

where $\delta(t_z)$ is the delta function, $\theta(t_z)$ is the unit step function, and the symbol $\otimes$ denotes the convolution. For several intervals with very high statistics, another exponential function with positive t_z is added to this empirical function, while for several intervals with low statistics, one or more components are reduced from this empirical function. In the 2D fit, all parameters of the empirical function are fixed to the values obtained from a fit to the t_z distribution of the J/ψ mass sidebands, defined by the region $75 < |m_{\mu^+\mu^-} - m_{J/\psi}| < 150$ MeV, in each interval. The t_z distribution for the mass sidebands of an example interval of $2 < p_{\mathrm{T}} < 3$ GeV and $3.0 < y < 3.5$ is shown in Figure 4.2, together with the fit result.

With all the four components taken into account, the 2D fit model is

$$f(m_{\mu^+\mu^-}, t_z) = N_{\mathrm{p}}S(m_{\mu^+\mu^-})\left(\delta(t_z)\otimes F_{\mathrm{res}}\right) + N_{\mathrm{n}}S(m_{\mu^+\mu^-})\left(\frac{1}{\tau_b}e^{-t_z/\tau_b}\otimes F_{\mathrm{res}}\right)$$
$$+ N_{\mathrm{tail}}S(m_{\mu^+\mu^-})H_{\mathrm{tail}}(t_z) + N_{\mathrm{bkg}}B(m_{\mu^+\mu^-})F_{\mathrm{bkg}}(t_z), \tag{4.8}$$

where N_{p}, N_{n}, N_{tail} and N_{bkg} are the yields of prompt J/ψ signals, non-prompt J/ψ signals, J/ψ signals with incorrect PV association and non-J/ψ backgrounds respectively, and the $S(m_{\mu^+\mu^-})$ and $B(m_{\mu^+\mu^-})$ are the fit models of the mass $m_{\mu^+\mu^-}$ for signals and

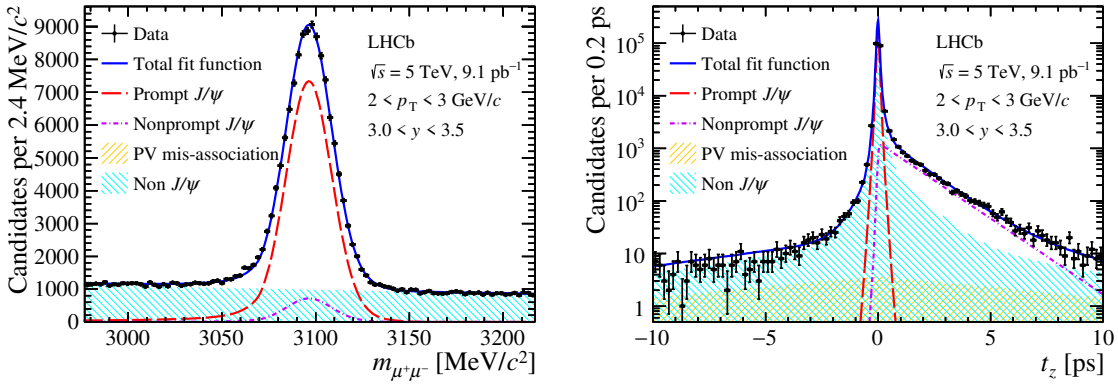

(a) Projection on invariant mass $m_{\mu^+\mu^-}$. (b) Projection on pseudo-proper time t_z.

Figure 4.6 Distributions of (a) invariant mass and (b) pseudo-proper time of the J/ψ candidates for an example interval corresponding to $2 < p_T < 3$ GeV and $3.0 < y < 3.5$. Projections of the two-dimensional fit are also shown.

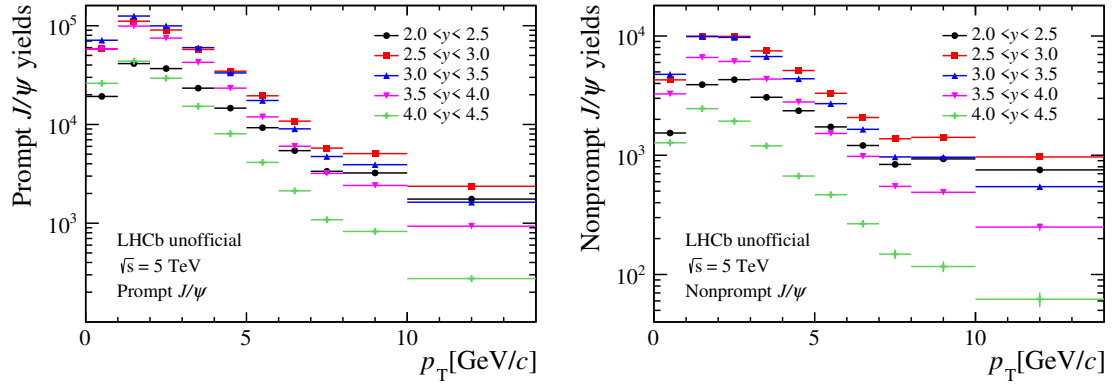

(a) Prompt J/ψ yield. (b) Non-prompt J/ψ yield.

Figure 4.7 Yields of (a) prompt and (b) non-prompt J/ψ mesons as a function of p_T in intervals of y.

backgrounds as described in Section 4.4.1. The projections of the 2D distribution, together with the fit, on $m_{\mu^+\mu^-}$ and t_z are shown in Figure 4.6 for an example interval of $2 < p_T < 3$ GeV and $3.0 < y < 3.5$. The yield N_{tail} is divided into two parts, $N_{\text{p}}^{\text{tail}}$ and $N_{\text{n}}^{\text{tail}}$, according to the ratio between prompt and non-prompt yields, and then $N_{\text{p}}^{\text{tail}}$ and $N_{\text{n}}^{\text{tail}}$ are added to the prompt and non-prompt yields respectively. The prompt and non-prompt yields as a function of p_T in intervals of y are shown in Figure 4.7. The total yield is about 1.4 (0.14) million for prompt (non-prompt) J/ψ mesons.

4.4.3 Check the 2D fit

As a check on the 2D fit, the mean pseudo-proper time of b-hadrons, the parameter τ_b in Eq. 4.8, is extracted from the 2D fit in each (p_T, y) interval, and the values are shown in Figure 4.8. The average of τ_b values in all the intervals is 1.410 ± 0.005 ps, consistent

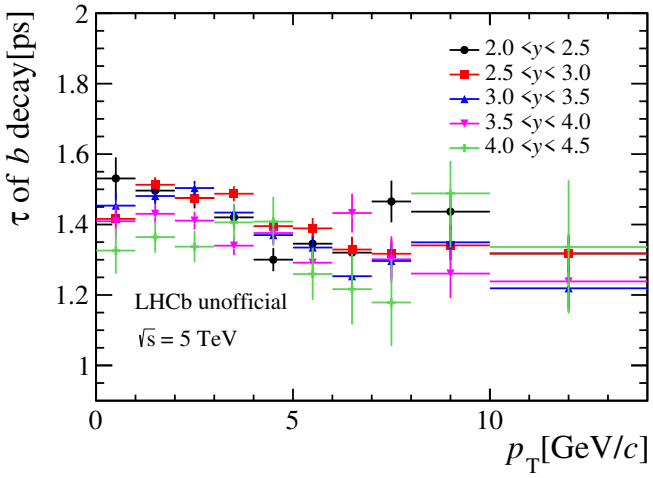

Figure 4.8 The mean pseudo-proper time of b-hadrons extracted from the 2D fit as a function of p_{T} in intervals of y.

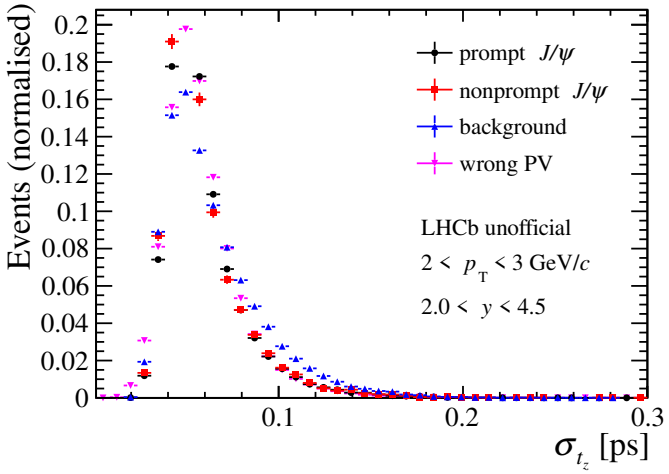

Figure 4.9 Comparison of the σ_{t_z} distributions for an example interval of $2 < p_{\mathrm{T}} < 3\,\mathrm{GeV}$ and $3.0 < y < 3.5$.

with that in the previous simulation study[172].

In addition, since the event-dependent variable σ_{t_z} is present in this 2D fit to the distribution of $m_{\mu^+\mu^-}$ and t_z, there will be potential bias on the yields if the σ_{t_z} distributions of the components are different[184]. A comparison of the σ_{t_z} distributions is shown in Figure 4.9 for an example interval of $2 < p_{\mathrm{T}} < 3\,\mathrm{GeV}$ and $3.0 < y < 3.5$. The distributions of prompt and non-prompt J/ψ signals are obtained from the full-simulation samples, while that of backgrounds from data sidebands and that of signals with wrong PV association from event mixing. A small difference among these distributions is seen, and thus it is necessary to check the bias of prompt and non-prompt J/ψ yields obtained from the 2D fit. For each (p_{T},y) intervals, 1000 pseudo-experiments are performed based on these σ_{t_z} distributions and the 2D fit model Eq. 4.8. In each pseudo-experiment, the $m_{\mu^+\mu^-}$, t_z and

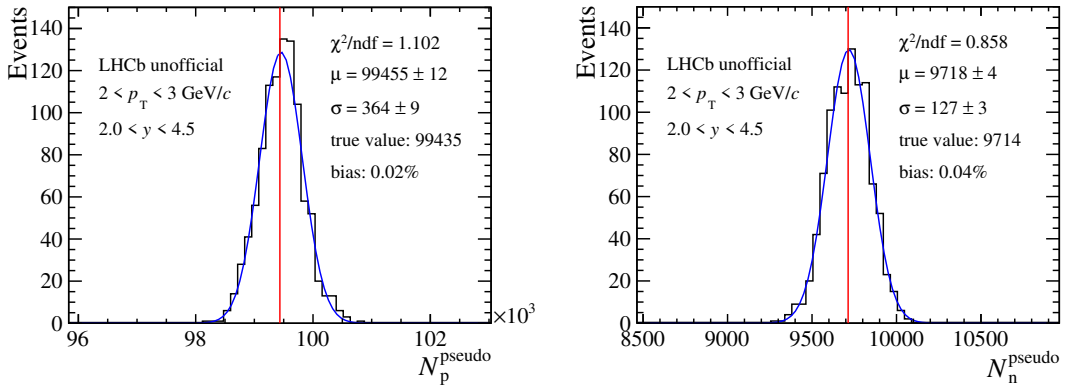

(a) Distribution of N_p^{pseudo}. (b) Distribution of N_n^{pseudo}.

Figure 4.10 Distributions of (a) N_p^{pseudo} and (b) N_n^{pseudo} obtained from pseudo-experiments for an example interval corresponding to $2 < p_T < 3$ GeV and $3.0 < y < 3.5$, together with the Gaussian fits. The red lines denote the true expected values from the 2D fit result.

σ_{t_z} of four components are generated independently, and the yields are assumed as Poisson random numbers with expected values from the 2D fit result. Then, the same 2D fit is performed to the generated distributions, and the prompt and non-prompt J/ψ yields, N_p^{pseudo} and N_n^{pseudo}, are extracted from each pseudo-experiment. The distributions of N_p^{pseudo} and N_n^{pseudo} are obtained from 1000 pseudo-experiments, as shown in Figure 4.10 for the interval with $2 < p_T < 3$ GeV and $3.0 < y < 3.5$, together with the Gaussian fits. The difference between the mean value of the yields from pseudo-experiments and the true expected value from the 2D fit result is an estimate of the bias. For all (p_T, y) intervals, the biases of prompt and non-prompt J/ψ yields are much less than the statistical uncertainties, and hence can be neglected.

4.5 Efficiency determination

The detection efficiency is determined in each (p_T, y) interval using simulated samples. The efficiency ε_{tot} is factorised into the product of four efficiencies: the geometrical acceptance ε_{acc}, the reconstruction-and-selection efficiency $\varepsilon_{rec\&sel}$, the PID efficiency ε_{PID}, and the trigger efficiency ε_{tri}, as

$$\varepsilon_{tot} = \varepsilon_{acc} \times \varepsilon_{rec\&sel} \times \varepsilon_{PID} \times \varepsilon_{tri}. \tag{4.9}$$

The efficiencies ε_{acc} and $\varepsilon_{rec\&sel}$ are evaluated separately for prompt and non-prompt J/ψ mesons. In order to reduce the uncertainty due to the limited sample size of simulation, especially for non-prompt J/ψ mesons, the efficiencies ε_{PID} and ε_{tri} are calculated combining the simulated samples of prompt and non-prompt J/ψ mesons, as the differences

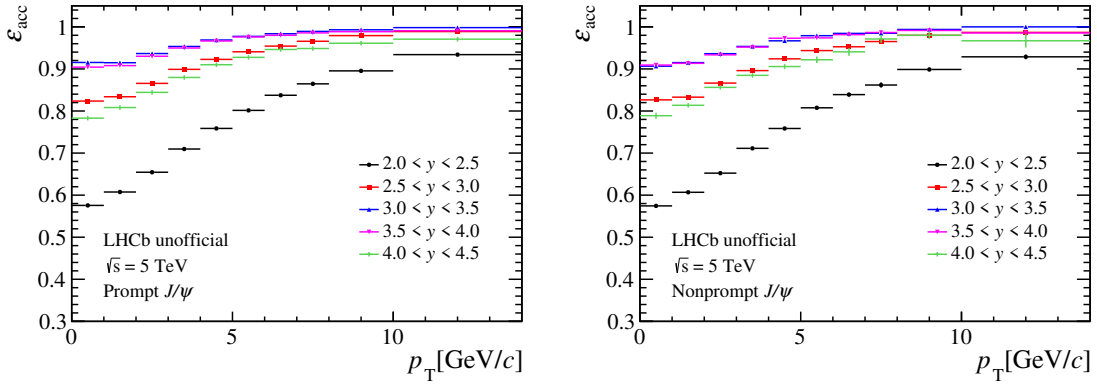

(a) ε_{acc} of prompt J/ψ mesons. (b) ε_{acc} of non-prompt J/ψ mesons.

Figure 4.11 Acceptance ε_{acc} of (a) prompt and (b) non-prompt J/ψ mesons as a function of p_T in intervals of y.

between the two production processes are observed to be negligible. The distribution of the number of SPD hits, nSPDHits, in simulation is weighted to match that in data to correct the effect of the detector occupancy in simulation, as described in Section 4.5.2. The efficiencies of track reconstruction and of PID are corrected using control channels in data, as detailed in Section 4.5.2 and Section 4.5.3 respectively.

4.5.1 Geometrical acceptance

The geometrical acceptance ε_{acc} of J/ψ mesons in each (p_T,y) interval is defined as the yield fraction of J/ψ mesons with both muons inside the LHCb acceptance in those generated in pp collisions,

$$\varepsilon_{acc} = \frac{N(J/\psi \text{ generated with di-muon in LHCb acceptance})}{N(J/\psi \text{ generated in } pp \text{ collisions})}. \tag{4.10}$$

For the di-muon inside the LHCb acceptance, it is required that the polar angles of the muon momentum directions with respect to the direction of beam z-axis are within $(10, 400)$ mrad. The acceptance ε_{acc} is determined as a function of p_T in intervals of y using the simulated sample at the generator level separately for prompt and non-prompt J/ψ mesons, as shown in Figure 4.11.

4.5.2 Reconstruction-and-selection efficiency

The reconstruction-and-selection efficiency $\varepsilon_{rec\&sel}$ of J/ψ mesons in each (p_T,y) interval is defined as the yield fraction of J/ψ mesons reconstructed and selected without PID and trigger requirements in those with both muons inside the LHCb acceptance,

$$\varepsilon_{rec\&sel} = \frac{N(J/\psi \text{ reconstructed and selected w/o PID and trigger})}{N(J/\psi \text{ generated with both muons in LHCb acceptance})}. \tag{4.11}$$

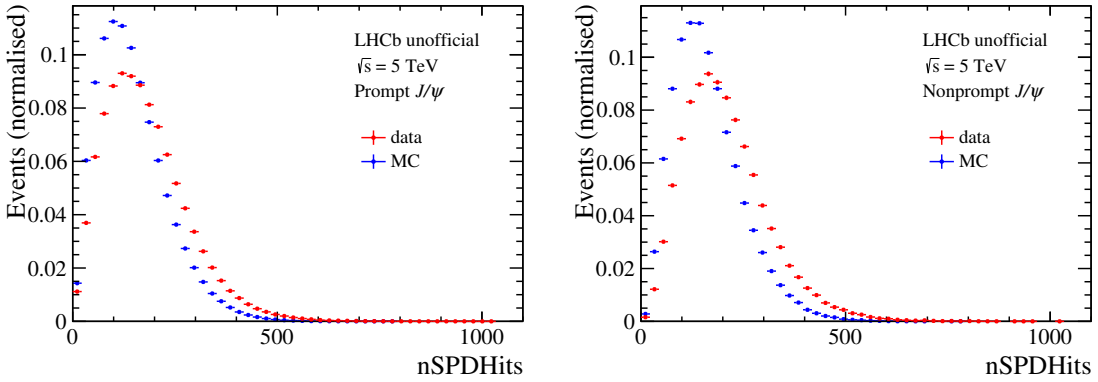

(a) nSPDHits of prompt J/ψ mesons. (b) nSPDHits of non-prompt J/ψ mesons.

Figure 4.12 Comparisons of nSPDHits distributions between data and simulation for (a) prompt and (b) non-prompt J/ψ mesons.

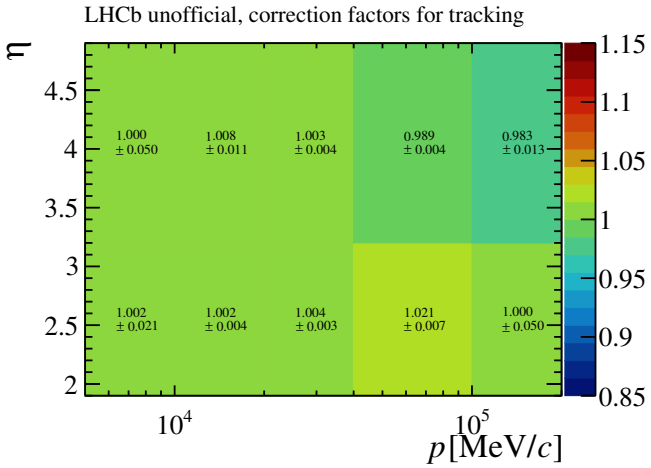

Figure 4.13 Correction factors of tracking efficiency in intervals of muon kinematics.

The reconstruction-and-selection efficiency $\varepsilon_{\text{rec\&sel}}$ is determined separately for prompt and non-prompt J/ψ mesons using the full-simulation sample.

The distributions of nSPDHits, which describes the multiplicity of the event, are found to be different between data and simulation, as shown in Figure 4.12. The distributions of prompt and non-prompt J/ψ mesons in data are obtained by the *sPlot* method[185] using the $m_{\mu^+\mu^-}$ and t_z as the discriminating variables based on the 2D fit result. In order to correct the effect of the detector occupancy, the distribution of nSPDHits in simulation is weighted to match that in data not only for the determination of $\varepsilon_{\text{rec\&sel}}$, but also for those of ε_{PID} and ε_{tri}.

It is also found out that the efficiency of track reconstruction in simulation should be corrected by that in data. The efficiency correction factors are obtained from dedicated data and simulation samples of $J/\psi \to \mu^+\mu^-$ decay in which one muon track is

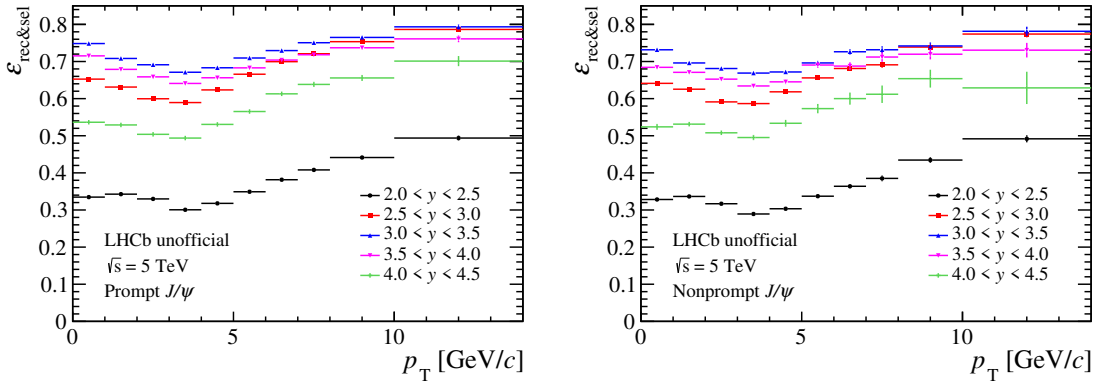

(a) $\varepsilon_{\text{rec\&sel}}$ of prompt J/ψ mesons. (b) $\varepsilon_{\text{rec\&sel}}$ of non-prompt J/ψ mesons.

Figure 4.14 Reconstruction-and-selection efficiency $\varepsilon_{\text{rec\&sel}}$ of (a) prompt and (b) non-prompt J/ψ mesons as a function of p_{T} in intervals of y.

fully reconstructed and the other track is reconstructed using a subset of tracking systems as a probe track[186]. The tracking efficiencies in these data and simulation samples are evaluated as the probability that the probe track can be fully reconstructed. The ratios of tracking efficiencies between data and simulation are considered as the factors to correct the tracking efficiency, which are shown in Figure 4.13 in intervals of muon kinematics.

With these corrections taken into account, the reconstruction-and-selection efficiencies of prompt and non-prompt J/ψ mesons are shown in Figure 4.14, as a function of p_{T} in intervals of y.

4.5.3 PID efficiency

The PID efficiency ε_{PID} of J/ψ mesons in each (p_{T},y) interval is defined as the yield fraction of J/ψ mesons reconstructed and selected without trigger but with PID requirements in those without trigger and PID requirements,

$$\varepsilon_{\text{PID}} = \frac{N(J/\psi \text{ reconstructed and selected w/ PID w/o trigger})}{N(J/\psi \text{ reconstructed and selected w/o PID and trigger})}. \tag{4.12}$$

The PID efficiency is determined using the full-simulation sample, with the single-muon identification efficiency evaluated by a tool called PIDCalib package using a dedicated data sample[187]. In this data sample, only one track of $J/\psi \to \mu^+\mu^-$ candidates is required to be identified as a muon, and the single-muon identification efficiency is the probability that the other track is also identified as a muon. The single-muon identification efficiency is determined in (p, η) intervals of the muon track, as shown in Figure 4.15. In practice,

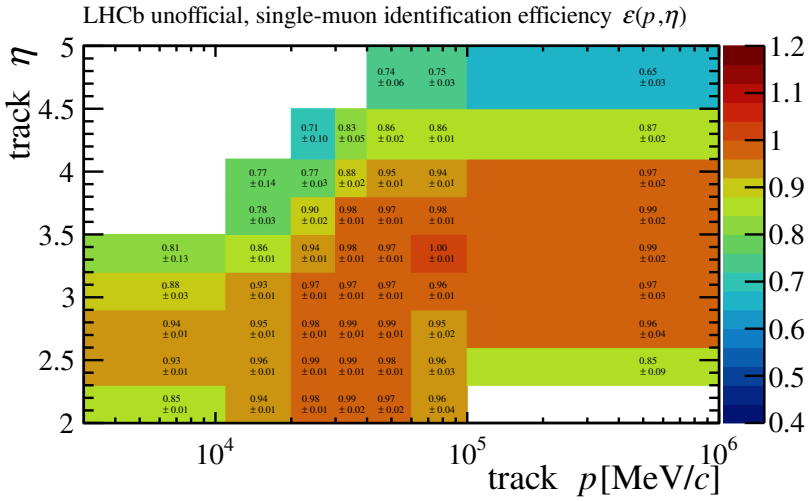

Figure 4.15 Single-muon identification efficiency in (p, η) intervals of the muon track.

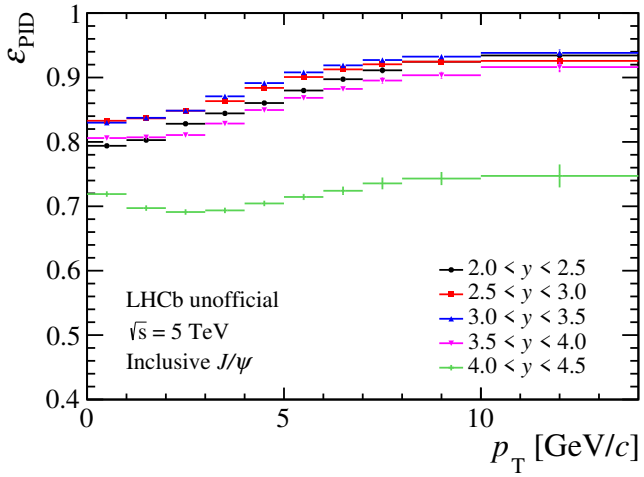

Figure 4.16 PID efficiency ε_{PID} of inclusive J/ψ mesons as a function of p_{T} in intervals of y. The efficiency is used for both prompt and non-prompt J/ψ mesons.

the PID efficiency of J/ψ mesons is calculated as

$$\varepsilon_{\text{PID}} = \frac{\sum_i^N \varepsilon(p_i^{\mu^+}, \eta_i^{\mu^+}) \times \varepsilon(p_i^{\mu^-}, \eta_i^{\mu^-})}{N(J/\psi \text{ reconstructed and selected w/o PID and trigger})}, \tag{4.13}$$

where the index i denotes each simulated event, and the $\varepsilon(p_i^{\mu^+}, \eta_i^{\mu^+})$ and $\varepsilon(p_i^{\mu^-}, \eta_i^{\mu^-})$ are the single-muon identification efficiencies evaluated from data. The PID efficiency is calculated with the simulated samples of prompt and non-prompt J/ψ mesons combined. It is shown in Figure 4.16 as a function of p_{T} in intervals of y.

4.5.4 Trigger efficiency

The trigger efficiency ε_{tri} of J/ψ mesons in each (p_{T}, y) interval is defined as the yield fraction of J/ψ mesons reconstructed and selected with PID and trigger requirements in

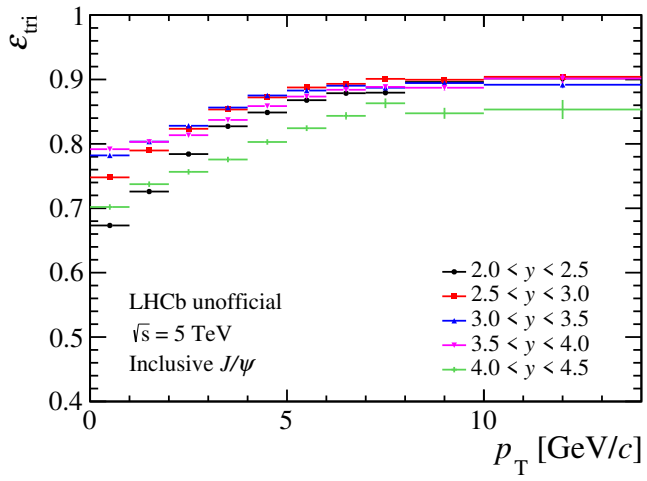

Figure 4.17 Trigger efficiency $\varepsilon_{\rm tri}$ of inclusive J/ψ mesons as a function of $p_{\rm T}$ in intervals of y. The efficiency is used for both prompt and non-prompt J/ψ mesons.

those with PID but without trigger requirements,

$$\varepsilon_{\rm tri} = \frac{N(J/\psi \text{ reconstructed and selected w/ PID and trigger})}{N(J/\psi \text{ reconstructed and selected w/ PID w/o trigger})}. \tag{4.14}$$

Since the offline selection criteria are stricter than the requirements of trigger line HLT2DiMuonJpsiTurbo, only the efficiencies of L0Muon and HLT1DiMuonHighMass trigger lines are taken into account. The trigger efficiency $\varepsilon_{\rm tri}$ is determined using the full-simulation sample combining simulated events of prompt and non-prompt J/ψ mesons. It is shown in Figure 4.17 as a function of $p_{\rm T}$ in intervals of y. Moreover, the efficiency $\varepsilon_{\rm tri}$ is validated using data separately for L0 trigger and HLT1 trigger, as detailed in Section 4.6.2.

4.5.5 Total efficiency

The total efficiency $\varepsilon_{\rm tot}$ is calculated as the product of the four efficiencies in each ($p_{\rm T}$,y) interval. As mentioned above, the efficiencies $\varepsilon_{\rm acc}$ and $\varepsilon_{\rm rec\&sel}$ are evaluated separately for prompt and non-prompt J/ψ mesons, and the efficiencies $\varepsilon_{\rm PID}$ and $\varepsilon_{\rm tri}$ are calculated combining the simulated samples of prompt and non-prompt J/ψ mesons. The total efficiencies $\varepsilon_{\rm tot}$ of prompt and non-prompt J/ψ mesons are shown in Figure 4.18.

4.6 Systematic uncertainties

A summary of systematic uncertainties is presented in Table 4.4. Uncertainties arising from signal extraction and efficiency determination are mostly evaluated in each ($p_{\rm T}$,y) interval, while those due to branching fraction and luminosity measurement are common

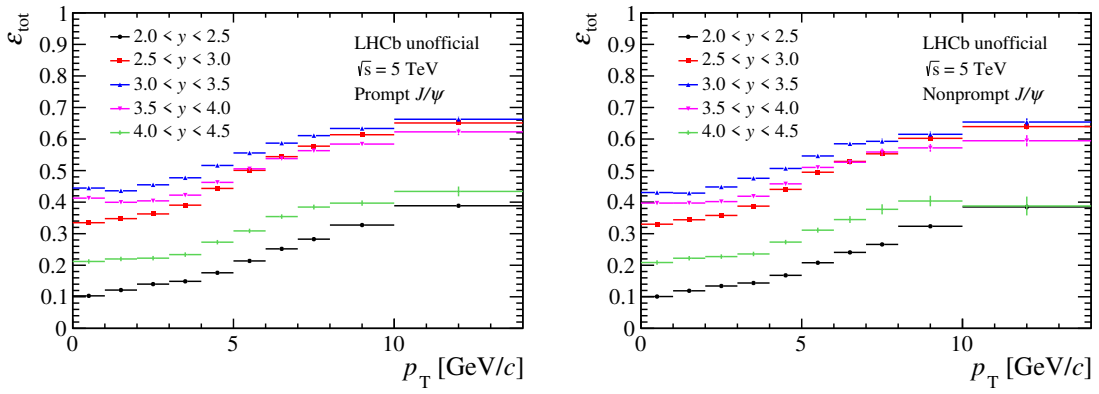

(a) ε_{tot} of prompt J/ψ mesons. (b) ε_{tot} of non-prompt J/ψ mesons.

Figure 4.18 Total efficiency ε_{tot} of (a) prompt and (b) non-prompt J/ψ mesons as a function of p_{T} in intervals of y.

Table 4.4 Relative systematic uncertainties on the measurement of the J/ψ production cross-section. The symbol $\oplus$ means addition in quadrature.

Source	Relative uncertainty	Correlations
Signal mass model	$< 2.0\%$	Uncorrelated
Background mass model	$< 0.7\%$	Correlated between intervals
Signal t_z model	$< 0.8\%$ (prompt) $< 14.7\%$ (non-prompt)	Correlated between p_{T} intervals
Background t_z model	$< 1.2\%$ (prompt) $< 4.0\%$ (non-prompt)	Uncorrelated
Tracking efficiency	$(2 \times 0.8\%) \oplus (< 3.7\%)$	Correlated between intervals
PID efficiency	$(< 2.2\%) \oplus (< 1.5\%)$	Correlated between intervals
L0-trigger efficiency	$< 1.9\%$	Correlated between intervals
HLT1-trigger efficiency	1.0%	Correlated between intervals
Simulation sample size	$< 3.7\%$ (prompt) $< 7.7\%$ (non-prompt)	Uncorrelated
$\mathcal{B}(J/\psi \to \mu^+\mu^-)$	0.6%	Correlated between intervals
Luminosity	2.0%	Correlated between intervals
Radiative tail	1.0%	Correlated between intervals

to all intervals. The details of the evaluation are discussed in the following.

4.6.1 Uncertainties related to signal extraction

An uncertainty is attributed to the choice of the probability density function used to model the di-muon invariant-mass distribution of the signal components. As an al-

ternative to the sum of two CB functions, the signal invariant-mass distribution is described by a model derived from simulation using the approach of kernel density estimation (KDE)[188]. To account for the resolution difference between data and simulation, the alternative model is convolved with a Gaussian function with zero mean and width varied freely. The default and alternative models are compared in each (p_{T},y) interval and the relative difference, which is up to 2.0%, is taken as a systematic uncertainty.

The exponential function describing the background is replaced by a linear function and the relative difference, varying up to 0.7%, is taken as a systematic uncertainty. The resulting uncertainty is considered as fully correlated between intervals.

An uncertainty is attributed to the method that is used to separate prompt and non-prompt J/ψ mesons. To evaluate this uncertainty in each (p_{T},y) interval, the same t_z probability density function of J/ψ signals is used to fit the simulation. While the relative differences between the fitted and the true yields are small for most intervals, they are significant for non-prompt J/ψ mesons in a few small-p_{T} intervals. These differences, varying up to 0.8% for prompt and 14.7% for non-prompt J/ψ mesons, are taken as systematic uncertainties, and are assumed to be fully correlated between p_{T} intervals and uncorrelated between y intervals as indicated by simulation.

As an alternative t_z description of the non-J/ψ background in each interval, the same empirical function is used but with the parameters fixed from a fit to the background distribution extracted by the *sPlot* method[185] using the $m_{\mu^+\mu^-}$ as the discriminating variable. The relative difference between the two methods varies up to 1.2% for prompt and 4.0% for non-prompt J/ψ mesons in different intervals.

4.6.2 Uncertainties related to efficiency determination

Systematic uncertainties related to the tracking efficiency are evaluated as follows. The correction factors obtained from dedicated data and simulation samples are found to depend on different event multiplicity variables[186]. This introduces a systematic uncertainty of 0.8% per track. In addition, the statistical uncertainties on these factors are propagated to the systematic uncertainties of the cross-sections, which vary up to 3.7% depending on the (p_{T},y) interval.

The PID efficiency is obtained using a dedicated calibration sample of $J/\psi \to \mu^+\mu^-$ candidates in which only one track is required to be identified as a muon. The uncertainties of the muon identification efficiencies due to the finite size of the calibration data sample are propagated to the systematic uncertainties of the cross-sections, which are up to 2.2%

in different intervals. Another uncertainty comes from the choice of interval scheme of the calibration sample. The resulting uncertainties vary up to 1.5% depending on the (p_{T},y) interval.

The trigger efficiency in simulation is validated with data. One muon is requested to pass the L0-trigger requirement such that the other muon can be regarded as an unbiased probe of the efficiency of one muon. The L0-trigger efficiency of the J/ψ candidate is the probability that at least one muon track passes the trigger requirement. The relative difference between data and simulation, varying up to 1.9% across intervals, is taken as a systematic uncertainty on the L0-trigger efficiency. The HLT1-trigger efficiency is determined using TIS events, *i.e.* that would fulfil the trigger requirement if the J/ψ signals were excluded[189]. The fraction of J/ψ candidates for which two tracks fulfil the HLT1-trigger requirement is treated as the efficiency for both data and simulation. The overall relative difference between data and simulation is 1.0%, and is taken as a systematic uncertainty on the HLT1-trigger efficiency common to all intervals.

The tail shape on the left side of the CB function is used to describe the effect of QED radiation, which leads to energy loss in some J/ψ candidates. A small fraction of the J/ψ signal lies outside the mass range of the fit. This signal loss is taken into account in the efficiency $\varepsilon_{\mathrm{rec\&sel}}$ estimated with the simulated sample. The imperfect modelling of the radiative decay is considered as a source of systematic uncertainty. Based on a comparison between the radiative tails in simulation and data a systematic uncertainty of 1.0% is assigned.

4.6.3 Other sources

The statistical uncertainties of the efficiencies due to the finite size of the simulated sample result in uncertainties on the cross-sections. The values range up to 3.7% for prompt and 7.7% for non-prompt J/ψ mesons depending on the (p_{T},y) interval.

The uncertainty on the $J/\psi \to \mu^+\mu^-$ branching fraction[9] results in an uncertainty on the measured cross-sections of 0.6%. The luminosity is determined using methods similar to those described in Ref. [171] and the relative uncertainty is 2.0%.

4.7 Production cross-sections

The measured double-differential cross-sections for prompt and non-prompt J/ψ mesons are shown in Figure 4.19 and listed in Tables A.1 and A.2 in Appendix A, for the

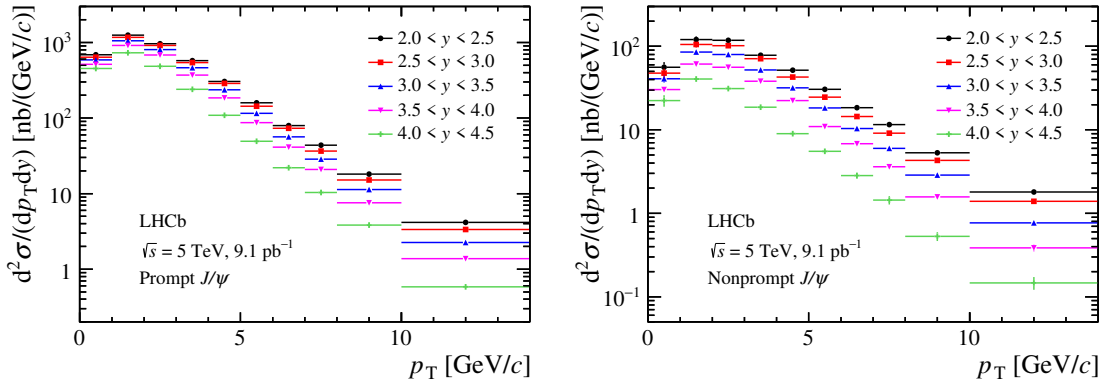

(a) Cross-sections for prompt J/ψ mesons. (b) Cross-sections for non-prompt J/ψ mesons.

Figure 4.19 Differential cross-sections for (a) prompt and (b) non-prompt J/ψ mesons as a function of p_T in intervals of y. The error bars represent the total uncertainties, which are partially correlated between intervals.

range $0 < p_T < 14\,\text{GeV}$ and $2.0 < y < 4.5$ with Δp_T between 1 and 4 GeV and $\Delta y = 0.5$. By integrating the double-differential results over p_T or y, the single-differential cross-sections $d\sigma/dp_T$ and $d\sigma/dy$ are obtained, and are listed in Tables A.3–A.6 in Appendix A. The $d\sigma/dp_T$ results include a further p_T interval in the range $14 < p_T < 20\,\text{GeV}$, which is not divided into y intervals due to the limited size of the data sample. The integrated cross-sections for prompt and non-prompt J/ψ mesons in the range $0 < p_T < 20\,\text{GeV}$ and $2.0 < y < 4.5$ are

$$\sigma_{\text{prompt } J/\psi} = 8.154 \pm 0.010 \pm 0.283\,\mu\text{b},$$
$$\sigma_{\text{non-prompt } J/\psi} = 0.820 \pm 0.003 \pm 0.034\,\mu\text{b},$$

where the first uncertainties are statistical and the second systematic. These results are obtained under the assumption that the polarisation of the J/ψ mesons is negligible. The J/ψ polarisation measurement at $\sqrt{s} = 7\,\text{TeV}$ [76] indicates that the polarisation parameters λ_θ, $\lambda_{\theta\phi}$ and λ_ϕ are consistent with zero while the central value of λ_θ is around -0.2 in the helicity frame. The polarisation affects the detection efficiency, and the dependence of the cross-sections on the polarisation is discussed in Section 4.7.1 in detail. When the polarisation parameter λ_θ is assumed to be -0.2 [76], the total cross-section decreases by 2.8% (2.9%) for prompt (non-prompt) J/ψ mesons.

The fraction of non-prompt J/ψ mesons is defined as the ratio between the non-prompt cross-section and the sum of prompt and non-prompt cross-sections, and the results in (p_T,y) intervals are shown in Figure 4.20 and listed in Table A.7 in Appendix A. The systematic uncertainties cancel mostly in the ratio. Only the uncertainties due to the t_z fit model and the size of simulated sample are included. The fraction increases as a function

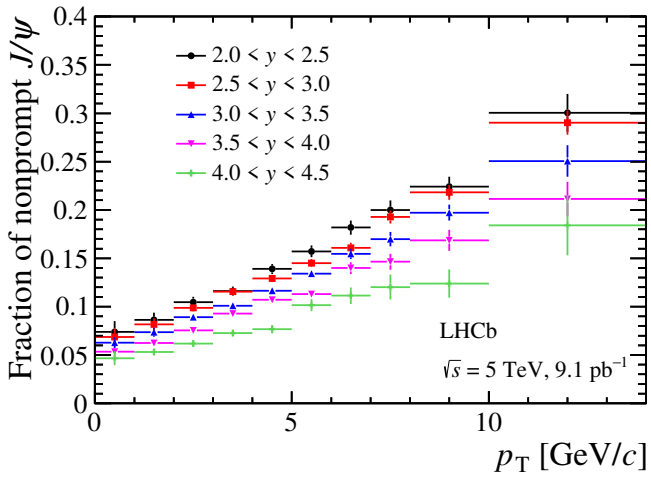

Figure 4.20 Fraction of non-prompt J/ψ mesons as a function of p_T in intervals of y. The error bars represent the total uncertainties, which are partially correlated between intervals.

of p_T, and for a given p_T, the fraction decreases with increasing y.

4.7.1 Dependence of cross-sections on the polarisation

The angular distribution of the $J/\psi \to \mu^+\mu^-$ decay is described by[76]

$$\frac{\mathrm{d}^2N}{\mathrm{d}\cos\theta\mathrm{d}\phi} \propto 1 + \lambda_\theta \cos^2\theta + \lambda_{\theta\phi} \sin 2\theta \cos\phi + \lambda_\phi \sin^2\theta \cos 2\phi, \tag{4.15}$$

where θ and ϕ are the polar and azimuthal angles between the direction of μ^+ and the chosen polarisation axis, and λ_θ, $\lambda_{\theta\phi}$ and λ_ϕ are polarisation parameters. In the helicity frame, the polarisation axis coincides with the flight direction of the J/ψ meson in the centre-of-mass frame of the colliding hadrons. The detection efficiency of the J/ψ mesons is a function of the polarisation, especially of λ_θ. Zero polarisation is assumed in the simulation since there is no prior knowledge of the polarisation of the J/ψ mesons in pp collisions at 5 TeV, and only small longitudinal polarisation have been found in the J/ψ polarisation analyses at the LHC[75-76].

To evaluate the change of results assuming a non-zero polarisation, the angular distribution of the muon tracks in rest frame of the J/ψ mesons in simulation is weighted to that of other polarisation scenarios, and then the change in the total efficiency, which impacts the cross-sections, is calculated. The relative change of the cross-section for a polarisation of $\lambda_\theta = -0.2$[76] in the helicity frame compared to zero polarisation in each (p_T,y) interval is shown in Figure 4.21 and given in Table A.16 in Appendix A. In addition, the relative change of the cross-section for a polarisation of $\lambda_\theta = -1$ (+1) in the helicity frame, which corresponds to the fully longitudinally (transversely) polarised scenario, compared to zero polarisation in each (p_T,y) interval is given in Table A.17 (A.18) in Appendix A.

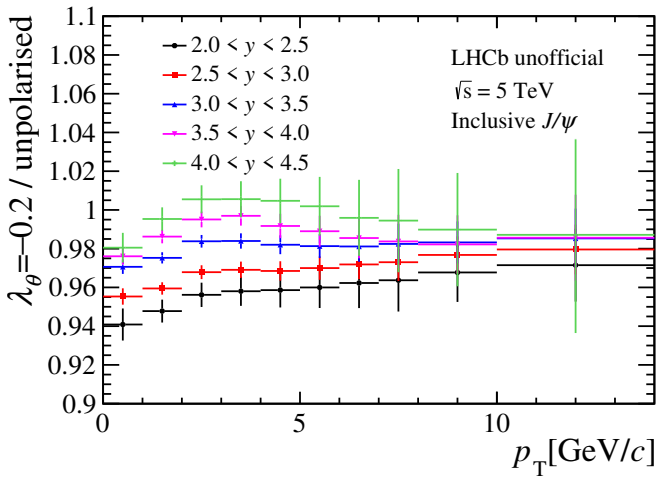

Figure 4.21 Relative changes of cross-sections for a polarisation of $\lambda_\theta = -0.2$ rather than zero in (p_T,y) intervals. The relative changes are applied to cross-sections of prompt and non-prompt J/ψ mesons.

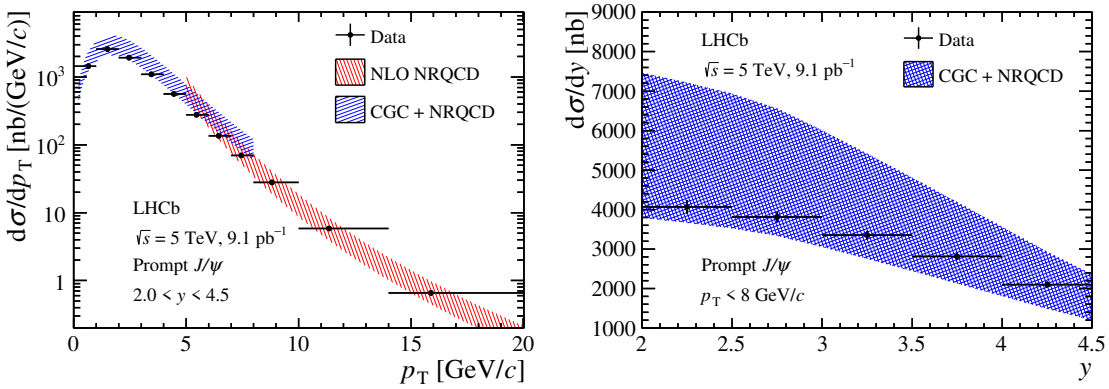

(a) dσ/dp_T for prompt J/ψ mesons. (b) dσ/dy for prompt J/ψ mesons.

Figure 4.22 Differential cross-sections (a) dσ/dp_T and (b) dσ/dy for prompt J/ψ mesons compared with NLO NRQCD calculations[66] and CGC+NRQCD calculations[69]. Uncertainties due to LDMEs determination, and due to renormalisation and factorisation scales are included in these predictions.

4.7.2 Comparison with theoretical models

The single-differential cross-sections for prompt J/ψ mesons are compared with NLO NRQCD calculations in the high-p_T region and with CGC+NRQCD calculations in the low-p_T region, as shown in Figure 4.22. For NLO NRQCD calculations, the LDMEs are fixed from the Tevatron data[66], and for CGC+NRQCD calculations[69], nonperturbative parameters are fixed by fits to the Tevatron and HERA data[78,190]. Uncertainties due to LDMEs determination and due to renormalisation and factorisation scales are considered in these calculations.

A comparison between single-differential cross-sections for nonprompt J/ψ mesons

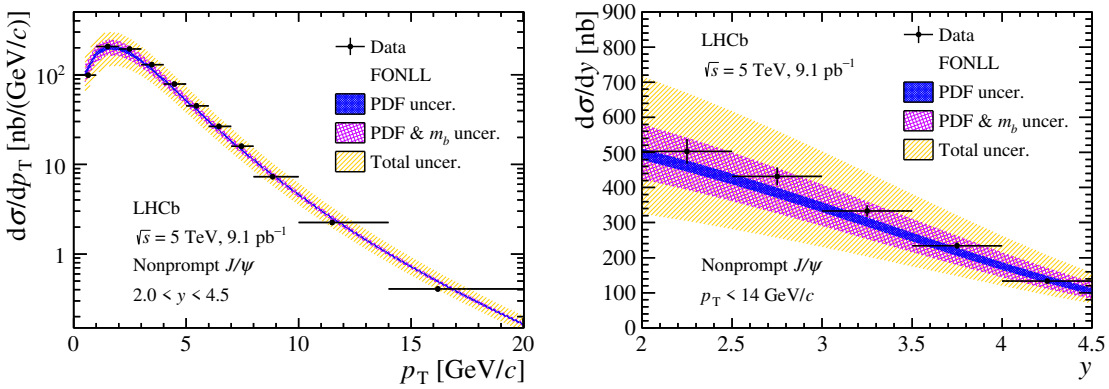

(a) $d\sigma/dp_T$ for non-prompt J/ψ mesons. (b) $d\sigma/dy$ for non-prompt J/ψ mesons.

Figure 4.23 Differential cross-sections (a) $d\sigma/dp_T$ and (b) $d\sigma/dy$ for non-prompt J/ψ mesons compared with FONLL calculations [96-97]. The orange band shows the total FONLL calculation uncertainty; the violet band shows the uncertainties of PDFs and that due to b-quark mass added in quadrature; the blue band shows only the uncertainties of PDFs.

and FONLL calculations [96-97] is shown in Figure 4.23. The FONLL approach provides cross-sections for b-quark production, and the branching fraction of the decay $b \to J/\psi X$, $(1.16 \pm 0.10)\%$ [9], is taken from measurements performed in e^+e^- collisions at the Large Electron-Positron (LEP) collider. The FONLL calculations take into account the uncertainties of PDFs, the uncertainty due to the b-quark mass, and that due to the scales of renormalisation and factorisation. The total uncertainty of FONLL is dominated by the latter source.

All these predictions are consistent with measured cross-sections of prompt and non-prompt J/ψ mesons. However, a more concrete conclusion still cannot be drawn owing to the large uncertainties of the predictions. In this case, the cross-section ratio between different centre-of-mass energies can be considered as a good observable to compare, because the uncertainties cancel a lot in the ratio for both theoretical calculations and experimental data.

4.7.3 Cross-section ratios

The production cross-sections of J/ψ mesons at 5 TeV are compared with those previously measured at 8 TeV [99] and 13 TeV [63] in the range $0 < p_T < 14$ GeV and $2.0 < y < 4.5$. The ratios of differential cross-sections for prompt J/ψ mesons between 8 TeV and 5 TeV measurements are shown in Figure 4.24, and those between 13 TeV and 5 TeV in Figure 4.25, both compared with NLO NRQCD and CGC+NRQCD calculations. The ratios for prompt J/ψ mesons are also listed in Tables A.8–A.11 in Appendix A. For non-prompt J/ψ mesons, the ratios of differential cross-sections between 8 TeV and

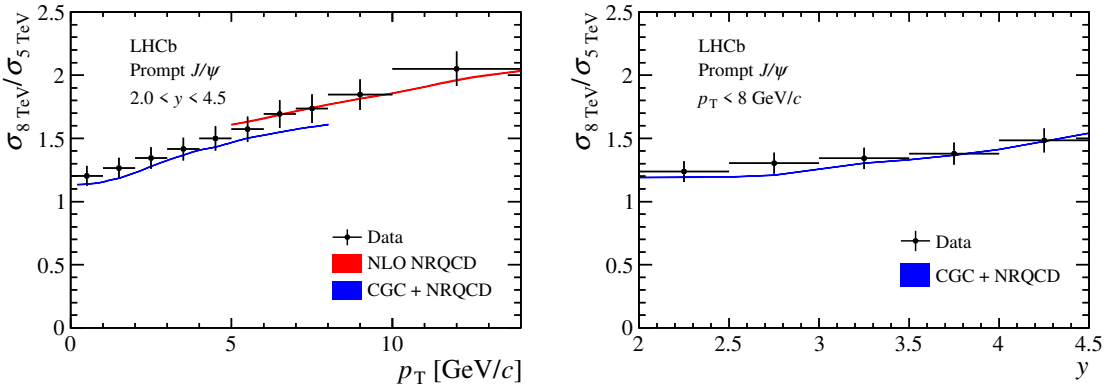

(a) Ratio vs. p_{T} for prompt J/ψ mesons. (b) Ratio vs. y for prompt J/ψ mesons.

Figure 4.24 Ratios of differential cross-sections between 8 TeV and 5 TeV measurements as a function of (a) p_{T} and (b) y for prompt J/ψ mesons compared with NLO NRQCD calculations[66] and CGC+NRQCD calculations[69]. Uncertainties due to the LDMEs determination, and due to renormalisation and factorisation scales are included in these predictions.

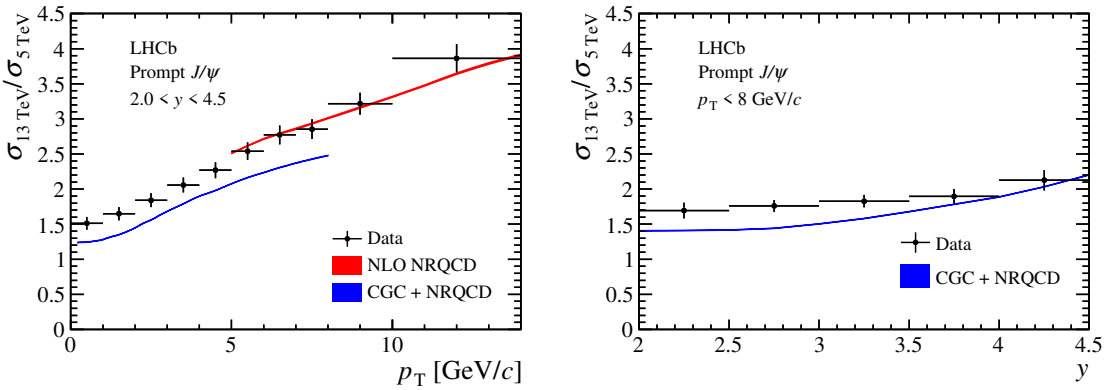

(a) Ratio vs. p_{T} for prompt J/ψ mesons. (b) Ratio vs. y for prompt J/ψ mesons.

Figure 4.25 Ratios of differential cross-sections between 13 TeV and 5 TeV measurements as a function of (a) p_{T} and (b) y for prompt J/ψ mesons compared with NLO NRQCD calculations[66] and CGC+NRQCD calculations[69]. Uncertainties due to the LDMEs determination, and due to renormalisation and factorisation scales are included in these predictions.

5 TeV measurements are shown in Figure 4.26, and those between 13 TeV and 5 TeV in Figure 4.27, compared with FONLL calculations. The ratios for non-prompt J/ψ mesons are also listed in Tables A.12–A.15 in Appendix A. Some of the systematic uncertainties are considered to fully cancel in the ratio, such as those due to branching fraction and the radiative tail. The uncertainties due to the t_z fit and simulation sample size are taken as uncorrelated between the two measurements, and therefore remain. All other systematic uncertainties are assumed to cancel only partially. For example, the systematic uncertainty due to the luminosity measurement is estimated to be correlated at 50%. The overall uncertainty on the measured ratio is dominated by the luminosity measurement for prompt J/ψ mesons, and by the t_z fit and the luminosity measurement for non-prompt

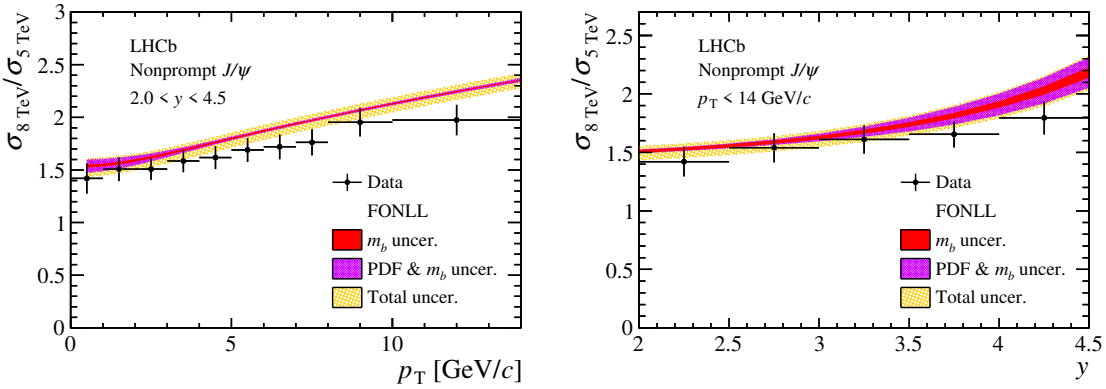

(a) Ratio vs. p_T for non-prompt J/ψ mesons. (b) Ratio vs. y for non-prompt J/ψ mesons.

Figure 4.26 Ratios of differential cross-sections between 8 TeV and 5 TeV measurements as a function of (a) p_T and (b) y for non-prompt J/ψ mesons compared with FONLL calculations [96-97]. The orange band shows the total FONLL calculation uncertainty; the violet band shows the uncertainties on PDFs and that due to b-quark mass added in quadrature; the red band shows only the uncertainty due to the b-quark mass.

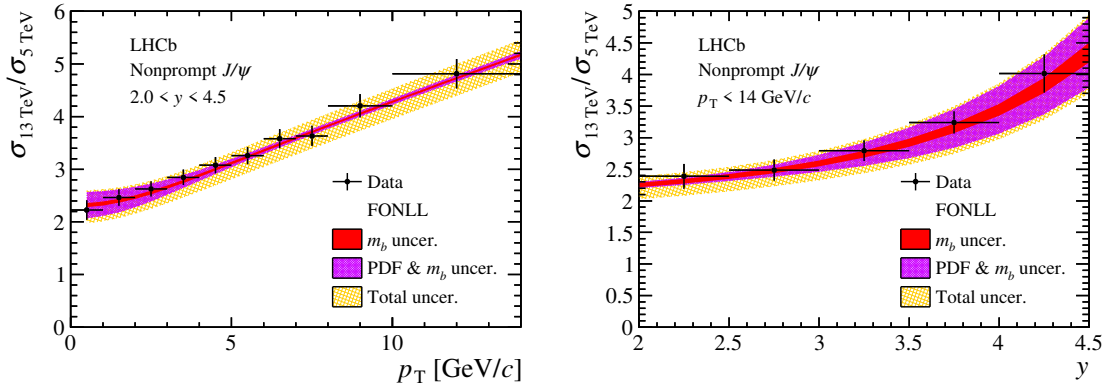

(a) Ratio vs. p_T for non-prompt J/ψ mesons. (b) Ratio vs. y for non-prompt J/ψ mesons.

Figure 4.27 Ratios of differential cross-sections between 13 TeV and 5 TeV measurements as a function of (a) p_T and (b) y for non-prompt J/ψ mesons compared with FONLL calculations [96-97]. The orange band shows the total FONLL calculation uncertainty; the violet band shows the uncertainties on PDFs and that due to b-quark mass added in quadrature; the red band shows only the uncertainty due to the b-quark mass.

J/ψ mesons. For the NLO NRQCD and CGC+NRQCD predictions of the cross-section ratios, the uncertainties due to LDMEs determination, and due to renormalisation and factorisation scales between different energies mostly cancel. For the FONLL calculations, the uncertainty on the ratio is dominated by the uncertainties of PDFs for the low-p_T and large-y regions and by the uncertainty due to the renormalisation and factorisation scales for the high-p_T and small-y regions.

Figures 4.24 and 4.25 show good agreement between NLO NRQCD calculations and the measurement results in the high-p_T region. The combination of CGC effective theory and NRQCD factorisation achieves a reasonable agreement between data and the-

ory in the low-p_{T} region but a small discrepancy is still observed, which indicates that a pure fixed-order calculation may be insufficient and Sudakov resummation[191] may be required. A comparison of Figures 4.24 and 4.25 suggests that the energy dependence of the cross-sections may differ between the theoretical calculation and the experimental measurements. Figures 4.26 and 4.27 show that the FONLL calculations agree with the experimental results for non-prompt J/ψ mesons.

4.8 Conclusion

The J/ψ production cross-sections in proton-proton collisions at a centre-of-mass energy $\sqrt{s} = 5\,\mathrm{TeV}$ are studied using a data sample corresponding to an integrated luminosity of $9.18 \pm 0.35\,\mathrm{pb}^{-1}$ collected by the LHCb detector. The J/ψ differential cross-sections, as a function of p_{T} and y, are measured separately for prompt and non-prompt J/ψ mesons in the range $0 < p_{\mathrm{T}} < 20\,\mathrm{GeV}$ and $2.0 < y < 4.5$. The J/ψ production cross-section ratios between 8 TeV and 5 TeV, and between 13 TeV and 5 TeV are also determined and compared with the theoretical predictions. The measured prompt J/ψ results are in good agreement with NLO NRQCD calculations in the high-p_{T} region. A small tension is observed between data for prompt J/ψ in the low-p_{T} region and CGC+NRQCD calculations, which may indicate the need for further corrections in the theory model. The FONLL calculations describe the measured results for non-prompt J/ψ mesons well.

CHAPTER 5 DOUBLE CHARMONIUM PRODUCTION MEASUREMENT

In this chapter, the measurement of di-J/ψ and J/ψ-$\psi(2S)$ production in pp collisions at $\sqrt{s} = 13\,\text{TeV}$ at the LHCb experiment is reported. The production cross-sections are measured with the J/ψ and $\psi(2S)$ mesons in the range $0 < p_{\text{T}} < 14\,\text{GeV}$ and $2.0 < y < 4.5$. The differential cross-sections of di-J/ψ and J/ψ-$\psi(2S)$ as functions of several kinematic variables are also measured, as well as the cross-section ratio between J/ψ-$\psi(2S)$ and di-J/ψ. For di-J/ψ production, the contributions from DPS and SPS are separated based on the differential cross-section $\text{d}\sigma/\text{d}\Delta y$. The effective cross-section σ_{eff} is extracted from DPS contribution, and the gluon TMD PDFs are studied via SPS process.

5.1 Analysis strategy

In this chapter, the symbol ψ is used to refer to J/ψ or $\psi(2S)$ meson, and di-ψ stands for di-J/ψ or J/ψ-$\psi(2S)$. For di-J/ψ, ψ_1 and ψ_2 denote two J/ψ mesons randomly. For J/ψ-$\psi(2S)$, ψ_1 denotes J/ψ meson and ψ_2 denotes $\psi(2S)$ meson. All the ψ candidates are reconstructed through the $\psi \to \mu^+\mu^-$ decay channel, and ψ_1 and ψ_2 candidates correspond to $\mu_1^+\mu_1^-$ and $\mu_2^+\mu_2^-$ final states respectively. The production cross-section of di-ψ production is calculated as

$$\sigma_{\text{di-}\psi} = \frac{N^{\text{corr}}(\text{di-}\psi)}{\mathcal{L} \times \mathcal{B}(\psi_1 \to \mu^+\mu^-) \times \mathcal{B}(\psi_2 \to \mu^+\mu^-)}, \tag{5.1}$$

where N^{corr} is the signal yield with efficiency correction, $\mathcal{L}$ is the integrated luminosity, and $\mathcal{B}$ is the branching fraction. The signal extraction is discussed in Sections 5.4, including the subtraction of combinatorial backgrounds and non-prompt contributions, and the efficiency correction is discussed in Section 5.5.

The differential cross-section of di-ψ production as a function of a kinematic variable u is calculated as

$$\frac{\text{d}\sigma_{\text{di-}\psi}}{\text{d}u} = \frac{\Delta N^{\text{corr}}(\text{di-}\psi)}{\mathcal{L} \times \mathcal{B}(\psi_1 \to \mu^+\mu^-) \times \mathcal{B}(\psi_2 \to \mu^+\mu^-) \times \Delta u}, \tag{5.2}$$

where ΔN^{corr} is the efficiency-corrected signal yield in a interval of the variable u, and Δu is the interval width. The following kinematic variables related to di-ψ production are used in this analysis:

- $p_{\text{T}}^{\text{di-}\psi}$, transverse momentum of di-ψ;

- $y_{\text{di-}\psi}$, rapidity of di-ψ;
- $m_{\text{di-}\psi}$, invariant mass of di-ψ;
- $\Delta y = |y_{\psi_1} - y_{\psi_2}|$, absolute difference in the rapidity between two ψ mesons;
- $\Delta\phi = |\phi_{\psi_1} - \phi_{\psi_2}|$, absolute difference in the azimuthal angle ϕ, defined in the laboratory frame, between two ψ mesons.

Another five variables are only used for di-J/ψ production: transverse momentum of either J/ψ meson $p_{\mathrm{T}}^{J/\psi}$, rapidity of either J/ψ meson $y_{J/\psi}$, and the transverse momentum asymmetry $\mathcal{A}_{p_{\mathrm{T}}}$ defined as

$$\mathcal{A}_{p_{\mathrm{T}}} = \left| \frac{p_{\mathrm{T}}^{J/\psi_1} - p_{\mathrm{T}}^{J/\psi_2}}{p_{\mathrm{T}}^{J/\psi_1} + p_{\mathrm{T}}^{J/\psi_2}} \right|, \tag{5.3}$$

and the angles θ_{CS} and ϕ_{CS} in the CS frame, which are defined in Section 2.6.2. Candidates in a given $p_{\mathrm{T}}^{J/\psi}$ ($y_{J/\psi}$) interval combine two sets of events requiring $p_{\mathrm{T}}^{J/\psi_1}$ (y_{J/ψ_1}) and $p_{\mathrm{T}}^{J/\psi_2}$ (y_{J/ψ_2}) within the interval respectively, and then the yield is divided by two.

5.2 Data and simulated samples

The data sample used in this analysis was collected by the LHCb detector in pp collisions at $\sqrt{s} = 13\,\text{TeV}$ in 2016, 2017, and 2018, corresponding to an integrated luminosity of $4.18 \pm 0.08\,\text{fb}^{-1}$ [171]. The data were taken with two different settings of magnet filed direction, MagDown and MagUp, and various trigger configurations. The trigger lines used in this analysis are L0DiMuon, HLT1DiMuonHighMass, and a dedicated HTL2 line called HLT2DPS:2x2mu. According to the selection criteria of these trigger lines, the data sets collected in each year are classified into different parts, and some of them with relatively large luminosity are chosen in this analysis, which are listed in Table 5.1. The selection criteria of the trigger lines for these chosen data sets are summarised in Table 5.2.

The di-ψ candidates are reconstructed using final states with two $\mu^+\mu^-$ pairs. It is required that at least one $\mu^+\mu^-$ pair fulfils the selection criteria of the L0DiMuon and HLT1DiMuonHighMass lines. The hardware trigger line L0DiMuon selects two muons with the product of their transverse momentum $p_{\mathrm{T}1} \times p_{\mathrm{T}2} > 1.3^2$, 1.5^2 or $1.8^2\,\text{GeV}^2$, and has a loose selection on the multiplicity, nSPDHits < 900. The HLT1DiMuonHighMass line requires two good-quality tracks with $p_{\mathrm{T}} > 0.3\,\text{GeV}$ and $p > 6\,\text{GeV}$, which are loosely identified as muons, to form a ψ candidate with high invariant mass, $m_{\mu^+\mu^-} > 2.7\,\text{GeV}$ or $2.9\,\text{GeV}$. In the HLT2DPS:2x2mu line, the selections listed in Table 5.2 are applied to both $\mu^+\mu^-$ pairs separately. Two ψ candidates are reconstructed with good vertex-fit quality,

Table 5.1 The chosen data sets in each year.

Data set	Short name	Luminosity
2016 part 1	16p1	$0.601\,\text{fb}^{-1}$
2016 part 2	16p2	$0.271\,\text{fb}^{-1}$
2016 part 3	16p3	$0.509\,\text{fb}^{-1}$
2017 part 1	17p1	$0.537\,\text{fb}^{-1}$
2017 part 2	17p2	$0.538\,\text{fb}^{-1}$
2018	18	$1.723\,\text{fb}^{-1}$

Table 5.2 Selection criteria of trigger lines for chosen data sets.

Trigger line	Variable	16p1	16p2	16p3/17p1	17p2/18
L0DiMuon	$p_{\text{T}1} \times p_{\text{T}2}$ [GeV^2]	$> (1.5)^2$	$> (1.3)^2$	$> (1.3)^2$	$> (1.8)^2$
	nSPDHits	< 900	< 900	< 900	< 900
HLT1DiMuonHighMass	track p_{T} [GeV]	> 0.3	> 0.3	> 0.3	> 0.3
	track p [GeV]	> 6	> 6	> 6	> 6
	track χ^2/ndf	< 4	< 4	< 4	< 4
	track PID	IsMuon	IsMuon	IsMuon	IsMuon
	$m_{\mu^+\mu^-}$ [GeV]	> 2.7	> 2.9	> 2.7	> 2.7
HLT2DPS:2x2mu	track ProbNNμ			> 0.1	> 0.1
	track ghost probability			< 0.4	< 0.4
	track χ^2/ndf	< 5	< 5	< 5	< 5
	vertex χ^2/ndf	< 25	< 25	< 25	< 25
	$\lvert m_{\mu^+\mu^-} - m_{\psi}\rvert$ [MeV]	< 120	< 120	< 120	< 120

and the invariant mass $m_{\mu^+\mu^-}$ is required to be within a range of $\pm 120\,\text{MeV}$ around the known J/ψ or $\psi(2S)$ mass[9]. For some of the chosen data sets, the requirements on track-fit quality and muon identification are tightened.

Simulated samples are required to study the behaviour of signals and determine the efficiency corrections. Due to the limited knowledge, no reliable simulation of di-ψ production is available. Thanks to the factorisation of the efficiencies for di-ψ candidates, the efficiencies can be determined by simulated events for single-ψ production, which is detailed in Section 5.5. The modeling method is the same as that used in the single-J/ψ production measurement, as described in Section 4.2. Two generator-level samples each with 6 million events (2 million for each year, 2016, 2017 and 2018) for single-J/ψ and

Table 5.3 Offline selection criteria. The track selections are applied to all the four muon tracks. The vertex selection is applied to both ψ vertices.

Variable	Value
track η	$1.9 < \eta < 4.9$
track p_{T}	$> 0.65\,\mathrm{GeV}$
track p	$> 3\,\mathrm{GeV}$
track χ^2/ndf	< 3
track ghost probability	< 0.3
track DLL_{μ}	> 0
ProbNNμ of muon tracks for J/ψ	> 0.4
ProbNNμ of muon tracks for $\psi(2S)$	> 0.9
di-muon vertex χ^2/ndf	< 8
$\lvert m_{\mu^+\mu^-} - m_{\psi}\rvert$	$< 120\,\mathrm{MeV}$
p_{T} of ψ	$0 < p_{\mathrm{T}} < 14\,\mathrm{GeV}$
y of ψ	$2.0 < y < 4.5$
pseudo-proper time t_z of ψ	$-2 < t_z < 10\,\mathrm{ps}$
t_z uncertainty σ_{t_z} of ψ	$< 0.3\,\mathrm{ps}$
$m(\mu_1^{\pm}\mu_2^{\pm})$	$> 220\,\mathrm{MeV}$
$\theta(\mu_1^{\pm}\mu_2^{\pm})$	$> 0.002\,\mathrm{rad}$
$\lvert z_{\mathrm{PV}}^{\psi_1} - z_{\mathrm{PV}}^{\psi_2}\rvert$	$< 0.1\,\mathrm{mm}$

single-$\psi(2S)$ production respectively are used for the determination of the acceptance. In order to determine the efficiency in this analysis, a full-simulation sample with 18 million (8 million) events for single-J/ψ (single-$\psi(2S)$) production is used. These events are simulated with four different trigger configurations corresponding to four settings of selection criteria that applied in the chosen data sets. Thus the full-simulation sample is divided into four sub-samples, which are labelled as MC16p1, MC16p2, MC17p1 and MC18 separately. In addition, a full-simulation sample of $\Upsilon \to J/\psi\, J/\psi\, \gamma$ decay with 2 million events is used to check the correlation between the efficiencies of two J/ψ mesons.

5.3 Offline selection

The offline selections are applied to di-ψ candidates to reduce the combinatorial background to a reasonable level and ensure the good quality of the fit to extract signals. The selection criteria are summarised in Table 5.3. All the four muon tracks with good track-fit

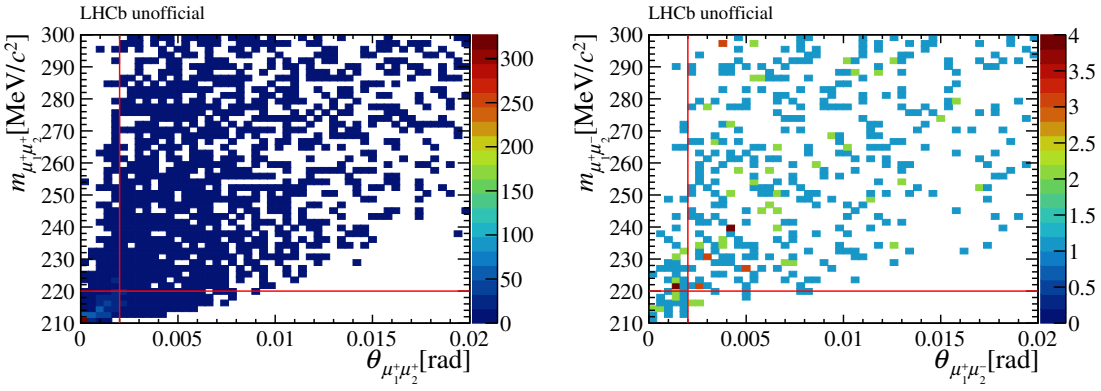

(a) $m(\mu_1^+\mu_2^+)$ and $\theta(\mu_1^+\mu_2^+)$. (b) $m(\mu_1^+\mu_2^-)$ and $\theta(\mu_1^+\mu_2^-)$.

Figure 5.1 Two dimensional distribution of (a) $m(\mu_1^+\mu_2^+)$ and $\theta(\mu_1^+\mu_2^+)$ in data. The red solid lines indicate the selection criteria. Two dimensional distribution of (b) $m(\mu_1^+\mu_2^-)$ and $\theta(\mu_1^+\mu_2^-)$ is also shown as a comparison.

quality are required to have $1.9 < \eta < 4.9$, $p_{\mathrm{T}} > 0.65\,\mathrm{GeV}$ and $p > 3\,\mathrm{GeV}$, and to form two good-quality di-muon vertices. The muon identification requirement is further tightened in the offline selection especially for the muon tracks of $\psi(2S)$ candidates. Similar to Eq. 4.2, the pseudo-proper time t_z of ψ candidate is defined as

$$t_z = \frac{z_\psi - z_{\mathrm{PV}}}{p_z/m_\psi}, \tag{5.4}$$

and both ψ candidates with $-2 < t_z < 10\,\mathrm{ps}$ and t_z uncertainty $\sigma_{t_z} < 0.3\,\mathrm{ps}$ are selected for further analysis. The fiducial kinematic region of this measurement is $0 < p_{\mathrm{T}} < 14\,\mathrm{GeV}$ and $2.0 < y < 4.5$ for both ψ mesons.

In addition, there are a few di-ψ candidates with cloned muon tracks. In this case, the $\mu_2^\pm$ tracks of the ψ_2 candidate is the clone of the $\mu_1^\pm$ tracks of the ψ_1 candidate, and therefore the invariant mass of $\mu_1^\pm\mu_2^\pm$, $m(\mu_1^\pm\mu_2^\pm)$, should be close to two times the mass of muon, and the angle between two tracks, $\theta(\mu_1^\pm\mu_2^\pm)$, should be close to zero. The 2D distribution of $m(\mu_1^+\mu_2^+)$ and $\theta(\mu_1^+\mu_2^+)$ in data, which is zoomed in for a better visualization of clone tracks, is shown in Figure 5.1(a). To reduce the clone tracks, the candidates with $m(\mu_1^\pm\mu_2^\pm) < 220\,\mathrm{MeV}$ or $\theta(\mu_1^\pm\mu_2^\pm) < 0.002\,\mathrm{rad}$ are removed, as indicated by the red lines in Figure 5.1(a). The fraction of the removed signals is studied in the 2D distribution of $m(\mu_1^+\mu_2^-)$ and $\theta(\mu_1^+\mu_2^-)$ as shown in Figure 5.1(b), since almost no clone track contributes to it. The fraction of candidates with $m(\mu_1^\pm\mu_2^\mp) < 220\,\mathrm{MeV}$ or $\theta(\mu_1^\pm\mu_2^\mp) < 0.002\,\mathrm{rad}$ is only 0.1%, which is negligible. Therefore, it is assumed that efficiency of the selection to remove clone tracks is 100%.

It is also possible that ψ_1 and ψ_2 candidates originate from two different PVs, which are called pile up events. A selection in the absolute difference in positions of the two

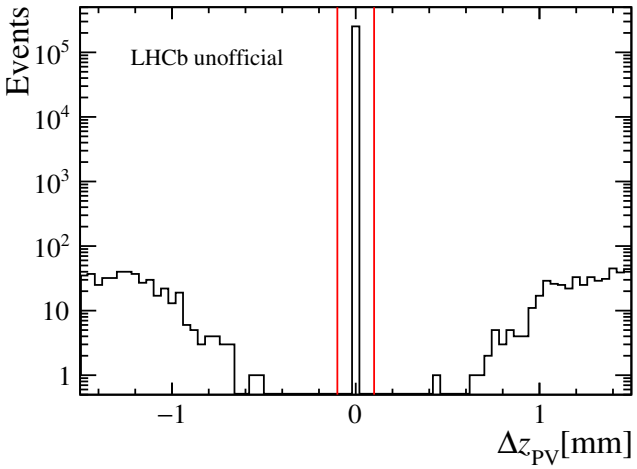

Figure 5.2 Distribution of $\Delta z_{\rm PV}$ in data. The red solid lines indicate the selection criterion.

associated PVs along the beam z-axis $\Delta z_{\rm PV} = z^{\psi_1}_{\rm PV} - z^{\psi_2}_{\rm PV}$ is applied in order to remove pile up events. The distribution of $\Delta z_{\rm PV}$ is shown in Figure 5.2, and the selection $|\Delta z_{\rm PV}| < 0.1$ mm is applied. The efficiency of this selection is assumed to be 100% since the contribution of pile up events is completely separated from the narrow peak around zero in the $\Delta z_{\rm PV}$ distribution as seen in Figure 5.2. However, a small fraction of ψ candidates may be associated to a wrong PV in two cases:

- The true PV is reconstructed, but the ψ candidate is associated to a wrong PV accidentally;
- The true PV is not reconstructed, so the ψ candidate is associated to the nearest reconstructed PV in this event.

For di-ψ signals, there are two corresponding cases:

- The true PV is reconstructed, one of the di-ψ is associated to the true PV, but the other is associated to a wrong PV accidentally;
- The true PV is not reconstructed, so two ψ candidates are both associated to the nearest reconstructed PV.

Other possible cases, if any, are double suppressed by the small probability of wrong PV association. Through the $\Delta z_{\rm PV}$ selection, di-ψ signals in the first case are rejected while those in the second case are kept. The impact of the wrong PV association is considered as a systematic uncertainty, as detailed in Section 5.7.1.

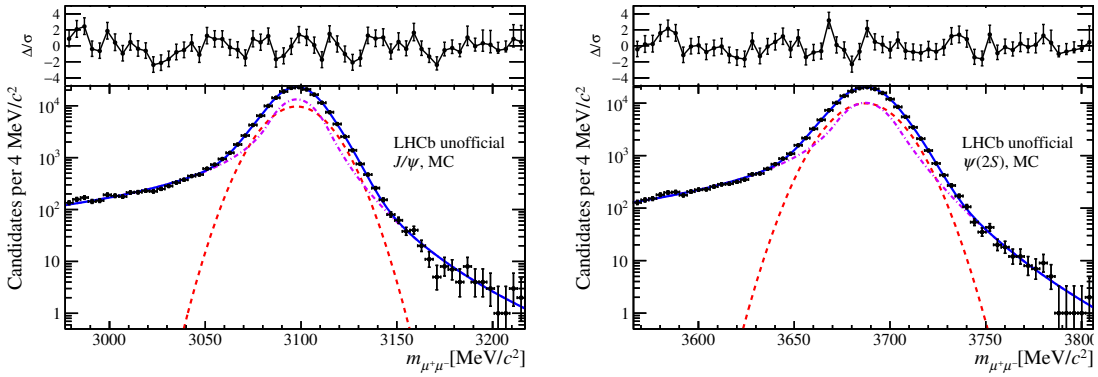

(a) Mass distribution of J/ψ signal. (b) Mass distribution of $\psi(2S)$ signal.

Figure 5.3 Mass distributions of (a) J/ψ and (b) $\psi(2S)$ signals in simulation together with the fit results.

5.4 Signal extraction

5.4.1 Subtraction of combinatorial backgrounds

The di-ψ signals are extracted by performing a 2D unbinned extended maximum likelihood fit to the 2D mass distribution of ψ_1 and ψ_2 candidates. For the one-dimensional mass distribution of ψ_1 and ψ_2 candidates, the signal is described by the sum of a double-sided Crystal Ball (DSCB) function and a Gaussian function with the common mean value (μ) but different widths (σ and σ_G). The DSCB function is defined as[183]

$$F(m;\mu,\sigma,\alpha_l,n_l,\alpha_r,n_r)=\begin{cases}(\frac{n_l}{\alpha_l})^{n_l}e^{-\frac{1}{2}\alpha_l^2}(\frac{n_l}{\alpha_l}-\alpha_l-\frac{m-\mu}{\sigma})^{-n_l}, & \frac{m-\mu}{\sigma}<-\alpha_l;\\ e^{-\frac{1}{2}(\frac{m-\mu}{\sigma})^2}, & -\alpha_l\le\frac{m-\mu}{\sigma}\le\alpha_r;\\ (\frac{n_r}{\alpha_r})^{n_r}e^{-\frac{1}{2}\alpha_r^2}(\frac{n_r}{\alpha_r}-\alpha_r-\frac{m-\mu}{\sigma})^{-n_r}, & \frac{m-\mu}{\sigma}>\alpha_r.\end{cases} \quad (5.5)$$

The mass fit model of the signal is

$$S(m_{\mu^+\mu^-};\mu,\sigma)=\beta\times F(m_{\mu^+\mu^-};\mu,\sigma,\alpha_l,n_l,\alpha_r,n_r)+(1-\beta)\times G(m_{\mu^+\mu^-};\mu,\sigma_G), \quad (5.6)$$

where $G(m_{\mu^+\mu^-};\mu,\sigma_G)$ denotes the Gaussian function, and all the tail parameters $(\alpha_l,n_l,\alpha_r,n_r)$, the fraction β and the ratio σ_G/σ are all fixed from simulation. Only the common mean value μ and one width σ are left as free shape parameters. The fit results for J/ψ and $\psi(2S)$ signals in simulation are shown in Figure 5.3 and Table 5.4. The distribution of combinatorial background is modelled with an exponential function, $B(m_{\mu^+\mu^-};\lambda)$.

The 2D mass distribution of di-J/ψ candidates should be symmetric with respect to $m_{\mu_1^+\mu_1^-}$ and $m_{\mu_2^+\mu_2^-}$ because J/ψ_1 and J/ψ_2 are classified randomly. There are three components:

Table 5.4 Results of mass fit for J/ψ and $\psi(2S)$ signals in simulation.

Parameters	J/ψ result	$\psi(2S)$ result
μ[MeV]	3097.71 ± 0.04	3687.13 ± 0.05
σ[MeV]	10.11 ± 0.15	11.56 ± 0.18
σ_G[MeV]	13.3 ± 0.3	14.4 ± 0.3
β	0.55 ± 0.03	0.49 ± 0.03
α_l	1.45 ± 0.07	1.33 ± 0.07
α_r	1.68 ± 0.13	1.50 ± 0.09
n_l	1.51 ± 0.08	1.63 ± 0.09
n_r	5.7 ± 0.8	8.1 ± 1.5

- di-J/ψ signal, $S(m_{\mu_1^+\mu_1^-};\mu,\sigma)\times S(m_{\mu_2^+\mu_2^-};\mu,\sigma)$;
- one J/ψ signal and one background,
  $S(m_{\mu_1^+\mu_1^-};\mu,\sigma)\times B(m_{\mu_2^+\mu_2^-};\lambda_1)+B(m_{\mu_1^+\mu_1^-};\lambda_1)\times S(m_{\mu_2^+\mu_2^-};\mu,\sigma)$;
- two backgrounds, $B(m_{\mu_1^+\mu_1^-};\lambda_2)\times B(m_{\mu_2^+\mu_2^-};\lambda_2)$.

The 2D fit model of di-J/ψ candidates can be defined as

$$\begin{aligned} f(m_{\mu_1^+\mu_1^-},m_{\mu_2^+\mu_2^-}) =& N_{\rm ss}\times S(m_{\mu_1^+\mu_1^-};\mu,\sigma)\times S(m_{\mu_2^+\mu_2^-};\mu,\sigma)\\ &+N_{\rm bs}\times\frac{1}{2}\big[S(m_{\mu_1^+\mu_1^-};\mu,\sigma)\times B(m_{\mu_2^+\mu_2^-};\lambda_1)\\ &\quad+B(m_{\mu_1^+\mu_1^-};\lambda_1)\times S(m_{\mu_2^+\mu_2^-};\mu,\sigma)\big]\\ &+N_{\rm bb}\times B(m_{\mu_1^+\mu_1^-};\lambda_2)\times B(m_{\mu_2^+\mu_2^-};\lambda_2), \end{aligned} \tag{5.7}$$

where $N_{\rm ss}$, $N_{\rm bs}$ and $N_{\rm bb}$ represent the yields of three components respectively. The 2D mass fit result for di-J/ψ candidates in data is shown in Figure 5.4 and Table 5.5.

For the 2D mass distribution of J/ψ -$\psi(2S)$ candidates, there are four components:

- J/ψ -$\psi(2S)$ signal, $S(m_{\mu_1^+\mu_1^-};\mu_1,\sigma_1)\times S(m_{\mu_2^+\mu_2^-};\mu_2,\sigma_2)$;
- one J/ψ signal and one background, $S(m_{\mu_1^+\mu_1^-};\mu_1,\sigma_1)\times B(m_{\mu_2^+\mu_2^-};\lambda_{P1})$;
- one $\psi(2S)$ signal and one background, $B(m_{\mu_1^+\mu_1^-};\lambda_{J1})\times S(m_{\mu_2^+\mu_2^-};\mu_2,\sigma_2)$;
- two backgrounds, $B(m_{\mu_1^+\mu_1^-};\lambda_{J2})\times B(m_{\mu_2^+\mu_2^-};\lambda_{P2})$.

The 2D fit model of J/ψ -$\psi(2S)$ candidates can be defined as

$$\begin{aligned} f(m_{\mu_1^+\mu_1^-},m_{\mu_2^+\mu_2^-}) =& N_{\rm ss}\times S(m_{\mu_1^+\mu_1^-};\mu_1,\sigma_1)\times S(m_{\mu_2^+\mu_2^-};\mu_2,\sigma_2)\\ &+N_{\rm sb}\times S(m_{\mu_1^+\mu_1^-};\mu_1,\sigma_1)\times B(m_{\mu_2^+\mu_2^-};\lambda_{P1})\\ &+N_{\rm bs}\times B(m_{\mu_1^+\mu_1^-};\lambda_{J1})\times S(m_{\mu_2^+\mu_2^-};\mu_2,\sigma_2)\\ &+N_{\rm bb}\times B(m_{\mu_1^+\mu_1^-};\lambda_{J2})\times B(m_{\mu_2^+\mu_2^-};\lambda_{P2}), \end{aligned} \tag{5.8}$$

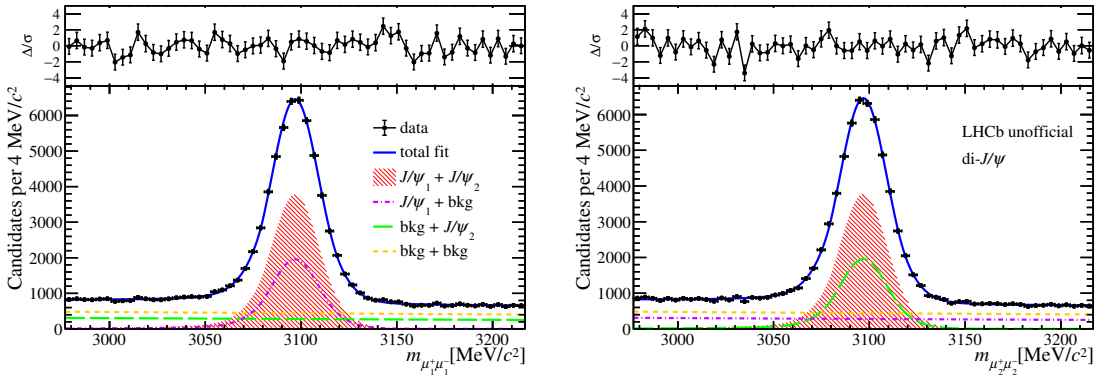

(a) Projection on $m_{\mu_1^+\mu_1^-}$. (b) Projection on $m_{\mu_2^+\mu_2^-}$.

Figure 5.4 Distributions of (a) $m_{\mu_1^+\mu_1^-}$ and (b) $m_{\mu_2^+\mu_2^-}$ for di-J/ψ candidates in data together with the projections of the two-dimensional fit.

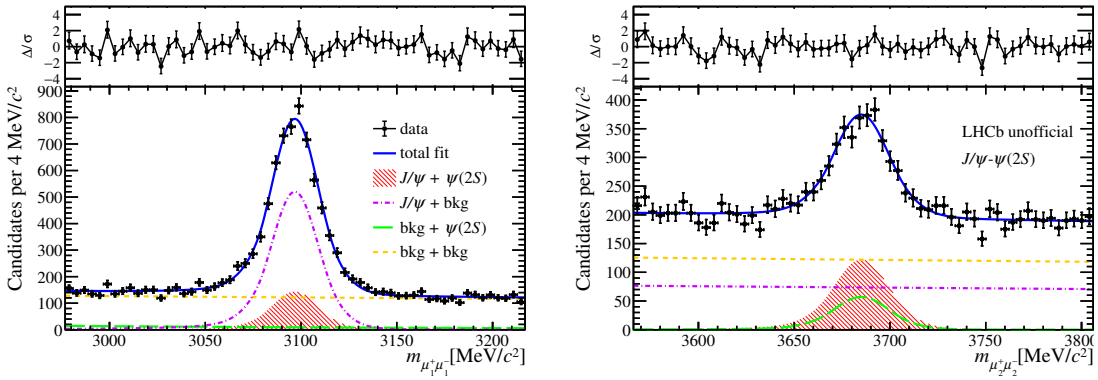

(a) Projection on $m_{\mu_1^+\mu_1^-}$. (b) Projection on $m_{\mu_2^+\mu_2^-}$.

Figure 5.5 Distributions of (a) $m_{\mu_1^+\mu_1^-}$ and (b) $m_{\mu_2^+\mu_2^-}$ for J/ψ-$\psi(2S)$ candidates in data together with the projections of the two-dimensional fit.

where $N_{\rm ss}$, $N_{\rm sb}$, $N_{\rm bs}$ and $N_{\rm bb}$ represent the yields of four components respectively. The 2D mass fit result for J/ψ-$\psi(2S)$ candidates in data is shown in Figure 5.5 and Table 5.6.

5.4.2 Subtraction of non-prompt contributions

The non-prompt contributions with one or two ψ mesons originating from b-hadron decays need to be subtracted in this analysis. It is fulfiled by performing a 2D maximum likelihood fit to the 2D t_z distribution of ψ_1 and ψ_2 signals with backgrounds subtracted. The 2D background-subtracted t_z distribution is extracted by applying the *sWeight*, obtained from *sPlot* method[185] using the $m_{\mu_1^+\mu_1^-}$ and $m_{\mu_2^+\mu_2^-}$ as the discriminating variables, to the data sample.

For the t_z distribution of single-ψ signals, the true t_z values for prompt J/ψ mesons are

Table 5.5 Results of two-dimensional mass fit for di-J/ψ candidates.

Parameters	Di-J/ψ result
N_{ss}	$(3.240 \pm 0.025) \times 10^4$
N_{bs}	$(3.355 \pm 0.031) \times 10^4$
N_{bb}	$(2.652 \pm 0.024) \times 10^4$
μ[MeV]	3096.93 ± 0.06
σ[MeV]	11.24 ± 0.05
$\lambda_1[(\mathrm{MeV})^{-1}]$	$(-8.8 \pm 1.1) \times 10^{-4}$
$\lambda_2[(\mathrm{MeV})^{-1}]$	$(-7.6 \pm 0.8) \times 10^{-4}$

Table 5.6 Results of two dimensional mass fit for J/ψ -$\psi(2S)$ candidates.

Parameters	J/ψ -$\psi(2S)$ result
N_{ss}	$(1.22 \pm 0.08) \times 10^3$
N_{sb}	$(4.42 \pm 0.11) \times 10^3$
N_{bs}	$(0.57 \pm 0.07) \times 10^3$
N_{bb}	$(7.31 \pm 0.13) \times 10^3$
μ_1[MeV]	3096.8 ± 0.3
μ_2[MeV]	3685.0 ± 0.8
σ_1[MeV]	11.1 ± 0.2
σ_2[MeV]	13.2 ± 0.8
$\lambda_{J1}[(\mathrm{MeV})^{-1}]$	$(-3.9 \pm 1.5) \times 10^{-3}$
$\lambda_{J2}[(\mathrm{MeV})^{-1}]$	$(-4.1 \pm 2.0) \times 10^{-4}$
$\lambda_{P1}[(\mathrm{MeV})^{-1}]$	$(-3.3 \pm 2.9) \times 10^{-4}$
$\lambda_{P2}[(\mathrm{MeV})^{-1}]$	$(-2.5 \pm 2.0) \times 10^{-4}$

assumed to follow the Dirac delta function $\delta(t_z)$, while those for non-prompt J/ψ mesons are assumed to follow an exponential function $E(t_z;\tau_b) = \frac{1}{\tau_b} e^{-t_z/\tau_b}$. These distributions are convolved with a resolution function F_{res} to model the detector resolution. For the case that the true PV is not reconstructed and two ψ candidates are both associated to the nearest reconstructed PV, the true PV and the wrongly associated PV are not correlated, which results in a long tail in the t_z distribution. This component can be modelled from data by event mixing, just the same as the method described in Section 4.4.2 in the J/ψ production measurement, and its t_z distribution is described by a histogram $H_{\mathrm{tail}}(t_z)$.

In the 2D t_z distribution of di-J/ψ signals with backgrounds subtracted, there are four

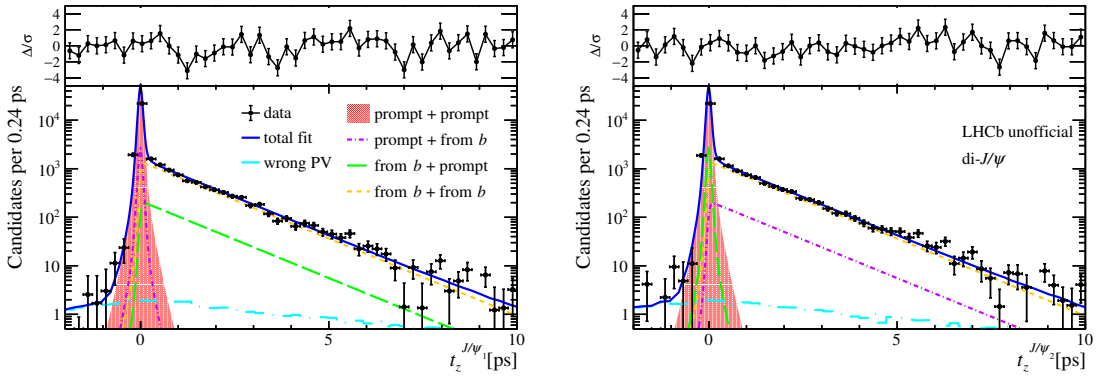

(a) Projection on t_z^{J/ψ_1}. (b) Projection on t_z^{J/ψ_2}.

Figure 5.6 Distributions of (a) t_z^{J/ψ_1} and (b) t_z^{J/ψ_2} for di-J/ψ signals with backgrounds subtracted in data together with the projections of the two-dimensional fit.

components:

- double prompt J/ψ mesons, $\left(\delta(t_z^{J/\psi_1}) \otimes F_{\text{res}}\right) \times \left(\delta(t_z^{J/\psi_2}) \otimes F_{\text{res}}\right)$;
- one prompt and one non-prompt J/ψ mesons, $\left(\delta(t_z^{J/\psi_1}) \otimes F_{\text{res}}\right) \times \left(E(t_z^{J/\psi_2};\tau_b) \otimes F_{\text{res}}\right) + \left(E(t_z^{J/\psi_1};\tau_b) \otimes F_{\text{res}}\right) \times \left(\delta(t_z^{J/\psi_2}) \otimes F_{\text{res}}\right)$;
- double non-prompt J/ψ mesons, $\left(E(t_z^{J/\psi_1};\tau_b) \otimes F_{\text{res}}\right) \times \left(E(t_z^{J/\psi_2};\tau_b) \otimes F_{\text{res}}\right)$;
- wrong PV events, $H_{\text{tail}}(t_z^{J/\psi_1}) \times H_{\text{tail}}(t_z^{J/\psi_2})$.

For di-J/ψ signals, the resolution function is considered as the sum of two Gaussian functions,

$$F_{\text{res}}(t_z; b, S_1, S_2, \beta') = \frac{\beta'}{\sqrt{2\pi}S_1\sigma_{t_z}} e^{-\frac{(t_z-b)^2}{S_1^2\sigma_{t_z}^2}} + \frac{1-\beta'}{\sqrt{2\pi}S_2\sigma_{t_z}} e^{-\frac{(t_z-b)^2}{S_2^2\sigma_{t_z}^2}}, \tag{5.9}$$

where S_1 nad S_2 are two scale factors to correct the imperfect estimation of σ_{t_z}, b is the bias of the t_z measurement, and β' is the proportion of one Gaussian function. The 2D t_z fit model of di-J/ψ signals can be defined as

$$\begin{aligned} f(t_z^{J/\psi_1}, t_z^{J/\psi_2}) =& N_{\text{pp}} \times \left(\delta(t_z^{J/\psi_1}) \otimes F_{\text{res}}\right) \times \left(\delta(t_z^{J/\psi_2}) \otimes F_{\text{res}}\right) \\ &+ N_{\text{np}} \times \frac{1}{2}\Big[\left(\delta(t_z^{J/\psi_1}) \otimes F_{\text{res}}\right) \times \left(E(t_z^{J/\psi_2};\tau_b) \otimes F_{\text{res}}\right) \\ &\qquad + \left(E(t_z^{J/\psi_1};\tau_b) \otimes F_{\text{res}}\right) \times \left(\delta(t_z^{J/\psi_2}) \otimes F_{\text{res}}\right)\Big] \\ &+ N_{\text{nn}} \times \left(E(t_z^{J/\psi_1};\tau_b) \otimes F_{\text{res}}\right) \times \left(E(t_z^{J/\psi_2};\tau_b) \otimes F_{\text{res}}\right) \\ &+ N_{\text{ww}} \times H_{\text{tail}}(t_z^{J/\psi_1}) \times H_{\text{tail}}(t_z^{J/\psi_2}), \end{aligned} \tag{5.10}$$

where N_{pp}, N_{np}, N_{nn} and N_{ww} represent the yields of four components respectively. The 2D t_z fit result for di-J/ψ signals in data is shown in Figure 5.6 and Table 5.7.

In the 2D t_z distribution of J/ψ-$\psi(2S)$ signals with backgrounds subtracted, there are

Table 5.7 Results of two-dimensional t_z fit for di-J/ψ signals.

Parameters	Di-J/ψ result
$N_{\rm pp}$	$(2.187 \pm 0.020) \times 10^4$
$N_{\rm np}$	$(0.246 \pm 0.009) \times 10^4$
$N_{\rm nn}$	$(0.802 \pm 0.012) \times 10^4$
$N_{\rm ww}$	$(0.005 \pm 0.003) \times 10^4$
b[ps]	$(-4.4 \pm 0.3) \times 10^{-3}$
S_1	1.012 ± 0.009
S_2	3.4 ± 0.4
β'	0.969 ± 0.007
τ_b[ps]	1.368 ± 0.013

five components:

- prompt J/ψ and $\psi(2S)$ mesons, $\left(\delta(t_z^{J/\psi}) \otimes F_{\rm res}\right) \times \left(\delta(t_z^{\psi(2S)}) \otimes F_{\rm res}\right)$;
- prompt J/ψ and non-prompt $\psi(2S)$ mesons, $\left(\delta(t_z^{J/\psi}) \otimes F_{\rm res}\right) \times \left(E(t_z^{\psi(2S)}; \tau_b) \otimes F_{\rm res}\right)$;
- non-prompt J/ψ and prompt $\psi(2S)$ mesons, $\left(E(t_z^{J/\psi}; \tau_b) \otimes F_{\rm res}\right) \times \left(\delta(t_z^{\psi(2S)}) \otimes F_{\rm res}\right)$;
- non-prompt J/ψ and $\psi(2S)$ mesons, $\left(E(t_z^{J/\psi}; \tau_b) \otimes F_{\rm res}\right) \times \left(E(t_z^{\psi(2S)}; \tau_b) \otimes F_{\rm res}\right)$;
- wrong PV events, $H_{\rm tail}(t_z^{J/\psi}) \times H_{\rm tail}(t_z^{\psi(2S)})$.

Due to the low statistics for J/ψ-$\psi(2S)$ signals, τ_b is fixed to the value of the di-J/ψ fit result, 1.368 ps, and the resolution function is considered as one Gaussian function both for J/ψ and $\psi(2S)$ signals,

$$F_{\rm res}(t_z; b, S) = \frac{1}{\sqrt{2\pi} S \sigma_{t_z}} e^{-\frac{(t_z - b)^2}{S^2 \sigma_{t_z}^2}}. \tag{5.11}$$

For the wrong PV events, the same shape obtained from event mixing in the di-J/ψ data sample is also used for J/ψ-$\psi(2S)$ signals. The 2D t_z fit model of J/ψ-$\psi(2S)$ signals can be defined as

$$\begin{aligned} f(t_z^{J/\psi}, t_z^{\psi(2S)}) =& N_{\rm pp} \times \left(\delta(t_z^{J/\psi}) \otimes F_{\rm res}\right) \times \left(\delta(t_z^{\psi(2S)}) \otimes F_{\rm res}\right) \\ &+ N_{\rm pn} \times \left(\delta(t_z^{J/\psi}) \otimes F_{\rm res}\right) \times \left(E(t_z^{\psi(2S)}) \otimes F_{\rm res}\right) \\ &+ N_{\rm np} \times \left(E(t_z^{J/\psi}) \otimes F_{\rm res}\right) \times \left(\delta(t_z^{\psi(2S)}) \otimes F_{\rm res}\right) \\ &+ N_{\rm nn} \times \left(E(t_z^{J/\psi}) \otimes F_{\rm res}\right) \times \left(E(t_z^{\psi(2S)}) \otimes F_{\rm res}\right) \\ &+ N_{\rm ww} \times H_{\rm tail}(t_z^{J/\psi}) \times H_{\rm tail}(t_z^{\psi(2S)}), \end{aligned} \tag{5.12}$$

where $N_{\rm pp}$, $N_{\rm pn}$, $N_{\rm np}$, $N_{\rm nn}$ and $N_{\rm ww}$ represent the yields of four components respectively. The 2D t_z fit result for J/ψ-$\psi(2S)$ signals in data is shown in Figure 5.7 and Table 5.8.

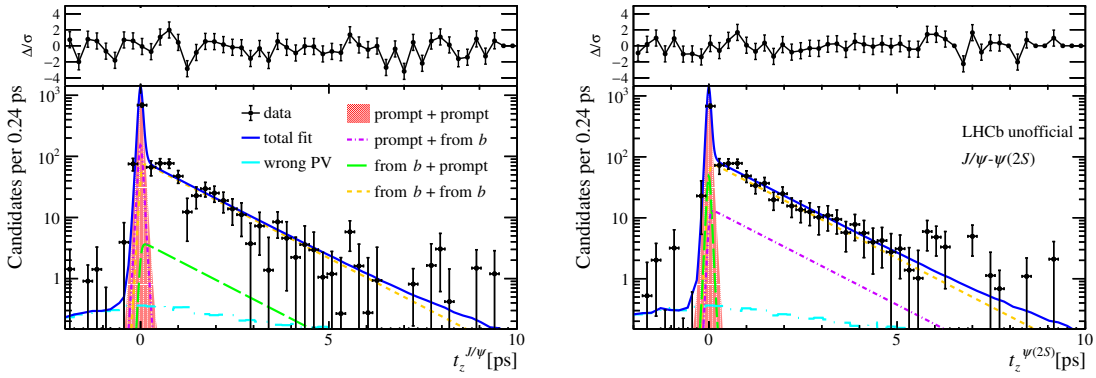

(a) Projection on $t_z^{J/\psi}$.

(b) Projection on $t_z^{\psi(2S)}$.

Figure 5.7 Distributions of (a) $t_z^{J/\psi}$ and (b) $t_z^{\psi(2S)}$ for J/ψ-$\psi(2S)$ signals with backgrounds subtracted in data together with the projections of the two-dimensional fit.

Table 5.8 Results of two-dimensional t_z fit for J/ψ-$\psi(2S)$ signals.

Parameters	J/ψ-$\psi(2S)$ result
$N_{\rm pp}$	629 ± 50
$N_{\rm pn}$	82 ± 24
$N_{\rm np}$	23 ± 14
$N_{\rm nn}$	476 ± 39
$N_{\rm ww}$	10 ± 18
b[ps]	$(-1.1 \pm 2.5) \times 10^{-3}$
S	1.16 ± 0.05

After subtracting non-prompt contributions, the yield of double prompt J/ψ signals is $(2.187 \pm 0.020) \times 10^4$, and the yield of double prompt J/ψ-$\psi(2S)$ signals is 629 ± 50.

5.4.3 Check the yield bias

A check of the yield bias similar to the description in Section 4.4.3 in the J/ψ production measurement is also performed in this analysis due to the presence of the event-dependent variable σ_{t_z} in the 2D t_z fit[184]. For the fit of di-ψ signals, 5000 pseudo-experiments are performed based on the 2D fit model and the σ_{t_z} distributions obtained from simulation, data sidebands and event mixing for different components separately. In each pseudo-experiment, the $t_z^{\psi_1}$, $t_z^{\psi_2}$, $\sigma_{t_z}^{\psi_1}$ and $\sigma_{t_z}^{\psi_2}$ of all the components are generated independently, and the yields are assumed as Poisson random numbers with expected values from the 2D fit result. Then, the same 2D t_z fit is performed to the generated distributions and the distributions of the yield $N_{\rm pp}^{\rm pseudo}$ are obtained from 5000 pseudo-experiments, as

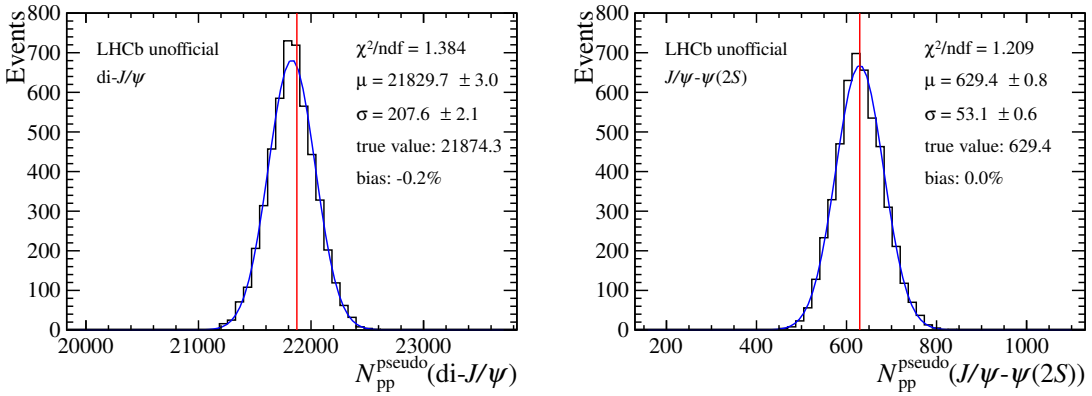

(a) Distribution of N_{pp}^{pseudo}(di-J/ψ). (b) Distribution of N_{pp}^{pseudo}(J/ψ -$\psi(2S)$).

Figure 5.8 Distributions of N_{pp}^{pseudo} of (a) di-J/ψ and (b) J/ψ -$\psi(2S)$ signals obtained from pseudo-experiments together with the Gaussian fits. The red lines denote the true expected values from the 2D t_z fit result.

shown in Figure 5.8 together with the Gaussian fits. A small bias for the fit of di-J/ψ signals, -0.2%, is seen but it is much less than the statistical uncertainty, and no obvious bias for the fit of J/ψ -$\psi(2S)$ signals can be seen in the figure due to the large statistical uncertainty. Therefore, the bias of the 2D t_z fit of di-J/ψ and J/ψ -$\psi(2S)$ signals is negligible.

5.5 Efficiency correction

Since the kinematics of di-ψ signals are not known a priori, the efficiency correction is performed event-by-event as

$$N^{\text{corr}} = \sum_i \frac{w_i}{\varepsilon_{\text{tot}i}}, \tag{5.13}$$

where the index i denotes each event in data, and w_i is the *sWeight* corresponding to the component of double prompt signals, and $\varepsilon_{\text{tot}i}$ is the detection efficiency of each event. The *sWeight* w_i is obtained from the *sPlot* method[185] on top of the weighted distribution with backgrounds subtracted using the $t_z^{\psi_1}$ and $t_z^{\psi_2}$ as the discriminating variables. The detection efficiency of each event $\varepsilon_{\text{tot}i}$ is factorised into the product of five efficiencies: the geometrical acceptance $\varepsilon_{\text{acc}i}$, the reconstruction-and-selection efficiency $\varepsilon_{\text{rec\&sel}i}$, the PID efficiency $\varepsilon_{\text{PID}i}$, the trigger efficiency $\varepsilon_{\text{tri}i}$ and an efficiency of global event cut (GEC) ε_{GEC}, as

$$\varepsilon_{\text{tot}i} = \varepsilon_{\text{acc}i} \times \varepsilon_{\text{rec\&sel}i} \times \varepsilon_{\text{PID}i} \times \varepsilon_{\text{tri}i} \times \varepsilon_{\text{GEC}}. \tag{5.14}$$

The $\varepsilon_{\rm GEC}$ is the efficiency of the global event cut, nSPDHits < 900, in the hardware trigger. It is common to all events and is described in Section 5.5.3. The rest efficiencies $\varepsilon_{{\rm acc}i}$, $\varepsilon_{{\rm rec\&sel}i}$, $\varepsilon_{{\rm PID}i}$ and $\varepsilon_{{\rm tri}i}$ rely purely on the $p_{\rm T}$ and y of both ψ mesons in each event. As long as the true $p_{\rm T}$ and y values of both ψ mesons are taken, it makes no difference whether the candidate is produced via SPS or DPS process, since the possible kinematic correlation between two ψ mesons is totally encoded in the $p_{\rm T}$ and y. On this basis, the efficiencies of each di-ψ candidate can be factorised into those of the two ψ mesons, since no information related to the correlation between them is used during the whole reconstruction and selection process. The efficiencies $\varepsilon_{{\rm acc}i}$, $\varepsilon_{{\rm rec\&sel}i}$ and $\varepsilon_{{\rm PID}i}$ of each di-ψ candidate can be factorised as the product of efficiencies of ψ_1 and ψ_2 mesons,

$$\varepsilon_i^{\text{di-}\psi} = \varepsilon^{\psi_1}(p_{{\rm T}\,i}^{\psi_1}, y_i^{\psi_1}) \times \varepsilon^{\psi_2}(p_{{\rm T}\,i}^{\psi_2}, y_i^{\psi_2}). \tag{5.15}$$

Taking advantage of the efficiency factorisation, the efficiencies $\varepsilon_{\rm acc}$ and $\varepsilon_{\rm rec\&sel}$ are estimated in $(p_{\rm T}, y)$ intervals of each ψ meson using the simulated single-ψ samples, as detailed in Section 5.5.1 and 5.5.2. The PID efficiency $\varepsilon_{\rm PID}$ is further factorised into the product of single-muon identification efficiency evaluated by the PIDCalib package[187], as described in Section 5.5.4. The trigger efficiency $\varepsilon_{{\rm tri}i}$ of each di-ψ candidate can be factorised as

$$\varepsilon_{{\rm tri}\,i}^{\text{di-}\psi} = \left[1 - \left(1 - \varepsilon_{\rm L0\&HLT1}^{\psi_1}(p_{{\rm T}\,i}^{\psi_1}, y_i^{\psi_1})\right)\left(1 - \varepsilon_{\rm L0\&HLT1}^{\psi_2}(p_{{\rm T}\,i}^{\psi_2}, y_i^{\psi_2})\right)\right] \varepsilon_{{\rm HLT2}i}^{\text{di-}\psi}, \tag{5.16}$$

where $\varepsilon_{\rm L0\&HLT1}$ is the L0-and-HLT1 trigger efficiency, and $\varepsilon_{\rm HLT2}$ is the HLT2 trigger efficiency. It is discussed in Section 5.5.5 in detail.

5.5.1 Geometrical acceptance

The geometrical acceptance of each di-ψ candidate can be factorised as

$$\varepsilon_{{\rm acc}\,i}^{\text{di-}\psi} = \varepsilon_{\rm acc}^{\psi_1}(p_{{\rm T}\,i}^{\psi_1}, y_i^{\psi_1}) \times \varepsilon_{\rm acc}^{\psi_2}(p_{{\rm T}\,i}^{\psi_2}, y_i^{\psi_2}). \tag{5.17}$$

The geometrical acceptance of ψ mesons $\varepsilon_{\rm acc}^{\psi}$ in each $(p_{\rm T},y)$ interval is defined as the yield fraction of ψ mesons with both muons inside the LHCb acceptance in those generated in pp collisions,

$$\varepsilon_{\rm acc}^{\psi} = \frac{N(\psi \text{ generated with di-muon in LHCb acceptance})}{N(\psi \text{ generated in } pp \text{ collisions})}. \tag{5.18}$$

For the di-muon inside the LHCb acceptance, it is required that the polar angles of the muon momentum directions with respect to the direction of beam z-axis are within $(10, 400)$ mrad. The acceptance of ψ mesons is determined using the simulated sample at

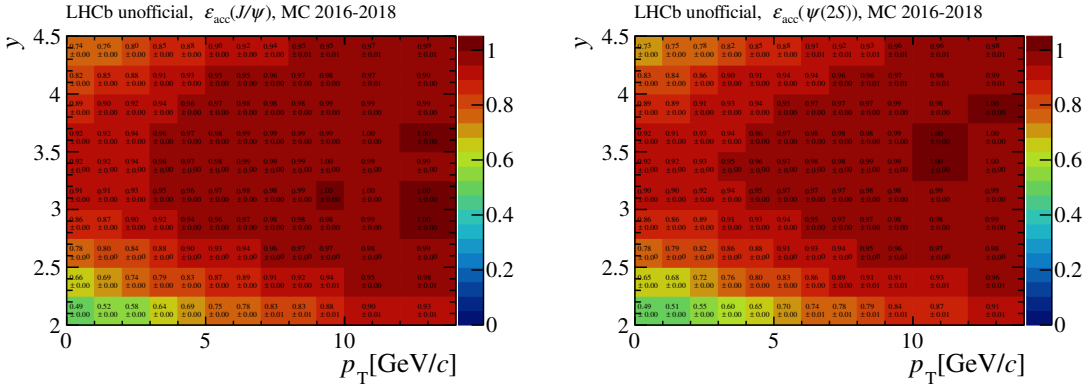

(a) $\varepsilon_{\text{acc}}^{J/\psi}$ for 2016–2018. (b) $\varepsilon_{\text{acc}}^{\psi(2S)}$ for 2016–2018.

Figure 5.9 Acceptances of (a) J/ψ and (b) $\psi(2S)$ mesons in (p_{T},y) intervals for 2016–2018.

the generator level with events of different magnet polarities, MagDown and MagUp, and different years, 2016–2018, combined. The acceptances $\varepsilon_{\text{acc}}^{J/\psi}$ and $\varepsilon_{\text{acc}}^{\psi(2S)}$ in (p_{T},y) intervals are shown in Figure 5.9.

5.5.2 Reconstruction-and-selection efficiency

The selections applied to the di-ψ candidates rather than to ψ_1 and ψ_2 candidates separately are $m(\mu_1^{\pm}\mu_2^{\pm}) > 220\,\text{MeV}$, $\theta(\mu_1^{\pm}\mu_2^{\pm}) > 0.002\,\text{rad}$ and $|\Delta z_{\text{PV}}| < 0.1\,\text{mm}$. The efficiency of these selections is assumed to be 100%, as discussed in Section 5.3. For each event, all the other offline selections are applied to the two reconstructed ψ candidates separately, thus the reconstruction-and-selection efficiency $\varepsilon_{\text{rec\&sel}}$ of each di-ψ candidate can be factorised as

$$\varepsilon_{\text{rec\&sel}\,i}^{\text{di-}\psi} = \varepsilon_{\text{rec\&sel}}^{\psi_1}(p_{\text{T}\,i}^{\psi_1}, y_i^{\psi_1}) \times \varepsilon_{\text{rec\&sel}}^{\psi_2}(p_{\text{T}\,i}^{\psi_2}, y_i^{\psi_2}). \tag{5.19}$$

The reconstruction-and-selection efficiency $\varepsilon_{\text{rec\&sel}}$ of ψ mesons in each (p_{T},y) interval is defined as the yield fraction of J/ψ mesons reconstructed and selected without PID and trigger requirements in those with both muons inside the LHCb acceptance,

$$\varepsilon_{\text{rec\&sel}}^{\psi} = \frac{N(\psi \text{ reconstructed and selected w/o PID and trigger})}{N(\psi \text{ generated with both muons in LHCb acceptance})}. \tag{5.20}$$

The reconstruction-and-selection efficiency $\varepsilon_{\text{rec\&sel}}$ of ψ mesons is determined using the full-simulation sample with events of different magnet polarities combined separately for different years.

The distributions of nSPDHits, which describes the multiplicity of the event, are different between di-ψ data and single-ψ simulation, as shown in Figure 5.10. The distributions in data are obtained by the *sPlot* method[185]. In order to correct the effect of

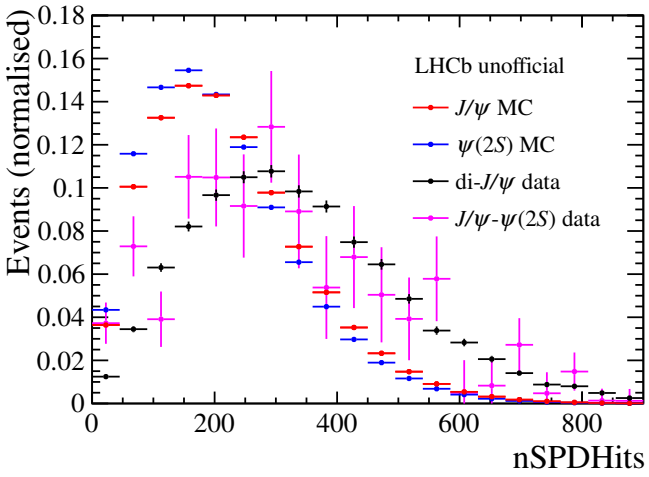

Figure 5.10 Comparisons of nSPDHits distributions between di-ψ data and single-ψ simulation.

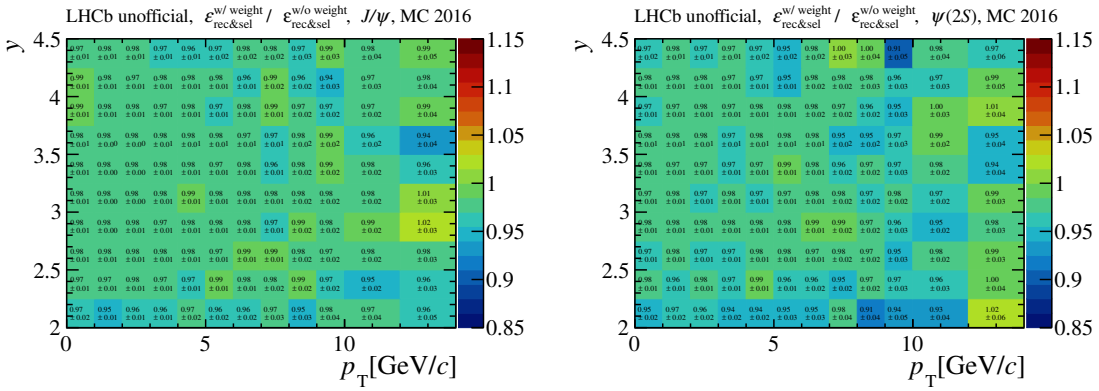

(a) Ratio for J/ψ mesons.

(b) Ratio for $\psi(2S)$ mesons.

Figure 5.11 Ratios of $\varepsilon_{\text{rec\&sel}}$ of (a) J/ψ and (b) $\psi(2S)$ mesons between with and without nSPDHits weight applied for 2016 simulation.

the detector occupancy, the distribution of nSPDHits in simulation is weighted to match that in data when determining the $\varepsilon_{\text{rec\&sel}}$ of ψ mesons. Since there are large statistical fluctuations in the nSPDHits distribution for J/ψ-$\psi(2S)$ data, it is assumed that the nSPDHits distribution of J/ψ-$\psi(2S)$ candidates is very close to that of di-J/ψ candidates and both distributions in J/ψ and $\psi(2S)$ simulation are weighted to match that in di-J/ψ data. The $\varepsilon_{\text{rec\&sel}}$ ratios between with and without nSPDHits weight applied are shown in Figure 5.11 for 2016 simulation. The comparison results for other years are similar to Figure 5.11. The efficiency $\varepsilon_{\text{rec\&sel}}$ of J/ψ ($\psi(2S)$) mesons decreases by about 2.3% (2.9%) after applying the nSPDHits weight.

It is also found out that the efficiency of track reconstruction in simulation should be corrected by that in data. The efficiency correction factors are obtained separately for each year from dedicated data and simulation samples of $J/\psi \to \mu^+\mu^-$ decay in which

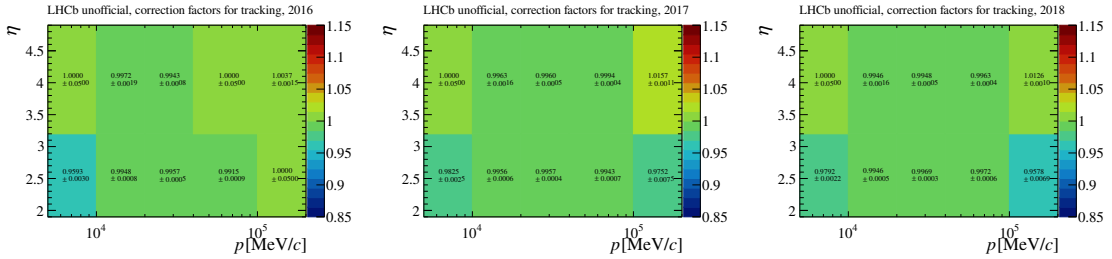

(a) Factors for 2016. (b) Factors for 2017. (c) Factors for 2018.

Figure 5.12 Correction factors of tracking efficiency in intervals of muon kinematics for (a) 2016, (b) 2017 and (c) 2018 simulation.

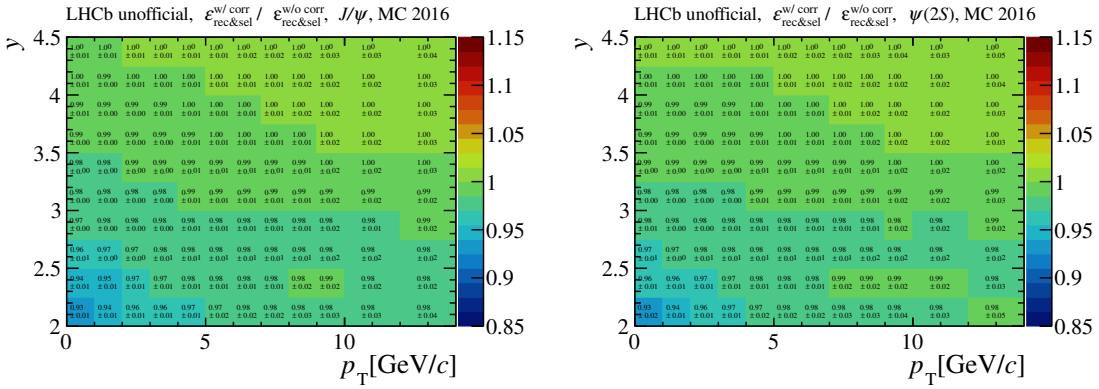

(a) Ratio for J/ψ mesons. (b) Ratio for $\psi(2S)$ mesons.

Figure 5.13 Ratios of $\varepsilon_{\text{rec\&sel}}$ of (a) J/ψ and (b) $\psi(2S)$ mesons between with and without tracking correction for 2016 simulation.

one muon track is fully reconstructed and the other track is reconstructed using a subset of tracking systems as a probe track[186]. The tracking efficiencies in these data and simulation samples are evaluated as the probability that the probe track can be fully reconstructed. The ratios of tracking efficiencies between data and simulation are considered as the factors to correct the tracking efficiency, which are shown in Figure 5.12 in intervals of muon kinematics. These correction factors cover the muon kinematic range $0.5 < p < 200\,\text{GeV}$ and $1.9 < \eta < 4.9$. For muon tracks outside this kinematic range, the correction factor is assigned to be 1.00 ± 0.05 as a conservative estimation. The $\varepsilon_{\text{rec\&sel}}$ ratios of J/ψ and $\psi(2S)$ mesons between with and without tracking correction are shown in Figure 5.13 for 2016 simulation as an example.

With these corrections taken into account, the reconstruction-and-selection efficiencies $\varepsilon^{J/\psi}_{\text{rec\&sel}}$ and $\varepsilon^{\psi(2S)}_{\text{rec\&sel}}$ are respectively shown in Figures 5.14 and 5.15, separately for different years.

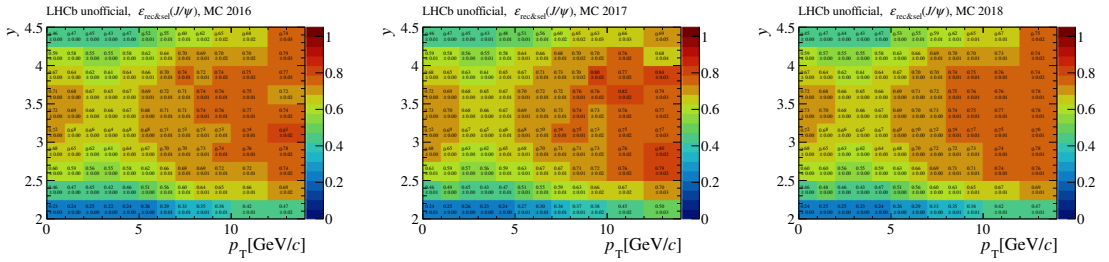

(a) $\varepsilon^{J/\psi}_{\text{rec\&sel}}$ for 2016. (b) $\varepsilon^{J/\psi}_{\text{rec\&sel}}$ for 2017. (c) $\varepsilon^{J/\psi}_{\text{rec\&sel}}$ for 2018.

Figure 5.14 Reconstruction-and-selection efficiencies of J/ψ mesons in (p_{T},y) intervals for (a) 2016, (b) 2017 and (c) 2018.

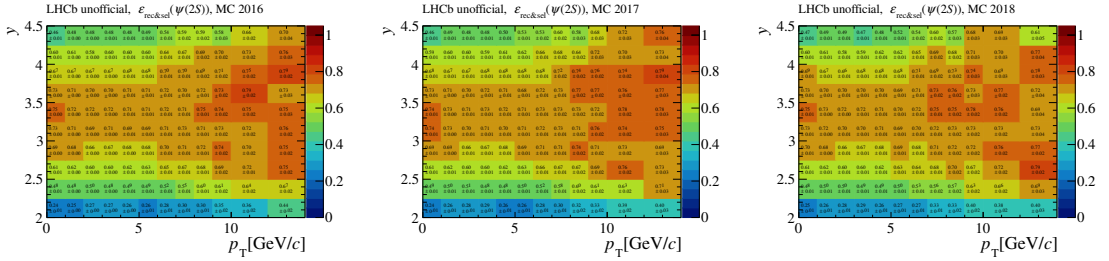

(a) $\varepsilon^{\psi(2S)}_{\text{rec\&sel}}$ for 2016. (b) $\varepsilon^{\psi(2S)}_{\text{rec\&sel}}$ for 2017. (c) $\varepsilon^{\psi(2S)}_{\text{rec\&sel}}$ for 2018.

Figure 5.15 Reconstruction-and-selection efficiencies of $\psi(2S)$ mesons in (p_{T},y) intervals for (a) 2016, (b) 2017 and (c) 2018.

5.5.3 Global-event-cut efficiency

In the L0DiMuon line, a global event cut nSPDHits < 900 is applied. Since the nSPDHits distributions are different in data and simulation, as shown in Figure 5.10, the global-event-cut efficiency ε_{GEC} is estimated by extrapolating the nSPDHits distribution in the di-ψ data sample with combinatorial backgrounds and non-prompt contributions subtracted using the *sPlot* method[185]. The nSPDHits distribution is described by one Γ function and the fit results for di-J/ψ and J/ψ -$\psi(2S)$ signals are shown in Figure 5.16. The ε_{GEC} for di-J/ψ signals is determined to be $99.35 \pm 0.07\%$. The uncertainty is obtained by varying the parameters of the fit function within their uncertainties with correlations considered. For J/ψ -$\psi(2S)$ signals, the ε_{GEC} is 99.33%, obtained from the fit result with very large statistical fluctuation, and the value is consistent with the ε_{GEC} for di-J/ψ. Therefore, it is assumed that ε_{GEC} is $99.35 \pm 0.07\%$ both for di-J/ψ and J/ψ -$\psi(2S)$ signals.

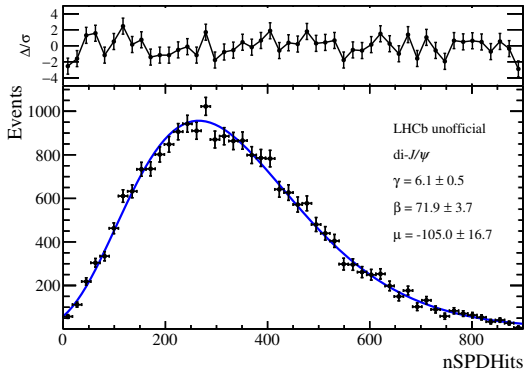

(a) Fit for di-J/ψ signals.

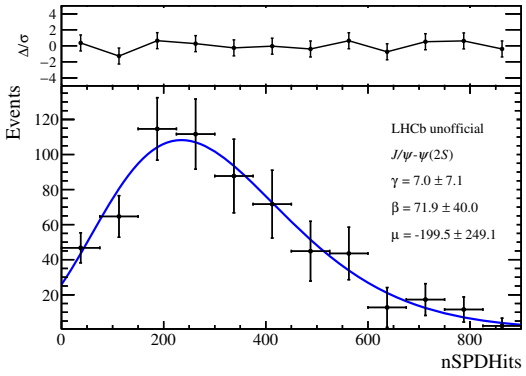

(b) Fit for J/ψ -$\psi(2S)$ signals.

Figure 5.16 Fits to the nSPDHits distributions of (a) di-J/ψ and (b) J/ψ -$\psi(2S)$ signals with a Γ function.

5.5.4 PID efficiency

The PID efficiency ε_{PID} of each di-ψ candidate can be factorised as

$$\begin{aligned}\varepsilon^{\text{di-}\psi}_{\text{PID}\,i} &= \varepsilon^{\psi_1}_{\text{PID}\,i} \times \varepsilon^{\psi_2}_{\text{PID}\,i} \\ &= \varepsilon^{\mu}_{\text{PID}}(p_i^{\mu_1^+}, \eta_i^{\mu_1^+}) \times \varepsilon^{\mu}_{\text{PID}}(p_i^{\mu_1^-}, \eta_i^{\mu_1^-}) \times \varepsilon^{\mu}_{\text{PID}}(p_i^{\mu_2^+}, \eta_i^{\mu_2^+}) \times \varepsilon^{\mu}_{\text{PID}}(p_i^{\mu_2^-}, \eta_i^{\mu_2^-}).\end{aligned} \tag{5.21}$$

The single-muon PID efficiency $\varepsilon^{\mu}_{\text{PID}}$ is evaluated by the PIDCalib package[187] using a dedicated data sample of $J/\psi \to \mu^+\mu^-$ candidates. The single-muon PID efficiency $\varepsilon^{\mu}_{\text{PID}}$ is determined as a function of (p^{μ}, η^{μ}, nSPDHits), separately for different magnet polarities and years. For the two muon tracks of J/ψ candidates, the PID requirement is IsMuon and DLL$\mu > 0$ and ProbNN$\mu > 0.4$, while for the two muon tracks of $\psi(2S)$ candidates, it is much stricter, IsMuon and DLL$\mu > 0$ and ProbNN$\mu > 0.9$. For example, the muon PID efficiencies $\varepsilon_{\text{PID}}(\mu)$ in the data set of 2016 MagDown are shown in Figure 5.17 for muon tracks of J/ψ candidates and in Figure 5.18 for muon tracks of $\psi(2S)$ candidates.

5.5.5 Trigger efficiency

The trigger efficiency ε_{tri} of each di-ψ candidate can be factorised as the product of the HLT2 trigger efficiency and the L0-and-HLT1 trigger efficiency as

$$\varepsilon^{\text{di-}\psi}_{\text{tri}\,i} = \varepsilon^{\text{di-}\psi}_{\text{HLT2}\,i} \times \varepsilon^{\text{di-}\psi}_{\text{L0\&HLT1}\,i}. \tag{5.22}$$

The online HLT2 reconstruction algorithm is the same as the offline algorithm and the offline selections are much tighter than the HLT2 requirements, so the HLT2 trigger efficiency $\varepsilon^{\text{di-}\psi}_{\text{HLT2}}$ should be 100%. Therefore, the trigger efficiency ε_{tri} of each di-ψ candidate

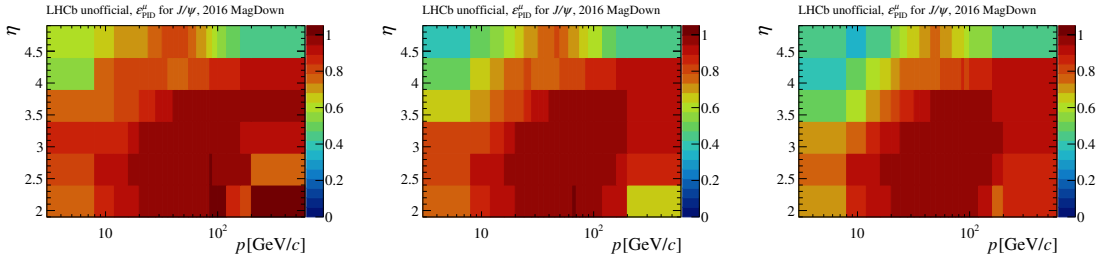

(a) 0 < nSPDHits < 200. (b) 200 < nSPDHits < 400. (c) 400 < nSPDHits < 900.

Figure 5.17 Single-muon PID efficiencies $\varepsilon^{\mu}_{\rm PID}$ for muon tracks of J/ψ candidates (IsMuon and DLL$\mu > 0$ and ProbNN$\mu > 0.4$) as functions of (p^{μ}, η^{μ}) in three intervals of nSPDHits for 2016 MagDown.

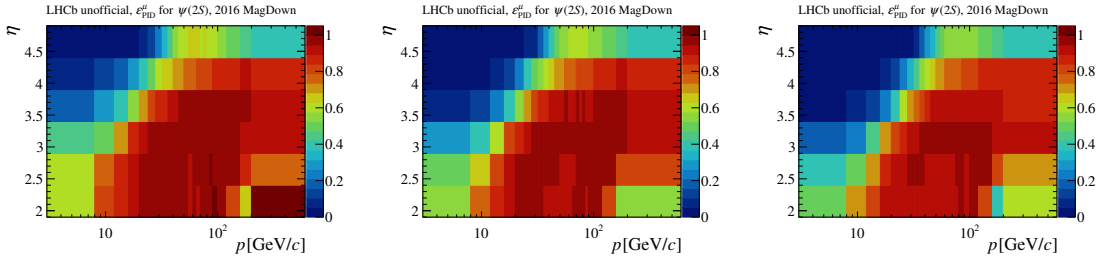

(a) 0 < nSPDHits < 200. (b) 200 < nSPDHits < 400. (c) 400 < nSPDHits < 900.

Figure 5.18 Single-muon PID efficiencies $\varepsilon^{\mu}_{\rm PID}$ for muon tracks of $\psi(2S)$ candidates (IsMuon and DLL$\mu > 0$ and ProbNN$\mu > 0.9$) as functions of (p^{μ}, η^{μ}) in three intervals of nSPDHits for 2016 MagDown.

equals to the L0-and-HLT1 trigger efficiency, and can be factorised as

$$\varepsilon^{\text{di-}\psi}_{\text{tri}\,i} = 1 - \left(1 - \varepsilon^{\psi_1}_{\text{L0\&HLT1}}(p^{\psi_1}_{\text{T}\,i}, y^{\psi_1}_{i})\right) \times \left(1 - \varepsilon^{\psi_2}_{\text{L0\&HLT1}}(p^{\psi_2}_{\text{T}\,i}, y^{\psi_2}_{i})\right), \tag{5.23}$$

since at least one $\mu^+\mu^-$ pair is required to fulfils the selection criteria of both L0 and HLT1 lines. The L0-and-HLT1 trigger efficiency $\varepsilon_{\text{L0\&HLT1}}$ of ψ mesons in each (p_{T},y) interval is defined as the yield fraction of ψ mesons reconstructed and selected with PID and trigger requirements in those with PID but without trigger requirements,

$$\varepsilon^{\psi}_{\text{L0\&HLT1}} = \frac{N(\psi \text{ reconstructed and selected w/ PID and trigger})}{N(\psi \text{ reconstructed and selected w/ PID w/o trigger})}. \tag{5.24}$$

The L0-and-HLT1 trigger efficiency $\varepsilon_{\text{L0\&HLT1}}$ of ψ mesons is determined using the full-simulated sub-samples, MC16p1, MC16p2, MC17p1 and MC18 corresponding to different settings of selection criteria in the L0 and HLT1 lines respectively. The nSPDHits weight is also applied in the determination of the $\varepsilon^{\psi}_{\text{L0\&HLT1}}$, and the trigger efficiency of J/ψ ($\psi(2S)$) increases by about 1.2% (1.5%) after applying the weight. The L0-and-HLT1 trigger efficiencies $\varepsilon^{J/\psi}_{\text{L0\&HLT1}}$ and $\varepsilon^{\psi(2S)}_{\text{L0\&HLT1}}$ are respectively shown in Figures 5.19 and 5.20, separately for four different sub-samples.

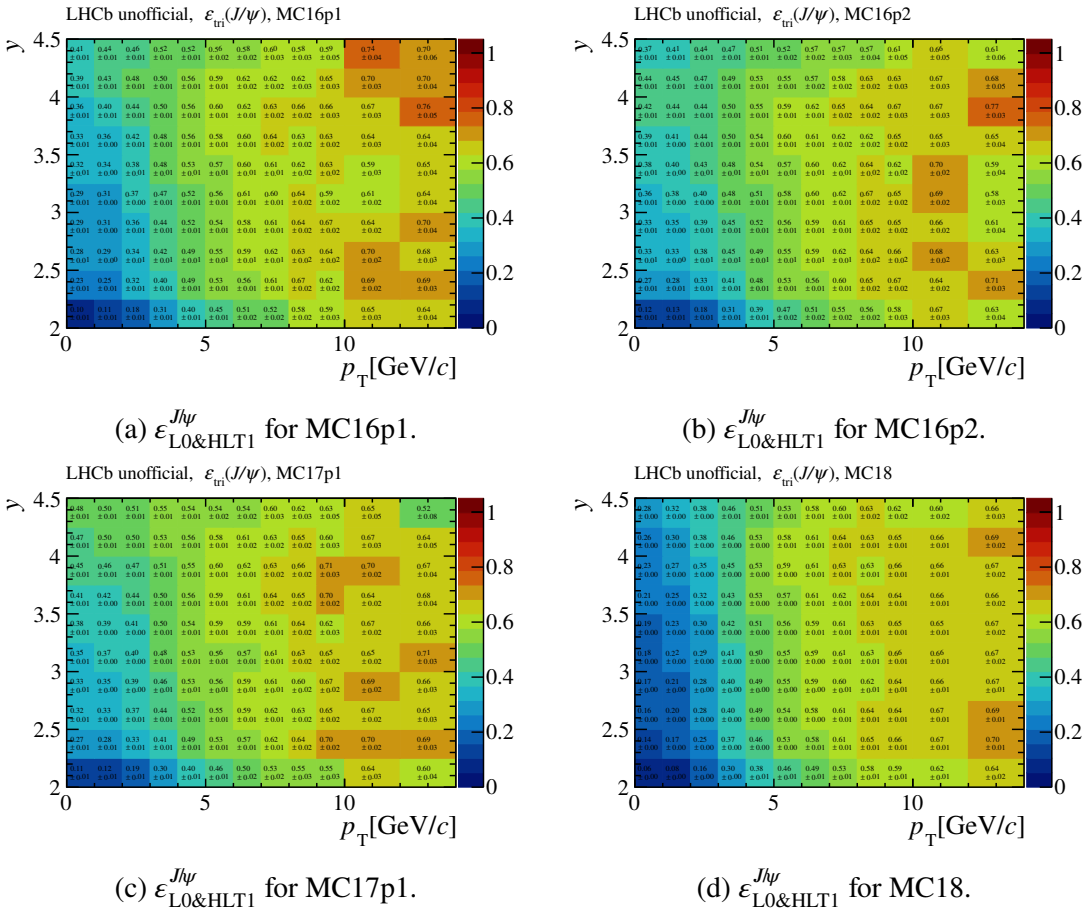

(a) $\varepsilon^{J/\psi}_{\rm L0\&HLT1}$ for MC16p1. (b) $\varepsilon^{J/\psi}_{\rm L0\&HLT1}$ for MC16p2.

(c) $\varepsilon^{J/\psi}_{\rm L0\&HLT1}$ for MC17p1. (d) $\varepsilon^{J/\psi}_{\rm L0\&HLT1}$ for MC18.

Figure 5.19 L0-and-HLT1 trigger efficiencies of J/ψ mesons in ($p_{\rm T}$,y) intervals for (a) MC16p1, (b) MC16p2, (c) MC17p1 and (d) MC18.

5.5.6 Efficiency correction as a function of ϕ

It is found out that the efficiencies $\varepsilon^{\psi}_{\rm rec\&sel}$, $\varepsilon^{\psi}_{\rm L0\&HLT1}$ and $\varepsilon^{\mu}_{\rm PID}$ slightly depend on the azimuthal angle ϕ of ψ candidate or muon track, which is the angle of the momentum direction projecting onto the x-y plane with respect to the x-axis in the laboratory frame. In this analysis, production cross-sections are studied as a function of ϕ-dependent variables, such as $\Delta\phi$, thus it is necessary to perform the efficiency correction as a function of ϕ. Due to the symmetry of the LHCb detector in the x-y plane, a new variable $\phi_0 = ||\phi| - \pi/2|$ is used, and the correction factor is denoted by κ^{ϕ_0}. The efficiency of each ψ candidate or each muon track has to be multiplied by the correction factor κ^{ϕ_0} according to its kinematics. The correction factors $\kappa^{\phi_0}_{\rm rec\&sel}$ and $\kappa^{\phi_0}_{\rm L0\&HLT1}$ are determined using the full-simulated sample, as a function of ϕ^{ψ}_0 in different $(p^{\psi}_{\rm T}, y_{\psi})$ intervals. The correction factor $\kappa^{\phi_0}_{\rm PID}$ for muon is obtained from the PIDCalib package[187] as a function of ϕ^{μ}_0 in different (p^{μ}, η^{μ}) intervals.

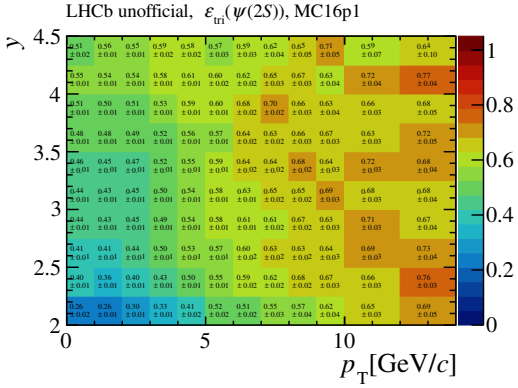

(a) $\varepsilon^{\psi(2S)}_{\rm L0\&HLT1}$ for MC16p1.

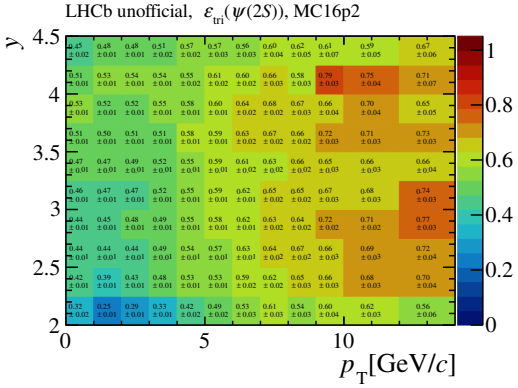

(b) $\varepsilon^{\psi(2S)}_{\rm L0\&HLT1}$ for MC16p2.

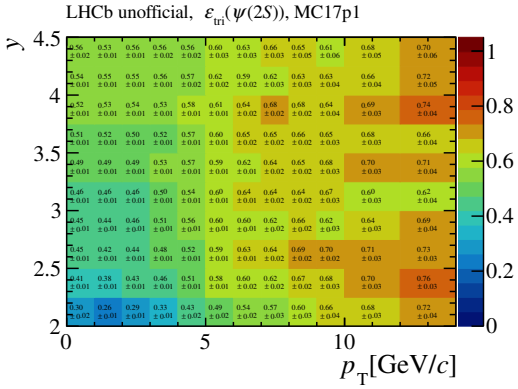

(c) $\varepsilon^{\psi(2S)}_{\rm L0\&HLT1}$ for MC17p1.

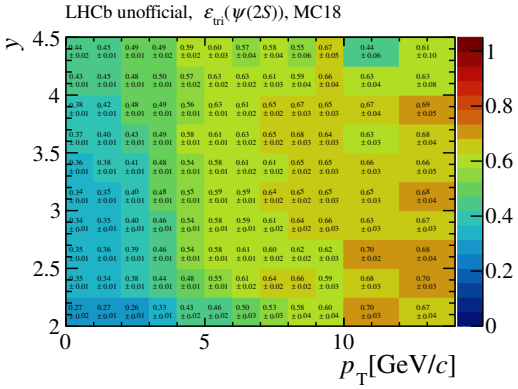

(d) $\varepsilon^{\psi(2S)}_{\rm L0\&HLT1}$ for MC18.

Figure 5.20 L0-and-HLT1 trigger efficiencies of $\psi(2S)$ mesons in ($p_{\rm T}$,y) intervals for (a) MC16p1, (b) MC16p2, (c) MC17p1 and (d) MC18.

5.5.7 Check the efficiency factorisation

For the PID efficiency and trigger efficiency, potential overlap of muon tracks at the muon stations may violate the factorisation assumption. It is verified by a full-simulation sample of $\Upsilon \to J/\psi\, J/\psi\, \gamma$ decay. Although the kinematics of J/ψ mesons in this sample are different from that in data, it is enough to provide a check of the efficiency factorisation in ($p_{\rm T}^{J/\psi_1}$,$p_{\rm T}^{J/\psi_2}$) and (y_{J/ψ_1},y_{J/ψ_2}) intervals. In each interval, the PID efficiency of di-J/ψ candidates $\varepsilon^{\text{di-}J/\psi}_{\rm PID}$ can be directly calculated as the fraction of events with all the four muons meeting the PID requirement in this simulated sample. It is compared with the product of PID efficiencies $\varepsilon^{J/\psi_1}_{\rm PID} \times \varepsilon^{J/\psi_2}_{\rm PID}$ determined in the same interval using the same sample. The ratio between $\varepsilon^{J/\psi_1}_{\rm PID} \times \varepsilon^{J/\psi_2}_{\rm PID}$ and $\varepsilon^{\text{di-}J/\psi}_{\rm PID}$,

$$R_{\rm PID} = \frac{\varepsilon^{J/\psi_1}_{\rm PID} \times \varepsilon^{J/\psi_2}_{\rm PID}}{\varepsilon^{\text{di-}J/\psi}_{\rm PID}}, \tag{5.25}$$

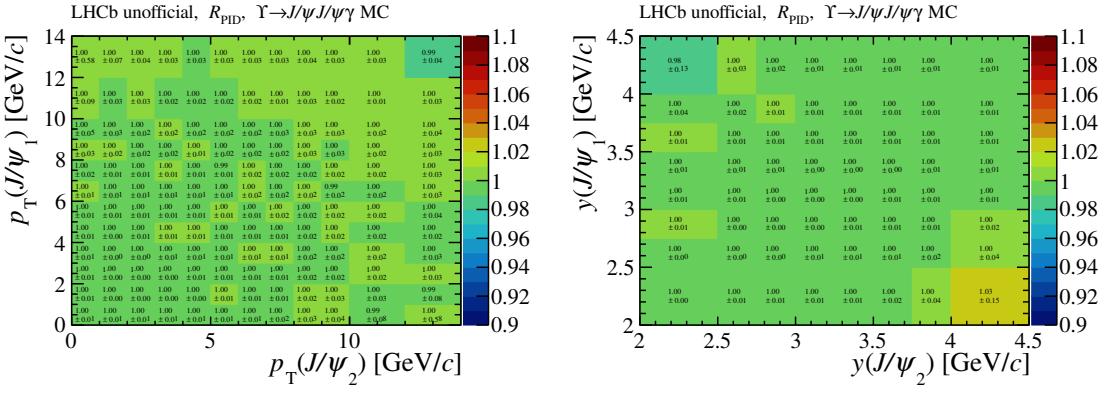

(a) $R_{\rm PID}$ in $(p_{\rm T}^{J/\psi_1}, p_{\rm T}^{J/\psi_2})$ intervals. (b) $R_{\rm PID}$ in $(y_{J/\psi_1}, y_{J/\psi_2})$ intervals.

Figure 5.21 Ratio of PID efficiency in (a) $(p_{\rm T}^{J/\psi_1}, p_{\rm T}^{J/\psi_2})$ and (b) $(y_{J/\psi_1}, y_{J/\psi_2})$ intervals for $\Upsilon \to J/\psi\, J/\psi\, \gamma$ simulation to check the efficiency factorisation.

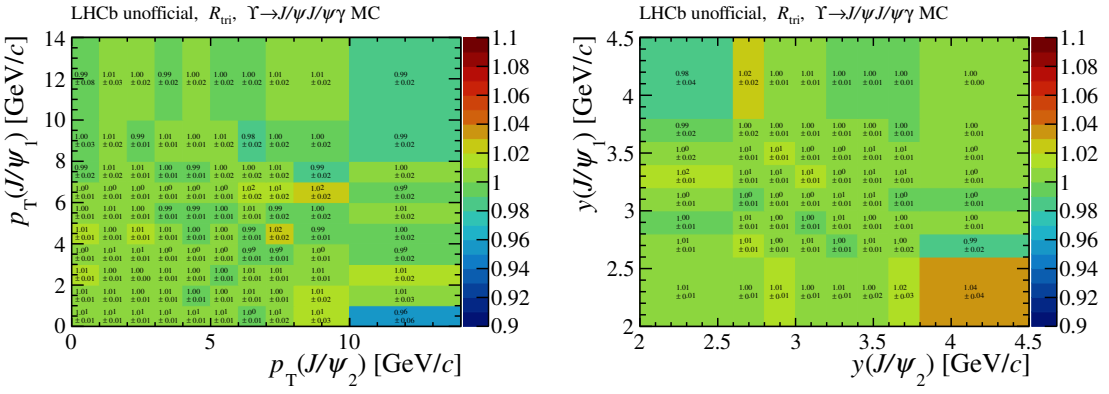

(a) $R_{\rm tri}$ in $(p_{\rm T}^{J/\psi_1}, p_{\rm T}^{J/\psi_2})$ intervals. (b) $R_{\rm tri}$ in $(y_{J/\psi_1}, y_{J/\psi_2})$ intervals.

Figure 5.22 Ratio of trigger efficiency in (a) $(p_{\rm T}^{J/\psi_1}, p_{\rm T}^{J/\psi_2})$ and (b) $(y_{J/\psi_1}, y_{J/\psi_2})$ intervals for $\Upsilon \to J/\psi\, J/\psi\, \gamma$ simulation to check the efficiency factorisation.

is shown in Figure 5.21 in $(p_{\rm T}^{J/\psi_1}, p_{\rm T}^{J/\psi_2})$ and $(y_{J/\psi_1}, y_{J/\psi_2})$ intervals. The ratios in all intervals are consistent with one, thus the impact of muon track overlap on the PID efficiency factorisation is negligible.

For the trigger efficiency of di-ψ signals, it is firstly verified by the $\Upsilon \to J/\psi\, J/\psi\, \gamma$ simulation that the HLT2 trigger efficiency $\varepsilon_{\rm HLT2}^{\text{di-}\psi}$ is indeed 100% after applying the offline selection. Then, to check its factorisation, a ratio is defined as

$$R_{\rm tri} = \frac{1-(1-\varepsilon_{\rm L0\&HLT1}^{J/\psi_1})\times(1-\varepsilon_{\rm L0\&HLT1}^{J/\psi_2})}{\varepsilon_{\rm L0\&HLT1}^{\text{di-}J/\psi}}, \tag{5.26}$$

and the values determined using the $\Upsilon \to J/\psi\, J/\psi\, \gamma$ simulation in $(p_{\rm T}^{J/\psi_1}, p_{\rm T}^{J/\psi_2})$ and $(y_{J/\psi_1}, y_{J/\psi_2})$ intervals are shown in Figure 5.22. All these values are consistent with one, so the impact of muon track overlap on the trigger efficiency factorisation is negligible as

well.

5.6 Cross-section determination

The cross-sections of di-J/ψ and J/ψ-$\psi(2S)$ production are calculated by

$$\sigma_{\text{di-}J/\psi} = \frac{N^{\text{corr}}(\text{di-}J/\psi)}{\mathcal{L} \times \left[\mathcal{B}(J/\psi \to \mu^+\mu^-)\right]^2}, \tag{5.27}$$

$$\sigma_{J/\psi\text{-}\psi(2S)} = \frac{N^{\text{corr}}(J/\psi\text{-}\psi(2S))}{\mathcal{L} \times \mathcal{B}(J/\psi \to \mu^+\mu^-) \times \mathcal{B}(\psi(2S) \to \mu^+\mu^-)}, \tag{5.28}$$

where efficiency-corrected yield N^{corr} is determined by Eq. 5.13 and its statistical uncertainty is calculated by $\sqrt{\sum_i (w_i/\varepsilon_{\text{tot}i})^2}$, the integrated luminosity is $4.18 \pm 0.08\,\text{fb}^{-1}$ measured using methods similar to those described in Ref. [171], and the branching fractions $\mathcal{B}(J/\psi \to \mu^+\mu^-)$ and $\mathcal{B}(\psi(2S) \to \mu^+\mu^-)$ are obtained from Ref. [9]. The branching fraction of J/ψ decay is $\mathcal{B}(J/\psi \to \mu^+\mu^-) = 5.961 \pm 0.033\%$ [9]. For the branching fraction of $\psi(2S)$ decay, the $\mathcal{B}(\psi(2S) \to e^+e^-) = (7.93 \pm 0.17) \times 10^{-3}$ [9] is used in the determination of the J/ψ-$\psi(2S)$ cross-section taking advantage of its much smaller uncertainty than that on $\mathcal{B}(\psi(2S) \to \mu^+\mu^-)$, under the assumption of the lepton universality in electromagnetic decays. The difference of the two branching fractions introduced by the mass difference between electron and muon is negligible. Therefore, the value $\mathcal{B}(\psi(2S) \to \mu^+\mu^-) = (7.93 \pm 0.17) \times 10^{-3}$ is used in this analysis. The cross-sections with both ψ mesons in the range $0 < p_{\text{T}} < 14\,\text{GeV}$ and $2.0 < y < 4.5$ are

$$\sigma_{\text{di-}J/\psi} = 16.36 \pm 0.28\,\text{nb},$$

$$\sigma_{J/\psi\text{-}\psi(2S)} = 4.49 \pm 0.71\,\text{nb},$$

where the uncertainties are statistical and verified by the bootstrapping approach [192] as described in the following.

5.6.1 Check the statistical uncertainty

As mentioned above, the *sWeight* w_i in Eq. 5.13, which is used in the determination of cross-sections, is obtained from the *sPlot* method [185] on top of the weighted distribution. It was pointed out that the statistical uncertainty calculated using $\sqrt{\sum_i (w_i/\varepsilon_{\text{tot}i})^2}$ may be incorrect and need to be verified, while the central value is still reliable [193]. The bootstrapping approach [192] is used to estimate the statistical uncertainty alternatively. New samples are obtained by repeatedly resampling the data set with replacement, in which case one event can be selected more than once. The sample size is taken as a Poisson

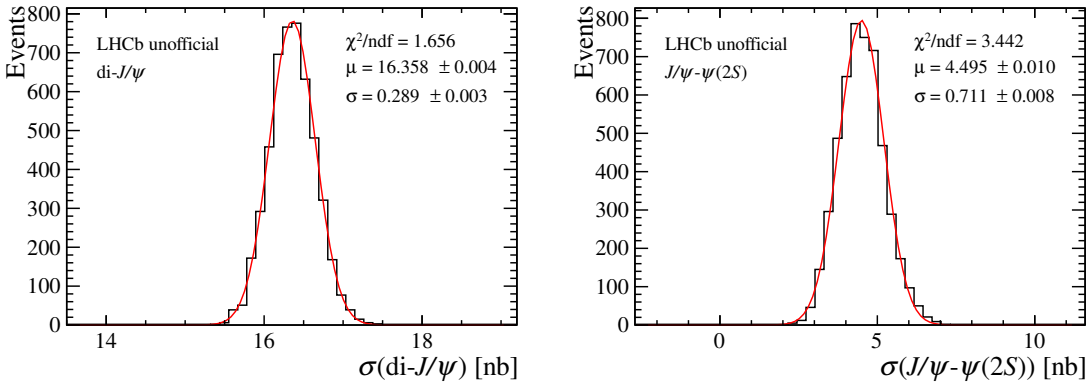

(a) Distribution of di-J/ψ cross-section. (b) Distribution of J/ψ-$\psi(2S)$ cross-section.

Figure 5.23 Distributions of (a) di-J/ψ and (b) J/ψ-$\psi(2S)$ cross-sections obtained from the bootstrapping approach together with the Gaussian fits.

random number with an expected value of the size of the data set. For each sample, a new value of cross-section can be extracted through the same method as that for the default result. The width of the cross-section distribution is considered as the estimate of the statistical uncertainty. By resampling the di-ψ data set, 5000 samples of real events are generated, and the distributions of di-J/ψ and J/ψ-$\psi(2S)$ cross-sections obtained from these samples are shown in Figure 5.23, together with the Gaussian fits. Both the widths are consistent with the statistical uncertainties propagated from those on the N^{corr} calculated by $\sqrt{\sum_i (w_i/\varepsilon_{\text{tot}i})^2}$.

5.7 Systematic uncertainties

A summary of systematic uncertainties is presented in Table 5.9. The details of the evaluation are discussed in the following. Because of the low statistics of the J/ψ-$\psi(2S)$ data, most of systematic uncertainties are studied using a toy J/ψ-$\psi(2S)$ sample with single-J/ψ and single-$\psi(2S)$ candidates in data combined randomly. The toy J/ψ-$\psi(2S)$ sample provides much more statistics to reduce the statistical fluctuation in the evaluation of systematic uncertainties. The same selection criteria as those for J/ψ-$\psi(2S)$ data are applied to the toy sample, and the same procedures of signal extraction and efficiency correction are performed.

5.7.1 Uncertainties related to signal extraction

An uncertainty is attributed to the choice of the probability density function used to model the ψ mass distribution. As an alternative to the sum of a DSCB function and

Table 5.9 Summary of relative systematic uncertainties on the measurement of di-J/ψ and J/ψ-$\psi(2S)$ production cross-section.

Source	Di-J/ψ	J/ψ-$\psi(2S)$
Signal mass model	1.7%	1.7%
Non-prompt contribution	2.4%	1.9%
Wrong PV association	0.8%	1.5%
Efficiency statistical uncertainty	0.2%	0.7%
Efficiency binning scheme	1.5%	2.1%
Correction factor binning scheme	0.3%	0.7%
Tracking efficiency	3.4%	3.3%
Trigger efficiency	0.7%	0.7%
Branching fraction	1.1%	2.2%
Luminosity	2.0%	2.0%
Total	5.4%	5.9%

a Gaussian function, the di-muon invariant-mass distribution of ψ signals is described by a model derived from simulation using the KDE approach[188]. To account for the resolution difference between data and simulation, the alternative model is convolved with a Gaussian function with zero mean and width varied freely. The relative difference of the extracted yields N_{ss} using the default and alternative models is 1.7% (1.7%) for di-J/ψ (J/ψ-$\psi(2S)$) signals, which is taken as the systematic uncertainty. For the measurement of differential cross-sections, this value is taken as the uncertainty common to all kinematic intervals.

An uncertainty is attributed to the choice of the variable used to subtract non-prompt contributions. As an alternative to the pseudo-proper time t_z, the variable $\log(\chi^2_{\mathrm{IP}})$ of ψ particle is used, where χ^2_{IP} is defined as the difference in the vertex-fit χ^2 of a given PV reconstructed with and without the particle under consideration. The fit model of prompt ψ signals is the sum of two Bukin functions[194] with the same peak position and the same peak asymmetry, while the fit model of non-prompt ψ signals is one Bukin function. Most shape parameters of Bukin functions are fixed from simulation. The component of wrong PV association is neglected in the 2D $\log(\chi^2_{\mathrm{IP}})$ fit model. The extracted yield of double prompt ψ signals N_{pp} is compared between the 2D t_z fit and the 2D $\log(\chi^2_{\mathrm{IP}})$ fit, and the relative difference, 2.4% (1.9%) for di-J/ψ (J/ψ-$\psi(2S)$) signals, is taken as the systematic uncertainty. For the measurement of differential cross-sections, this value is taken as the

uncertainty common to all kinematic intervals.

As mentioned in Section 5.3, a small fraction of ψ candidates in the di-ψ data may be associated to a wrong PV in two cases. The first case is that the true PV is reconstructed but one of the di-ψ candidates is associated to a wrong PV accidentally, while the second case is that the true PV is not reconstructed and both ψ candidates are associated to the nearest reconstructed PV in this event. The fraction of the first case is estimated as the fraction of events with $|\Delta z_{\mathrm{PV}}| > 0.1$ using the simulated sample of $\Upsilon \to J/\psi\, J/\psi\, \gamma$ decay. The value is $0.65 \pm 0.02\%$, which is considered as the fraction both for di-J/ψ and J/ψ-$\psi(2S)$ signals. The second case is a component in the 2D t_z fit. The ratio of yields $N_{\mathrm{ww}}/N_{\mathrm{ss}}$ is $0.16 \pm 0.08\%$ for di-J/ψ signals and $0.80 \pm 1.51\%$ for J/ψ-$\psi(2S)$ signals. With the fractions of two cases added together, the fraction of wrong PV events is 0.8% (1.5%) for di-J/ψ (J/ψ-$\psi(2S)$) signals, which is taken as a systematic uncertainty. For the measurement of differential cross-sections, the fraction is studied in several intervals of rapidities, $y_{\text{di-}J/\psi}$ or $y_{J/\psi}$ using the same method. The maximum value in these intervals, 1.5% (2.2%) for di-J/ψ (J/ψ-$\psi(2S)$) signals, is taken as the uncertainty common to all kinematic intervals.

5.7.2 Uncertainties related to efficiency determination

The limited statistics of the samples used to determine the efficiencies can introduce a systematic uncertainty. The propagation of the efficiency statistical uncertainties is studied by pseudo-experiments, in which the efficiency is sampled by Gaussian distributions with the corresponding central value as the mean and the statistical uncertainty as the width. The width of the cross-section distribution obtained from pseudo-experiments is taken as the systematic uncertainty propagated from the efficiency statistical uncertainties. It is 0.2% (0.7%) for di-J/ψ (J/ψ-$\psi(2S)$) signals. For the measurement of differential cross-sections, it varies up to 1.1% (3.0%) for di-J/ψ (J/ψ-$\psi(2S)$) signals depending on the kinematic intervals.

The binning scheme of efficiencies is another source of systematic uncertainty. For the PID efficiency of single-muon $\varepsilon^{\mu}_{\mathrm{PID}}$ obtained from the PIDCalib package[187], it is studied by varying the (p^{μ}, η^{μ}, nSPDHits) binning schemes, and the relative difference in the cross-sections is taken as an uncertainty. For the rest efficiencies, $\varepsilon^{\psi}_{\mathrm{acc}}$, $\varepsilon^{\psi}_{\mathrm{rec\&sel}}$ and $\varepsilon^{\psi}_{\mathrm{tri}}$, which are determined in $(p^{\psi}_{\mathrm{T}}, y_{\psi})$ intervals from simulated samples, an alternative approach of KDE[188] is used. Rather than the ratio of two numbers in each interval, the efficiency is determined as the ratio of two functions of $(p^{\psi}_{\mathrm{T}}, y_{\psi})$, which are obtained by

the KDE approach using simulated samples. The relative difference in the cross-sections between the default and alternative approaches is quoted as the systematic uncertainty separately for efficiencies ε_{acc}, $\varepsilon_{\text{rec\&sel}}$ and ε_{tri}. With the uncertainties related to the four efficiency terms added in quadrature, the systematic uncertainty due to the binning scheme of efficiencies is 1.5% (2.8%) for di-J/ψ (J/ψ-$\psi(2S)$) signals. For the measurement of differential cross-sections, it varies up to 6.6% (5.5%) for di-J/ψ (J/ψ-$\psi(2S)$) signals depending on the kinematic intervals.

In addition, a systematic uncertainty is attributed to the binning scheme of correction factors κ^{ϕ_0} as well. it is studied by varying the binning scheme, and the relative difference in the cross-sections is 0.3% (0.7%) for di-J/ψ (J/ψ-$\psi(2S)$) signals, which is taken as the systematic uncertainty due to the correction factor binning scheme. For the measurement of differential cross-sections, it varies up to 5.8% (3.4%) for di-J/ψ (J/ψ-$\psi(2S)$) signals depending on the kinematic intervals.

Two sources of systematic uncertainties related to the tracking efficiency correction are taken into account. One is propagated from the statistical uncertainties of the correction factors due to the limited sample size. It is studied by pseudo-experiments, and the uncertainty is 1.2% (0.9%) for di-J/ψ (J/ψ-$\psi(2S)$) signals. Besides, these correction factors are found to depend on different multiplicity variables, which introduces a systematic uncertainty of 0.8% per track. It is 3.2% for di-J/ψ and J/ψ-$\psi(2S)$ signals containing four muon tracks. With the uncertainties from two sources added in quadrature, the systematic uncertainty related to the tracking efficiency correction is 3.4% (3.3%) for di-J/ψ (J/ψ-$\psi(2S)$) signals. For the measurement of differential cross-sections, the first one varies up to 3.8% (4.2%) for di-J/ψ (J/ψ-$\psi(2S)$) signals, while the second one is considered to be common to all kinematic intervals.

The trigger efficiency in simulation is validated with the single-J/ψ data. The L0-and-HLT1 trigger efficiency $\varepsilon^{J/\psi}_{\text{L0\&HLT1}}$ is determined using TIS events, *i.e.* that would fulfil the trigger requirement if the J/ψ signals were excluded[189]. The fraction of J/ψ candidates for which two tracks fulfil the requirement of L0 and HLT1 trigger is treated as the efficiency both for data and simulation. The relative difference in the di-J/ψ cross-section between data and simulation is 0.7%, and is taken as a systematic uncertainty. For J/ψ-$\psi(2S)$ signals, due to the low statistics of the $\psi(2S)$ TIS sample, the correction of efficiency $\varepsilon_{\text{L0\&HLT1}}$ determined using the J/ψ TIS events both for data and simulation is also applied to $\psi(2S)$ mesons. The relative difference in the J/ψ-$\psi(2S)$ cross-section between

data and simulation is 0.7%, and is taken as a systematic uncertainty. For the measurement of differential cross-sections, the quoted uncertainty varies up to 7.9% (7.5%) for di-J/ψ (J/ψ-$\psi(2S)$) signals depending on the kinematic intervals.

5.7.3 Other sources

The uncertainty on the branching fractions $\mathcal{B}(J/\psi \to \mu^+\mu^-) = 5.961 \pm 0.033\%$ and $\mathcal{B}(\psi(2S) \to e^+e^-) = (7.93 \pm 0.17) \times 10^{-3}$ [9] results in an uncertainty of 1.1% (2.2%) on the measured cross-sections of di-J/ψ (J/ψ-$\psi(2S)$) production.

The luminosity is determined using methods similar to those described in Ref. [171] and the relative uncertainty is 2.0%.

5.8 Cross-section results of di-J/ψ production

The cross-section of di-J/ψ production with both J/ψ mesons in the fiducial range $0 < p_{\mathrm{T}} < 14\,\mathrm{GeV}$ and $2.0 < y < 4.5$ is

$$\sigma_{\text{di-}J/\psi} = 16.36 \pm 0.28(\text{stat.}) \pm 0.88(\text{syst.})\,\text{nb},$$

where the first uncertainty is statistical and the second is systematic, assuming negligible polarisation of the J/ψ mesons. The detection efficiency of J/ψ mesons depends on their polarisation, especially by the polarisation parameter λ_θ [63,76]. If the polarisation parameter λ_θ is assumed to be $\lambda_\theta = +0.2$ (-0.2) for both J/ψ mesons in the helicity frame , the cross-section of di-J/ψ production changes by $+6.2\%$ (-6.3%).

5.8.1 Differential cross-sections

The differential cross-section of di-J/ψ production is measured as functions of Δy, $\Delta\phi$, $\mathcal{A}_{p_{\mathrm{T}}}$, $p_{\mathrm{T}}^{\text{di-}J/\psi}$, $y_{\text{di-}J/\psi}$, $m_{\text{di-}J/\psi}$, $p_{\mathrm{T}}^{J/\psi}$, $y_{J/\psi}$, θ_{CS} and ϕ_{CS}. In each interval of these kinematic variables, the 2D mass fit and the 2D t_z fit are performed to subtract combinatorial backgrounds and non-prompt contributions. In the 2D t_z fit model, the wrong-PV component is omitted, parameters τ_b, β' and the ratio S_2/S_1 are fixed to the values of the fit result in Table 5.7. The systematic uncertainties on differential cross-sections are presented in Section 5.7 separately for every source. With statistical and systematic uncertainties considered, differential cross-sections of di-J/ψ production are shown in Figure 5.24, and are listed in Tables B.1–B.10 in Appendix B.

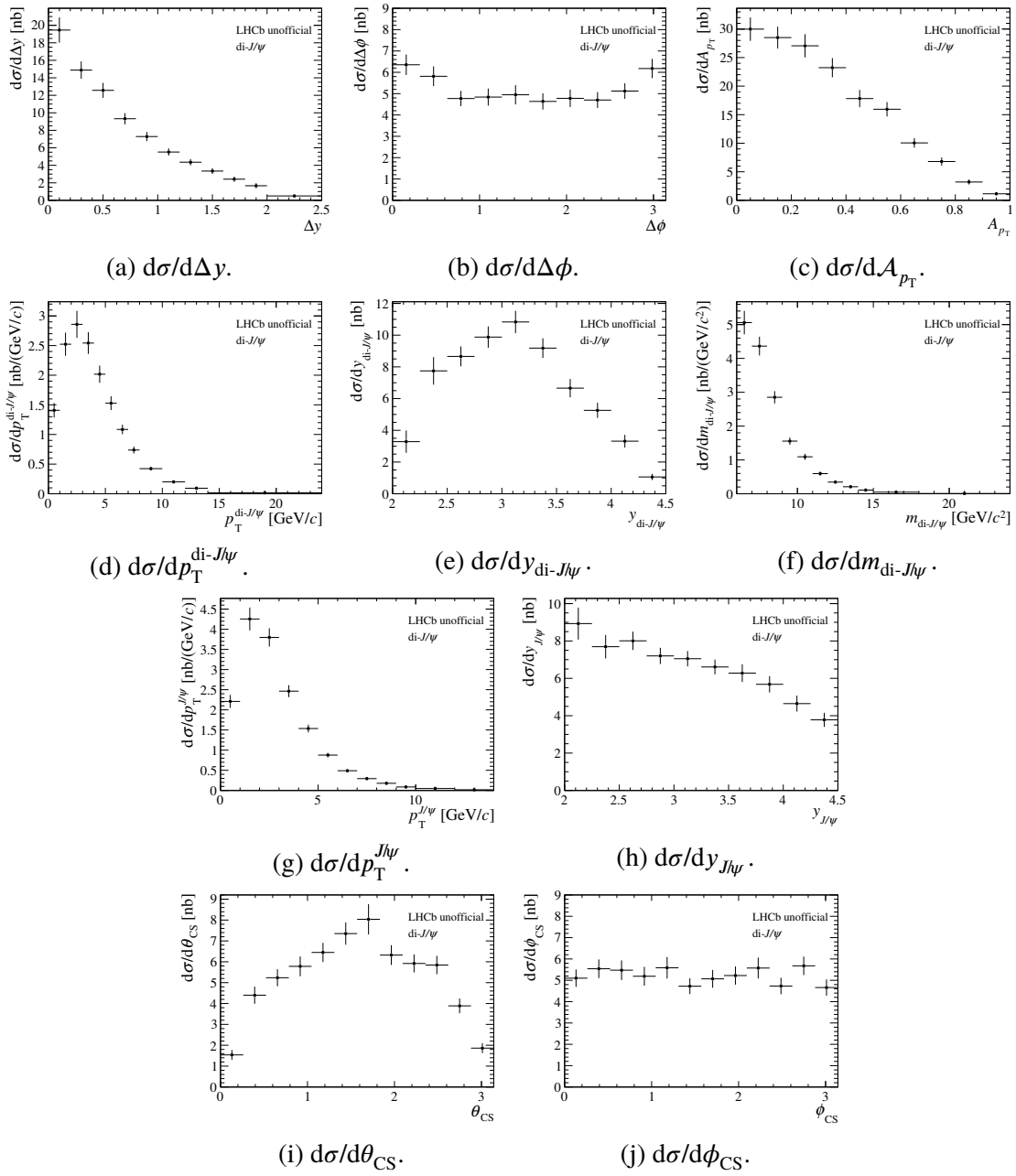

(a) $\mathrm{d}\sigma/\mathrm{d}\Delta y$. (b) $\mathrm{d}\sigma/\mathrm{d}\Delta\phi$. (c) $\mathrm{d}\sigma/\mathrm{d}\mathcal{A}_{p_\mathrm{T}}$.

(d) $\mathrm{d}\sigma/\mathrm{d}p_\mathrm{T}^{\text{di-}J/\psi}$. (e) $\mathrm{d}\sigma/\mathrm{d}y_{\text{di-}J/\psi}$. (f) $\mathrm{d}\sigma/\mathrm{d}m_{\text{di-}J/\psi}$.

(g) $\mathrm{d}\sigma/\mathrm{d}p_\mathrm{T}^{J/\psi}$. (h) $\mathrm{d}\sigma/\mathrm{d}y_{J/\psi}$.

(i) $\mathrm{d}\sigma/\mathrm{d}\theta_\mathrm{CS}$. (j) $\mathrm{d}\sigma/\mathrm{d}\phi_\mathrm{CS}$.

Figure 5.24 Differential cross-section of di-J/ψ production as a function of (a) Δy, (b) $\Delta\phi$, (c) $\mathcal{A}_{p_\mathrm{T}}$, (d) $p_\mathrm{T}^{\text{di-}J/\psi}$, (e) $y_{\text{di-}J/\psi}$, (f) $m_{\text{di-}J/\psi}$, (g) $p_\mathrm{T}^{J/\psi}$, (h) $y_{J/\psi}$, (i) θ_CS and (j) ϕ_CS. The error bars represent the statistical and systematic uncertainties added in quadrature.

5.8.2 Separation of DPS contribution

As pointed out in Ref. [152] and confirmed in previous measurements by the D0 collaboration[139] and the ATLAS collaboration[140], the DPS contribution can be extracted from the differential cross-section $\mathrm{d}\sigma/\mathrm{d}\Delta y$ with a data-driven prediction for the DPS mechanism. It is assumed that the measured cross-section of di-J/ψ production in the range $1.8 < \Delta y < 2.5$ is completely contributed by DPS process, and then the DPS

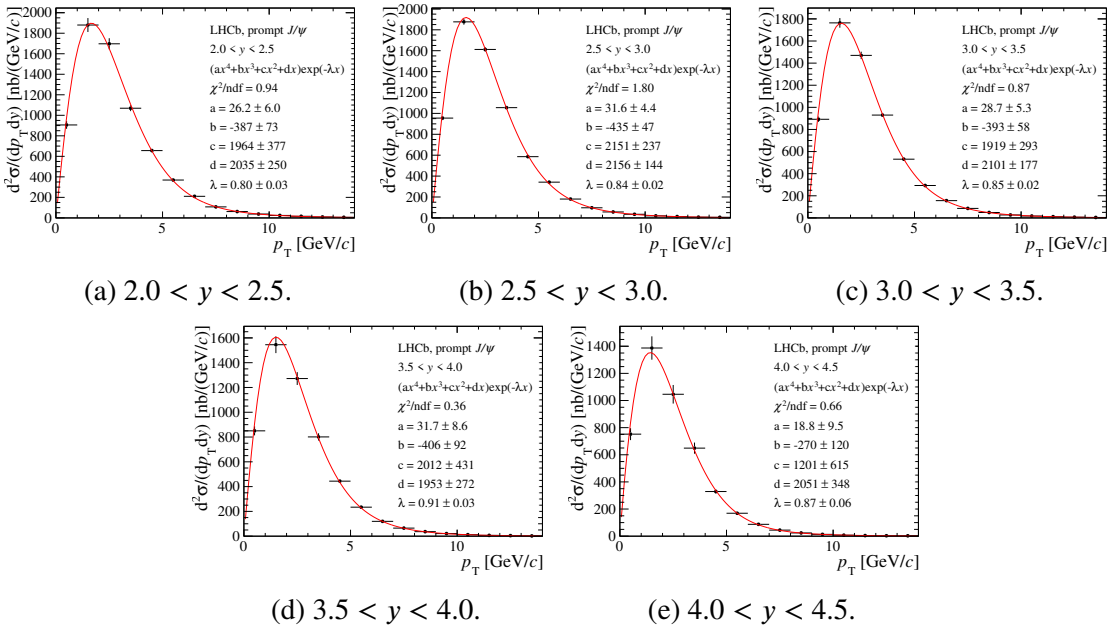

(a) $2.0 < y < 2.5$. (b) $2.5 < y < 3.0$. (c) $3.0 < y < 3.5$.

(d) $3.5 < y < 4.0$. (e) $4.0 < y < 4.5$.

Figure 5.25 Differential cross-sections of prompt J/ψ production as a function of p_{T} in intervals of y, together with the empirical-function fits. The data points are taken from Ref. [63].

cross-section is extrapolated to the whole range $0 < \Delta y < 2.5$ following the shape of $\mathrm{d}\sigma/\mathrm{d}\Delta y$ provided by the DPS prediction.

According to Eq. 2.46, the DPS cross-section $\sigma^{\mathrm{DPS}}_{\text{di-}J/\psi}$ of di-J/ψ production can be expressed as

$$\sigma^{\mathrm{DPS}}_{\text{di-}J/\psi} = \frac{1}{2}\frac{\sigma^2_{J/\psi}}{\sigma_{\mathrm{eff}}}, \tag{5.29}$$

where $\sigma_{J/\psi}$ is the cross-section of single-J/ψ production, and the effective cross-section σ_{eff} does not affect the shape of DPS differential cross-section. The shape is predicted using a large number of pseudo-experiments, where two uncorrelated J/ψ mesons are produced according to the measured differential distribution $\mathrm{d}^2\sigma/(\mathrm{d}p_{\mathrm{T}}\mathrm{d}y)$ of single prompt J/ψ production[63], uniformly distributed over the azimuthal angle ϕ. The p_{T} spectra of J/ψ mesons in y intervals are interpolated by an empirical function $(ax^4 + bx^3 + cx^2 + dx)e^{-\lambda x}$, the fits to the p_{T} spectra with the empirical function are shown in Figure 5.25. A linear interpolation is applied to the y distribution of J/ψ mesons. In each pseudo-experiment, the four-momenta of both J/ψ mesons can be calculated with the generated $(p_{\mathrm{T}}, y, \phi)$ values, and then the di-J/ψ kinematic variables are determined. Then, DPS shapes of di-J/ψ differential cross-sections are obtained from these pseudo-experiments, although the integrated DPS cross-section is unknown. For example, the normalised DPS shapes of Δy and $\Delta\phi$ are shown in Figure 5.26. The rapidity difference Δy approximately follows a triangle distribution ending at $\Delta y = 2.5$, and the $\Delta\phi$ distribution is flat for DPS

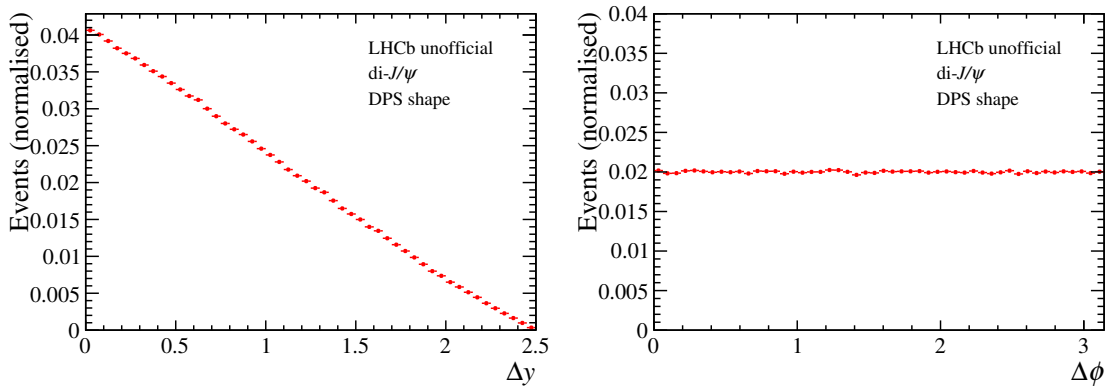

(a) Distribution of Δy. (b) Distribution of $\Delta\phi$.

Figure 5.26 Normalised DPS shapes of (a) Δy and (b) $\Delta\phi$ obtained from pseudo-experiments.

process.

The cross-section of di-J/ψ production in the DPS-dominated range $1.8 < \Delta y < 2.5$ is

$$\sigma_{\text{di-}J/\psi}\,(1.8 < \Delta y < 2.5) = 0.582 \pm 0.082(\text{stat.}) \pm 0.062(\text{syst.})\,\text{nb}$$

The relative statistic uncertainty is 11.9% and the relative systematic uncertainty is 10.7%. The fraction of the DPS cross-section between the DPS-dominated Δy range and the whole Δy range is

$$f^{\text{DPS}}_{1.8<\Delta y<2.5} = \frac{\sigma^{\text{DPS}}_{\text{di-}J/\psi}\,(1.8 < \Delta y < 2.5)}{\sigma^{\text{DPS}}_{\text{di-}J/\psi}} = 0.068,$$

which is determined according to the DPS shape in Figure 5.26(a). For the fraction $f^{\text{DPS}}_{1.8<\Delta y<2.5}$, three sources of systematic uncertainties are taken into account:

- The first is due to the choice of the DPS-dominated range. Three alternative ranges are studied: (a) $1.85 < \Delta y < 2.50$, (b) $1.8 < \Delta y < 2.5, 0 < \Delta\phi < \frac{1}{2}\pi$ and (c) $1.8 < \Delta y < 2.5, \frac{1}{2}\pi < \Delta\phi < \pi$. The maximum relative difference in the fraction $f^{\text{DPS}}_{1.8<\Delta y<2.5}$ is 3.5%, which is taken as the systematic uncertainty.
- The second is due to the interpolation of single-J/ψ differential cross-sections. As an alternative to the fit with the empirical function, histograms are directly used to generate (p_{T},y) values in the pseudo-experiments. The relative difference in the fraction $f^{\text{DPS}}_{1.8<\Delta y<2.5}$ is 3.3%, which is taken as the systematic uncertainty.
- The uncertainties from single-J/ψ production measurement propagate into the fraction $f^{\text{DPS}}_{1.8<\Delta y<2.5}$. It is studied by varying the single-J/ψ differential cross-sections within their uncertainties. The systematic uncertainty on the fraction $f^{\text{DPS}}_{1.8<\Delta y<2.5}$ is 1.8%.

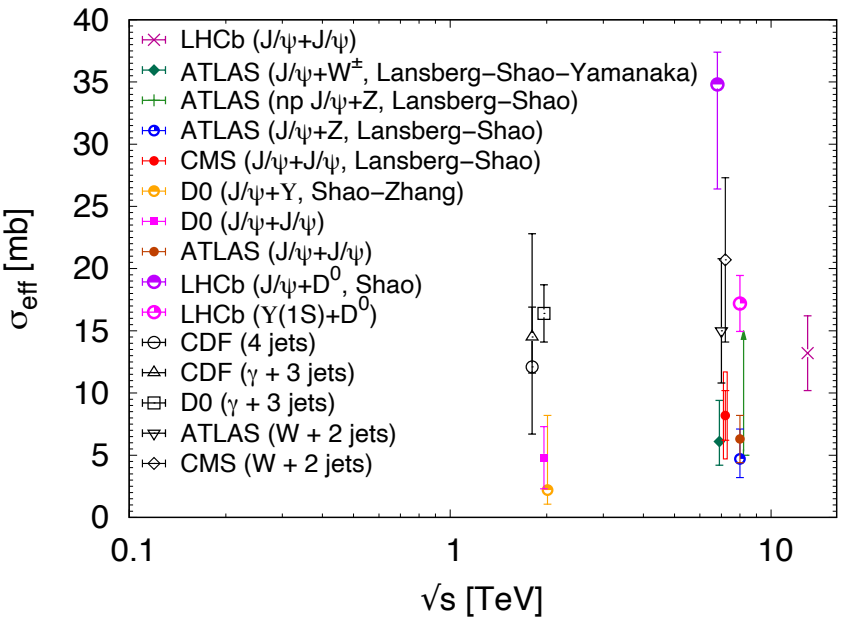

Figure 5.27 The extracted values of σ_{eff} from different measurements in pp or $p\bar{p}$ collisions. The result from this analysis is shown as a crimson cross. The figure is reproduced from Ref. [148].

The DPS cross-section of di-J/ψ production with both J/ψ mesons in the fiducial range $0 < p_{\text{T}} < 14\,\text{GeV}$ and $2.0 < y < 4.5$ can be calculated as the cross-section in the DPS-dominated range $\sigma_{\text{di-}J/\psi}\,(1.8 < \Delta y < 2.5)$ divided by the fraction $f^{\text{DPS}}_{1.8<\Delta y<2.5}$, and the result is

$$\sigma^{\text{DPS}}_{\text{di-}J/\psi} = 8.6 \pm 1.2(\text{stat.}) \pm 1.0(\text{syst.})\,\text{nb}.$$

According to Eq. 2.46, the effective cross-section σ_{eff} can be extracted as

$$\sigma_{\text{eff}} = \frac{1}{2}\frac{\sigma^2_{J/\psi}}{\sigma^{\text{DPS}}_{\text{di-}J/\psi}} = 13.1 \pm 1.8(\text{stat.}) \pm 2.3(\text{syst.})\,\text{mb},$$

where the cross-section of prompt J/ψ production in the range $0 < p_{\text{T}} < 14\,\text{GeV}$ and $2.0 < y < 4.5$ is $\sigma_{J/\psi} = 15.03 \pm 0.03(\text{stat.}) \pm 0.94(\text{syst.})\,\mu\text{b}$ [63], and the the systematic uncertainties on $\sigma^{\text{DPS}}_{\text{di-}J/\psi}$ and $\sigma_{J/\psi}$ are treated as uncorrelated. The σ_{eff} result is compatible with other extracted values from different measurements in pp and $p\bar{p}$ collisions, as shown in Figure 5.27.

With the DPS cross-section subtracted, the SPS cross-section of di-J/ψ production with both J/ψ mesons in the fiducial range $0 < p_{\text{T}} < 14\,\text{GeV}$ and $2.0 < y < 4.5$ is

$$\sigma^{\text{SPS}}_{\text{di-}J/\psi} = 7.9 \pm 1.2(\text{stat.}) \pm 1.1(\text{syst.})\,\text{nb}.$$

In the subtraction of the DPS cross-section from the total, the systematic uncertainties due to signal mass model, non-prompt contribution, wrong PV association, multiplicity

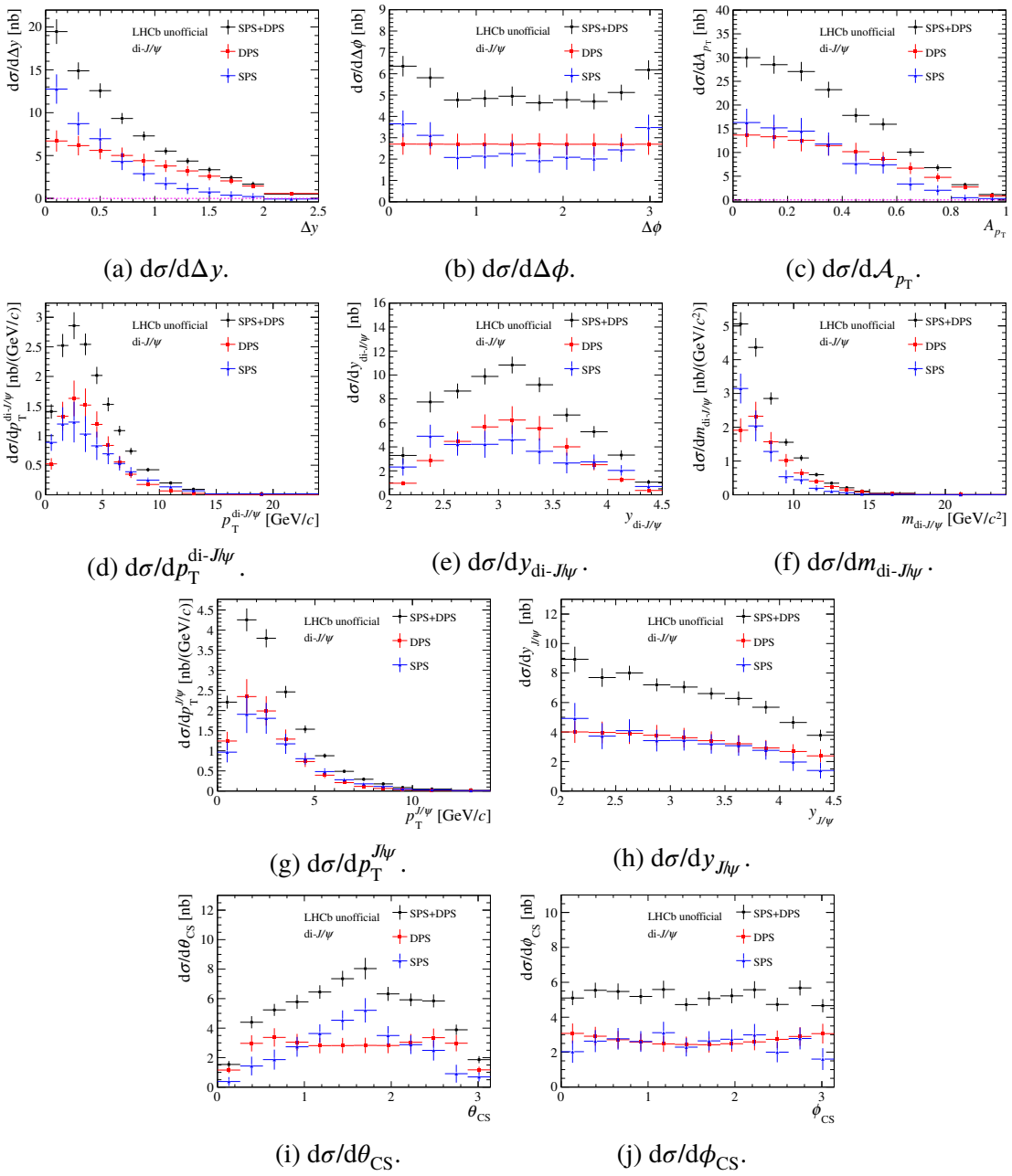

(a) $\mathrm{d}\sigma/\mathrm{d}\Delta y$. (b) $\mathrm{d}\sigma/\mathrm{d}\Delta\phi$. (c) $\mathrm{d}\sigma/\mathrm{d}\mathcal{A}_{p_\mathrm{T}}$.

(d) $\mathrm{d}\sigma/\mathrm{d}p_\mathrm{T}^{\text{di-}J/\psi}$. (e) $\mathrm{d}\sigma/\mathrm{d}y_{\text{di-}J/\psi}$. (f) $\mathrm{d}\sigma/\mathrm{d}m_{\text{di-}J/\psi}$.

(g) $\mathrm{d}\sigma/\mathrm{d}p_\mathrm{T}^{J/\psi}$. (h) $\mathrm{d}\sigma/\mathrm{d}y_{J/\psi}$.

(i) $\mathrm{d}\sigma/\mathrm{d}\theta_\mathrm{CS}$. (j) $\mathrm{d}\sigma/\mathrm{d}\phi_\mathrm{CS}$.

Figure 5.28 Differential cross-section of di-J/ψ production for SPS+DPS, DPS and SPS as a function of (a) Δy, (b) $\Delta\phi$, (c) $\mathcal{A}_{p_\mathrm{T}}$, (d) $p_\mathrm{T}^{\text{di-}J/\psi}$, (e) $y_{\text{di-}J/\psi}$, (f) $m_{\text{di-}J/\psi}$, (g) $p_\mathrm{T}^{J/\psi}$, (h) $y_{J/\psi}$, (i) θ_CS and (j) ϕ_CS. The error bars represent the statistical and systematic uncertainties added in quadrature.

dependence of the tracking efficiency correction, branching fraction and luminosity measurements are assumed as completely correlated between the total and DPS cross-sections, and the rest are assumed as uncorrelated.

5.8.3 DPS and SPS differential cross-sections

The differential cross-sections for DPS process can be obtained by scaling the normalised DPS shapes to the integrated DPS cross-section, and the result are shown in Fig-

ure 5.28 as red data points. The differential cross-sections including both SPS and DPS (SPS+DPS) contributions are also shown in Figure 5.28 as black data points, which are the same as those in Figure 5.24. With the DPS differential cross-sections subtracted from the SPS+DPS differential cross-sections, the SPS differential cross-sections are obtained and shown in Figure 5.28 as blue data points, and can be used for further study of gluon TMD PDFs. The differential cross-sections for SPS process are also listed in Tables B.11–B.20 in Appendix B.

Figure 5.28(a) shows that the Δy distribution for DPS process is wider than that for SPS process. The SPS cross-sections are consistent with zero in the range $1.8 < \Delta y < 2.5$, which verifies the choice of the DPS-dominated range in the separation of DPS contribution. As shown in Figure 5.28(b), the $\Delta\phi$ distribution for DPS process is flat, and that for SPS process peaks at $\Delta\phi = 0$ and π. The distributions of $\mathcal{A}_{p_{\mathrm{T}}}$ and $m_{\text{di-}J/\psi}$ for DPS process are both a bit wider than those for SPS process, as shown in Figures 5.28(c) and 5.28(f). The di-J/ψ mass spectrum for SPS process can be used to search for and study the exotic states. The $X(6900)$ peak which has been observed by the LHCb collaboration in the di-J/ψ mass spectrum recently[195] is very narrow, and its production ratio with respect to the whole di-J/ψ spectrum is measured to be only $1.1 \pm 0.4(\text{stat.}) \pm 0.3(\text{syst.})\%$. Therefore, it is not seen in this wide mass spectrum in Figure 5.28(f). Figure 5.28(d) shows that the $p_{\mathrm{T}}^{\text{di-}J/\psi}$ spectrum for SPS process seems a bit wider than that for DPS process. The differential cross-sections $\mathrm{d}\sigma/\mathrm{d}p_{\mathrm{T}}^{\text{di-}J/\psi}$ and $\mathrm{d}\sigma/\mathrm{d}\phi_{\mathrm{CS}}$ for SPS process in the TMD region, $p_{\mathrm{T}}^{\text{di-}J/\psi} < \langle m_{\text{di-}J/\psi} \rangle/2$, can be used to study gluon TMD PDFs, as detailed in Section 5.8.5.

5.8.4 Comparison with SPS predictions

The incomplete (no loops) NLO color-singlet (NLO* CS) predictions[120] of di-J/ψ production in SPS process can be obtained from HELAC-Onia[196-197], an automatic matrix element generator for heavy quarkonium physics.

The SPS differential cross-sections are compared with the NLO* CS predictions, as shown in Fig. 5.29. The data points for SPS+DPS are shown in Fig. 5.29 as well. The theoretical uncertainties include uncertainties due to factorisation and renormalisation scales and PDF uncertainties. The uncertainties from the variation of factorisation and renormalisation scales are dominant. The predicted and measured results are consistent within the large theoretical uncertainties.

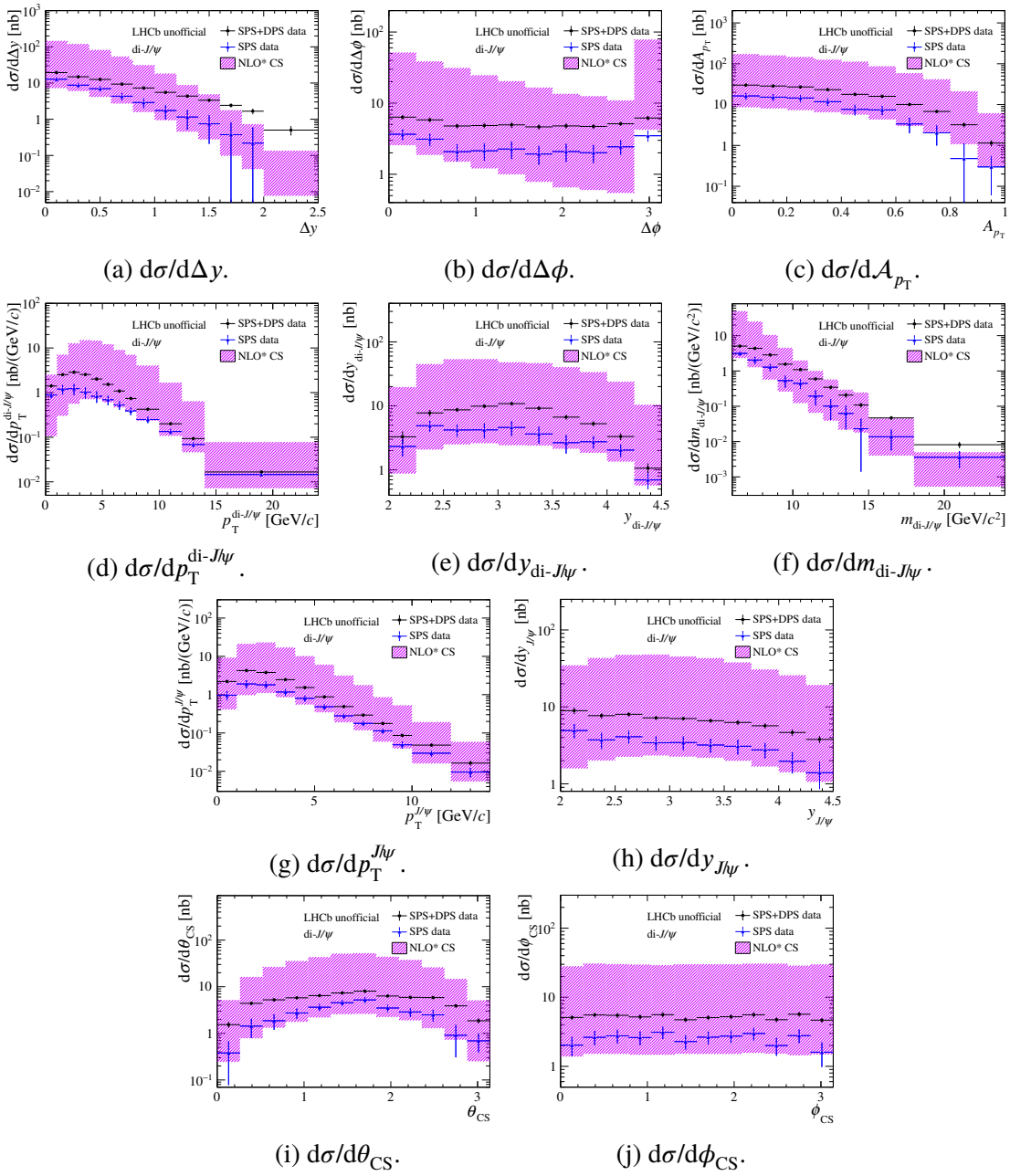

(a) $\mathrm{d}\sigma/\mathrm{d}\Delta y$. (b) $\mathrm{d}\sigma/\mathrm{d}\Delta\phi$. (c) $\mathrm{d}\sigma/\mathrm{d}\mathcal{A}_{p_\mathrm{T}}$.

(d) $\mathrm{d}\sigma/\mathrm{d}p_\mathrm{T}^{\text{di-}J/\psi}$. (e) $\mathrm{d}\sigma/\mathrm{d}y_{\text{di-}J/\psi}$. (f) $\mathrm{d}\sigma/\mathrm{d}m_{\text{di-}J/\psi}$.

(g) $\mathrm{d}\sigma/\mathrm{d}p_\mathrm{T}^{J/\psi}$. (h) $\mathrm{d}\sigma/\mathrm{d}y_{J/\psi}$.

(i) $\mathrm{d}\sigma/\mathrm{d}\theta_{\mathrm{CS}}$. (j) $\mathrm{d}\sigma/\mathrm{d}\phi_{\mathrm{CS}}$.

Figure 5.29 Differential cross-section of di-J/ψ production for SPS+DPS and SPS as a function of (a) Δy, (b) $\Delta\phi$, (c) $\mathcal{A}_{p_\mathrm{T}}$, (d) $p_\mathrm{T}^{\text{di-}J/\psi}$, (e) $y_{\text{di-}J/\psi}$, (f) $m_{\text{di-}J/\psi}$, (g) $p_\mathrm{T}^{J/\psi}$, (h) $y_{J/\psi}$, (i) θ_{CS} and (j) ϕ_{CS}, compared with the NLO* CS predictions for SPS[120,196-197].

5.8.5 Study of gluon TMD PDFs

As described in Section 2.6.2, the gluon TMD PDFs f_1^g and $h_1^{\perp g}$ inside unpolarised protons, representing unpolarised and linearly polarised gluons respectively, can be probed by the $p_\mathrm{T}^{\text{di-}J/\psi}$ spectrum and the ϕ_{CS} distribution in the TMD region, $p_\mathrm{T}^{\text{di-}J/\psi} < \langle m_{\text{di-}J/\psi} \rangle/2$. The information related to the gluon transverse momentum k_T on f_1^g was extracted for the first time from the $p_\mathrm{T}^{\text{di-}J/\psi}$ spectrum by theorists[126] based on

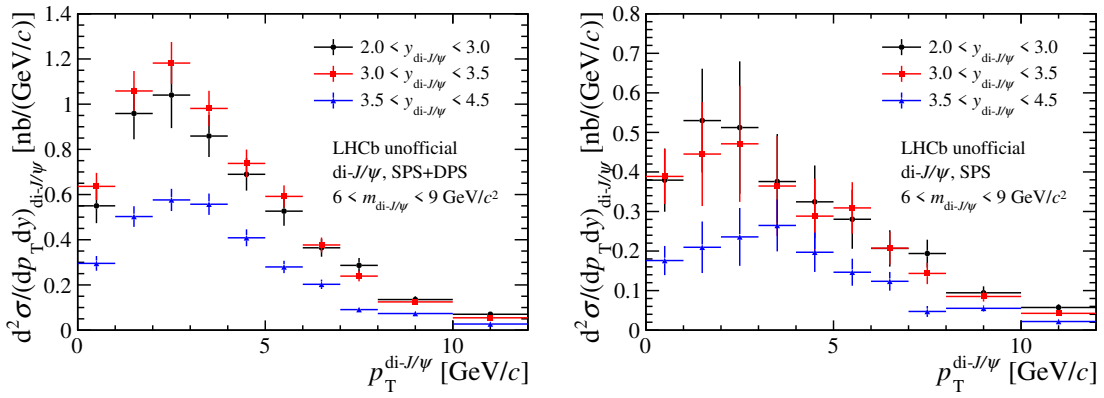

(a) $p_{\mathrm{T}}^{\text{di-}J/\psi}$ spectrum for SPS+DPS. (b) $p_{\mathrm{T}}^{\text{di-}J/\psi}$ spectrum for SPS.

Figure 5.30 Differential cross-section of di-J/ψ production as a function of $p_{\mathrm{T}}^{\text{di-}J/\psi}$ in three different intervals of $y_{\text{di-}J/\psi}$ with $6 < m_{\text{di-}J/\psi} < 9\,\text{GeV}$ for (a) SPS+DPS and (b) SPS. The cross-section is divided by the widths of $p_{\mathrm{T}}^{\text{di-}J/\psi}$ interval and the $y_{\text{di-}J/\psi}$ interval.

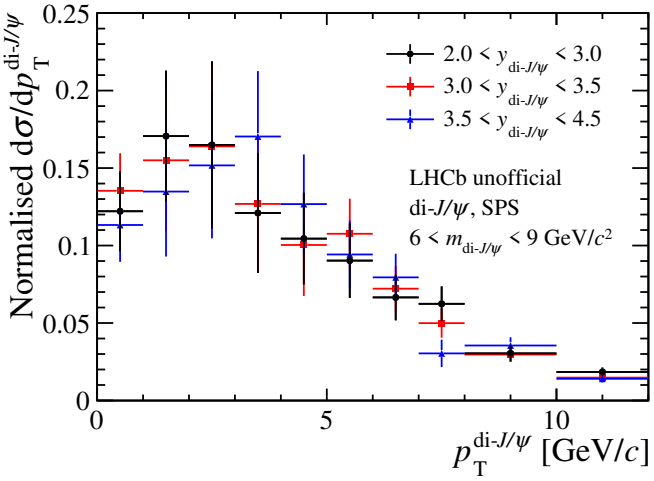

Figure 5.31 Normalised $p_{\mathrm{T}}^{\text{di-}J/\psi}$ spectra in three different intervals of $y_{\text{di-}J/\psi}$ with $6 < m_{\text{di-}J/\psi} < 9\,\text{GeV}$ in SPS.

the previous measurement of di-J/ψ production by the LHCb collaboration[130], and the extracted value is $\langle k_{\mathrm{T}}^2 \rangle = 3.3 \pm 0.8\,\text{GeV}^2$. With much more statistics in this analysis, the $p_{\mathrm{T}}^{\text{di-}J/\psi}$ spectrum is measured in different intervals of $y_{\text{di-}J/\psi}$ and $m_{\text{di-}J/\psi}$, which provides more information for the study of the gluon TMD PDF f_1^g. The other TMD PDF $h_1^{\perp g}$, which has not been observed, is probed through the ϕ_{CS} distribution in the TMD region in this analysis.

It was pointed out by theorists in Ref. [125] that the variation of the momentum fractions $x_{1,2} = m_{\text{di-}J/\psi}\, e^{\pm y_{\text{di-}J/\psi}} / \sqrt{s}$ does not have any significant impact on the shape of the $p_{\mathrm{T}}^{\text{di-}J/\psi}$ spectrum. In order to test this, the $p_{\mathrm{T}}^{\text{di-}J/\psi}$ spectrum is measured in three different intervals of $y_{\text{di-}J/\psi}$ with $6 < m_{\text{di-}J/\psi} < 9\,\text{GeV}$, as shown in Figure 5.30 both for SPS+DPS and SPS, and the results are listed in Tables B.21 and B.22 in Appendix B. Regarding

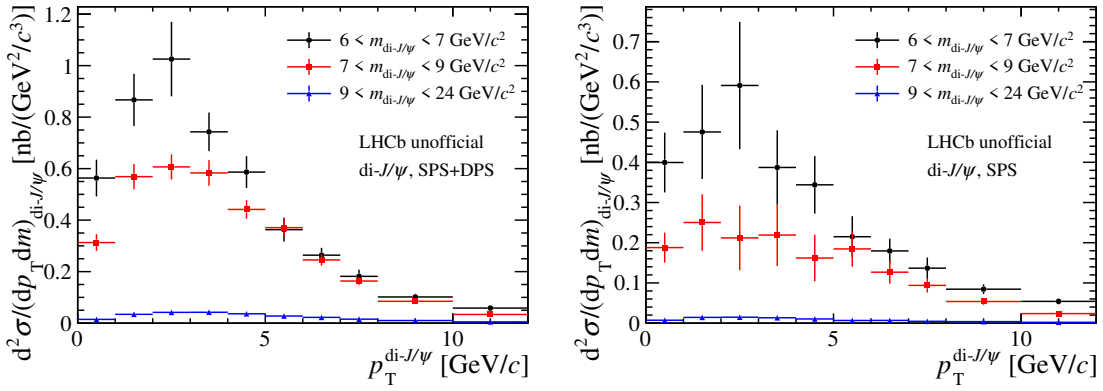

(a) $p_{\mathrm{T}}^{\text{di-}J/\psi}$ spectrum for SPS+DPS. (b) $p_{\mathrm{T}}^{\text{di-}J/\psi}$ spectrum for SPS.

Figure 5.32 Differential cross-section of di-J/ψ production as a function of $p_{\mathrm{T}}^{\text{di-}J/\psi}$ in three different intervals of $m_{\text{di-}J/\psi}$ for (a) SPS+DPS and (b) SPS. The cross-section is divided by the widths of $p_{\mathrm{T}}^{\text{di-}J/\psi}$ interval and the $m_{\text{di-}J/\psi}$ interval.

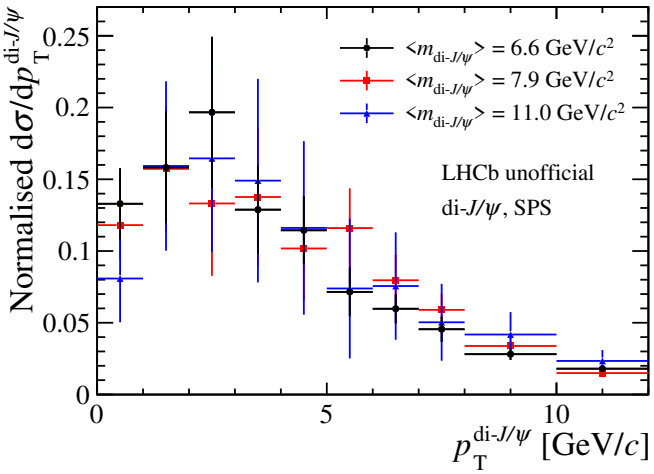

Figure 5.33 Normalised $p_{\mathrm{T}}^{\text{di-}J/\psi}$ spectra in three intervals of $m_{\text{di-}J/\psi}$ with different expected values $\langle m_{\text{di-}J/\psi}\rangle$ in SPS.

the SPS results, the subtraction of DPS contribution is performed using the same method as described in Section 5.8.2. Normalised $p_{\mathrm{T}}^{\text{di-}J/\psi}$ spectra in three different intervals of $y_{\text{di-}J/\psi}$ with $6 < m_{\text{di-}J/\psi} < 9$ GeV are shown in Figure 5.31 to compare their shapes. All these three distributions are consistent with each other within the large uncertainties. In this case, the following measurements related to gluon TMD PDFs are performed in the whole fiducial range of rapidity $2.0 < y < 4.5$.

In addition, the study of the dependence of gluon TMD PDFs on scale, requires the measurements of $p_{\mathrm{T}}^{\text{di-}J/\psi}$ spectrum at different $\langle m_{\text{di-}J/\psi}\rangle$. Thus, the p_{T} spectrum of di-J/ψ is measured in three intervals of $m_{\text{di-}J/\psi}$ with the expected value $\langle m_{\text{di-}J/\psi}\rangle = 6.6$, 7.9 and 11.0 GeV respectively, as shown in Figure 5.32 both for SPS+DPS and SPS, and the results are listed in Tables B.23 and B.24 in Appendix B. Normalised $p_{\mathrm{T}}^{\text{di-}J/\psi}$ spectra in

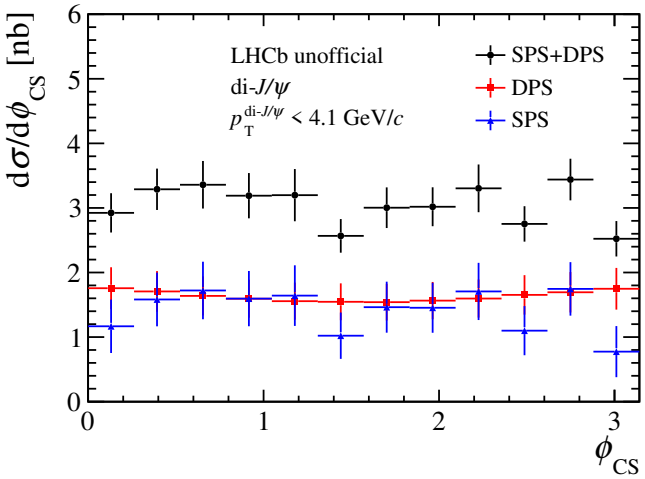

Figure 5.34 Distribution of ϕ_{CS} for SPS+DPS, DPS and SPS in the TMD region $p_T^{\text{di-}J/\psi} < 4.1$ GeV. The error bars represent the statistical and systematic uncertainties added in quadrature.

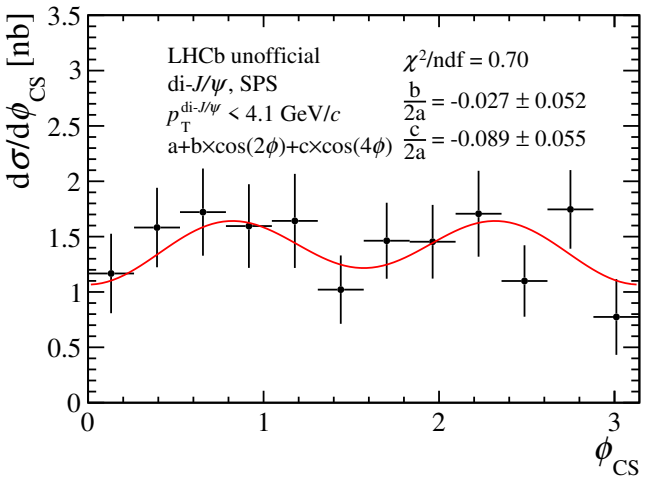

Figure 5.35 Distribution of ϕ_{CS} for SPS in the TMD region $p_T^{\text{di-}J/\psi} < 4.1$ GeV, together with the fit using the function $a + b \times \cos 2\phi_{CS} + c \times \cos 4\phi_{CS}$. The error bars represent the statistical and uncorrelated systematic uncertainties added in quadrature.

three different intervals of $m_{\text{di-}J/\psi}$ are shown in Figure 5.33 to compare their shapes. As predicted by theorists in Ref. [125], the p_T spectrum in the TMD region will broaden as $m_{\text{di-}J/\psi}$ increases, but no obvious broadening of the p_T spectrum is seen in Figure 5.33 due to the large uncertainties.

As mentioned in Section 2.6.2, the presence of polarised gluons, denoted by the TMD PDF $h_1^{\perp g}$, inside the unpolarised proton leads to asymmetries of the ϕ_{CS} distribution in the TMD region. In this analysis, the ϕ_{CS} distribution is measured in the TMD region $p_T^{\text{di-}J/\psi} < 4.1$ GeV, since the expected value of $m_{\text{di-}J/\psi}$ in the whole fiducial range is $\langle m_{\text{di-}J/\psi} \rangle = 8.2$ GeV. The distributions for SPS+DPS, DPS and SPS are shown in Fig-

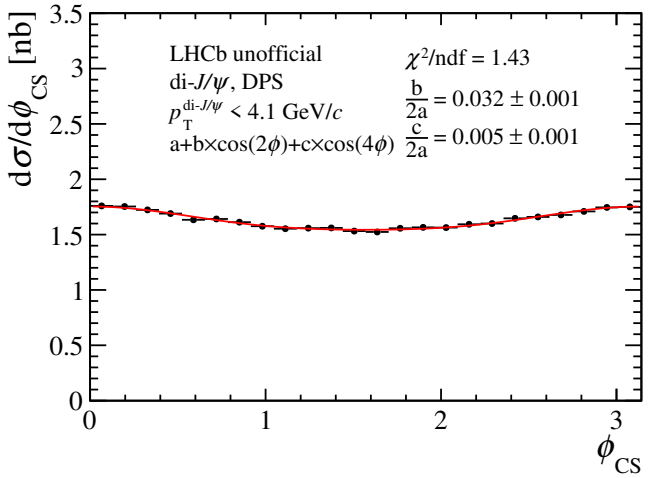

Figure 5.36 Distribution of ϕ_{CS} for DPS in the TMD region $p_{\text{T}}^{\text{di-}J/\psi} < 4.1$ GeV, together with the fit using the function $a + b \times \cos 2\phi_{\text{CS}} + c \times \cos 4\phi_{\text{CS}}$. The error bars only represent uncertainties due to the finite number of pseudo-experiments based on the single-J/ψ production cross-sections.

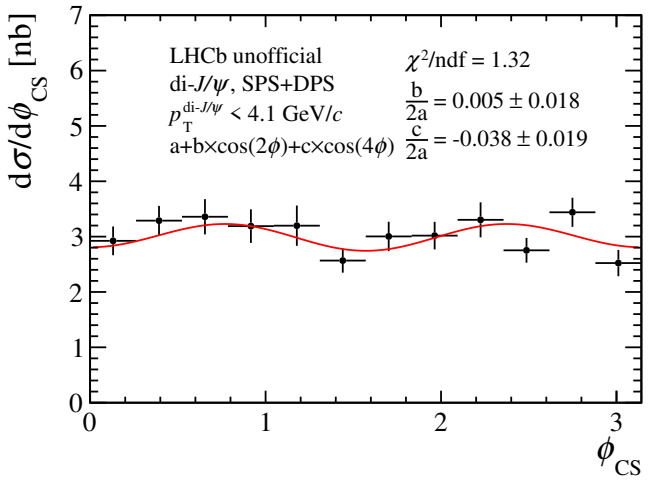

Figure 5.37 Distribution of ϕ_{CS} for SPS+DPS in the TMD region $p_{\text{T}}^{\text{di-}J/\psi} < 4.1$ GeV, together with the fit using the function $a + b \times \cos 2\phi_{\text{CS}} + c \times \cos 4\phi_{\text{CS}}$. The error bars represent the statistical and uncorrelated systematic uncertainties added in quadrature.

ure 5.34. According to Eq. 2.33, the ϕ_{CS} distribution for SPS can be described by the function

$$F(\phi_{\text{CS}}; a, b, c) = a + b \times \cos 2\phi_{\text{CS}} + c \times \cos 4\phi_{\text{CS}}, \tag{5.30}$$

where the parameter ratios $\frac{b}{2a}$ and $\frac{c}{2a}$ respectively equal to the expected values $\langle \cos 2\phi_{\text{CS}} \rangle$ and $\langle \cos 4\phi_{\text{CS}} \rangle$ defined in Eq. 2.38 and 2.39. A fit is performed to the SPS distribution using the function $F(\phi_{\text{CS}}; a, b, c)$ as shown in Figure 5.35. For systematic uncertainties, only the uncertainties propagated from the statistical uncertainties of efficiencies and tracking correction factors are considered as uncorrelated between intervals, and the rest are assumed as correlated. The uncertainties on the values of $\text{d}\sigma/\text{d}\phi_{\text{CS}}$ in Figure 5.35 are the

statistical and uncorrelated systematical uncertainties added in quadrature. The correlated systematic uncertainties between intervals are not considered in the fit, since they will overestimate the uncertainties on the parameter ratios $\frac{b}{2a}$ and $\frac{c}{2a}$. The expected values $\langle\cos 2\phi_{\mathrm{CS}}\rangle$ and $\langle\cos 4\phi_{\mathrm{CS}}\rangle$ can also be calculated as

$$\langle\cos 2\phi_{\mathrm{CS}}\rangle = \frac{\sum_i \frac{\mathrm{d}\sigma}{\mathrm{d}\phi_{\mathrm{CS}}}\big|_i \Delta\phi_{\mathrm{CS}i} \cos 2\phi_{\mathrm{CS}i}}{\sum_i \frac{\mathrm{d}\sigma}{\mathrm{d}\phi_{\mathrm{CS}}}\big|_i \Delta\phi_{\mathrm{CS}i}}, \tag{5.31}$$

$$\langle\cos 4\phi_{\mathrm{CS}}\rangle = \frac{\sum_i \frac{\mathrm{d}\sigma}{\mathrm{d}\phi_{\mathrm{CS}}}\big|_i \Delta\phi_{\mathrm{CS}i} \cos 4\phi_{\mathrm{CS}i}}{\sum_i \frac{\mathrm{d}\sigma}{\mathrm{d}\phi_{\mathrm{CS}}}\big|_i \Delta\phi_{\mathrm{CS}i}}, \tag{5.32}$$

where the index i denotes each interval, $\Delta\phi_{\mathrm{CS}i}$ is the interval width and $\phi_{\mathrm{CS}i}$ is the interval centre. The results of $\langle\cos 2\phi_{\mathrm{CS}}\rangle$ and $\langle\cos 4\phi_{\mathrm{CS}}\rangle$ extracted from the ϕ_{CS} distribution for SPS are

$$\langle\cos 2\phi_{\mathrm{CS}}\rangle = -0.029 \pm 0.050(\mathrm{stat.}) \pm 0.009(\mathrm{syst.}),$$
$$\langle\cos 4\phi_{\mathrm{CS}}\rangle = -0.087 \pm 0.052(\mathrm{stat.}) \pm 0.013(\mathrm{syst.}),$$

where the systematic uncertainties cancel a lot, and the statistical uncertainties are dominant. These two values are both consistent with zero within the large statistical uncertainties. A relatively large part of the statistical uncertainty arises from the subtraction of DPS contribution. A fit with the same function $F(\phi_{\mathrm{CS}}; a, b, c)$ is also performed to the ϕ_{CS} distribution for DPS. Since the uncertainties for DPS are all assigned to the integrated cross-section and do not affect the shape of ϕ_{CS} distribution, they are excluded in the fit to the DPS distribution. The result of the parameter ratio $\frac{c}{2a}$ for DPS is more than one magnitude smaller than the central value for SPS, so the $\langle\cos 4\phi_{\mathrm{CS}}\rangle$ can be directly extracted in the ϕ_{CS} distribution for SPS+DPS. The same fit is performed to the SPS+DPS distribution, as shown in Figure 5.37. And according to Eq. 5.32, the extracted value of $\langle\cos 4\phi_{\mathrm{CS}}\rangle$ from the SPS+DPS distribution is

$$\langle\cos 4\phi_{\mathrm{CS}}\rangle = -0.038 \pm 0.018(\mathrm{stat.}) \pm 0.003(\mathrm{syst.}),$$

where the systematic uncertainties cancel mostly, and the relative statistical uncertainty is smaller than that of the extracted value from the SPS distribution. A small difference between the measured $\langle\cos 4\phi_{\mathrm{CS}}\rangle$ and zero is found, but they are still consistent within two standard deviations. Therefore, only a hint for azimuthal asymmetries is seen in this analysis, and the precision is still limited by the large statistical fluctuation.

5.9 Cross-section results of J/ψ-$\psi(2S)$ production

The cross-section of J/ψ-$\psi(2S)$ production with both J/ψ and $\psi(2S)$ mesons in the range $0 < p_{\mathrm{T}} < 14\,\mathrm{GeV}$ and $2.0 < y < 4.5$ is

$$\sigma_{J/\psi\text{-}\psi(2S)} = 4.49 \pm 0.71(\mathrm{stat.}) \pm 0.26(\mathrm{syst.})\,\mathrm{nb},$$

where the first uncertainty is statistical and the second is systematic. The uncertainty on the result of J/ψ-$\psi(2S)$ production is dominated by the statistical uncertainty. The cross-section is measured assuming negligible polarisation of the J/ψ and $\psi(2S)$ mesons. If the polarisation parameter λ_θ is assumed to be $\lambda_\theta = +0.2$ (-0.2) for both J/ψ and $\psi(2S)$ mesons in the helicity frame, the cross-section of J/ψ-$\psi(2S)$ production changes by $+6.5\%$ (-6.6%).

According to Eq. 2.46, the ratio between the product of single-J/ψ and single-$\psi(2S)$ cross-sections and the J/ψ-$\psi(2S)$ cross-section $\frac{\sigma_{J/\psi}\sigma_{\psi(2S)}}{\sigma_{J/\psi\text{-}\psi(2S)}}$ can be interpreted as the effective cross-section σ_{eff} if the J/ψ-$\psi(2S)$ production is totally contributed by DPS process. Since the production cross-section of $\psi(2S)$ mesons $\sigma_{\psi(2S)}$ is only measured in the range $p_{\mathrm{T}}^{\psi(2S)} > 2\,\mathrm{GeV}$ by the LHCb collaboration, the ratio is only available in the fiducial range $0\ (2) < p_{\mathrm{T}}^{J/\psi\,(\psi(2S))} < 14\,\mathrm{GeV}$ and $2.0 < y_{J/\psi\,(\psi(2S))} < 4.5$. In this fiducial range, the single-J/ψ cross-section is $\sigma_{J/\psi} = 15.03 \pm 0.03(\mathrm{stat.}) \pm 0.94(\mathrm{syst.})\,\mu\mathrm{b}$[63], the single-$\psi(2S)$ cross-section is $\sigma_{\psi(2S)} = 1.423 \pm 0.005(\mathrm{stat.}) \pm 0.099(\mathrm{syst.})\,\mu\mathrm{b}$[64], and the cross-section of J/ψ-$\psi(2S)$ production is

$$\sigma_{J/\psi\text{-}\psi(2S)} = 3.14 \pm 0.57(\mathrm{stat.}) \pm 0.18(\mathrm{syst.})\,\mathrm{nb},$$

In the range $0\ (2) < p_{\mathrm{T}}^{J/\psi\,(\psi(2S))} < 14\,\mathrm{GeV}$ and $2.0 < y_{J/\psi\,(\psi(2S))} < 4.5$, the ratio is

$$\frac{\sigma_{J/\psi}\sigma_{\psi(2S)}}{\sigma_{J/\psi\text{-}\psi(2S)}} = 6.8 \pm 1.2(\mathrm{stat.}) \pm 0.7(\mathrm{syst.})\,\mathrm{mb},$$

where the systematic uncertainties of the single-J/ψ, single-$\psi(2S)$ and J/ψ-$\psi(2S)$ cross-sections are treated as uncorrelated.

5.9.1 Differential cross-sections

The differential cross-section of J/ψ-$\psi(2S)$ production is measured as functions of Δy, $\Delta\phi$, $p_{\mathrm{T}}^{J/\psi\text{-}\psi(2S)}$, $y_{J/\psi\text{-}\psi(2S)}$ and $m_{J/\psi\text{-}\psi(2S)}$. Due to the limitation of statistics, the differential cross-sections of J/ψ-$\psi(2S)$ production are calculated using the *sWeight* based on the global fit rather than the fit in each kinematic interval. The correlation between these kinematic variables and discriminating variables used in the *sPlot* method leads to

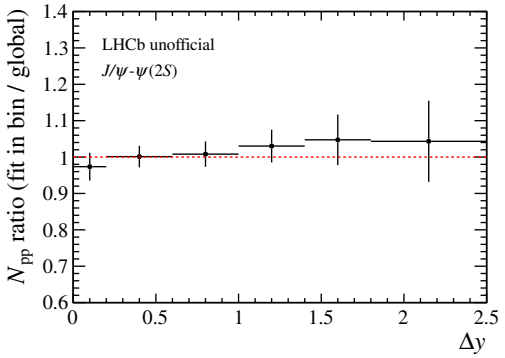

(a) Correction factors in Δy intervals.

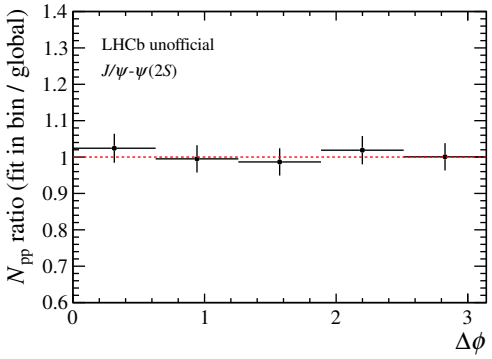

(b) Correction factors in $\Delta\phi$ intervals.

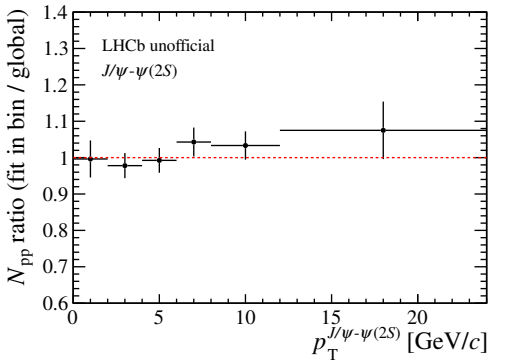

(c) Correction factors in $p_{\mathrm{T}}^{J/\psi\text{-}\psi(2S)}$ intervals.

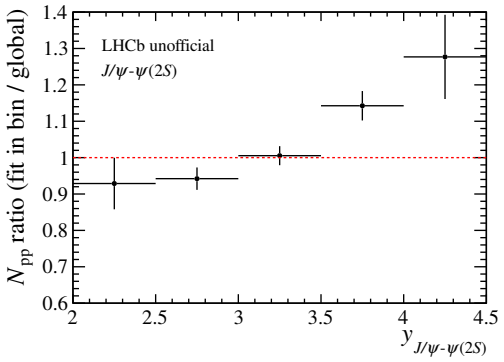

(d) Correction factors in $y_{J/\psi\text{-}\psi(2S)}$ intervals.

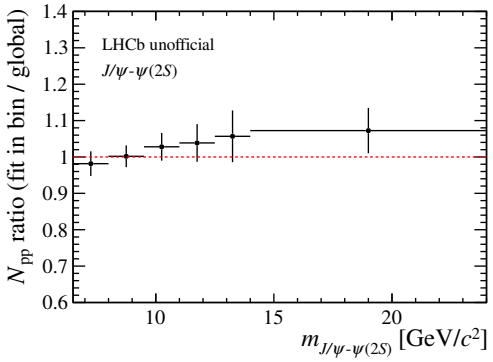

(e) Correction factors in $m_{J/\psi\text{-}\psi(2S)}$ intervals.

Figure 5.38 Correction factors for yields of J/ψ-$\psi(2S)$ signals in intervals of (a) Δy, (b) $\Delta\phi$, (c) $p_{\mathrm{T}}^{J/\psi\text{-}\psi(2S)}$, (d) $y_{J/\psi\text{-}\psi(2S)}$ and (e) $m_{J/\psi\text{-}\psi(2S)}$.

the biases of yields. These biases are corrected by the study of the toy J/ψ-$\psi(2S)$ sample with single-J/ψ and single-$\psi(2S)$ candidates in data combined randomly. The yield in each interval is extracted from the toy sample in two ways: using the *sWeight* based on the global fit, and directly from the fit in each kinematic interval. The ratio of yields between these two ways are taken as the correction factors, as shown in Figure 5.38. The error bars in Figure 5.38 come from the limited size of the toy sample, and they are considered as another systematic uncertainty on differential cross-sections of J/ψ-$\psi(2S)$ production. It varies up to 10.7% depending on the kinematic intervals. Other systematic uncertain-

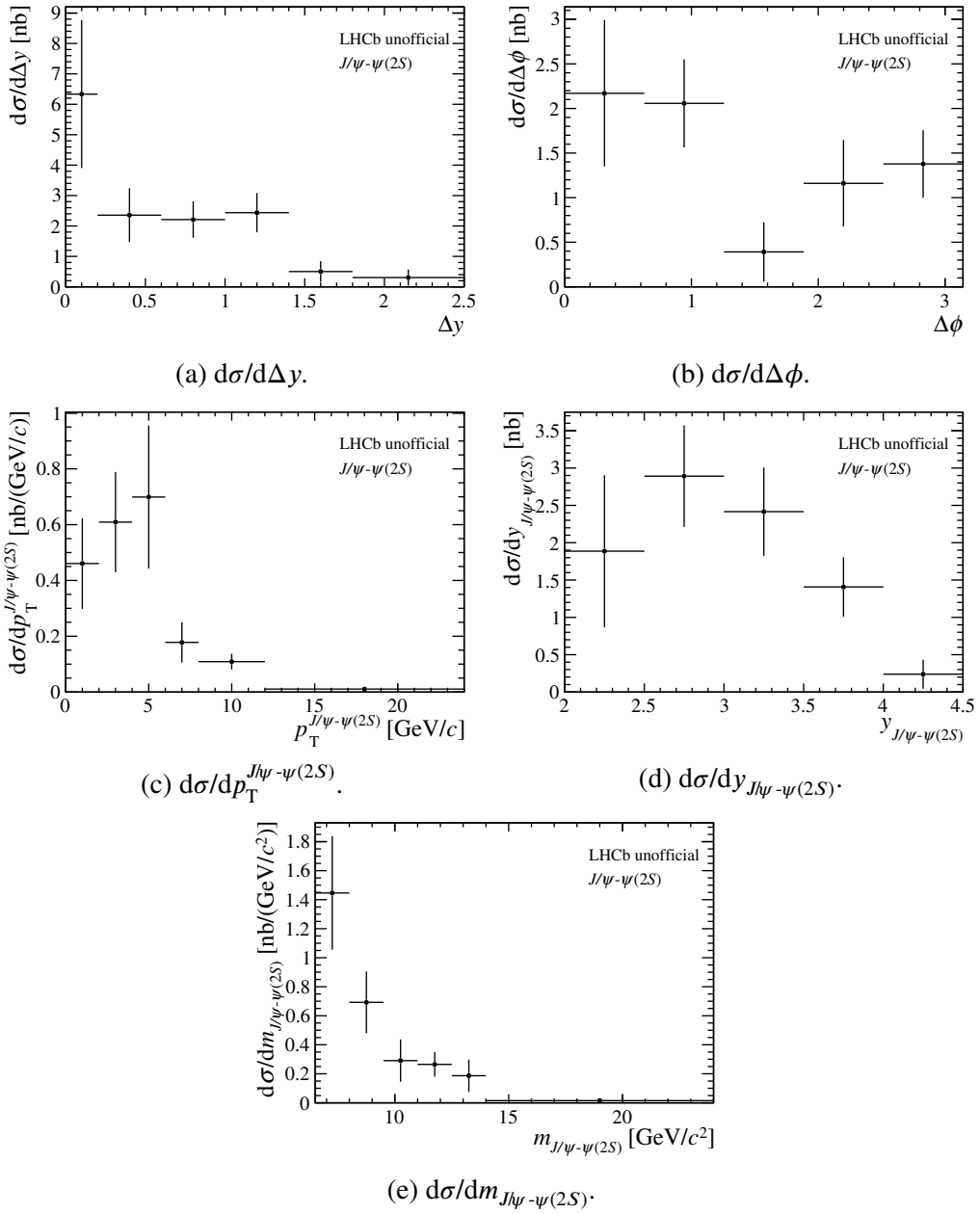

(a) $\mathrm{d}\sigma/\mathrm{d}\Delta y$.

(b) $\mathrm{d}\sigma/\mathrm{d}\Delta\phi$.

(c) $\mathrm{d}\sigma/\mathrm{d}p_{\mathrm{T}}^{J\!/\!\psi\text{-}\psi(2S)}$.

(d) $\mathrm{d}\sigma/\mathrm{d}y_{J\!/\!\psi\text{-}\psi(2S)}$.

(e) $\mathrm{d}\sigma/\mathrm{d}m_{J\!/\!\psi\text{-}\psi(2S)}$.

Figure 5.39 Differential cross-section of $J\!/\!\psi\text{-}\psi(2S)$ production as a function of (a) Δy, (b) $\Delta\phi$, (c) $p_{\mathrm{T}}^{J\!/\!\psi\text{-}\psi(2S)}$, (d) $y_{J\!/\!\psi\text{-}\psi(2S)}$ and (e) $m_{J\!/\!\psi\text{-}\psi(2S)}$. The error bars represent the statistical and systematic uncertainties added in quadrature.

ties on differential cross-sections are presented in Section 5.7 separately for every source. With biases corrected and statistical and systematic uncertainties taken into account, differential cross-sections of $J\!/\!\psi\text{-}\psi(2S)$ production are shown in Figure 5.39, and are listed in Tables B.25–B.29 in Appendix B.

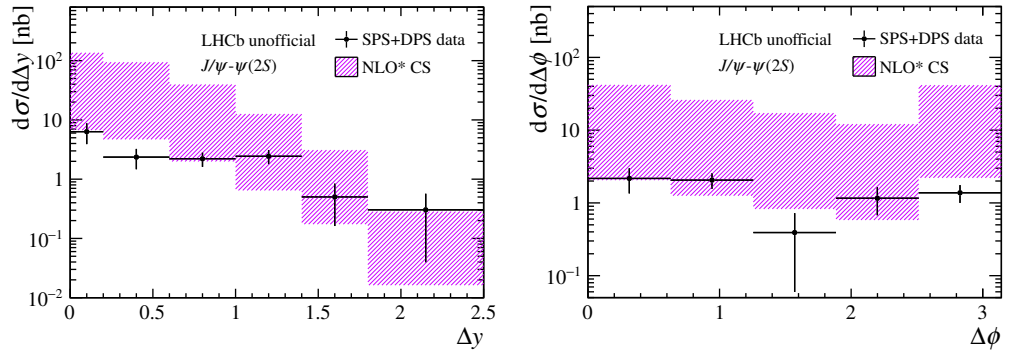

(a) $\mathrm{d}\sigma/\mathrm{d}\Delta y$.

(b) $\mathrm{d}\sigma/\mathrm{d}\Delta\phi$.

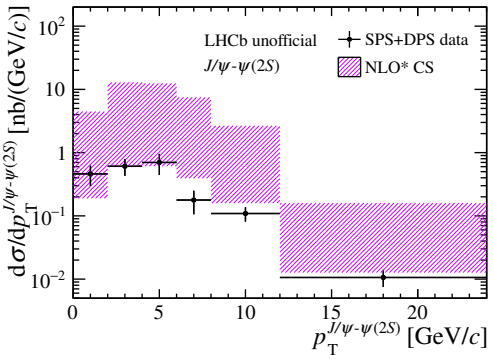

(c) $\mathrm{d}\sigma/\mathrm{d}p_{\mathrm{T}}^{J/\psi\text{-}\psi(2S)}$.

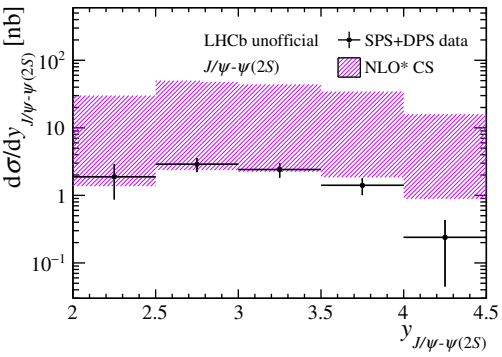

(d) $\mathrm{d}\sigma/\mathrm{d}y_{J/\psi\text{-}\psi(2S)}$.

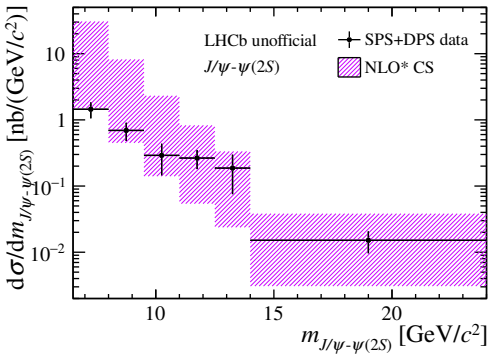

(e) $\mathrm{d}\sigma/\mathrm{d}m_{J/\psi\text{-}\psi(2S)}$.

Figure 5.40 Differential cross-section of J/ψ-$\psi(2S)$ production for SPS+DPS as a function of (a) Δy, (b) $\Delta\phi$, (c) $p_{\mathrm{T}}^{J/\psi\text{-}\psi(2S)}$, (d) $y_{J/\psi\text{-}\psi(2S)}$ and (e) $m_{J/\psi\text{-}\psi(2S)}$, compared with the NLO* CS predictions for SPS[120,196-197].

5.9.2 Comparison with SPS predictions

The NLO* CS predictions[120] of J/ψ-$\psi(2S)$ production in SPS process can be obtained from HELAC-Onia[196-197] as well. The NLO* CS predictions are compared with the measured SPS+DPS results of J/ψ-$\psi(2S)$ production as shown in Figure 5.40, since the SPS and DPS contributions are unable to be separated because of the limitation of statistics. The predictions seem larger than the SPS+DPS data points, but they are still

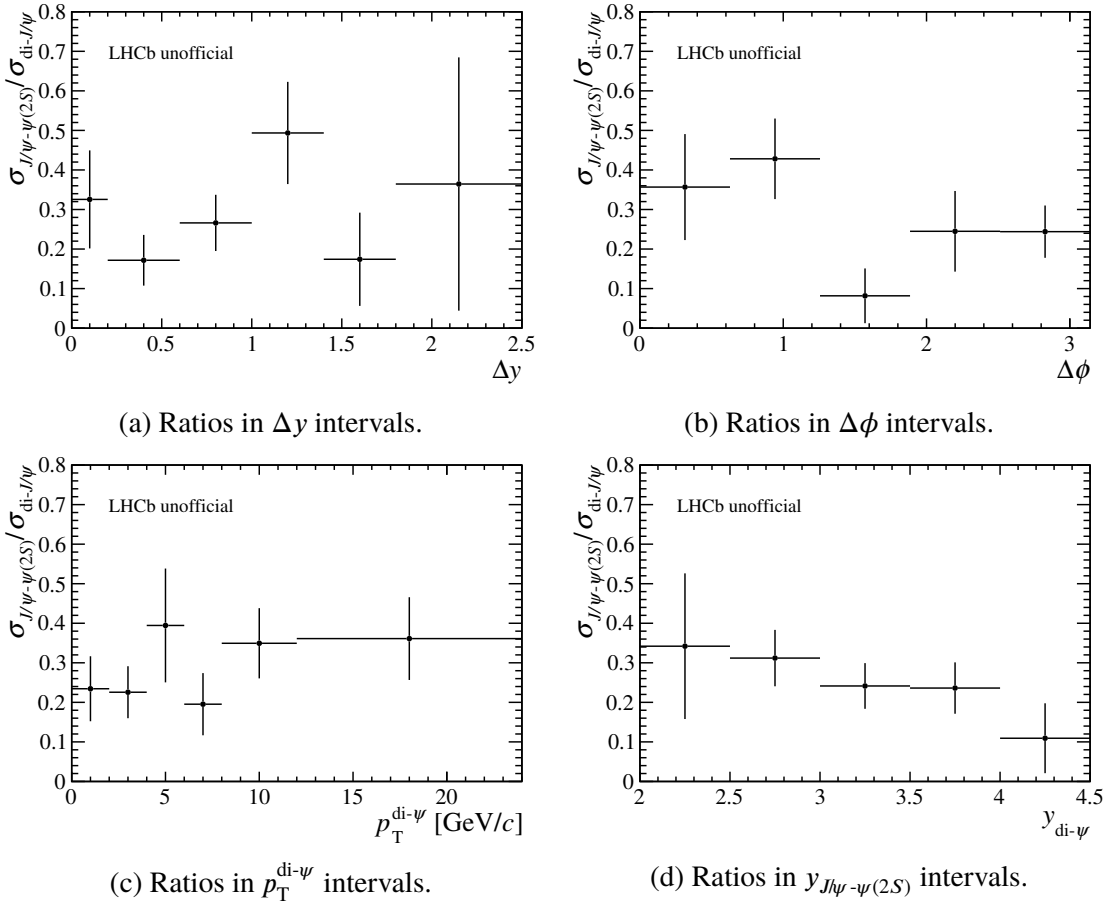

(a) Ratios in Δy intervals.

(b) Ratios in $\Delta\phi$ intervals.

(c) Ratios in $p_{\text{T}}^{\text{di-}\psi}$ intervals.

(d) Ratios in $y_{J/\psi\text{-}\psi(2S)}$ intervals.

Figure 5.41 Cross-section ratios between J/ψ-$\psi(2S)$ and di-J/ψ production as a function of (a) Δy, (b) $\Delta\phi$, (c) $p_{\text{T}}^{\text{di-}\psi}$ and (d) $y_{\text{di-}\psi}$. The error bars represent the statistical and systematic uncertainties added in quadrature.

consistent within the large uncertainties.

5.9.3 Cross-section ratio between di-J/ψ and J/ψ-$\psi(2S)$ production

The cross-section ratio between J/ψ-$\psi(2S)$ and di-J/ψ production is

$$\frac{\sigma_{J/\psi\text{-}\psi(2S)}}{\sigma_{\text{di-}J/\psi}} = 0.274 \pm 0.044(\text{stat.}) \pm 0.008(\text{syst.}),$$

where the systematic uncertainties due to the signal mass model, non-prompt contribution, wrong PV association, efficiency and correction factor binning scheme, multiplicity dependence of the tracking efficiency, trigger efficiency and luminosity measurement are assumed as completely correlated. The uncertainty propagated from branching fractions is 2.2% on the ratio, and the rest uncertainties are considered as uncorrelated. The uncertainty on the cross-section ratio is dominated by the statistical uncertainty.

The cross-section ratios are also measured as functions of Δy, $\Delta\phi$, $p_{\text{T}}^{\text{di-}\psi}$ and $y_{\text{di-}\psi}$, as shown in Figure 5.41. The results are also presented in Tables B.30–B.33 in Appendix B.

5.10 Conclusion

The cross-sections of di-J/ψ and J/ψ-$\psi(2S)$ production in pp collisions at $\sqrt{s} = 13\,\text{TeV}$ are measured using a data sample corresponding to an integrated luminosity of $4.18 \pm 0.08\,\text{fb}^{-1}$ collected by the LHCb experiment. For di-J/ψ production, the contributions from DPS and SPS are separated based on the differential cross-section as a function of Δy. The effective cross-section σ_{eff} is extracted for di-J/ψ production in DPS, and the result is consistent with the others measured through various processes. The differential cross-sections for di-J/ψ production in SPS are consistent with the NLO* CS predictions within the large theoretical uncertainties. The gluon TMD PDFs are probed via the $p_{\text{T}}^{\text{di-}J/\psi}$ spectrum and the ϕ_{CS} distribution of di-J/ψ production. No obvious broadening of the $p_{\text{T}}^{\text{di-}J/\psi}$ spectrum with the increasing $m_{\text{di-}J/\psi}$ is seen in the TMD region due to the large statistical uncertainties. A hint with a significance of around two standard deviations for azimuthal asymmetry is seen, and the precision is still limited by the large statistical fluctuation. The differential cross-sections of J/ψ-$\psi(2S)$ production are measured, as well as the cross-section ratio between J/ψ-$\psi(2S)$ and di-J/ψ. The NLO* CS predictions for SPS process seems larger than the cross-sections of J/ψ-$\psi(2S)$ production including both SPS and DPS contributions, but they are still consistent within the large theoretical uncertainties.

CHAPTER 6 SUMMARY AND PROSPECT

In summary, the measurement of J/ψ production cross-sections in pp collisions at $\sqrt{s} = 5\,\text{TeV}$, and the measurement of production cross-sections of double charmonium, including di-J/ψ and J/ψ-$\psi(2S)$, in pp collisions at $\sqrt{s} = 13\,\text{TeV}$ are presented in this thesis. The measured results provide tests of various theoretical descriptions of charmonium production mechanism in the QCD framework and useful information on the inner structure of proton. Such tests and information are helpful to advance our knowledge of the strong interaction.

The J/ψ production cross-sections in pp collisions at $\sqrt{s} = 5\,\text{TeV}$ are measured separately for prompt and non-prompt J/ψ mesons using a data sample corresponding to an integrated luminosity of $9.18 \pm 0.35\,\text{pb}^{-1}$ collected by the LHCb experiment. The production cross-sections are measured differentially as a function of p_T and y and separately for prompt and non-prompt J/ψ mesons. With the assumption of unpolarised J/ψ mesons, the production cross-sections integrated over the kinematic range $0 < p_\text{T} < 20\,\text{GeV}$ and $2.0 < y < 4.5$ are

$$\sigma_{\text{prompt } J/\psi} = 8.154 \pm 0.010(\text{stat.}) \pm 0.283(\text{syst.})\,\mu\text{b},$$
$$\sigma_{\text{non-prompt } J/\psi} = 0.820 \pm 0.003(\text{stat.}) \pm 0.034(\text{syst.})\,\mu\text{b},$$

where the first uncertainties are statistical and the second are systematic. The cross-section ratios of J/ψ production in pp collisions between 8 TeV and 5 TeV, and between 13 TeV and 5 TeV are also determined and compared with the corresponding theoretical predictions. The measured prompt J/ψ ratios are in good agreement with NLO NRQCD calculations in the high-p_T region, while a small tension is observed between data for prompt J/ψ in the low-p_T region and CGC+NRQCD calculations, which may indicate the need for further theoretical corrections. The FONLL calculations agree with the measured results for non-prompt J/ψ mesons well.

The cross-sections of di-J/ψ and J/ψ-$\psi(2S)$ production in pp collisions at $\sqrt{s} = 13\,\text{TeV}$ are measured using a data sample corresponding to an integrated luminosity of $4.18 \pm 0.08\,\text{fb}^{-1}$ collected by the LHCb experiment. The cross-sections with the J/ψ and $\psi(2S)$ mesons in the range $0 < p_\text{T} < 14\,\text{GeV}$ and $2.0 < y < 4.5$ are

$$\sigma_{\text{di-}J/\psi} = 16.36 \pm 0.28(\text{stat.}) \pm 0.88(\text{syst.})\,\text{nb},$$
$$\sigma_{J/\psi\text{-}\psi(2S)} = 4.46 \pm 0.72(\text{stat.}) \pm 0.26(\text{syst.})\,\text{nb},$$

where the first uncertainties are statistical and the second are systematic, assuming negligible polarisation of the J/ψ and $\psi(2S)$ mesons. The differential cross-sections of di-J/ψ and J/ψ -$\psi(2S)$ production are also measured as functions of several kinematic variables. For di-J/ψ production, DPS and SPS contributions are separated based on the differential cross-section $\mathrm{d}\sigma/\mathrm{d}\Delta y$ since DPS contribution is dominant in the large Δy region. The effective cross-section σ_{eff} extracted from DPS contribution is

$$\sigma_{\mathrm{eff}} = 13.1 \pm 1.8(\mathrm{stat.}) \pm 2.3(\mathrm{syst.})\,\mathrm{mb},$$

where the first uncertainty is statistical and the second is systematic, and the result is compatible with others extracted from different processes at different centre-of-mass energies. The differential cross-sections for SPS process are consistent with the NLO* CS predictions within the large theoretical uncertainties. In addition, the gluon TMD PDFs are probed via the $p_{\mathrm{T}}^{\text{di-}J/\psi}$ spectrum and the ϕ_{CS} distribution in the TMD region, $p_{\mathrm{T}}^{\text{di-}J/\psi} < \langle m_{\text{di-}J/\psi} \rangle/2$. No obvious broadening of the $p_{\mathrm{T}}^{\text{di-}J/\psi}$ spectrum as $m_{\text{di-}J/\psi}$ increases is seen due to the large statistical uncertainties. In the study of ϕ_{CS} distribution, a hint with a significance of around two standard deviations for azimuthal asymmetry is seen, but the precision is still limited by the large statistical fluctuation. For J/ψ -$\psi(2S)$ production, the separation of DPS and SPS contributions is impracticable currently due to the limitation of statistics. The NLO* CS predictions for SPS process seems larger than the cross-sections of J/ψ -$\psi(2S)$ production including both SPS and DPS contributions, but they are still consistent within the large theoretical uncertainties. The cross-section ratio between J/ψ -$\psi(2S)$ and di-J/ψ production is also measured. The experimental studies of di-J/ψ and J/ψ -$\psi(2S)$ production are both statistically limited, and more data are required to improve the measurement precision.

After a long shutdown of more than three years for maintenance, consolidation and upgrade, the LHC restarted in 2022. At the same time, the LHCb detector has been upgraded, so that it can operate at a instantaneous luminosity 5 times higher than before. By the end of 2030, it is expected to collect at least 50 fb^{-1} of pp collision data, which makes further experimental studies of charmonium production possible. For conventional production measurements, data can reach higher p_{T} and provide a more comprehensive test of theory. Precise measurements of charmonium polarisation, especially in each fiducial region, are also helpful to pin down the complexity of the charmonium production mechanism. Furthermore, more precise information on the charmonium production mechanism and the inner structure of proton can be extracted from the measurements of double char-

monium production. For di-J/ψ production, gluon TMD PDFs can be probed with higher precision. For J/ψ-$\psi(2S)$ production, DPS and SPS contributions can be separated for further studies of the feed-down to di-J/ψ states. All of these possible measurements in the near future will further improve our understanding of the strong interaction.

REFERENCES

[1] Aubert J J, et al. Experimental observation of a heavy particle J[J/OL]. Phys. Rev. Lett., 1974, 33: 1404-1406. DOI: 10.1103/PhysRevLett.33.1404.

[2] Augustin J E, et al. Discovery of a narrow resonance in e^+e^- annihilation[J/OL]. Phys. Rev. Lett., 1974, 33: 1406-1408. DOI: 10.1103/PhysRevLett.33.1406.

[3] Abrams G S, et al. The discovery of a second narrow resonance in e^+e^- annihilation[J/OL]. Phys. Rev. Lett., 1974, 33: 1453-1455. DOI: 10.1103/PhysRevLett.33.1453.

[4] Appelquist T, De Rujula A, Politzer H D, et al. Charmonium spectroscopy[J/OL]. Phys. Rev. Lett., 1975, 34: 365. DOI: 10.1103/PhysRevLett.34.365.

[5] Eichten E, Gottfried K, Kinoshita T, et al. The spectrum of charmonium[J/OL]. Phys. Rev. Lett., 1975, 34: 369-372. DOI: 10.1103/PhysRevLett.34.369.

[6] Eichten E, Gottfried K, Kinoshita T, et al. Charmonium: The model[J/OL]. Phys. Rev. D, 1978, 17: 3090. DOI: 10.1103/PhysRevD.17.3090.

[7] Bjorken J D, Glashow S L. Elementary particles and SU(4)[J/OL]. Phys. Lett., 1964, 11: 255-257. DOI: 10.1016/0031-9163(64)90433-0.

[8] Glashow S L, Iliopoulos J, Maiani L. Weak interactions with lepton-hadron symmetry[J/OL]. Phys. Rev. D, 1970, 2: 1285-1292. DOI: 10.1103/PhysRevD.2.1285.

[9] Workman R L, Others. Review of particle physics[J/OL]. PTEP, 2022, 2022: 083C01. DOI: 10.1093/ptep/ptac097.

[10] Okubo S. ϕ meson and unitary symmetry model[J/OL]. Phys. Lett., 1963, 5: 165-168. DOI: 10.1016/S0375-9601(63)92548-9.

[11] Zweig G. An SU(3) model for strong interaction symmetry and its breaking. Version 2[M]. 1964: 22-101.

[12] Iizuka J. Systematics and phenomenology of meson family[J/OL]. Prog. Theor. Phys. Suppl., 1966, 37: 21-34. DOI: 10.1143/PTPS.37.21.

[13] Aaij R, et al. Measurement of J/ψ production cross-sections in pp collisions at $\sqrt{s} = 5\,\text{TeV}$ [J/OL]. JHEP, 2021, 11: 181. DOI: 10.1007/JHEP11(2021)181.

[14] Yang C N, Mills R L. Conservation of isotopic spin and isotopic gauge invariance[J/OL]. Phys. Rev., 1954, 96: 191-195. DOI: 10.1103/PhysRev.96.191.

[15] Gell-Mann M. A schematic model of baryons and mesons[J/OL]. Phys. Lett., 1964, 8: 214-215. DOI: 10.1016/S0031-9163(64)92001-3.

[16] Zweig G. An SU(3) model for strong interaction symmetry and its breaking. Version 1[Z]. 1964.

[17] Bjorken J D. Asymptotic sum rules at infinite momentum[J/OL]. Phys. Rev., 1969, 179: 1547-1553. DOI: 10.1103/PhysRev.179.1547.

[18] Bloom E D, et al. High-energy inelastic e-p scattering at 6-degrees and 10-degrees[J/OL]. Phys. Rev. Lett., 1969, 23: 930-934. DOI: 10.1103/PhysRevLett.23.930.

[19] Breidenbach M, Friedman J I, Kendall H W, et al. Observed behavior of highly inelastic electron-proton scattering[J/OL]. Phys. Rev. Lett., 1969, 23: 935-939. DOI: 10.1103/PhysRevLett.23.935.

[20] Feynman R P. Very high-energy collisions of hadrons[J/OL]. Phys. Rev. Lett., 1969, 23: 1415-1417. DOI: 10.1103/PhysRevLett.23.1415.

[21] Gross D J, Wilczek F. Ultraviolet behavior of nonabelian gauge theories[J/OL]. Phys. Rev. Lett., 1973, 30: 1343-1346. DOI: 10.1103/PhysRevLett.30.1343.

[22] Politzer H D. Reliable perturbative results for strong interactions?[J/OL]. Phys. Rev. Lett., 1973, 30: 1346-1349. DOI: 10.1103/PhysRevLett.30.1346.

[23] Greenberg O W. Spin and unitary spin independence in a paraquark model of baryons and Mesons[J/OL]. Phys. Rev. Lett., 1964, 13: 598-602. DOI: 10.1103/PhysRevLett.13.598.

[24] Han M Y, Nambu Y. Three triplet model with double SU(3) symmetry[J/OL]. Phys. Rev., 1965, 139: B1006-B1010. DOI: 10.1103/PhysRev.139.B1006.

[25] Richter B. e^+e^- –> hadrons[C]//17th International Conference on High-Energy Physics. 1974: IV.37-55.

[26] Bettini A. Introduction to elementary particle physics[M/OL]. 2nd ed. Cambridge University Press, 2014. DOI: 10.1017/CBO9781107279483.

[27] Thomson M. Modern particle physics[M/OL]. Cambridge University Press, 2013. DOI: 10.1017/CBO9781139525367.

[28] Drell S D, Yan T M. Partons and their applications at high-energies[J/OL]. Annals Phys., 1971, 66: 578. DOI: 10.1016/0003-4916(71)90071-6.

[29] Collins J C, Sterman G F. Soft partons in QCD[J/OL]. Nucl. Phys. B, 1981, 185: 172-188. DOI: 10.1016/0550-3213(81)90370-9.

[30] Collins J C, Soper D E. Parton distribution and decay functions[J/OL]. Nucl. Phys. B, 1982, 194: 445-492. DOI: 10.1016/0550-3213(82)90021-9.

[31] Gribov V N, Lipatov L N. Deep inelastic e-p scattering in perturbation theory[J]. Sov. J. Nucl. Phys., 1972, 15: 438-450.

[32] Lipatov L N. The parton model and perturbation theory[J]. Yad. Fiz., 1974, 20: 181-198.

[33] Altarelli G, Parisi G. Asymptotic freedom in parton language[J/OL]. Nucl. Phys. B, 1977, 126: 298-318. DOI: 10.1016/0550-3213(77)90384-4.

[34] Dokshitzer Y L. Calculation of the structure functions for deep inelastic scattering and e^+e^- annihilation by perturbation theory in quantum chromodynamics.[J]. Sov. Phys. JETP, 1977, 46: 641-653.

[35] Collins J. Foundations of perturbative QCD: volume 32[M]. Cambridge University Press, 2013.

[36] Collins J. CSS Equation, *etc.*, follow from structure of TMD factorization[A]. 2012. arXiv: 1212.5974.

[37] Bykov A A, Dremin I M, Leonidov A V. Potential models of quarkonium[J/OL]. Sov. Phys. Usp., 1984, 27: 321-338. DOI: 10.1070/PU1984v027n05ABEH004291.

[38] Buchmuller W, Tye S H H. Quarkonia and quantum chromodynamics[J/OL]. Phys. Rev. D, 1981, 24: 132. DOI: 10.1103/PhysRevD.24.132.

[39] Quigg C, Rosner J L. Quantum mechanics with applications to quarkonium[J/OL]. Phys. Rept., 1979, 56: 167-235. DOI: 10.1016/0370-1573(79)90095-4.

[40] Braaten E. Introduction to the NRQCD factorization approach to heavy quarkonium[C]//3rd International Workshop on Particle Physics Phenomenology. 1996.

[41] Einhorn M B, Ellis S D. Hadronic production of the new resonances: Probing gluon distributions [J/OL]. Phys. Rev. D, 1975, 12: 2007. DOI: 10.1103/PhysRevD.12.2007.

[42] Carlson C E, Suaya R. Hadronic production of ψ/J mesons[J/OL]. Phys. Rev. D, 1976, 14: 3115. DOI: 10.1103/PhysRevD.14.3115.

[43] Ellis S D, Einhorn M B, Quigg C. Comment on hadronic production of psions[J/OL]. Phys. Rev. Lett., 1976, 36: 1263. DOI: 10.1103/PhysRevLett.36.1263.

[44] Chang C H. Hadronic production of J/ψ associated with a gluon[J/OL]. Nucl. Phys. B, 1980, 172: 425-434. DOI: 10.1016/0550-3213(80)90175-3.

[45] Berger E L, Jones D L. Inelastic photoproduction of J/ψ and Υ by gluons[J/OL]. Phys. Rev. D, 1981, 23: 1521-1530. DOI: 10.1103/PhysRevD.23.1521.

[46] Baier R, Ruckl R. Hadronic production of J/ψ and Υ: Transverse momentum distributions [J/OL]. Phys. Lett. B, 1981, 102: 364-370. DOI: 10.1016/0370-2693(81)90636-5.

[47] Baier R, Ruckl R. On inelastic leptoproduction of heavy quarkonium states[J/OL]. Nucl. Phys. B, 1982, 201: 1-15. DOI: 10.1016/0550-3213(82)90374-1.

[48] Baier R, Ruckl R. Hadronic collisions: A quarkonium factory[J/OL]. Z. Phys. C, 1983, 19: 251. DOI: 10.1007/BF01572254.

[49] Schuler G A. Quarkonium production and decays[D/OL]. Hamburg U., 1994. DOI: 10.48550 /arXiv.hep-ph/9403387.

[50] Lansberg J P. J/ψ, ψ' and Υ production at hadron colliders: A Review[J/OL]. Int. J. Mod. Phys. A, 2006, 21: 3857-3916. DOI: 10.1142/S0217751X06033180.

[51] Abe F, et al. $J/\psi, \psi' \to \mu^+\mu^-$ and $B \to J/\psi, \psi'$ cross-sections[C/OL]//27th International Conference on High-energy Physics. 1994. DOI: 10.48550/arXiv.hep-ex/9412013.

[52] Braaten E, Doncheski M A, Fleming S, et al. Fragmentation production of J/ψ and ψ' at the Tevatron[J/OL]. Phys. Lett. B, 1994, 333: 548-554. DOI: 10.1016/0370-2693(94)90182-1.

[53] Krämer M. Quarkonium production at high-energy colliders[J/OL]. Prog. Part. Nucl. Phys., 2001, 47: 141-201. DOI: 10.1016/S0146-6410(01)00154-5.

[54] Barbieri R, Gatto R, Remiddi E. Singular binding dependence in the hadronic widths of 1^{++} and 1^{+-} heavy quark anti-quark bound states[J/OL]. Phys. Lett. B, 1976, 61: 465-468. DOI: 10.1016/0370-2693(76)90729-2.

[55] Barbieri R, Caffo M, Gatto R, et al. Strong QCD corrections to P-wave quarkonium decays [J/OL]. Phys. Lett. B, 1980, 95: 93-95. DOI: 10.1016/0370-2693(80)90407-4.

[56] Bodwin G T, Braaten E, Lepage G P. Rigorous QCD analysis of inclusive annihilation and production of heavy quarkonium[J/OL]. Phys. Rev. D, 1995, 51: 1125-1171. DOI: 10.1103/Ph ysRevD.55.5853.

[57] Cho P L, Leibovich A K. Color octet quarkonia production[J/OL]. Phys. Rev. D, 1996, 53: 150-162. DOI: 10.1103/PhysRevD.53.150.

[58] Cho P L, Leibovich A K. Color octet quarkonia production. 2.[J/OL]. Phys. Rev. D, 1996, 53: 6203-6217. DOI: 10.1103/PhysRevD.53.6203.

[59] Lepage G P, Magnea L, Nakhleh C, et al. Improved nonrelativistic QCD for heavy quark physics [J/OL]. Phys. Rev. D, 1992, 46: 4052-4067. DOI: 10.1103/PhysRevD.46.4052.

[60] Braaten E. Quarkonium polarization in the NRQCD factorization framework[J/OL]. Int. J. Mod. Phys. A, 1997, 12: 3941-3950. DOI: 10.1142/S0217751X97002097.

[61] Bodwin G T, Braaten E, Lepage G P. Rigorous QCD predictions for decays of P-wave quarkonia [J/OL]. Phys. Rev. D, 1992, 46: R1914-R1918. DOI: 10.1103/PhysRevD.46.R1914.

[62] Abe F, et al. J/ψ and $\psi(2S)$ production in $p\overline{p}$ collisions at $\sqrt{s} = 1.8$ TeV[J/OL]. Phys. Rev. Lett., 1997, 79: 572-577. DOI: 10.1103/PhysRevLett.79.572.

[63] Aaij R, et al. Measurement of forward J/ψ production cross-sections in pp collisions at $\sqrt{s} = 13$ TeV[J/OL]. JHEP, 2015, 10: 172. DOI: 10.1007/JHEP10(2015)172.

[64] Aaij R, et al. Measurement of $\psi(2S)$ production cross-sections in proton-proton collisions at $\sqrt{s} = 7$ and 13 TeV[J/OL]. Eur. Phys. J. C, 2020, 80(3): 185. DOI: 10.1140/epjc/s10052-020 -7638-y.

[65] Shao H S, Han H, Ma Y Q, et al. Yields and polarizations of prompt J/ψ and $\psi(2S)$ production in hadronic collisions[J/OL]. JHEP, 2015, 05: 103. DOI: 10.1007/JHEP05(2015)103.

[66] Ma Y Q, Wang K, Chao K T. $J/\psi\,(\psi')$ production at the Tevatron and LHC at $\mathcal{O}(\alpha_s^4 v^4)$ in nonrelativistic QCD[J/OL]. Phys. Rev. Lett., 2011, 106: 042002. DOI: 10.1103/PhysRevLett. 106.042002.

[67] Chapon E, et al. Prospects for quarkonium studies at the high-luminosity LHC[J/OL]. Prog. Part. Nucl. Phys., 2022, 122: 103906. DOI: 10.1016/j.ppnp.2021.103906.

[68] Echevarria M G. Proper TMD factorization for quarkonia production: $pp \to \eta_{c,b}$ as a study case [J/OL]. JHEP, 2019, 10: 144. DOI: 10.1007/JHEP10(2019)144.

[69] Ma Y Q, Venugopalan R. Comprehensive description of J/ψ production in proton-proton collisions at collider energies[J/OL]. Phys. Rev. Lett., 2014, 113(19): 192301. DOI: 10.1103/Ph ysRevLett.113.192301.

[70] Chung H S. Review of quarkonium production: Status and prospects[J/OL]. PoS, 2018, Confinement2018: 007. DOI: 10.22323/1.336.0007.

[71] Zhang Y J, Ma Y Q, Wang K, et al. QCD radiative correction to color-octet J/ψ inclusive production at B Factories[J/OL]. Phys. Rev. D, 2010, 81: 034015. DOI: 10.1103/PhysRevD.8 1.034015.

[72] Abulencia A, et al. Polarization of J/ψ and $\psi(2S)$ mesons produced in $p\overline{p}$ collisions at $\sqrt{s} = 1.96$ TeV[J/OL]. Phys. Rev. Lett., 2007, 99: 132001. DOI: 10.1103/PhysRevLett.99 .132001.

[73] Braaten E, Kniehl B A, Lee J. Polarization of prompt J/ψ at the Tevatron[J/OL]. Phys. Rev. D, 2000, 62: 094005. DOI: 10.1103/PhysRevD.62.094005.

[74] Beneke M, Rothstein I Z. ψ' polarization as a test of color octet quarkonium production[J/OL]. Phys. Lett. B, 1996, 372: 157-164. DOI: 10.1016/0370-2693(96)00030-5.

[75] Chatrchyan S, et al. Measurement of the prompt J/ψ and $\psi(2S)$ polarizations in pp collisions at $\sqrt{s} = 7$ TeV[J/OL]. Phys. Lett. B, 2013, 727: 381-402. DOI: 10.1016/j.physletb.2013.10.055.

[76] Aaij R, et al. Measurement of J/ψ polarization in pp collisions at $\sqrt{s} = 7$ TeV[J/OL]. Eur. Phys. J. C, 2013, 73(11): 2631. DOI: 10.1140/epjc/s10052-013-2631-3.

[77] Aaij R, et al. Measurement of $\psi(2S)$ polarisation in pp collisions at $\sqrt{s} = 7$ TeV[J/OL]. Eur. Phys. J. C, 2014, 74(5): 2872. DOI: 10.1140/epjc/s10052-014-2872-9.

[78] Chao K T, Ma Y Q, Shao H S, et al. J/ψ polarization at hadron colliders in nonrelativistic QCD [J/OL]. Phys. Rev. Lett., 2012, 108: 242004. DOI: 10.1103/PhysRevLett.108.242004.

[79] Butenschoen M, Kniehl B A. J/ψ polarization at Tevatron and LHC: Nonrelativistic-QCD factorization at the crossroads[J/OL]. Phys. Rev. Lett., 2012, 108: 172002. DOI: 10.1103/Phys RevLett.108.172002.

[80] Gong B, Wan L P, Wang J X, et al. Polarization for prompt J/ψ and $\psi(2S)$ production at the Tevatron and LHC[J/OL]. Phys. Rev. Lett., 2013, 110(4): 042002. DOI: 10.1103/PhysRevLet t.110.042002.

[81] Affolder T, et al. Measurement of J/ψ and $\psi(2S)$ polarization in $p\bar{p}$ collisions at $\sqrt{s} = 1.8$ TeV [J/OL]. Phys. Rev. Lett., 2000, 85: 2886-2891. DOI: 10.1103/PhysRevLett.85.2886.

[82] Artoisenet P, Lansberg J P, Maltoni F. Hadroproduction of J/ψ and Υ in association with a heavy-quark pair[J/OL]. Phys. Lett. B, 2007, 653: 60-66. DOI: 10.1016/j.physletb.2007.04.031.

[83] Campbell J M, Maltoni F, Tramontano F. QCD corrections to J/ψ and Υ production at hadron colliders[J/OL]. Phys. Rev. Lett., 2007, 98: 252002. DOI: 10.1103/PhysRevLett.98.252002.

[84] Cacciari M, Greco M, Nason P. The p_{T} spectrum in heavy flavor hadroproduction[J/OL]. JHEP, 1998, 05: 007. DOI: 10.1088/1126-6708/1998/05/007.

[85] Gelis F, Iancu E, Jalilian-Marian J, et al. The color glass condensate[J/OL]. Ann. Rev. Nucl. Part. Sci., 2010, 60: 463-489. DOI: 10.1146/annurev.nucl.010909.083629.

[86] Adare A, et al. Ground and excited charmonium state production in $p + p$ collisions at $\sqrt{s} = 200$ GeV[J/OL]. Phys. Rev. D, 2012, 85: 092004. DOI: 10.1103/PhysRevD.85.092004.

[87] Aamodt K, et al. Rapidity and transverse momentum dependence of inclusive J/ψ production in pp collisions at $\sqrt{s} = 7$ TeV[J/OL]. Phys. Lett. B, 2011, 704: 442-455. DOI: 10.1016/j.phys letb.2011.09.054.

[88] Aaij R, et al. Measurement of J/ψ production in pp collisions at $\sqrt{s} = 7$ TeV[J/OL]. Eur. Phys. J. C, 2011, 71: 1645. DOI: 10.1140/epjc/s10052-011-1645-y.

[89] Aad G, et al. Measurement of the differential cross-sections of inclusive, prompt and non-prompt J/ψ production in proton-proton collisions at $\sqrt{s} = 7$ TeV[J/OL]. Nucl. Phys. B, 2011, 850: 387-444. DOI: 10.1016/j.nuclphysb.2011.05.015.

[90] Adamczyk L, et al. J/ψ production at high transverse momenta in $p + p$ and Au+Au collisions at $\sqrt{s_{\mathrm{NN}}} = 200$ GeV[J/OL]. Phys. Lett. B, 2013, 722: 55-62. DOI: 10.1016/j.physletb.2013.04 .010.

[91] Aaij R, et al. Measurement of $\psi(2S)$ meson production in pp collisions at $\sqrt{s} = 7$ TeV[J/OL]. Eur. Phys. J. C, 2012, 72: 2100. DOI: 10.1140/epjc/s10052-012-2100-4.

[92] Ma Y Q, Wang K, Chao K T. A complete NLO calculation of the J/ψ and ψ' production at hadron colliders[J/OL]. Phys. Rev. D, 2011, 84: 114001. DOI: 10.1103/PhysRevD.84.114001.

[93] Nason P, Dawson S, Ellis R K. The total cross-section for the production of heavy quarks in hadronic collisions[J/OL]. Nucl. Phys. B, 1988, 303: 607-633. DOI: 10.1016/0550-3213(88)90422-1.

[94] Nason P, Dawson S, Ellis R K. The one particle inclusive differential cross-section for heavy quark production in hadronic collisions[J/OL]. Nucl. Phys. B, 1989, 327: 49-92. DOI: 10.1016/0550-3213(89)90286-1.

[95] Cacciari M, Greco M. Large p_{T} hadroproduction of heavy quarks[J/OL]. Nucl. Phys. B, 1994, 421: 530-544. DOI: 10.1016/0550-3213(94)90515-0.

[96] Cacciari M, Frixione S, Houdeau N, et al. Theoretical predictions for charm and bottom production at the LHC[J/OL]. JHEP, 2012, 10: 137. DOI: 10.1007/JHEP10(2012)137.

[97] Cacciari M, Mangano M L, Nason P. Gluon PDF constraints from the ratio of forward heavy-quark production at the LHC at $\sqrt{s} = 7$ and 13 TeV[J/OL]. Eur. Phys. J. C, 2015, 75(12): 610. DOI: 10.1140/epjc/s10052-015-3814-x.

[98] Aaij R, et al. Measurement of J/ψ production in pp collisions at $\sqrt{s} = 2.76$ TeV[J/OL]. JHEP, 2013, 02: 041. DOI: 10.1007/JHEP02(2013)041.

[99] Aaij R, et al. Production of J/ψ and Υ mesons in pp collisions at $\sqrt{s} = 8$ TeV[J/OL]. JHEP, 2013, 06: 064. DOI: 10.1007/JHEP06(2013)064.

[100] Aaboud M, et al. Measurement of quarkonium production in proton-lead and proton-proton collisions at 5.02 TeV with the ATLAS detector[J/OL]. Eur. Phys. J. C, 2018, 78(3): 171. DOI: 10.1140/epjc/s10052-018-5624-4.

[101] Aad G, et al. Measurement of the differential cross-sections of prompt and non-prompt production of J/ψ and $\psi(2S)$ in pp collisions at $\sqrt{s} = 7$ and 8 TeV with the ATLAS detector[J/OL]. Eur. Phys. J. C, 2016, 76(5): 283. DOI: 10.1140/epjc/s10052-016-4050-8.

[102] Zakareishvili T. Measurement of the production cross-section of J/ψ and $\psi(2S)$ mesons at high transverse momentum in pp collisions at $\sqrt{s} = 13$ TeV with the ATLAS detector[J/OL]. J. Phys. Conf. Ser., 2020, 1690(1): 012160. DOI: 10.1088/1742-6596/1690/1/012160.

[103] Sirunyan A M, et al. Measurement of prompt and non-prompt J/ψ production in pp and pPb collisions at $\sqrt{s_{\mathrm{NN}}} = 5.02$ TeV[J/OL]. Eur. Phys. J. C, 2017, 77(4): 269. DOI: 10.1140/epjc/s10052-017-4828-3.

[104] Khachatryan V, et al. Prompt and non-prompt J/ψ production in pp collisions at $\sqrt{s} = 7$ TeV [J/OL]. Eur. Phys. J. C, 2011, 71: 1575. DOI: 10.1140/epjc/s10052-011-1575-8.

[105] Chatrchyan S, et al. J/ψ and $\psi(2S)$ production in pp collisions at $\sqrt{s} = 7$ TeV[J/OL]. JHEP, 2012, 02: 011. DOI: 10.1007/JHEP02(2012)011.

[106] Acharya S, et al. Prompt and non-prompt J/ψ production cross sections at mid-rapidity in proton-proton collisions at $\sqrt{s} = 5.02$ and 13 TeV[J/OL]. JHEP, 2022, 03: 190. DOI: 10.1007/JHEP03(2022)190.

[107] Sirunyan A M, et al. Measurement of quarkonium production cross-sections in pp collisions at $\sqrt{s} = 13$ TeV[J/OL]. Phys. Lett. B, 2018, 780: 251-272. DOI: 10.1016/j.physletb.2018.02.033.

[108] Abelev B, et al. Measurement of prompt J/ψ and beauty hadron production cross sections at mid-rapidity in pp collisions at $\sqrt{s} = 7$ TeV[J/OL]. JHEP, 2012, 11: 065. DOI: 10.1007/JHEP 11(2012)065.

[109] Abelev B, et al. Inclusive J/ψ production in pp collisions at $\sqrt{s} = 2.76$ TeV[J/OL]. Phys. Lett. B, 2012, 718: 295-306. DOI: 10.1016/j.physletb.2012.10.078.

[110] Adam J, et al. J/ψ suppression at forward rapidity in Pb-Pb collisions at $\sqrt{s_{\mathrm{NN}}} = 5.02$ TeV [J/OL]. Phys. Lett. B, 2017, 766: 212-224. DOI: 10.1016/j.physletb.2016.12.064.

[111] Acharya S, et al. Inclusive J/ψ production at mid-rapidity in pp collisions at $\sqrt{s} = 5.02$ TeV [J/OL]. JHEP, 2019, 10: 084. DOI: 10.1007/JHEP10(2019)084.

[112] Acharya S, et al. Inclusive quarkonium production in pp collisions at $\sqrt{s} = 5.02$ TeV[J/OL]. Eur. Phys. J. C, 2023, 83(1): 61. DOI: 10.1140/epjc/s10052-022-10896-8.

[113] Abelev B B, et al. Measurement of quarkonium production at forward rapidity in pp collisions at $\sqrt{s} = 7$ TeV[J/OL]. Eur. Phys. J. C, 2014, 74(8): 2974. DOI: 10.1140/epjc/s10052-014-2974-4.

[114] Acharya S, et al. Energy dependence of forward-rapidity J/ψ and $\psi(2S)$ production in pp collisions at the LHC[J/OL]. Eur. Phys. J. C, 2017, 77(6): 392. DOI: 10.1140/epjc/s10052-017 -4940-4.

[115] Acharya S, et al. Inclusive J/ψ production at mid-rapidity in pp collisions at $\sqrt{s} = 13$ TeV [J/OL]. Eur. Phys. J. C, 2021, 81(12): 1121. DOI: 10.1140/epjc/s10052-021-09873-4.

[116] Adam J, et al. Inclusive quarkonium production at forward rapidity in pp collisions at $\sqrt{s} = 8$ TeV[J/OL]. Eur. Phys. J. C, 2016, 76(4): 184. DOI: 10.1140/epjc/s10052-016-3987-y.

[117] Aad G, et al. Measurement of the production cross-section of $\psi(2S) \to J/\psi(\to \mu^+\mu^-)\pi^+\pi^-$ in pp collisions at $\sqrt{s} = 7$ TeV at ATLAS[J/OL]. JHEP, 2014, 09: 079. DOI: 10.1007/JHEP09 (2014)079.

[118] Sirunyan A M, et al. Measurement of prompt $\psi(2S)$ production cross sections in proton-lead and proton-proton collisions at $\sqrt{s_{\mathrm{NN}}} = 5.02$ TeV[J/OL]. Phys. Lett. B, 2019, 790: 509-532. DOI: 10.1016/j.physletb.2019.01.058.

[119] Borschensky C, Kulesza A. Double parton scattering in pair production of J/ψ mesons at the LHC revisited[J/OL]. Phys. Rev. D, 2017, 95(3): 034029. DOI: 10.1103/PhysRevD.95.034029.

[120] Lansberg J P, Shao H S. Production of $J/\psi + \eta_c$ versus $J/\psi + J/\psi$ at the LHC: Importance of real α_s^5 corrections[J/OL]. Phys. Rev. Lett., 2013, 111: 122001. DOI: 10.1103/PhysRevLett.11 1.122001.

[121] Lansberg J P, Shao H S, Yamanaka N, et al. Prompt J/ψ -pair production at the LHC: Impact of loop-induced contributions and of the colour-octet mechanism[J/OL]. Eur. Phys. J. C, 2019, 79 (12): 1006. DOI: 10.1140/epjc/s10052-019-7523-8.

[122] Sridhar K, Martin A D, Stirling W J. J/ψ production at the Tevatron and HERA: The effect of k_{T} smearing[J/OL]. Phys. Lett. B, 1998, 438: 211-216. DOI: 10.1016/S0370-2693(98)00956-3.

[123] Lansberg J P, Shao H S. J/ψ -pair production at large momenta: Indications for double parton scatterings and large α_s^5 contributions[J/OL]. Phys. Lett. B, 2015, 751: 479-486. DOI: 10.1016/j.physletb.2015.10.083.

[124] Mulders P J, Rodrigues J. Transverse momentum dependence in gluon distribution and fragmentation functions[J/OL]. Phys. Rev. D, 2001, 63: 094021. DOI: 10.1103/PhysRevD.63.094021.

[125] Scarpa F, Boer D, Echevarria M G, et al. Studies of gluon TMDs and their evolution using quarkonium-pair production at the LHC[J/OL]. Eur. Phys. J. C, 2020, 80(2): 87. DOI: 10.1140/epjc/s10052-020-7619-1.

[126] Lansberg J P, Pisano C, Scarpa F, et al. Pinning down the linearly-polarised gluons inside unpolarised protons using quarkonium-pair production at the LHC[J/OL]. Phys. Lett. B, 2018, 784: 217-222. DOI: 10.1016/j.physletb.2018.08.004.

[127] Collins J C, Soper D E. Angular distribution of di-leptons in high-energy hadron collisions [J/OL]. Phys. Rev. D, 1977, 16: 2219. DOI: 10.1103/PhysRevD.16.2219.

[128] Lansberg J P, Pisano C, Schlegel M. Associated production of a dilepton and a $\Upsilon(J/\psi)$ at the LHC as a probe of gluon transverse momentum dependent distributions[J/OL]. Nucl. Phys. B, 2017, 920: 192-210. DOI: 10.1016/j.nuclphysb.2017.04.011.

[129] Schweitzer P, Teckentrup T, Metz A. Intrinsic transverse parton momenta in deeply inelastic reactions[J/OL]. Phys. Rev. D, 2010, 81: 094019. DOI: 10.1103/PhysRevD.81.094019.

[130] Aaij R, et al. Measurement of the J/ψ pair production cross-section in pp collisions at $\sqrt{s} = 13$ TeV[J/OL]. JHEP, 2017, 06: 047. DOI: 10.1007/JHEP06(2017)047.

[131] Lansberg J P. New observables in inclusive production of quarkonia[J/OL]. Phys. Rept., 2020, 889: 1-106. DOI: 10.1016/j.physrep.2020.08.007.

[132] Gaunt J R, Stirling W J. Double parton scattering singularity in one-loop integrals[J/OL]. JHEP, 2011, 06: 048. DOI: 10.1007/JHEP06(2011)048.

[133] Diehl M, Kasemets T, Keane S. Correlations in double parton distributions: Effects of evolution [J/OL]. JHEP, 2014, 05: 118. DOI: 10.1007/JHEP05(2014)118.

[134] Aad G, et al. Measurement of hard double-parton interactions in $W(\rightarrow l\nu)$ + 2-jet events at $\sqrt{s} = 7$ TeV with the ATLAS detector[J/OL]. New J. Phys., 2013, 15: 033038. DOI: 10.1088/1367-2630/15/3/033038.

[135] Chatrchyan S, et al. Study of double parton scattering using W + 2-jet events in proton-proton collisions at $\sqrt{s} = 7$ TeV[J/OL]. JHEP, 2014, 03: 032. DOI: 10.1007/JHEP03(2014)032.

[136] Abe F, et al. Study of four jet events and evidence for double parton interactions in $p\bar{p}$ collisions at $\sqrt{s} = 1.8$ TeV[J/OL]. Phys. Rev. D, 1993, 47: 4857-4871. DOI: 10.1103/PhysRevD.47.4857.

[137] Abe F, et al. Double parton scattering in $\bar{p}p$ collisions at $\sqrt{s} = 1.8$ TeV[J/OL]. Phys. Rev. D, 1997, 56: 3811-3832. DOI: 10.1103/PhysRevD.56.3811.

[138] Abazov V M, et al. Double parton interactions in $\gamma+$ 3-jet events in $p\bar{p}$ collisions $\sqrt{s} = 1.96$ TeV. [J/OL]. Phys. Rev. D, 2010, 81: 052012. DOI: 10.1103/PhysRevD.81.052012.

[139] Abazov V M, et al. Observation and studies of double J/ψ production at the Tevatron[J/OL]. Phys. Rev. D, 2014, 90(11): 111101. DOI: 10.1103/PhysRevD.90.111101.

[140] Aaboud M, et al. Measurement of the prompt J/ψ pair production cross-section in pp collisions at $\sqrt{s} = 8$ TeV with the ATLAS detector[J/OL]. Eur. Phys. J. C, 2017, 77(2): 76. DOI: 10.1140/epjc/s10052-017-4644-9.

[141] Aaij R, et al. Observation of double charm production involving open charm in pp collisions at $\sqrt{s} = 7$ TeV[J/OL]. JHEP, 2012, 06: 141. DOI: 10.1007/JHEP06(2012)141.

[142] Aaij R, et al. Production of associated Υ and open charm hadrons in pp collisions at $\sqrt{s} = 7$ and 8 TeV via double parton scattering[J/OL]. JHEP, 2016, 07: 052. DOI: 10.1007/JHEP07(2016)052.

[143] Shao H S, Zhang Y J. Complete study of hadroproduction of a Υ meson associated with a prompt J/ψ [J/OL]. Phys. Rev. Lett., 2016, 117(6): 062001. DOI: 10.1103/PhysRevLett.117.062001.

[144] Lansberg J P, Shao H S. Associated production of a quarkonium and a Z boson at one loop in a quark-hadron-duality approach[J/OL]. JHEP, 2016, 10: 153. DOI: 10.1007/JHEP10(2016)153.

[145] Lansberg J P, Shao H S. Phenomenological analysis of associated production of $Z^0 + b$ in the $b\to J/\psi X$ decay channel at the LHC[J/OL]. Nucl. Phys. B, 2017, 916: 132-142. DOI: 10.1016/j.nuclphysb.2017.01.002.

[146] Lansberg J P, Shao H S, Yamanaka N. Indication for double parton scatterings in $W+$ prompt J/ψ production at the LHC[J/OL]. Phys. Lett. B, 2018, 781: 485-491. DOI: 10.1016/j.physletb.2018.04.020.

[147] Shao H S. J/ψ meson production in association with an open charm hadron at the LHC: A reappraisal[J/OL]. Phys. Rev. D, 2020, 102(3): 034023. DOI: 10.1103/PhysRevD.102.034023.

[148] Shao H S. Associated production in pp and heavy ion collisions[J/OL]. PoS, 2021, LHCP2020: 172. DOI: 10.22323/1.382.0172.

[149] Badier J, et al. Evidence for $\psi\psi$ production in π^- interactions at 150- GeV/c and 280- GeV/c [J/OL]. Phys. Lett. B, 1982, 114: 457-460. DOI: 10.1016/0370-2693(82)90091-0.

[150] Badier J, et al. $\psi\psi$ production and limits on beauty meson production from 400- GeV/c protons [J/OL]. Phys. Lett. B, 1985, 158: 85. DOI: 10.1016/0370-2693(85)90745-2.

[151] Aaij R, et al. Observation of J/ψ pair production in pp collisions at $\sqrt{s} = 7$ TeV[J/OL]. Phys. Lett. B, 2012, 707: 52-59. DOI: 10.1016/j.physletb.2011.12.015.

[152] Kom C H, Kulesza A, Stirling W J. Pair production of J/ψ as a probe of double parton scattering at LHCb[J/OL]. Phys. Rev. Lett., 2011, 107: 082002. DOI: 10.1103/PhysRevLett.107.082002.

[153] Khachatryan V, et al. Measurement of prompt J/ψ pair production in pp collisions at $\sqrt{s} = 7$ TeV[J/OL]. JHEP, 2014, 09: 094. DOI: 10.1007/JHEP09(2014)094.

[154] Mobs E. The CERN accelerator complex - August 2018. Complexe des accélérateurs du CERN - Août 2018[EB/OL]. 2018. http://cds.cern.ch/record/2636343.

[155] Evans L. The Large Hadron Collider[J/OL]. Phil. Trans. Roy. Soc. Lond. A, 2012, 370: 831-858. DOI: 10.1098/rsta.2011.0453.

[156] Wenninger J. The LHC collider[J/OL]. Comptes Rendus Physique, 2015, 16: 347-355. DOI: 10.1016/j.crhy.2015.03.005.

[157] Alves A A, Jr., et al. The LHCb detector at the LHC[J/OL]. JINST, 2008, 3: S08005. DOI: 10.1088/1748-0221/3/08/S08005.

[158] Aaij R, et al. LHCb detector performance[J/OL]. Int. J. Mod. Phys. A, 2015, 30(07): 1530022. DOI: 10.1142/S0217751X15300227.

[159] Thorne R S, Martin A D, Stirling W J, et al. Parton distributions and QCD at LHCb[C/OL]// 16th International Workshop on Deep Inelastic Scattering and Related Subjects. 2008: 30. DOI: 10.48550/arXiv.0808.1847.

[160] Lindner R. LHCb layout. LHCb schema.[EB/OL]. 2008. https://cds.cern.ch/record/1087860.

[161] Christiansen J. Requirements to the L0 front-end electronics; 2001 ed.[R/OL]. Geneva: CERN, 2001. http://cds.cern.ch/record/691647.

[162] Christiansen J. Requirements to the L1 front-end electronics; 2003 ed.[R/OL]. Geneva: CERN, 2003. https://cds.cern.ch/record/691555.

[163] Aaij R, et al. Performance of the LHCb Vertex Locator[J/OL]. JINST, 2014, 9: P09007. DOI: 10.1088/1748-0221/9/09/P09007.

[164] Arink R, et al. Performance of the LHCb Outer Tracker[J/OL]. JINST, 2014, 9(01): P01002. DOI: 10.1088/1748-0221/9/01/P01002.

[165] Adinolfi M, et al. Performance of the LHCb RICH detector at the LHC[J/OL]. Eur. Phys. J. C, 2013, 73: 2431. DOI: 10.1140/epjc/s10052-013-2431-9.

[166] Abellán Beteta C, et al. Calibration and performance of the LHCb calorimeters in Run 1 and 2 at the LHC[A]. 2020. arXiv: 2008.11556.

[167] Archilli F, et al. Performance of the muon identification at LHCb[J/OL]. JINST, 2013, 8: P10020. DOI: 10.1088/1748-0221/8/10/P10020.

[168] Hocker A, et al. TMVA - Toolkit for multivariate data analysis[A]. 2007. arXiv: physics/0703039.

[169] Aaij R, et al. Design and performance of the LHCb trigger and full real-time reconstruction in Run 2 of the LHC[J/OL]. JINST, 2019, 14(04): P04013. DOI: 10.1088/1748-0221/14/04/P04013.

[170] Benson S, Gligorov V V, Vesterinen M A, et al. The LHCb Turbo stream[J/OL]. J. Phys. Conf. Ser., 2015, 664(8): 082004. DOI: 10.1088/1742-6596/664/8/082004.

[171] Aaij R, et al. Precision luminosity measurements at LHCb[J/OL]. JINST, 2014, 9(12): P12005. DOI: 10.1088/1748-0221/9/12/P12005.

[172] Qian W. J/ψ production study at the LHCb experiment[D/OL]. Orsay, LAL, 2010. http://cds.cern.ch/record/1475409.

[173] Sjostrand T, Mrenna S, Skands P Z. A brief introduction to PYTHIA 8.1[J/OL]. Comput. Phys. Commun., 2008, 178: 852-867. DOI: 10.1016/j.cpc.2008.01.036.

[174] Sjostrand T, Mrenna S, Skands P Z. PYTHIA 6.4 physics and manual[J/OL]. JHEP, 2006, 05: 026. DOI: 10.1088/1126-6708/2006/05/026.

[175] Belyaev I, et al. Handling of the generation of primary events in Gauss, the LHCb simulation framework[J/OL]. J. Phys. Conf. Ser., 2011, 331: 032047. DOI: 10.1088/1742-6596/331/3/032047.

[176] Bargiotti M, Vagnoni V. Heavy quarkonia sector in PYTHIA 6.324: Tuning, validation and perspectives at LHC(b)[R/OL]. Geneva: CERN, 2007. https://cds.cern.ch/record/1042611.

[177] Lange D J. The EvtGen particle decay simulation package[J/OL]. Nucl. Instrum. Meth. A, 2001, 462: 152-155. DOI: 10.1016/S0168-9002(01)00089-4.

[178] Davidson N, Przedzinski T, Was Z. PHOTOS interface in C++: Technical and physics documentation[J/OL]. Comput. Phys. Commun., 2016, 199: 86-101. DOI: 10.1016/j.cpc.2015.09.013.

[179] Allison J, et al. Geant4 developments and applications[J/OL]. IEEE Trans. Nucl. Sci., 2006, 53: 270. DOI: 10.1109/TNS.2006.869826.

[180] Agostinelli S, et al. GEANT4–a simulation toolkit[J/OL]. Nucl. Instrum. Meth. A, 2003, 506: 250-303. DOI: 10.1016/S0168-9002(03)01368-8.

[181] Clemencic M, Corti G, Easo S, et al. The LHCb simulation application, Gauss: Design, evolution and experience[J/OL]. J. Phys. Conf. Ser., 2011, 331: 032023. DOI: 10.1088/1742-6596/331/3/032023.

[182] De Cian M, Farry S, Seyfert P, et al. Fast neural-net based fake track rejection in the LHCb reconstruction[R/OL]. Geneva: CERN, 2017. https://cds.cern.ch/record/2255039.

[183] Skwarnicki T. A study of the radiative CASCADE transitions between the Υ' and Υ resonances [D/OL]. Cracow, INP, 1986. http://www-library.desy.de/preparch/desy/int_rep/f31-86-02.pdf.

[184] Punzi G. Comments on likelihood fits with variable resolution[J]. eConf, 2003, C030908: WELT002.

[185] Pivk M, Le Diberder F R. SPlot: A statistical tool to unfold data distributions[J/OL]. Nucl. Instrum. Meth. A, 2005, 555: 356-369. DOI: 10.1016/j.nima.2005.08.106.

[186] Aaij R, et al. Measurement of the track reconstruction efficiency at LHCb[J/OL]. JINST, 2015, 10(02): P02007. DOI: 10.1088/1748-0221/10/02/P02007.

[187] Anderlini L, Contu A, Jones C R, et al. The PIDCalib package[R/OL]. Geneva: CERN, 2016. https://cds.cern.ch/record/2202412.

[188] Cranmer K S. Kernel estimation in high-energy physics[J/OL]. Comput. Phys. Commun., 2001, 136: 198-207. DOI: 10.1016/S0010-4655(00)00243-5.

[189] Tolk S, Albrecht J, Dettori F, et al. Data driven trigger efficiency determination at LHCb[R/OL]. Geneva: CERN, 2014. http://cds.cern.ch/record/1701134.

[190] Albacete J L, Dumitru A, Fujii H, et al. CGC predictions for p+Pb collisions at the LHC[J/OL]. Nucl. Phys. A, 2013, 897: 1-27. DOI: 10.1016/j.nuclphysa.2012.09.012.

[191] Contopanagos H, Laenen E, Sterman G F. Sudakov factorization and resummation[J/OL]. Nucl. Phys. B, 1997, 484: 303-330. DOI: 10.1016/S0550-3213(96)00567-6.

[192] Efron B. Bootstrap Methods: Another Look at the Jackknife[J/OL]. Annals Statist., 1979, 7(1): 1-26. DOI: 10.1214/aos/1176344552.

[193] Langenbruch C. Parameter uncertainties in weighted unbinned maximum likelihood fits[J/OL]. Eur. Phys. J. C, 2022, 82(5): 393. DOI: 10.1140/epjc/s10052-022-10254-8.

[194] Bukin A D. Fitting function for asymmetric peaks[A]. 2007. arXiv: 0711.4449.

[195] Aaij R, et al. Observation of structure in the J/ψ -pair mass spectrum[J/OL]. Sci. Bull., 2020, 65(23): 1983-1993. DOI: 10.1016/j.scib.2020.08.032.

[196] Shao H S. HELAC-Onia: An automatic matrix element generator for heavy quarkonium physics [J/OL]. Comput. Phys. Commun., 2013, 184: 2562-2570. DOI: 10.1016/j.cpc.2013.05.023.

[197] Shao H S. HELAC-Onia 2.0: An upgraded matrix-element and event generator for heavy quarkonium physics[J/OL]. Comput. Phys. Commun., 2016, 198: 238-259. DOI: 10.1016/j.cpc.2015.09.011.

APPENDIX A RESULT TABLES OF J/ψ PRODUCTION

The measured double-differential cross-sections $\mathrm{d}^2\sigma/(\mathrm{d}p_\mathrm{T}\mathrm{d}y)$ for prompt and non-prompt J/ψ mesons in pp collisions at $\sqrt{s} = 5$ TeV are listed in Tables A.1 and A.2. For results in these two tables, the first uncertainties are statistical, the second are correlated systematic uncertainties shared between intervals, the third are uncorrelated systematic uncertainties, and the last are correlated between p_T intervals and uncorrelated between y intervals. The single-differential cross-sections $\mathrm{d}\sigma/\mathrm{d}p_\mathrm{T}$ and $\mathrm{d}\sigma/\mathrm{d}y$ are listed in Tables A.3–A.6. The fractions of non-prompt J/ψ mesons in (p_T,y) intervals are listed in Table A.7.

The ratios of differential cross-sections for prompt J/ψ mesons between 8 TeV and 5 TeV measurements and between 13 TeV and 5 TeV are listed in Tables A.8–A.11. The ratios of differential cross-sections for non-prompt J/ψ mesons between 8 TeV and 5 TeV measurements and between 13 TeV and 5 TeV are listed in Tables A.12–A.15.

The relative change of the cross-section for a polarisation of $\lambda_\theta = -0.2$ in the helicity frame compared to zero polarisation in each (p_T,y) interval is given in Table A.16. In addition, the relative change of the cross-section for a polarisation of $\lambda_\theta = -1$ $(+1)$ in the helicity frame, which corresponds to the fully longitudinally (transversely) polarised scenario, compared to zero polarisation in each (p_T,y) interval is given in Table A.17 (A.18).

Table A.1 Double-differential production cross-sections $d^2\sigma/(dp_T dy)$ [nb/GeV] for prompt J/ψ mesons.

p_T [GeV]	$2.0 < y < 2.5$	$2.5 < y < 3.0$
0–1	$686.03 \pm 6.80 \pm 35.11 \pm 9.03 \pm 4.92$	$640.03 \pm 3.70 \pm 22.97 \pm 2.78 \pm 5.06$
1–2	$1253.23 \pm 8.66 \pm 55.59 \pm 15.31 \pm 9.82$	$1173.73 \pm 4.95 \pm 39.14 \pm 4.68 \pm 7.58$
2–3	$964.82 \pm 6.79 \pm 40.41 \pm 12.19 \pm 5.23$	$917.24 \pm 4.09 \pm 30.11 \pm 2.86 \pm 3.76$
3–4	$575.26 \pm 4.74 \pm 21.54 \pm 7.51 \pm 2.89$	$540.97 \pm 2.82 \pm 17.21 \pm 2.52 \pm 1.80$
4–5	$305.38 \pm 2.89 \pm 10.65 \pm 2.93 \pm 1.28$	$286.82 \pm 1.76 \pm 8.98 \pm 1.74 \pm 1.10$
5–6	$159.48 \pm 1.84 \pm 5.44 \pm 1.51 \pm 0.72$	$143.21 \pm 1.12 \pm 4.46 \pm 1.11 \pm 0.49$
6–7	$79.23 \pm 1.19 \pm 2.63 \pm 1.02 \pm 0.26$	$73.00 \pm 0.75 \pm 2.26 \pm 0.66 \pm 0.25$
7–8	$43.60 \pm 0.82 \pm 1.43 \pm 0.77 \pm 0.01$	$36.67 \pm 0.52 \pm 1.13 \pm 0.32 \pm 0.00$
8–10	$18.11 \pm 0.34 \pm 0.59 \pm 0.24 \pm 0.08$	$15.17 \pm 0.23 \pm 0.47 \pm 0.15 \pm 0.04$
10–14	$4.15 \pm 0.11 \pm 0.13 \pm 0.07 \pm 0.02$	$3.34 \pm 0.07 \pm 0.11 \pm 0.04 \pm 0.01$
p_T [GeV]	$3.0 < y < 3.5$	$3.5 < y < 4.0$
0–1	$589.31 \pm 3.22 \pm 19.72 \pm 1.82 \pm 2.99$	$515.07 \pm 2.78 \pm 17.29 \pm 1.72 \pm 0.30$
1–2	$1056.67 \pm 4.29 \pm 34.89 \pm 4.63 \pm 4.82$	$911.86 \pm 3.68 \pm 30.29 \pm 2.93 \pm 0.63$
2–3	$804.99 \pm 3.45 \pm 26.10 \pm 6.15 \pm 1.60$	$681.00 \pm 3.04 \pm 22.56 \pm 1.99 \pm 1.78$
3–4	$461.97 \pm 2.24 \pm 14.45 \pm 1.89 \pm 0.81$	$370.70 \pm 2.08 \pm 11.71 \pm 1.36 \pm 0.55$
4–5	$236.68 \pm 1.47 \pm 7.28 \pm 0.94 \pm 0.29$	$185.30 \pm 1.36 \pm 5.81 \pm 1.72 \pm 0.32$
5–6	$115.63 \pm 0.95 \pm 3.55 \pm 1.17 \pm 0.17$	$86.71 \pm 0.86 \pm 2.75 \pm 0.78 \pm 0.01$
6–7	$56.50 \pm 0.64 \pm 1.73 \pm 0.42 \pm 0.03$	$41.09 \pm 0.57 \pm 1.34 \pm 0.38 \pm 0.10$
7–8	$28.48 \pm 0.44 \pm 0.87 \pm 0.28 \pm 0.10$	$20.85 \pm 0.39 \pm 0.71 \pm 0.28 \pm 0.03$
8–10	$11.35 \pm 0.19 \pm 0.35 \pm 0.11 \pm 0.03$	$7.59 \pm 0.16 \pm 0.27 \pm 0.11 \pm 0.01$
10–14	$2.26 \pm 0.06 \pm 0.08 \pm 0.04 \pm 0.00$	$1.38 \pm 0.05 \pm 0.05 \pm 0.03 \pm 0.01$
p_T [GeV]	$4.0 < y < 4.5$	
0–1	$452.31 \pm 3.21 \pm 17.49 \pm 2.85 \pm 2.79$	
1–2	$731.38 \pm 4.04 \pm 27.48 \pm 3.52 \pm 0.74$	
2–3	$485.71 \pm 3.25 \pm 19.15 \pm 3.16 \pm 0.50$	
3–4	$240.13 \pm 2.17 \pm 9.05 \pm 2.68 \pm 0.21$	
4–5	$108.46 \pm 1.33 \pm 4.16 \pm 1.18 \pm 0.25$	
5–6	$49.12 \pm 0.84 \pm 1.90 \pm 0.59 \pm 0.08$	
6–7	$22.06 \pm 0.52 \pm 0.86 \pm 0.35 \pm 0.02$	
7–8	$10.36 \pm 0.34 \pm 0.40 \pm 0.24 \pm 0.03$	
8–10	$3.82 \pm 0.14 \pm 0.15 \pm 0.09 \pm 0.01$	
10–14	$0.58 \pm 0.04 \pm 0.02 \pm 0.02 \pm 0.00$	

Table A.2 Double-differential production cross-sections $d^2\sigma/(dp_T dy)$ [nb/GeV] for non-prompt J/ψ mesons.

p_T [GeV]	$2.0 < y < 2.5$	$2.5 < y < 3.0$
0–1	$56.02 \pm 1.88 \pm 2.87 \pm 1.35 \pm 7.96$	$47.72 \pm 1.00 \pm 1.71 \pm 0.48 \pm 5.71$
1–2	$120.67 \pm 2.48 \pm 5.35 \pm 1.88 \pm 9.89$	$105.37 \pm 1.37 \pm 3.51 \pm 2.07 \pm 7.81$
2–3	$117.89 \pm 2.23 \pm 4.94 \pm 2.46 \pm 5.15$	$101.93 \pm 1.26 \pm 3.35 \pm 1.12 \pm 3.66$
3–4	$78.32 \pm 1.67 \pm 2.93 \pm 1.36 \pm 2.57$	$71.20 \pm 0.97 \pm 2.27 \pm 0.52 \pm 1.68$
4–5	$51.65 \pm 1.24 \pm 1.80 \pm 0.89 \pm 1.18$	$42.83 \pm 0.69 \pm 1.34 \pm 0.41 \pm 0.99$
5–6	$30.55 \pm 0.84 \pm 1.04 \pm 0.51 \pm 0.64$	$24.58 \pm 0.48 \pm 0.77 \pm 0.30 \pm 0.43$
6–7	$18.43 \pm 0.60 \pm 0.61 \pm 0.39 \pm 0.22$	$14.39 \pm 0.36 \pm 0.45 \pm 0.22 \pm 0.22$
7–8	$11.57 \pm 0.45 \pm 0.38 \pm 0.36 \pm 0.01$	$9.13 \pm 0.27 \pm 0.28 \pm 0.13 \pm 0.00$
8–10	$5.29 \pm 0.19 \pm 0.17 \pm 0.12 \pm 0.07$	$4.31 \pm 0.13 \pm 0.13 \pm 0.06 \pm 0.03$
10–14	$1.80 \pm 0.07 \pm 0.06 \pm 0.08 \pm 0.02$	$1.39 \pm 0.05 \pm 0.04 \pm 0.02 \pm 0.01$
p_T [GeV]	$3.0 < y < 3.5$	$3.5 < y < 4.0$
0–1	$40.73 \pm 0.84 \pm 1.36 \pm 0.38 \pm 3.55$	$30.25 \pm 0.76 \pm 1.02 \pm 0.40 \pm 0.34$
1–2	$85.36 \pm 1.15 \pm 2.82 \pm 1.56 \pm 5.16$	$61.11 \pm 1.00 \pm 2.03 \pm 0.60 \pm 0.64$
2–3	$79.84 \pm 1.00 \pm 2.59 \pm 1.19 \pm 1.59$	$55.94 \pm 0.89 \pm 1.85 \pm 0.79 \pm 1.80$
3–4	$51.96 \pm 0.75 \pm 1.62 \pm 0.49 \pm 0.75$	$38.20 \pm 0.69 \pm 1.21 \pm 0.42 \pm 0.59$
4–5	$31.75 \pm 0.55 \pm 0.98 \pm 0.27 \pm 0.28$	$22.43 \pm 0.49 \pm 0.70 \pm 0.31 \pm 0.36$
5–6	$18.22 \pm 0.40 \pm 0.56 \pm 0.26 \pm 0.17$	$10.97 \pm 0.33 \pm 0.35 \pm 0.16 \pm 0.01$
6–7	$10.36 \pm 0.29 \pm 0.32 \pm 0.20 \pm 0.03$	$6.83 \pm 0.25 \pm 0.22 \pm 0.12 \pm 0.11$
7–8	$6.00 \pm 0.22 \pm 0.18 \pm 0.09 \pm 0.10$	$3.60 \pm 0.17 \pm 0.12 \pm 0.10 \pm 0.03$
8–10	$2.87 \pm 0.10 \pm 0.09 \pm 0.04 \pm 0.02$	$1.57 \pm 0.08 \pm 0.06 \pm 0.06 \pm 0.01$
10–14	$0.77 \pm 0.04 \pm 0.03 \pm 0.03 \pm 0.00$	$0.39 \pm 0.03 \pm 0.01 \pm 0.01 \pm 0.01$
p_T [GeV]	$4.0 < y < 4.5$	
0–1	$22.40 \pm 0.90 \pm 0.87 \pm 0.45 \pm 3.29$	
1–2	$40.68 \pm 1.11 \pm 1.53 \pm 0.61 \pm 0.82$	
2–3	$31.22 \pm 0.91 \pm 1.23 \pm 0.71 \pm 0.52$	
3–4	$18.68 \pm 0.66 \pm 0.70 \pm 0.44 \pm 0.22$	
4–5	$9.00 \pm 0.42 \pm 0.34 \pm 0.18 \pm 0.26$	
5–6	$5.51 \pm 0.30 \pm 0.21 \pm 0.14 \pm 0.10$	
6–7	$2.84 \pm 0.20 \pm 0.11 \pm 0.09 \pm 0.02$	
7–8	$1.44 \pm 0.13 \pm 0.06 \pm 0.07 \pm 0.04$	
8–10	$0.53 \pm 0.06 \pm 0.02 \pm 0.02 \pm 0.01$	
10–14	$0.15 \pm 0.02 \pm 0.01 \pm 0.01 \pm 0.01$	

Table A.3 Single-differential production cross-sections $d\sigma/dp_T$ [nb/GeV] for prompt J/ψ mesons. The first uncertainties are statistical, the second are correlated systematic uncertainties shared between intervals, and the last are uncorrelated systematic uncertainties.

p_T [GeV]	$2.0 < y < 4.5$
0–1	$1441.38 \pm 4.70 \pm 53.61 \pm 5.09$
1–2	$2563.43 \pm 6.08 \pm 90.61 \pm 8.64$
2–3	$1926.88 \pm 4.86 \pm 67.32 \pm 7.22$
3–4	$1094.51 \pm 3.34 \pm 36.15 \pm 4.34$
4–5	$561.32 \pm 2.08 \pm 18.10 \pm 2.05$
5–6	$277.07 \pm 1.32 \pm 8.89 \pm 1.21$
6–7	$135.95 \pm 0.86 \pm 4.34 \pm 0.69$
7–8	$69.98 \pm 0.59 \pm 2.23 \pm 0.48$
8–10	$28.02 \pm 0.25 \pm 0.90 \pm 0.17$
10–14	$5.85 \pm 0.08 \pm 0.19 \pm 0.05$
14–20	$0.66 \pm 0.02 \pm 0.02 \pm 0.02$

Table A.4 Single-differential production cross-sections $d\sigma/dp_T$ [nb/GeV] for non-prompt J/ψ mesons. The first uncertainties are statistical, the second are correlated systematic uncertainties shared between intervals, and the last are uncorrelated systematic uncertainties.

p_T [GeV]	$2.0 < y < 4.5$
0–1	$98.56 \pm 1.29 \pm 6.61 \pm 0.80$
1–2	$206.60 \pm 1.70 \pm 10.03 \pm 1.65$
2–3	$193.41 \pm 1.51 \pm 7.58 \pm 1.57$
3–4	$129.17 \pm 1.14 \pm 4.56 \pm 0.83$
4–5	$78.83 \pm 0.83 \pm 2.66 \pm 0.54$
5–6	$44.91 \pm 0.57 \pm 1.49 \pm 0.34$
6–7	$26.43 \pm 0.41 \pm 0.86 \pm 0.25$
7–8	$15.88 \pm 0.31 \pm 0.51 \pm 0.20$
8–10	$7.29 \pm 0.14 \pm 0.24 \pm 0.08$
10–14	$2.24 \pm 0.05 \pm 0.07 \pm 0.05$
14–20	$0.41 \pm 0.02 \pm 0.01 \pm 0.01$

Table A.5 Single-differential production cross-sections $d\sigma/dy$ [nb] for prompt J/ψ mesons. The first uncertainties are statistical, the second are correlated systematic uncertainties shared between intervals, and the last are uncorrelated systematic uncertainties.

y	$0 < p_T < 14$ GeV	$0 < p_T < 8$ GeV
2.0–2.5	$4119.9 \pm 14.3 \pm 170.6 \pm 34.3$	$4067.0 \pm 14.3 \pm 169.1 \pm 34.1$
2.5–3.0	$3855.4 \pm 8.3 \pm 126.8 \pm 21.3$	$3811.7 \pm 8.2 \pm 125.4 \pm 21.2$
3.0–3.5	$3382.0 \pm 7.0 \pm 109.1 \pm 13.7$	$3350.2 \pm 7.0 \pm 108.1 \pm 13.6$
3.5–4.0	$2833.3 \pm 6.2 \pm 92.6 \pm 5.9$	$2812.6 \pm 6.2 \pm 91.8 \pm 5.9$
4.0–4.5	$2109.5 \pm 6.7 \pm 80.0 \pm 7.8$	$2099.5 \pm 6.7 \pm 79.6 \pm 7.8$

Table A.6 Single-differential production cross-sections $d\sigma/dy$ [nb] for non-prompt J/ψ mesons. The first uncertainties are statistical, the second are correlated systematic uncertainties shared between intervals, and the last are uncorrelated systematic uncertainties.

y	$0 < p_T < 14$ GeV
2.0–2.5	$502.9 \pm 4.5 \pm 20.0 \pm 28.1$
2.5–3.0	$431.3 \pm 2.5 \pm 14.0 \pm 20.8$
3.0–3.5	$333.0 \pm 2.1 \pm 10.7 \pm 11.9$
3.5–4.0	$234.0 \pm 1.8 \pm 7.6 \pm 4.1$
4.0–4.5	$133.4 \pm 1.9 \pm 5.1 \pm 5.4$

Table A.7 Fraction of non-prompt J/ψ mesons (in %) in (p_{T},y) intervals. The first uncertainties are statistical and the second are systematic.

p_{T} [GeV]	$2.0 < y < 2.5$	$2.5 < y < 3.0$	$3.0 < y < 3.5$
0–1	$7.4 \pm 0.3 \pm 1.1$	$6.8 \pm 0.1 \pm 0.8$	$6.3 \pm 0.1 \pm 0.6$
1–2	$8.6 \pm 0.2 \pm 0.7$	$8.2 \pm 0.1 \pm 0.6$	$7.4 \pm 0.1 \pm 0.5$
2–3	$10.5 \pm 0.2 \pm 0.5$	$9.9 \pm 0.1 \pm 0.4$	$8.9 \pm 0.1 \pm 0.2$
3–4	$11.6 \pm 0.3 \pm 0.4$	$11.5 \pm 0.2 \pm 0.3$	$10.1 \pm 0.2 \pm 0.2$
4–5	$13.9 \pm 0.4 \pm 0.4$	$12.9 \pm 0.2 \pm 0.3$	$11.6 \pm 0.2 \pm 0.1$
5–6	$15.7 \pm 0.5 \pm 0.4$	$14.5 \pm 0.3 \pm 0.3$	$13.4 \pm 0.3 \pm 0.2$
6–7	$18.2 \pm 0.6 \pm 0.4$	$16.1 \pm 0.4 \pm 0.3$	$15.5 \pm 0.5 \pm 0.3$
7–8	$20.0 \pm 0.8 \pm 0.6$	$19.3 \pm 0.6 \pm 0.2$	$17.0 \pm 0.7 \pm 0.3$
8–10	$22.4 \pm 0.9 \pm 0.5$	$21.8 \pm 0.7 \pm 0.3$	$19.7 \pm 0.8 \pm 0.3$
10–14	$30.0 \pm 1.4 \pm 1.4$	$29.0 \pm 1.2 \pm 0.5$	$25.1 \pm 1.3 \pm 0.9$
p_{T} [GeV]	$3.5 < y < 4$	$4 < y < 4.5$	
0–1	$5.3 \pm 0.1 \pm 0.1$	$4.6 \pm 0.2 \pm 0.7$	
1–2	$6.2 \pm 0.1 \pm 0.1$	$5.3 \pm 0.1 \pm 0.1$	
2–3	$7.5 \pm 0.1 \pm 0.3$	$6.2 \pm 0.2 \pm 0.2$	
3–4	$9.3 \pm 0.2 \pm 0.2$	$7.3 \pm 0.3 \pm 0.2$	
4–5	$10.7 \pm 0.2 \pm 0.2$	$7.7 \pm 0.4 \pm 0.2$	
5–6	$11.3 \pm 0.4 \pm 0.1$	$10.2 \pm 0.6 \pm 0.2$	
6–7	$14.0 \pm 0.5 \pm 0.3$	$11.1 \pm 0.8 \pm 0.2$	
7–8	$14.6 \pm 0.8 \pm 0.3$	$12.0 \pm 1.2 \pm 0.5$	
8–10	$16.9 \pm 0.9 \pm 0.6$	$12.4 \pm 1.4 \pm 0.5$	
10–14	$21.1 \pm 1.7 \pm 0.7$	$18.4 \pm 2.8 \pm 1.4$	

Table A.8 Cross-section ratios between 8 TeV and 5 TeV measurements for prompt J/ψ mesons as a function of p_{T} with $2.0 < y < 4.5$. The first uncertainties are statistical and the second are systematic.

p_{T} [GeV]	$2.0 < y < 4.5$
0–1	$1.20 \pm 0.01 \pm 0.08$
1–2	$1.27 \pm 0.01 \pm 0.08$
2–3	$1.34 \pm 0.01 \pm 0.09$
3–4	$1.42 \pm 0.01 \pm 0.09$
4–5	$1.50 \pm 0.01 \pm 0.10$
5–6	$1.57 \pm 0.01 \pm 0.10$
6–7	$1.69 \pm 0.01 \pm 0.11$
7–8	$1.74 \pm 0.02 \pm 0.11$
8–10	$1.85 \pm 0.02 \pm 0.12$
10–14	$2.05 \pm 0.03 \pm 0.13$

Table A.9 Cross-section ratios between 8 TeV and 5 TeV measurements for prompt J/ψ mesons as a function of y with $p_{\mathrm{T}} < 8\,\mathrm{GeV}$. The first uncertainties are statistical and the second are systematic.

y	$0 < p_{\mathrm{T}} < 8\,\mathrm{GeV}$
2.0–2.5	$1.24 \pm 0.01 \pm 0.08$
2.5–3.0	$1.30 \pm 0.00 \pm 0.08$
3.0–3.5	$1.34 \pm 0.00 \pm 0.09$
3.5–4.0	$1.38 \pm 0.00 \pm 0.09$
4.0–4.5	$1.48 \pm 0.01 \pm 0.10$

Table A.10 Cross-section ratios between 13 TeV and 5 TeV measurements for prompt J/ψ mesons as a function of p_{T} with $2.0 < y < 4.5$. The first uncertainties are statistical and the second is systematic.

p_{T} [GeV]	$2.0 < y < 4.5$
0–1	$1.51 \pm 0.01 \pm 0.08$
1–2	$1.65 \pm 0.01 \pm 0.09$
2–3	$1.84 \pm 0.01 \pm 0.09$
3–4	$2.06 \pm 0.01 \pm 0.10$
4–5	$2.27 \pm 0.01 \pm 0.11$
5–6	$2.54 \pm 0.02 \pm 0.12$
6–7	$2.77 \pm 0.03 \pm 0.13$
7–8	$2.85 \pm 0.03 \pm 0.13$
8–10	$3.22 \pm 0.04 \pm 0.15$
10–14	$3.86 \pm 0.07 \pm 0.18$

Table A.11 Cross-section ratios between 13 TeV and 5 TeV measurements for prompt J/ψ mesons as a function of y with $p_{\mathrm{T}} < 8$ GeV. The first uncertainties are statistical and the second are systematic.

y	$0 < p_{\mathrm{T}} < 8$ GeV
2.0–2.5	$1.70 \pm 0.01 \pm 0.10$
2.5–3.0	$1.76 \pm 0.01 \pm 0.08$
3.0–3.5	$1.83 \pm 0.01 \pm 0.08$
3.5–4.0	$1.90 \pm 0.01 \pm 0.10$
4.0–4.5	$2.13 \pm 0.01 \pm 0.13$

Table A.12 Cross-section ratios between 8 TeV and 5 TeV measurements for non-prompt J/ψ mesons as a function of p_{T} with $2.0 < y < 4.5$. The first uncertainties are statistical and the second are systematic.

p_{T} [GeV]	$2.0 < y < 4.5$
0–1	$1.42 \pm 0.03 \pm 0.14$
1–2	$1.51 \pm 0.02 \pm 0.11$
2–3	$1.51 \pm 0.02 \pm 0.10$
3–4	$1.59 \pm 0.02 \pm 0.10$
4–5	$1.62 \pm 0.02 \pm 0.11$
5–6	$1.69 \pm 0.03 \pm 0.11$
6–7	$1.72 \pm 0.03 \pm 0.11$
7–8	$1.76 \pm 0.04 \pm 0.12$
8–10	$1.95 \pm 0.04 \pm 0.13$
10–14	$1.97 \pm 0.05 \pm 0.13$

Table A.13 Cross-section ratios between 8 TeV and 5 TeV measurements for non-prompt J/ψ mesons as a function of y with $p_{\mathrm{T}} < 14$ GeV. The first uncertainties are statistical and the second are systematic.

y	$0 < p_{\mathrm{T}} < 14$ GeV
2.0–2.5	$1.42 \pm 0.02 \pm 0.12$
2.5–3.0	$1.54 \pm 0.01 \pm 0.13$
3.0–3.5	$1.61 \pm 0.01 \pm 0.12$
3.5–4.0	$1.65 \pm 0.02 \pm 0.11$
4.0–4.5	$1.80 \pm 0.03 \pm 0.14$

Table A.14 Cross-section ratios between 13 TeV and 5 TeV measurements for non-prompt J/ψ mesons as a function of p_{T} with $2.0 < y < 4.5$. The first uncertainties are statistical and the second are systematic.

p_{T} [GeV]	$2.0 < y < 4.5$
0–1	$2.23 \pm 0.05 \pm 0.17$
1–2	$2.46 \pm 0.03 \pm 0.16$
2–3	$2.62 \pm 0.03 \pm 0.14$
3–4	$2.85 \pm 0.04 \pm 0.14$
4–5	$3.08 \pm 0.05 \pm 0.15$
5–6	$3.26 \pm 0.06 \pm 0.15$
6–7	$3.58 \pm 0.07 \pm 0.17$
7–8	$3.63 \pm 0.09 \pm 0.17$
8–10	$4.21 \pm 0.10 \pm 0.20$
10–14	$4.81 \pm 0.14 \pm 0.24$

Table A.15 Cross-section ratios between 13 TeV and 5 TeV measurements for non-prompt J/ψ mesons as a function of y with $p_{\mathrm{T}} < 14$ GeV. The first uncertainties are statistical and the second are systematic.

y	$0 < p_{\mathrm{T}} < 14$ GeV
2.0–2.5	$2.39 \pm 0.03 \pm 0.19$
2.5–3.0	$2.49 \pm 0.02 \pm 0.17$
3.0–3.5	$2.79 \pm 0.03 \pm 0.16$
3.5–4.0	$3.24 \pm 0.04 \pm 0.17$
4.0–4.5	$4.02 \pm 0.08 \pm 0.29$

Table A.16 Relative changes of cross-sections (in %), for a polarisation of $\lambda_\theta = -0.2$ rather than zero, in (p_T,y) intervals.

p_T [GeV]	$2.0 < y < 2.5$	$2.5 < y < 3.0$	$3.0 < y < 3.5$	$3.5 < y < 4.0$	$4.0 < y < 4.5$
0–1	-5.91 ± 0.83	-4.47 ± 0.42	-2.94 ± 0.37	-2.39 ± 0.43	-1.95 ± 0.77
1–2	-5.22 ± 0.59	-4.05 ± 0.32	-2.47 ± 0.29	-1.38 ± 0.35	-0.47 ± 0.60
2–3	-4.38 ± 0.63	-3.21 ± 0.36	-1.62 ± 0.33	-0.49 ± 0.41	0.55 ± 0.72
3–4	-4.20 ± 0.75	-3.09 ± 0.42	-1.60 ± 0.40	-0.30 ± 0.51	0.56 ± 0.93
4–5	-4.14 ± 0.90	-3.15 ± 0.50	-1.80 ± 0.49	-0.83 ± 0.63	0.47 ± 1.16
5–6	-4.00 ± 1.06	-3.00 ± 0.61	-1.87 ± 0.62	-1.10 ± 0.80	0.19 ± 1.52
6–7	-3.77 ± 1.30	-2.81 ± 0.76	-1.89 ± 0.79	-1.45 ± 1.05	-0.41 ± 1.96
7–8	-3.63 ± 1.61	-2.70 ± 0.96	-1.76 ± 1.04	-1.63 ± 1.37	-0.55 ± 2.66
8–10	-3.23 ± 1.52	-2.32 ± 0.96	-1.68 ± 1.08	-1.78 ± 1.50	-1.02 ± 2.92
10–14	-2.85 ± 1.88	-2.04 ± 1.28	-1.47 ± 1.54	-1.44 ± 2.22	-1.29 ± 5.07
14–20	-1.55 ± 1.87 ($2.0 < y < 4.5$)				

Table A.17 Relative change of cross-sections (in %), for a polarisation of $\lambda_\theta = -1$ rather than zero, in (p_T,y) intervals.

p_T [GeV]	$2.0 < y < 2.5$	$2.5 < y < 3.0$	$3.0 < y < 3.5$	$3.5 < y < 4.0$	$4.0 < y < 4.5$
0–1	-30.6 ± 0.6	-24.6 ± 0.3	-17.4 ± 0.3	-18.0 ± 0.3	-24.9 ± 0.6
1–2	-27.8 ± 0.4	-22.8 ± 0.2	-15.2 ± 0.2	-13.4 ± 0.3	-16.2 ± 0.5
2–3	-24.3 ± 0.5	-18.9 ± 0.3	-10.5 ± 0.3	-7.5 ± 0.4	-8.8 ± 0.7
3–4	-23.5 ± 0.6	-18.2 ± 0.3	-10.2 ± 0.4	-5.8 ± 0.5	-5.2 ± 0.9
4–5	-23.2 ± 0.7	-18.5 ± 0.4	-11.3 ± 0.4	-7.3 ± 0.6	-3.9 ± 1.1
5–6	-22.6 ± 0.8	-17.8 ± 0.5	-11.8 ± 0.5	-8.8 ± 0.7	-4.8 ± 1.5
6–7	-21.5 ± 1.0	-16.9 ± 0.6	-11.8 ± 0.7	-9.8 ± 1.0	-5.8 ± 1.9
7–8	-21.1 ± 1.3	-16.3 ± 0.8	-11.1 ± 0.9	-10.4 ± 1.2	-7.2 ± 2.5
8–10	-19.2 ± 1.2	-14.3 ± 0.8	-10.7 ± 1.0	-11.2 ± 1.3	-8.3 ± 2.8
10–14	-16.9 ± 1.6	-12.6 ± 1.1	-9.3 ± 1.4	-9.0 ± 2.0	-11.0 ± 4.6
14–20	-10.2 ± 1.7 ($2.0 < y < 4.5$)				

Table A.18 Relative changes of cross-sections (in %), for a polarisation of $\lambda_\theta = +1$ rather than zero, in (p_{T},y) intervals.

p_{T} [GeV]	$2.0 < y < 2.5$	$2.5 < y < 3.0$	$3.0 < y < 3.5$	$3.5 < y < 4.0$	$4.0 < y < 4.5$
0–1	28.2 ± 1.2	19.6 ± 0.6	11.8 ± 0.5	12.4 ± 0.5	19.8 ± 1.0
1–2	23.9 ± 0.8	17.3 ± 0.4	9.9 ± 0.3	8.4 ± 0.4	10.7 ± 0.7
2–3	19.0 ± 0.8	13.1 ± 0.4	6.2 ± 0.4	4.2 ± 0.4	5.1 ± 0.8
3–4	18.1 ± 1.0	12.5 ± 0.5	6.1 ± 0.4	3.2 ± 0.5	2.8 ± 1.0
4–5	17.7 ± 1.1	12.8 ± 0.6	6.8 ± 0.6	4.1 ± 0.7	2.1 ± 1.2
5–6	17.1 ± 1.3	12.2 ± 0.8	7.2 ± 0.7	5.1 ± 0.9	2.6 ± 1.6
6–7	15.8 ± 1.6	11.3 ± 1.0	7.2 ± 0.9	5.8 ± 1.2	3.2 ± 2.1
7–8	15.3 ± 2.0	10.8 ± 1.2	6.7 ± 1.2	6.2 ± 1.6	4.0 ± 2.9
8–10	13.4 ± 1.9	9.2 ± 1.2	6.3 ± 1.3	6.6 ± 1.7	4.7 ± 3.2
10–14	11.4 ± 2.3	7.8 ± 1.6	5.5 ± 1.8	5.1 ± 2.5	6.5 ± 5.7
14–20	6.0 ± 2.1 ($2.0 < y < 4.5$)				

APPENDIX B RESULT TABLES OF DOUBLE CHARMONIUM PRODUCTION

The measured differential cross-sections of di-J/ψ production as functions of Δy, $\Delta\phi$, $\mathcal{A}_{p_{\mathrm{T}}}$, $p_{\mathrm{T}}^{\text{di-}J/\psi}$, $y_{\text{di-}J/\psi}$, $m_{\text{di-}J/\psi}$, $p_{\mathrm{T}}^{J/\psi}$, $y_{J/\psi}$, θ_{CS} and ϕ_{CS} are listed in Tables B.1–B.10. The differential cross-sections of di-J/ψ production for SPS process are listed in Tables B.11–B.20. The differential cross-sections $\mathrm{d}\sigma/\mathrm{d}p_{\mathrm{T}}^{\text{di-}J/\psi}$ in three different intervals of $y_{\text{di-}J/\psi}$ with $6 < m_{\text{di-}J/\psi} < 9\,\mathrm{GeV}$ are listed in Tables B.21 and B.22 for SPS+DPS and SPS separately. The differential cross-sections $\mathrm{d}\sigma/\mathrm{d}p_{\mathrm{T}}^{\text{di-}J/\psi}$ in three intervals of $m_{\text{di-}J/\psi}$ are listed in Tables B.23 and B.24 for SPS+DPS and SPS separately.

The measured differential cross-sections of J/ψ-$\psi(2S)$ production as functions of Δy, $\Delta\phi$, $p_{\mathrm{T}}^{J/\psi\text{-}\psi(2S)}$, $y_{J/\psi\text{-}\psi(2S)}$ and $m_{J/\psi\text{-}\psi(2S)}$ are listed in Tables B.25–B.29. The cross-section ratios between J/ψ-$\psi(2S)$ and di-J/ψ production as functions of Δy, $\Delta\phi$, $p_{\mathrm{T}}^{\text{di-}\psi}$ and $y_{\text{di-}\psi}$ are listed in Tables B.30–B.33.

Table B.1 Differential cross-sections $\mathrm{d}\sigma/\mathrm{d}\Delta y$ [nb] of di-J/ψ production. The first uncertainties are statistical, and the second are systematic uncertainties.

Δy	$\mathrm{d}\sigma/\mathrm{d}\Delta y$ [nb]
0.0–0.2	$19.46 \pm 0.87 \pm 1.15$
0.2–0.4	$14.88 \pm 0.56 \pm 0.81$
0.4–0.6	$12.57 \pm 0.50 \pm 0.69$
0.6–0.8	$9.32 \pm 0.37 \pm 0.52$
0.8–1.0	$7.29 \pm 0.33 \pm 0.41$
1.0–1.2	$5.52 \pm 0.28 \pm 0.31$
1.2–1.4	$4.36 \pm 0.27 \pm 0.24$
1.4–1.6	$3.34 \pm 0.26 \pm 0.21$
1.6–1.8	$2.42 \pm 0.26 \pm 0.15$
1.8–2.0	$1.67 \pm 0.23 \pm 0.18$
2.0–2.5	$0.50 \pm 0.13 \pm 0.05$

Table B.2 Differential cross-sections $\mathrm{d}\sigma/\mathrm{d}\Delta\phi$ [nb] of di-J/ψ production. The first uncertainties are statistical, and the second are systematic uncertainties.

$\Delta\phi/\pi$	$\mathrm{d}\sigma/\mathrm{d}\Delta\phi$ [nb]
0.0–0.1	$6.35 \pm 0.30 \pm 0.37$
0.1–0.2	$5.81 \pm 0.31 \pm 0.34$
0.2–0.3	$4.77 \pm 0.24 \pm 0.27$
0.3–0.4	$4.84 \pm 0.30 \pm 0.27$
0.4–0.5	$4.95 \pm 0.35 \pm 0.29$
0.5–0.6	$4.64 \pm 0.27 \pm 0.27$
0.6–0.7	$4.78 \pm 0.30 \pm 0.27$
0.7–0.8	$4.70 \pm 0.25 \pm 0.27$
0.8–0.9	$5.12 \pm 0.23 \pm 0.29$
0.9–1.0	$6.18 \pm 0.29 \pm 0.35$

Table B.3 Differential cross-sections $\mathrm{d}\sigma/\mathrm{d}\mathcal{A}_{p_\mathrm{T}}$ [nb] of di-J/ψ production. The first uncertainties are statistical, and the second are systematic uncertainties.

$\mathcal{A}_{p_\mathrm{T}}$	$\mathrm{d}\sigma/\mathrm{d}\mathcal{A}_{p_\mathrm{T}}$ [nb]
0.0–0.1	$29.98 \pm 1.17 \pm 1.68$
0.1–0.2	$28.50 \pm 1.04 \pm 1.59$
0.2–0.3	$27.06 \pm 1.34 \pm 1.52$
0.3–0.4	$23.23 \pm 1.06 \pm 1.30$
0.4–0.5	$17.82 \pm 1.04 \pm 1.10$
0.5–0.6	$15.95 \pm 0.80 \pm 0.98$
0.6–0.7	$10.06 \pm 0.64 \pm 0.56$
0.7–0.8	$6.79 \pm 0.59 \pm 0.37$
0.8–0.9	$3.21 \pm 0.38 \pm 0.21$
0.9–1.0	$1.14 \pm 0.18 \pm 0.08$

Table B.4 Differential cross-sections $\mathrm{d}\sigma/\mathrm{d}p_{\mathrm{T}}^{\text{di-}J/\psi}$ [nb/GeV] of di-J/ψ production. The first uncertainties are statistical, and the second are systematic uncertainties.

$p_{\mathrm{T}}^{\text{di-}J/\psi}$ [GeV]	$\mathrm{d}\sigma/\mathrm{d}p_{\mathrm{T}}^{\text{di-}J/\psi}$ [nb/GeV]
0–1	$1.408 \pm 0.089 \pm 0.083$
1–2	$2.523 \pm 0.126 \pm 0.150$
2–3	$2.858 \pm 0.158 \pm 0.164$
3–4	$2.542 \pm 0.110 \pm 0.146$
4–5	$2.017 \pm 0.081 \pm 0.120$
5–6	$1.527 \pm 0.073 \pm 0.091$
6–7	$1.085 \pm 0.048 \pm 0.065$
7–8	$0.738 \pm 0.038 \pm 0.044$
8–10	$0.424 \pm 0.018 \pm 0.027$
10–12	$0.200 \pm 0.011 \pm 0.013$
12–14	$0.093 \pm 0.007 \pm 0.005$
14–24	$0.017 \pm 0.001 \pm 0.001$

Table B.5 Differential cross-sections $\mathrm{d}\sigma/\mathrm{d}y_{\text{di-}J/\psi}$ [nb] of di-J/ψ production. The first uncertainties are statistical, and the second are systematic uncertainties.

$y_{\text{di-}J/\psi}$	$\mathrm{d}\sigma/\mathrm{d}y_{\text{di-}J/\psi}$ [nb]
2.00–2.25	$3.28 \pm 0.64 \pm 0.29$
2.25–2.50	$7.75 \pm 0.53 \pm 0.69$
2.50–2.75	$8.66 \pm 0.36 \pm 0.52$
2.75–3.00	$9.88 \pm 0.32 \pm 0.59$
3.00–3.25	$10.83 \pm 0.32 \pm 0.62$
3.25–3.50	$9.18 \pm 0.30 \pm 0.54$
3.50–3.75	$6.66 \pm 0.21 \pm 0.54$
3.75–4.00	$5.26 \pm 0.19 \pm 0.44$
4.00–4.25	$3.31 \pm 0.19 \pm 0.35$
4.25–4.50	$1.06 \pm 0.16 \pm 0.12$

Table B.6 Differential cross-sections $\mathrm{d}\sigma/\mathrm{d}m_{\text{di-}J/\psi}$ [nb/GeV] of di-J/ψ production. The first uncertainties are statistical, and the second are systematic uncertainties.

$m_{\text{di-}J/\psi}$ [GeV]	$\mathrm{d}\sigma/\mathrm{d}m_{\text{di-}J/\psi}$ [nb/GeV]
6–7	$5.059 \pm 0.200 \pm 0.283$
7–8	$4.364 \pm 0.131 \pm 0.244$
8–9	$2.851 \pm 0.092 \pm 0.155$
9–10	$1.555 \pm 0.067 \pm 0.085$
10–11	$1.092 \pm 0.062 \pm 0.062$
11–12	$0.595 \pm 0.049 \pm 0.034$
12–13	$0.344 \pm 0.037 \pm 0.026$
13–14	$0.207 \pm 0.029 \pm 0.016$
14–15	$0.108 \pm 0.015 \pm 0.008$
15–18	$0.047 \pm 0.005 \pm 0.003$
18–24	$0.008 \pm 0.002 \pm 0.001$

Table B.7 Differential cross-sections $\mathrm{d}\sigma/\mathrm{d}p_{\mathrm{T}}^{J/\psi}$ [nb/GeV] of di-J/ψ production. The first uncertainties are statistical, and the second are systematic uncertainties.

$p_{\mathrm{T}}^{J/\psi}$ [GeV]	$\mathrm{d}\sigma/\mathrm{d}p_{\mathrm{T}}^{J/\psi}$ [nb/GeV]
0–1	$2.209 \pm 0.093 \pm 0.132$
1–2	$4.255 \pm 0.124 \pm 0.255$
2–3	$3.798 \pm 0.090 \pm 0.208$
3–4	$2.464 \pm 0.062 \pm 0.135$
4–5	$1.536 \pm 0.044 \pm 0.085$
5–6	$0.878 \pm 0.027 \pm 0.048$
6–7	$0.489 \pm 0.019 \pm 0.028$
7–8	$0.293 \pm 0.013 \pm 0.016$
8–9	$0.177 \pm 0.010 \pm 0.011$
9–10	$0.086 \pm 0.007 \pm 0.005$
10–12	$0.048 \pm 0.003 \pm 0.003$
12–14	$0.016 \pm 0.002 \pm 0.001$

Table B.8 Differential cross-sections $\mathrm{d}\sigma/\mathrm{d}y_{J/\psi}$ [nb] of di-J/ψ production. The first uncertainties are statistical, and the second are systematic uncertainties.

$y_{J/\psi}$	$\mathrm{d}\sigma/\mathrm{d}y_{J/\psi}$ [nb]
2.00–2.25	$8.93 \pm 0.56 \pm 0.65$
2.25–2.50	$7.69 \pm 0.29 \pm 0.56$
2.50–2.75	$8.01 \pm 0.21 \pm 0.44$
2.75–3.00	$7.20 \pm 0.18 \pm 0.39$
3.00–3.25	$7.05 \pm 0.16 \pm 0.38$
3.25–3.50	$6.61 \pm 0.15 \pm 0.36$
3.50–3.75	$6.28 \pm 0.15 \pm 0.45$
3.75–4.00	$5.68 \pm 0.15 \pm 0.41$
4.00–4.25	$4.65 \pm 0.16 \pm 0.39$
4.25–4.50	$3.78 \pm 0.20 \pm 0.32$

Table B.9 Differential cross-sections $\mathrm{d}\sigma/\mathrm{d}\theta_{\mathrm{CS}}$ [nb] of di-J/ψ production. The first uncertainties are statistical, and the second are systematic uncertainties.

θ_{CS}/π	$\mathrm{d}\sigma/\mathrm{d}\theta_{\mathrm{CS}}$ [nb]
0/12–1/12	$1.54 \pm 0.21 \pm 0.10$
1/12–2/12	$4.40 \pm 0.29 \pm 0.30$
2/12–3/12	$5.24 \pm 0.28 \pm 0.30$
3/12–4/12	$5.78 \pm 0.35 \pm 0.32$
4/12–5/12	$6.45 \pm 0.28 \pm 0.36$
5/12–6/12	$7.35 \pm 0.34 \pm 0.41$
6/12–7/12	$8.04 \pm 0.54 \pm 0.48$
7/12–8/12	$6.32 \pm 0.28 \pm 0.38$
8/12–9/12	$5.92 \pm 0.27 \pm 0.33$
9/12–10/12	$5.85 \pm 0.29 \pm 0.33$
10/12–11/12	$3.89 \pm 0.26 \pm 0.24$
11/12–12/12	$1.86 \pm 0.21 \pm 0.11$

Table B.10 Differential cross-sections $d\sigma/d\phi_{CS}$ [nb] of di-J/ψ production. The first uncertainties are statistical, and the second are systematic uncertainties.

ϕ_{CS}/π	$d\sigma/d\phi_{CS}$ [nb]
0/12–1/12	$5.10 \pm 0.29 \pm 0.28$
1/12–2/12	$5.54 \pm 0.31 \pm 0.31$
2/12–3/12	$5.47 \pm 0.34 \pm 0.31$
3/12–4/12	$5.19 \pm 0.33 \pm 0.29$
4/12–5/12	$5.59 \pm 0.39 \pm 0.32$
5/12–6/12	$4.72 \pm 0.26 \pm 0.27$
6/12–7/12	$5.07 \pm 0.30 \pm 0.29$
7/12–8/12	$5.22 \pm 0.30 \pm 0.30$
8/12–9/12	$5.57 \pm 0.36 \pm 0.33$
9/12–10/12	$4.73 \pm 0.27 \pm 0.28$
10/12–11/12	$5.68 \pm 0.29 \pm 0.32$
11/12–12/12	$4.66 \pm 0.28 \pm 0.26$

Table B.11 Differential cross-sections $d\sigma/d\Delta y$ [nb] of di-J/ψ production in SPS. The first uncertainties are statistical, and the second are systematic uncertainties.

Δy	$d\sigma/d\Delta y$ [nb]
0.0–0.2	$12.76 \pm 1.29 \pm 1.13$
0.2–0.4	$8.72 \pm 1.03 \pm 0.85$
0.4–0.6	$6.97 \pm 0.94 \pm 0.74$
0.6–0.8	$4.32 \pm 0.80 \pm 0.62$
0.8–1.0	$2.89 \pm 0.70 \pm 0.53$
1.0–1.2	$1.74 \pm 0.60 \pm 0.43$
1.2–1.4	$1.15 \pm 0.53 \pm 0.37$
1.4–1.6	$0.75 \pm 0.45 \pm 0.31$
1.6–1.8	$0.37 \pm 0.39 \pm 0.24$
1.8–2.0	$0.22 \pm 0.31 \pm 0.22$
2.0–2.5	$-0.07 \pm 0.16 \pm 0.08$

Table B.12 Differential cross-sections $d\sigma/d\Delta\phi$ [nb] of di-J/ψ production in SPS. The first uncertainties are statistical, and the second are systematic uncertainties.

$\Delta\phi/\pi$	$d\sigma/d\Delta\phi$ [nb]
0.0–0.1	$3.65 \pm 0.48 \pm 0.39$
0.1–0.2	$3.11 \pm 0.49 \pm 0.37$
0.2–0.3	$2.08 \pm 0.45 \pm 0.33$
0.3–0.4	$2.14 \pm 0.48 \pm 0.33$
0.4–0.5	$2.26 \pm 0.52 \pm 0.34$
0.5–0.6	$1.93 \pm 0.47 \pm 0.33$
0.6–0.7	$2.09 \pm 0.48 \pm 0.33$
0.7–0.8	$2.01 \pm 0.46 \pm 0.33$
0.8–0.9	$2.43 \pm 0.44 \pm 0.34$
0.9–1.0	$3.48 \pm 0.48 \pm 0.37$

Table B.13 Differential cross-sections $d\sigma/d\mathcal{A}_{p_T}$ [nb] of di-J/ψ production in SPS. The first uncertainties are statistical, and the second are systematic uncertainties.

$\mathcal{A}_{p_T}$	$d\sigma/d\mathcal{A}_{p_T}$ [nb]
0.0–0.1	$16.31 \pm 2.26 \pm 1.83$
0.1–0.2	$15.19 \pm 2.15 \pm 1.76$
0.2–0.3	$14.50 \pm 2.22 \pm 1.67$
0.3–0.4	$11.78 \pm 1.93 \pm 1.48$
0.4–0.5	$7.65 \pm 1.77 \pm 1.32$
0.5–0.6	$7.41 \pm 1.44 \pm 1.14$
0.6–0.7	$3.37 \pm 1.14 \pm 0.77$
0.7–0.8	$2.04 \pm 0.90 \pm 0.54$
0.8–0.9	$0.48 \pm 0.54 \pm 0.32$
0.9–1.0	$0.30 \pm 0.21 \pm 0.10$

Table B.14 Differential cross-sections $\mathrm{d}\sigma/\mathrm{d}p_{\mathrm{T}}^{\text{di-}J/\psi}$ [nb/GeV] of di-J/ψ production in SPS. The first uncertainties are statistical, and the second are systematic uncertainties.

$p_{\mathrm{T}}^{\text{di-}J/\psi}$ [GeV]	$\mathrm{d}\sigma/\mathrm{d}p_{\mathrm{T}}^{\text{di-}J/\psi}$ [nb/GeV]
0–1	$0.886 \pm 0.116 \pm 0.084$
1–2	$1.196 \pm 0.225 \pm 0.173$
2–3	$1.229 \pm 0.279 \pm 0.201$
3–4	$1.026 \pm 0.241 \pm 0.184$
4–5	$0.827 \pm 0.186 \pm 0.149$
5–6	$0.693 \pm 0.139 \pm 0.107$
6–7	$0.529 \pm 0.092 \pm 0.074$
7–8	$0.390 \pm 0.062 \pm 0.048$
8–10	$0.249 \pm 0.031 \pm 0.028$
10–12	$0.134 \pm 0.014 \pm 0.013$
12–14	$0.069 \pm 0.008 \pm 0.005$
14–24	$0.015 \pm 0.001 \pm 0.001$

Table B.15 Differential cross-sections $\mathrm{d}\sigma/\mathrm{d}y_{\text{di-}J/\psi}$ [nb] of di-J/ψ production in SPS. The first uncertainties are statistical, and the second are systematic uncertainties.

$y_{\text{di-}J/\psi}$	$\mathrm{d}\sigma/\mathrm{d}y_{\text{di-}J/\psi}$ [nb]
2.00–2.25	$2.32 \pm 0.65 \pm 0.29$
2.25–2.50	$4.89 \pm 0.67 \pm 0.69$
2.50–2.75	$4.20 \pm 0.72 \pm 0.59$
2.75–3.00	$4.21 \pm 0.86 \pm 0.72$
3.00–3.25	$4.59 \pm 0.94 \pm 0.77$
3.25–3.50	$3.63 \pm 0.84 \pm 0.68$
3.50–3.75	$2.66 \pm 0.60 \pm 0.62$
3.75–4.00	$2.75 \pm 0.40 \pm 0.46$
4.00–4.25	$2.04 \pm 0.26 \pm 0.36$
4.25–4.50	$0.70 \pm 0.16 \pm 0.12$

Table B.16 Differential cross-sections $\mathrm{d}\sigma/\mathrm{d}m_{\text{di-}J/\psi}$ [nb/GeV] of di-J/ψ production in SPS. The first uncertainties are statistical, and the second are systematic uncertainties.

$m_{\text{di-}J/\psi}$ [GeV]	$\mathrm{d}\sigma/\mathrm{d}m_{\text{di-}J/\psi}$ [nb/GeV]
6–7	$3.147 \pm 0.336 \pm 0.286$
7–8	$2.039 \pm 0.353 \pm 0.290$
8–9	$1.283 \pm 0.240 \pm 0.190$
9–10	$0.535 \pm 0.159 \pm 0.117$
10–11	$0.446 \pm 0.110 \pm 0.078$
11–12	$0.194 \pm 0.075 \pm 0.047$
12–13	$0.101 \pm 0.050 \pm 0.033$
13–14	$0.063 \pm 0.035 \pm 0.020$
14–15	$0.023 \pm 0.019 \pm 0.011$
15–18	$0.014 \pm 0.007 \pm 0.004$
18–24	$0.004 \pm 0.002 \pm 0.001$

Table B.17 Differential cross-sections $\mathrm{d}\sigma/\mathrm{d}p_{\mathrm{T}}^{J/\psi}$ [nb/GeV] of di-J/ψ production in SPS. The first uncertainties are statistical, and the second are systematic uncertainties.

$p_{\mathrm{T}}^{J/\psi}$ [GeV]	$\mathrm{d}\sigma/\mathrm{d}p_{\mathrm{T}}^{J/\psi}$ [nb/GeV]
0–1	$0.966 \pm 0.198 \pm 0.159$
1–2	$1.907 \pm 0.354 \pm 0.303$
2–3	$1.807 \pm 0.295 \pm 0.246$
3–4	$1.173 \pm 0.192 \pm 0.160$
4–5	$0.804 \pm 0.112 \pm 0.095$
5–6	$0.484 \pm 0.062 \pm 0.052$
6–7	$0.280 \pm 0.035 \pm 0.029$
7–8	$0.178 \pm 0.021 \pm 0.017$
8–9	$0.114 \pm 0.014 \pm 0.011$
9–10	$0.049 \pm 0.009 \pm 0.006$
10–12	$0.030 \pm 0.004 \pm 0.003$
12–14	$0.010 \pm 0.002 \pm 0.001$

Table B.18 Differential cross-sections $d\sigma/dy_{J/\psi}$ [nb] of di-J/ψ production in SPS. The first uncertainties are statistical, and the second are systematic uncertainties.

$y_{J/\psi}$	$d\sigma/dy_{J/\psi}$ [nb]
2.00–2.25	$4.92 \pm 0.79 \pm 0.68$
2.25–2.50	$3.72 \pm 0.63 \pm 0.61$
2.50–2.75	$4.09 \pm 0.59 \pm 0.50$
2.75–3.00	$3.42 \pm 0.56 \pm 0.47$
3.00–3.25	$3.44 \pm 0.53 \pm 0.44$
3.25–3.50	$3.19 \pm 0.51 \pm 0.43$
3.50–3.75	$3.08 \pm 0.48 \pm 0.49$
3.75–4.00	$2.76 \pm 0.44 \pm 0.45$
4.00–4.25	$1.97 \pm 0.41 \pm 0.44$
4.25–4.50	$1.39 \pm 0.39 \pm 0.37$

Table B.19 Differential cross-sections $d\sigma/d\theta_{CS}$ [nb] of di-J/ψ production in SPS. The first uncertainties are statistical, and the second are systematic uncertainties.

θ_{CS}/π	$d\sigma/d\theta_{CS}$ [nb]
0/12–1/12	$0.38 \pm 0.27 \pm 0.14$
1/12–2/12	$1.43 \pm 0.51 \pm 0.38$
2/12–3/12	$1.87 \pm 0.55 \pm 0.40$
3/12–4/12	$2.73 \pm 0.55 \pm 0.38$
4/12–5/12	$3.64 \pm 0.49 \pm 0.39$
5/12–6/12	$4.53 \pm 0.52 \pm 0.42$
6/12–7/12	$5.21 \pm 0.67 \pm 0.48$
7/12–8/12	$3.50 \pm 0.49 \pm 0.41$
8/12–9/12	$2.88 \pm 0.51 \pm 0.39$
9/12–10/12	$2.49 \pm 0.55 \pm 0.41$
10/12–11/12	$0.91 \pm 0.49 \pm 0.35$
11/12–12/12	$0.69 \pm 0.27 \pm 0.15$

Table B.20 Differential cross-sections $\mathrm{d}\sigma/\mathrm{d}\phi_{\mathrm{CS}}$ [nb] of di-J/ψ production in SPS. The first uncertainties are statistical, and the second are systematic uncertainties.

ϕ_{CS}/π	$\mathrm{d}\sigma/\mathrm{d}\phi_{\mathrm{CS}}$ [nb]
0/12–1/12	$2.03 \pm 0.52 \pm 0.37$
1/12–2/12	$2.63 \pm 0.51 \pm 0.36$
2/12–3/12	$2.76 \pm 0.51 \pm 0.35$
3/12–4/12	$2.61 \pm 0.49 \pm 0.33$
4/12–5/12	$3.11 \pm 0.52 \pm 0.34$
5/12–6/12	$2.29 \pm 0.43 \pm 0.31$
6/12–7/12	$2.65 \pm 0.45 \pm 0.32$
7/12–8/12	$2.74 \pm 0.46 \pm 0.33$
8/12–9/12	$2.99 \pm 0.51 \pm 0.36$
9/12–10/12	$2.00 \pm 0.47 \pm 0.34$
10/12–11/12	$2.78 \pm 0.50 \pm 0.37$
11/12–12/12	$1.60 \pm 0.51 \pm 0.36$

Table B.21 Differential cross-sections $\mathrm{d}\sigma/\mathrm{d}p_{\mathrm{T}}^{\text{di-}J/\psi}$ [nb/GeV] of di-J/ψ production in intervals of $y_{\text{di-}J/\psi}$ with $6 < m_{\text{di-}J/\psi} < 9\,\mathrm{GeV}$. The first uncertainties are statistical, and the second are systematic uncertainties.

$p_{\mathrm{T}}^{\text{di-}J/\psi}$ [GeV]	$2.0 < y_{\text{di-}J/\psi} < 3.0$	$3.0 < y_{\text{di-}J/\psi} < 3.5$	$3.5 < y_{\text{di-}J/\psi} < 4.5$
0–1	$0.550 \pm 0.069 \pm 0.033$	$0.318 \pm 0.023 \pm 0.019$	$0.295 \pm 0.027 \pm 0.017$
1–2	$0.959 \pm 0.099 \pm 0.057$	$0.529 \pm 0.031 \pm 0.031$	$0.503 \pm 0.034 \pm 0.030$
2–3	$1.040 \pm 0.133 \pm 0.060$	$0.591 \pm 0.032 \pm 0.034$	$0.576 \pm 0.036 \pm 0.033$
3–4	$0.859 \pm 0.079 \pm 0.049$	$0.491 \pm 0.027 \pm 0.028$	$0.557 \pm 0.035 \pm 0.032$
4–5	$0.690 \pm 0.059 \pm 0.041$	$0.369 \pm 0.021 \pm 0.022$	$0.409 \pm 0.028 \pm 0.024$
5–6	$0.527 \pm 0.057 \pm 0.031$	$0.296 \pm 0.017 \pm 0.018$	$0.280 \pm 0.022 \pm 0.017$
6–7	$0.364 \pm 0.033 \pm 0.022$	$0.188 \pm 0.012 \pm 0.011$	$0.203 \pm 0.017 \pm 0.012$
7–8	$0.287 \pm 0.028 \pm 0.017$	$0.120 \pm 0.009 \pm 0.007$	$0.091 \pm 0.011 \pm 0.005$
8–10	$0.135 \pm 0.013 \pm 0.009$	$0.062 \pm 0.004 \pm 0.004$	$0.073 \pm 0.006 \pm 0.005$
10–12	$0.070 \pm 0.007 \pm 0.005$	$0.027 \pm 0.002 \pm 0.002$	$0.027 \pm 0.003 \pm 0.002$

Table B.22 Differential cross-sections $\mathrm{d}\sigma/\mathrm{d}p_{\mathrm{T}}^{\text{di-}J/\psi}$ [nb/GeV] of di-J/ψ production in SPS in intervals of $y_{\text{di-}J/\psi}$ with $6 < m_{\text{di-}J/\psi} < 9\,\text{GeV}$. The first uncertainties are statistical, and the second are systematic uncertainties.

$p_{\mathrm{T}}^{\text{di-}J/\psi}$ [GeV]	$2.0 < y_{\text{di-}J/\psi} < 3.0$	$3.0 < y_{\text{di-}J/\psi} < 3.5$	$3.5 < y_{\text{di-}J/\psi} < 4.5$
0–1	$0.379 \pm 0.073 \pm 0.031$	$0.194 \pm 0.029 \pm 0.019$	$0.176 \pm 0.032 \pm 0.018$
1–2	$0.530 \pm 0.116 \pm 0.061$	$0.223 \pm 0.053 \pm 0.038$	$0.210 \pm 0.054 \pm 0.037$
2–3	$0.512 \pm 0.153 \pm 0.068$	$0.236 \pm 0.059 \pm 0.043$	$0.236 \pm 0.060 \pm 0.041$
3–4	$0.376 \pm 0.104 \pm 0.060$	$0.182 \pm 0.051 \pm 0.037$	$0.265 \pm 0.054 \pm 0.037$
4–5	$0.324 \pm 0.079 \pm 0.048$	$0.144 \pm 0.038 \pm 0.028$	$0.197 \pm 0.041 \pm 0.028$
5–6	$0.280 \pm 0.066 \pm 0.034$	$0.155 \pm 0.026 \pm 0.019$	$0.146 \pm 0.029 \pm 0.018$
6–7	$0.207 \pm 0.040 \pm 0.023$	$0.104 \pm 0.017 \pm 0.012$	$0.123 \pm 0.020 \pm 0.012$
7–8	$0.194 \pm 0.031 \pm 0.017$	$0.072 \pm 0.011 \pm 0.007$	$0.047 \pm 0.012 \pm 0.006$
8–10	$0.094 \pm 0.014 \pm 0.008$	$0.043 \pm 0.005 \pm 0.004$	$0.055 \pm 0.007 \pm 0.005$
10–12	$0.057 \pm 0.008 \pm 0.004$	$0.021 \pm 0.003 \pm 0.002$	$0.022 \pm 0.003 \pm 0.002$

Table B.23 Differential cross-sections $\mathrm{d}\sigma/\mathrm{d}p_{\mathrm{T}}^{\text{di-}J/\psi}$ [nb/GeV] of di-J/ψ production in intervals of $m_{\text{di-}J/\psi}$ [GeV]. The first uncertainties are statistical, and the second are systematic uncertainties.

$p_{\mathrm{T}}^{\text{di-}J/\psi}$ [GeV]	$6 < m_{\text{di-}J/\psi} < 7\,\text{GeV}$	$7 < m_{\text{di-}J/\psi} < 9\,\text{GeV}$	$9 < m_{\text{di-}J/\psi} < 24\,\text{GeV}$
0–1	$0.563 \pm 0.063 \pm 0.033$	$0.626 \pm 0.053 \pm 0.037$	$0.217 \pm 0.035 \pm 0.013$
1–2	$0.867 \pm 0.087 \pm 0.051$	$1.138 \pm 0.071 \pm 0.067$	$0.512 \pm 0.056 \pm 0.030$
2–3	$1.025 \pm 0.132 \pm 0.059$	$1.213 \pm 0.069 \pm 0.069$	$0.627 \pm 0.046 \pm 0.036$
3–4	$0.743 \pm 0.062 \pm 0.043$	$1.167 \pm 0.074 \pm 0.067$	$0.632 \pm 0.053 \pm 0.036$
4–5	$0.587 \pm 0.051 \pm 0.035$	$0.883 \pm 0.050 \pm 0.053$	$0.544 \pm 0.039 \pm 0.032$
5–6	$0.363 \pm 0.041 \pm 0.022$	$0.742 \pm 0.050 \pm 0.044$	$0.413 \pm 0.032 \pm 0.025$
6–7	$0.264 \pm 0.024 \pm 0.016$	$0.491 \pm 0.032 \pm 0.029$	$0.335 \pm 0.026 \pm 0.020$
7–8	$0.182 \pm 0.024 \pm 0.011$	$0.327 \pm 0.022 \pm 0.019$	$0.231 \pm 0.020 \pm 0.014$
8–10	$0.102 \pm 0.010 \pm 0.007$	$0.170 \pm 0.011 \pm 0.011$	$0.152 \pm 0.010 \pm 0.010$
10–12	$0.059 \pm 0.007 \pm 0.004$	$0.067 \pm 0.006 \pm 0.004$	$0.073 \pm 0.006 \pm 0.005$

Table B.24 Differential cross-sections $\mathrm{d}\sigma/\mathrm{d}p_{\mathrm{T}}^{\text{di-}J/\psi}$ [nb/GeV] of di-J/ψ production in SPS in intervals of $m_{\text{di-}J/\psi}$ [GeV]. The first uncertainties are statistical, and the second are systematic uncertainties.

$p_{\mathrm{T}}^{\text{di-}J/\psi}$ [GeV]	$6 < m_{\text{di-}J/\psi} < 7\,\mathrm{GeV}$	$7 < m_{\text{di-}J/\psi} < 9\,\mathrm{GeV}$	$9 < m_{\text{di-}J/\psi} < 24\,\mathrm{GeV}$
0–1	$0.400 \pm 0.067 \pm 0.032$	$0.376 \pm 0.064 \pm 0.038$	$0.109 \pm 0.038 \pm 0.015$
1–2	$0.475 \pm 0.103 \pm 0.055$	$0.501 \pm 0.114 \pm 0.081$	$0.214 \pm 0.070 \pm 0.037$
2–3	$0.591 \pm 0.146 \pm 0.062$	$0.424 \pm 0.131 \pm 0.093$	$0.221 \pm 0.073 \pm 0.048$
3–4	$0.387 \pm 0.079 \pm 0.047$	$0.438 \pm 0.126 \pm 0.087$	$0.200 \pm 0.081 \pm 0.051$
4–5	$0.344 \pm 0.062 \pm 0.036$	$0.324 \pm 0.093 \pm 0.068$	$0.156 \pm 0.067 \pm 0.046$
5–6	$0.215 \pm 0.046 \pm 0.022$	$0.369 \pm 0.073 \pm 0.050$	$0.099 \pm 0.054 \pm 0.037$
6–7	$0.180 \pm 0.026 \pm 0.015$	$0.253 \pm 0.047 \pm 0.033$	$0.102 \pm 0.042 \pm 0.028$
7–8	$0.137 \pm 0.024 \pm 0.010$	$0.188 \pm 0.029 \pm 0.020$	$0.068 \pm 0.030 \pm 0.019$
8–10	$0.084 \pm 0.010 \pm 0.006$	$0.108 \pm 0.014 \pm 0.011$	$0.056 \pm 0.017 \pm 0.012$
10–12	$0.054 \pm 0.007 \pm 0.004$	$0.048 \pm 0.006 \pm 0.004$	$0.031 \pm 0.009 \pm 0.006$

Table B.25 Differential cross-sections $\mathrm{d}\sigma/\mathrm{d}\Delta y$ [nb] of J/ψ-$\psi(2S)$ production. The first uncertainties are statistical, and the second are systematic uncertainties.

Δy	$\mathrm{d}\sigma/\mathrm{d}\Delta y$ [nb]
0.0–0.2	$6.33 \pm 2.37 \pm 0.55$
0.2–0.6	$2.36 \pm 0.87 \pm 0.15$
0.6–1.0	$2.21 \pm 0.58 \pm 0.15$
1.0–1.4	$2.44 \pm 0.62 \pm 0.19$
1.4–1.8	$0.50 \pm 0.34 \pm 0.05$
1.8–2.5	$0.30 \pm 0.26 \pm 0.04$

Table B.26 Differential cross-sections $\mathrm{d}\sigma/\mathrm{d}\Delta\phi$ [nb] of J/ψ-$\psi(2S)$ production. The first uncertainties are statistical, and the second are systematic uncertainties.

$\Delta\phi/\pi$	$\mathrm{d}\sigma/\mathrm{d}\Delta\phi$ [nb]
0.0–0.2	$16.31 \pm 0.80 \pm 1.22$
0.2–0.4	$15.47 \pm 0.47 \pm 1.12$
0.4–0.6	$2.94 \pm 0.33 \pm 0.24$
0.6–0.8	$8.73 \pm 0.48 \pm 0.64$
0.8–1.0	$10.36 \pm 0.36 \pm 0.76$

Table B.27 Differential cross-sections $\mathrm{d}\sigma/\mathrm{d}p_{\mathrm{T}}^{J/\psi\text{-}\psi(2S)}$ [nb/GeV] of J/ψ-$\psi(2S)$ production. The first uncertainties are statistical, and the second are systematic uncertainties.

$p_{\mathrm{T}}^{J/\psi\text{-}\psi(2S)}$ [GeV]	$\mathrm{d}\sigma/\mathrm{d}p_{\mathrm{T}}^{J/\psi\text{-}\psi(2S)}$ [nb/GeV]
0–2	$0.461 \pm 0.158 \pm 0.039$
2–4	$0.609 \pm 0.174 \pm 0.045$
4–6	$0.699 \pm 0.252 \pm 0.049$
6–8	$0.178 \pm 0.071 \pm 0.013$
8–12	$0.109 \pm 0.027 \pm 0.008$
12–24	$0.011 \pm 0.003 \pm 0.001$

Table B.28 Differential cross-sections $\mathrm{d}\sigma/\mathrm{d}y_{J/\psi\text{-}\psi(2S)}$ [nb] of J/ψ-$\psi(2S)$ production. The first uncertainties are statistical, and the second are systematic uncertainties.

$y_{J/\psi\text{-}\psi(2S)}$	$\mathrm{d}\sigma/\mathrm{d}y_{J/\psi\text{-}\psi(2S)}$ [nb]
2.0–2.5	$1.89 \pm 0.99 \pm 0.22$
2.5–3.0	$2.89 \pm 0.64 \pm 0.21$
3.0–3.5	$2.42 \pm 0.57 \pm 0.16$
3.5–4.0	$1.41 \pm 0.38 \pm 0.12$
4.0–4.5	$0.24 \pm 0.19 \pm 0.04$

Table B.29 Differential cross-sections $\mathrm{d}\sigma/\mathrm{d}m_{J/\psi\text{-}\psi(2S)}$ [nb/GeV] of J/ψ-$\psi(2S)$ production. The first uncertainties are statistical, and the second are systematic uncertainties.

$m_{J/\psi\text{-}\psi(2S)}$ [GeV]	$\mathrm{d}\sigma/\mathrm{d}m_{J/\psi\text{-}\psi(2S)}$ [nb/GeV]
6.5–8.0	$1.446 \pm 0.378 \pm 0.101$
8.0–9.5	$0.693 \pm 0.207 \pm 0.047$
9.5–11.0	$0.291 \pm 0.144 \pm 0.023$
11.0–12.5	$0.265 \pm 0.082 \pm 0.022$
12.5–14.0	$0.187 \pm 0.110 \pm 0.019$
14.0–24.0	$0.015 \pm 0.005 \pm 0.001$

Table B.30 Cross-section ratios between J/ψ-$\psi(2S)$ and di-J/ψ production $\sigma_{J/\psi\text{-}\psi(2S)}/\sigma_{\text{di-}J/\psi}$ in intervals of Δy. The first uncertainties are statistical, and the second are systematic uncertainties.

Δy	$\sigma_{J/\psi\text{-}\psi(2S)}/\sigma_{\text{di-}J/\psi}$
0.0–2.2	$0.33 \pm 0.12 \pm 0.02$
0.2–0.6	$0.17 \pm 0.06 \pm 0.01$
0.6–1.0	$0.27 \pm 0.07 \pm 0.01$
1.0–1.4	$0.49 \pm 0.13 \pm 0.03$
1.4–1.8	$0.17 \pm 0.12 \pm 0.01$
1.8–2.5	$0.36 \pm 0.32 \pm 0.05$

Table B.31 Cross-section ratios between J/ψ-$\psi(2S)$ and di-J/ψ production $\sigma_{J/\psi\text{-}\psi(2S)}/\sigma_{\text{di-}J/\psi}$ in intervals of $\Delta\phi$. The first uncertainties are statistical, and the second are systematic uncertainties.

$\Delta\phi/\pi$	$\sigma_{J/\psi\text{-}\psi(2S)}/\sigma_{\text{di-}J/\psi}$
0–2	$0.36 \pm 0.13 \pm 0.02$
2–4	$0.43 \pm 0.10 \pm 0.02$
4–6	$0.08 \pm 0.07 \pm 0.00$
6–8	$0.24 \pm 0.10 \pm 0.01$
8–12	$0.24 \pm 0.06 \pm 0.01$

Table B.32 Cross-section ratios between J/ψ-$\psi(2S)$ and di-J/ψ $\sigma_{J/\psi\text{-}\psi(2S)}/\sigma_{\text{di-}J/\psi}$ in intervals of $p_{\text{T}}^{\text{di-}\psi}$ [GeV]. The first uncertainties are statistical, and the second are systematic uncertainties.

$p_{\text{T}}^{\text{di-}\psi}$ [GeV]	$\sigma_{J/\psi\text{-}\psi(2S)}/\sigma_{\text{di-}J/\psi}$
0–2	$0.23 \pm 0.08 \pm 0.01$
2–4	$0.23 \pm 0.06 \pm 0.01$
4–6	$0.39 \pm 0.14 \pm 0.02$
6–8	$0.20 \pm 0.08 \pm 0.01$
8–12	$0.35 \pm 0.09 \pm 0.02$
12–24	$0.36 \pm 0.10 \pm 0.03$

Table B.33 Cross-section ratios between J/ψ -$\psi(2S)$ and di-J/ψ $\sigma_{J/\psi\text{-}\psi(2S)}/\sigma_{\text{di-}J/\psi}$ in intervals of $y_{\text{di-}\psi}$. The first uncertainties are statistical, and the second are systematic uncertainties.

$y_{\text{di-}\psi}$	$\sigma_{J/\psi\text{-}\psi(2S)}/\sigma_{\text{di-}J/\psi}$
2.0–2.5	$0.34 \pm 0.18 \pm 0.03$
2.5–3.0	$0.31 \pm 0.07 \pm 0.01$
3.0–3.5	$0.24 \pm 0.06 \pm 0.01$
3.5–4.0	$0.24 \pm 0.06 \pm 0.01$
4.0–4.5	$0.11 \pm 0.09 \pm 0.01$

APPENDIX C PERSONAL CONTRIBUTION TO THE LHCB UPGRADE

The goal of LHCb upgrade is to increase statistics by around 10 times during the third run (Run 3) and the fourth run (Run 4) of LHC. It requires the upgraded detector to be operated at a instantaneous luminosity 5 times higher than before, and replaces the electronics of all sub-detectors to cope with a hardware triggerless readout at 40 MHz. For the tracker system, the current T1-T3 stations will be fully replaced by the Scintillating Fibre (SciFi) tracker system based on the scintillating fibre technology. The author heavily participated in LHCb upgrade activities related to the SciFi tracker, including the quality assurance of the front-end electronics, and the analysis of the SciFi test beam data.

For the front-end electronics, the PACIFIC ASIC is developed to process and digitise the analogue signal from the Silicon photomultiplier (SiPM) arrays of the SciFi tracker. A quality assurance (QA) system is designed to test the PACIFIC ASIC and its carrier board (each board carries 4 ASICs). More than 20k ASICs and around 2.5k carrier boards were produced and to be tested by the QA system. The author

- developed the software of the QA system both for PACIFIC ASIC and its carrier board;
- participated in the QA test of PACIFIC ASICs for pre-production (∼1k ASICs) at Heidelberg University, and the QA test of carrier boards for pre-production (∼50 boards) at Tsinghua University;
- analysed the QA test results of pre-production, and then optimised the QA procedure, tuned working parameters and QA criteria of the ASICs and boards for production based on the test results with the help of electronics experts;
- took the responsibility of the QA test of PACIFIC carrier boards for production at Tsinghua University (∼1.5k boards);
- participated in the QA test of the SciFi front-end read-out boxes at CERN.

The SciFi Tracker test beam was performed several times to study the performance of the tracker. The test beam at the CERN SPS in July 2018 was the first slice test of two full width scintillating fibre modules coupled to a full set of nearly final version of the front-end readout electronics. The goal of this test beam was to qualify complete chain of front-end electronics, and to verify the full system performance, especially for the studies of single

hit resolution, hit efficiency, and signal spillover into next bunch crossing. The author took over one of the analysis frameworks for SciFi test beam, and analysed the single-hit resolution at different positions along the fibre and under various configurations, including shaper settings, digitization threshold settings and clustering algorithm settings.

ACKNOWLEDGEMENTS

感谢导师的悉心指导。
感谢清华高能物理中心其他老师的帮助。
感谢北大 LHCb 组老师们的帮助。
感谢同学们的帮助。
感谢理论家。
感谢 LHCb 的实验家与工程师。

声 明

本人郑重声明：所呈交的学位论文，是本人在导师指导下，独立进行研究工作所取得的成果。尽我所知，除文中已经注明引用的内容外，本学位论文的研究成果不包含任何他人享有著作权的内容。对本论文所涉及的研究工作做出贡献的其他个人和集体，均已在文中以明确方式标明。

签 名：许士 日 期：2023.5.26

RESUME

Li Xu was born on 6th July 1996 in Haian, Jiangsu, China.

He began his bachelor's study in the Department of Engineering Physics, Tsinghua University in September 2014, majoring in engineering physics, and got a Bachelor of Engineering degree in July 2018.

He has started to pursue a doctor's degree in Physics in the Department of Engineering Physics, Tsinghua University since September 2018. During this period, he has made academic achievements as follows.

Journal article

[1] LHCb Collaboration, Aaij R, et al. Measurement of J/ψ production cross-sections in pp collisions at $\sqrt{s} = 5$ TeV[J/OL]. JHEP, 2021, 11: 181.

[2] Li Xu (on behalf of the LHCb Collaboration). Heavy flavour production in pp collisions at LHCb[C/OL]. Nucl. Part. Phys. Proc., 2022, 318-323: 7-11.

COMMENTS FROM THESIS SUPERVISOR

质子-质子碰撞中粲偶素的产生是粒子物理实验和理论研究的热点课题，而粲偶素对产生更是这一领域的前沿，对于深入理解强相互作用尤其是它在低能标下的非微扰效应具有重要科学意义。许立首先基于 LHCb 质心系能量为 5TeV 的质子-质子碰撞数据分别测量了瞬发和来自底强子衰变的 J/ψ 产生截面，在这一新的能量点下精确检验了 NRQCD、色玻璃凝聚 CGC 和 FONLL 等 QCD 理论计算，发现低横动量下 CGC+NRQCD 理论计算结果与不同能量下的瞬发 J/ψ 产生截面比与数据不一致。许立还利用 LHCb Run2 的 13TeV 的质子-质子碰撞数据，对双 J/ψ 以及 J/ψ-$\psi(2S)$ 的粲偶素对产生截面进行了精确测量，研究质子中胶子的横动量依赖 (TMD) 分布函数和质子中部分子之间的关联。对于 J/ψ 介子对产生，他在统计上区分了双部分子散射 (DPS) 与单部分子散射 (SPS) 的贡献，并从 DPS 贡献中提取出了部分子相互作用的有效截面, 与其他实验的测量结果基本一致。在 SPS 贡献中他利用介子对的横动量谱和 J/ψ 介子的方位角分布研究了胶子的 TMD 分布函数，在现有精度下没有观察到理论预言的横动量谱随其质量增大而变宽的现象；而测量的方位角分布显示出两倍标准差的不对称性，暗示非极化质子中可能存在线性极化的胶子。他还首次观测到 J/ψ-$\psi(2S)$ 介子对产生，但由于统计量不足无法区分 DPS 与 SPS 的贡献。该论文的两项实验数据分析工作，包括 J/ψ 和 $\psi(2S)$ 的信号拟合、瞬发和底强子信号的分离、探测器效率估计、截面计算、DPS 和 SPS 贡献的区分、方位角分布计算、系统误差分析等都由许立独立完成。他的工作为理解质子-质子碰撞中重夸克偶素产生机制以及质子中胶子的部分子分布函数提供了重要的实验参考。论文写作表述清晰、内容详实，是一篇优秀的博士论文。

RESOLUTION OF THESIS DEFENSE COMMITTEE

量子色动力学 (QCD) 是描述强相互作用的基本理论。粲偶素在质子-质子 pp 对撞中的产生是检验微扰 QCD 方法和研究 QCD 非微扰效应的理想过程。论文基于 LHCb 实验研究了粲偶素及粲偶素对的产生机制，并对 QCD 理论进行了精确检验。选题具有重要科学意义。

论文的主要工作和创新性成果为:

1. 测量了 5TeV 的 pp 对撞中瞬发和来自底强子衰变的 J/ψ 介子的产生截面。瞬发截面在高横动量与非相对论 QCD(NRQCD) 理论预言相符，而在低横动量与色玻璃凝聚 +NRQCD 计算结果有偏离; 来自底强子衰变的截面和固定项加次领头对数项的计算结果相符。

2. 测量了 13TeV 的 pp 对撞中 J/ψ 介子对和 $J/\psi-\psi(2S)$ 介子对的产生截面及其随多个运动学变量的变化。对 J/ψ 介子对，区分了双部分子散射 (DPS) 与单部分子散射 (SPS) 的贡献，测量了 DPS 过程有效截面，SPS 截面与次领头色单态理论计算相符，在 SPS 贡献中发现非极化质子中可能存在线性极化的胶子。$J/\psi-\psi(2S)$ 介子对总截面低于次领头色单态理论计算。

论文写作规范、数据详实、叙述清晰，反映出作者具有扎实的专业基础知识和实验技能，具备独立从事科学研究的能力。

答辩过程表达清楚，回答问题正确。经答辩委员会表决，一致同意通过博士学位论文答辩，建议授予许立同学理学博士学位，并推荐参评优秀博士论文。